



UNIVERSITÀ DEGLI STUDI DI MILANO
DIPARTIMENTO DI CHIMICA

Doctorate School in Industrial Chemistry – XXIX Cycle

**NEW APPROACHES FOR THE DESIGN, SCREENING AND
CHARACTERIZATION OF INNOVATIVE
SEMICONDUCTOR/OVERLAYER ARCHITECTURES FOR
PHOTO-DRIVEN WATER ELECTROLYSIS**

Tutor: **Prof. Sandra Rondinini**

Co-tutor: **Dott. Alessandro Minguzzi**

**Ph.D. Thesis of
Sara Morandi
Matricola: R10513**

Accademic Year: 2015/2016

Index

Index.....	2
Introduction.....	6
1. A strategy for competitive, secure and sustainable energy: Energy 2020	6
2. Water splitting.....	13
3. Photo Electrochemical Water splitting (PEC-WS).....	16
3.1 Semiconductors.....	17
3.2 Hematite (α -Fe ₂ O ₃) [40, 41].....	24
3.3 Overlayers.....	26
4. Work summary.....	29
Experimental section.....	34
1. Electrochemical techniques.....	34
1.1. Cyclic voltammetry [1].....	34
1.2. Potentiostatic techniques	37
1.3. Reference electrode: the calibration of saturated calomel electrode (SCE)	38
1.4. Scanning Electrochemical Microscopy (SECM) [5,6].....	41
1.4.1. UME tip	43
1.4.2. Operational mode.....	44
1.4.3. Approach curves.....	47
1.4.4. Generation-collection mode	48
1.4.5. Imaging.....	49
2. Chemical-physical techniques.....	51
2.1 Scanning Electron Microscopy (SEM).....	51

2.2	Transmission Electron Microscopy (TEM)	52
3.	Working electrodes for the electrochemical analysis	54
3.1	Tip preparation	54
3.2	Arrays preparation	55
3.3	Lab-scale electrodes preparation	57
3.4	Cavity-Microelectrodes (C-MEs)	57
3.5	Synthesis of hematite ($\alpha - \text{Fe}_2\text{O}_3$)	61
	Results and discussion	63
1.	Rapid screening of oxygen evolution reaction electrocatalysts deposited onto titanium sheets by SECM	63
1.1.	Introduction	63
1.2.	Experimental	67
1.2.1.	Sample preparation	67
1.2.2.	Tip preparation	68
1.2.3.	Arrays characterization by SECM	69
1.2.4.	Arrays characterization by SECM double pulse method	69
1.3.	Result and discussion	72
1.3.1.	Oxygen evolution electrocatalysts SECM screening	72
1.3.2.	Evaluation of oxygen evolution electrocatalysts by double pulse method	74
1.4.	Conclusions	80
2.	Study of different OER overlayers deposited onto hematite	81
2.1.	Introduction	81
2.2.	Experimental	85
2.2.1.	Synthesis of hematite	85
2.2.2.	Amorphous IrO_x deposition through SECM direct mode	85
2.2.3.	Sample preparation (array)	86
2.2.4.	Sample preparation (lab-scale electrodes)	87
2.2.5.	Tip preparation	87

2.2.6.	Arrays characterization by SECM.....	88
2.2.7.	Lab-scale electrodes characterization.....	89
2.2.8.	Evaluation of active surfaces through the study of electrode capacitances	90
2.3.	Result and discussion.....	92
2.3.1.	Amorphous Ir oxide.....	92
2.3.2.	Oxygen evolution photoelectrocatalysts SECM screening by a white light optical fiber	95
2.3.3.	Evaluation of Co _{0.9} /Ni _{0.1} photoelectrocatalyst by SECM images and double pulse method	104
2.3.4.	Evaluation of Fe _{0.6} Ni _{0.4} -based photoelectrocatalysts as lab-scale electrodes.....	107
2.3.5.	Evaluation of active surfaces through the study of electrode capacitances	109
2.4.	Conclusions.....	113
3.	Study of TiO ₂ , WO ₃ and BiVO ₄ nanoparticles prepared by cathodic corrosion methods ...	115
3.1.	Introduction.....	115
3.2.	Experimental.....	116
3.2.1.	NPs synthesis.....	116
3.2.2.	Sample preparation.....	117
3.2.3.	Tip preparation	120
3.3.	Result and discussion.....	121
3.4.	Conclusions.....	153
4.	The cavity-microelectrode (C-ME) as a tip for SECM.....	154
4.1	Introduction.....	154
4.2	Experimental.....	157
4.3	Result and discussion.....	159
4.3.1	Feedback mode.....	159
4.3.2	Stability of the C-ME	161
4.4	Conclusion	164
5.	Hematite/NiOOH architecture	165

5.1. Introduction.....	165
5.2. Experimental.....	167
5.2.1. Hematite/NiOOH preparation	167
5.2.2. Hematite/NiOOH characterization by SECM	168
5.2.3. Tip preparation	169
5.3. Result and discussion.....	170
5.4. Conclusion	172
Conclusions.....	176
Ringraziamenti.....	178

Introduction

1. A strategy for competitive, secure and sustainable energy: Energy 2020

The development of clean energy technologies around the world is progressing rapidly.

The European Council in 2007 adopted ambitious energy and climate change objectives for 2020: greenhouse gas emissions reduction by 20%, rising to 30% if the conditions are favourable, increment in the sharing of renewable energy to 20%, and improvement in energy efficiency up to 20%.

Total Primary Energy Supply (TPES), i.e. the extraction of energy from natural sources, has comparably increased in the last 40 years (**Figure 1**):

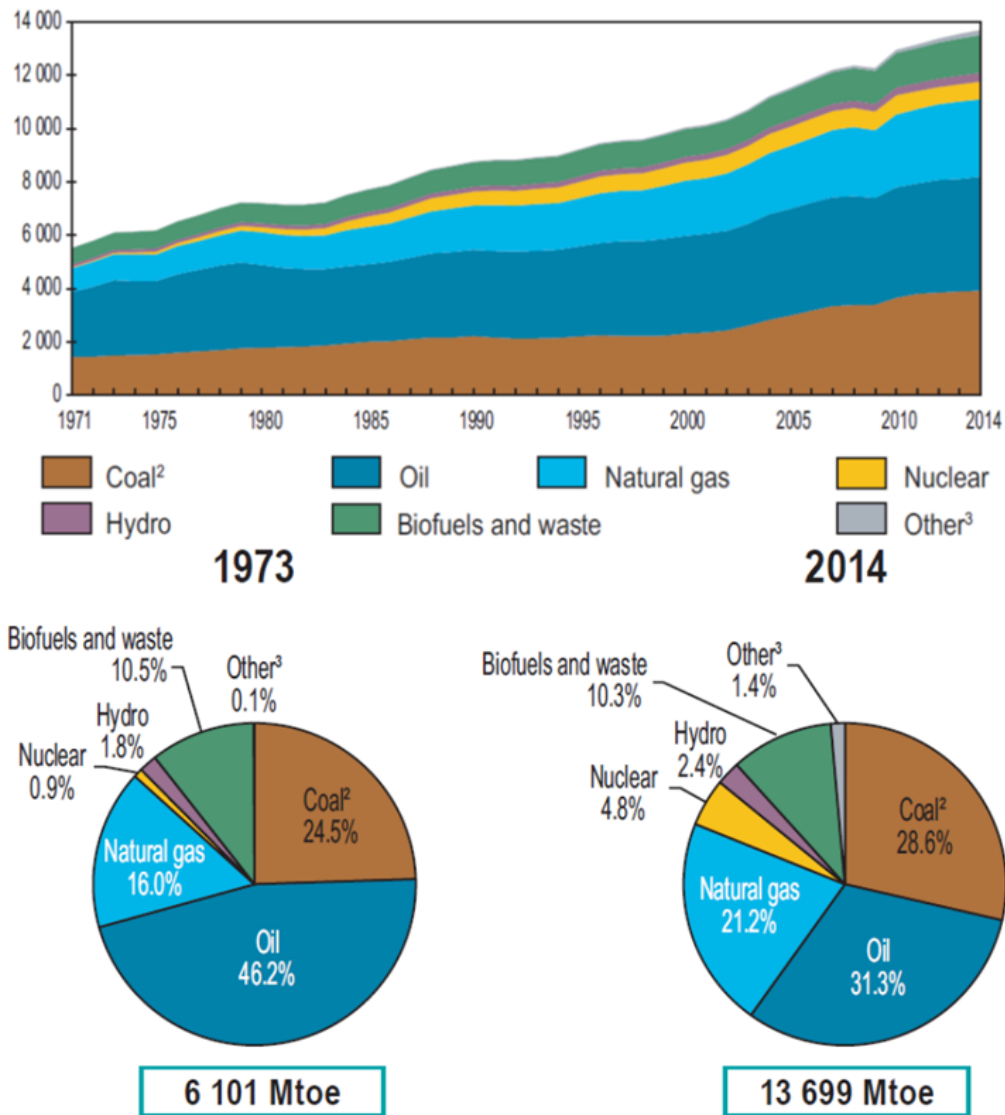


Figure 1: World TPES from 1971 to 2014 by fuel. ²Peat and oil shale are indicated with coal; ³“Other” includes geothermal, solar, wind, heat, etc.
 [International Energy Agency, Key world energy statistics[©], 2016, Pag. 6]

Unfortunately, while these targets have been positive and ambitious, the world is still largely dependent on fossil fuels to satisfy the current growth in global energy demand (**Figure 2**).

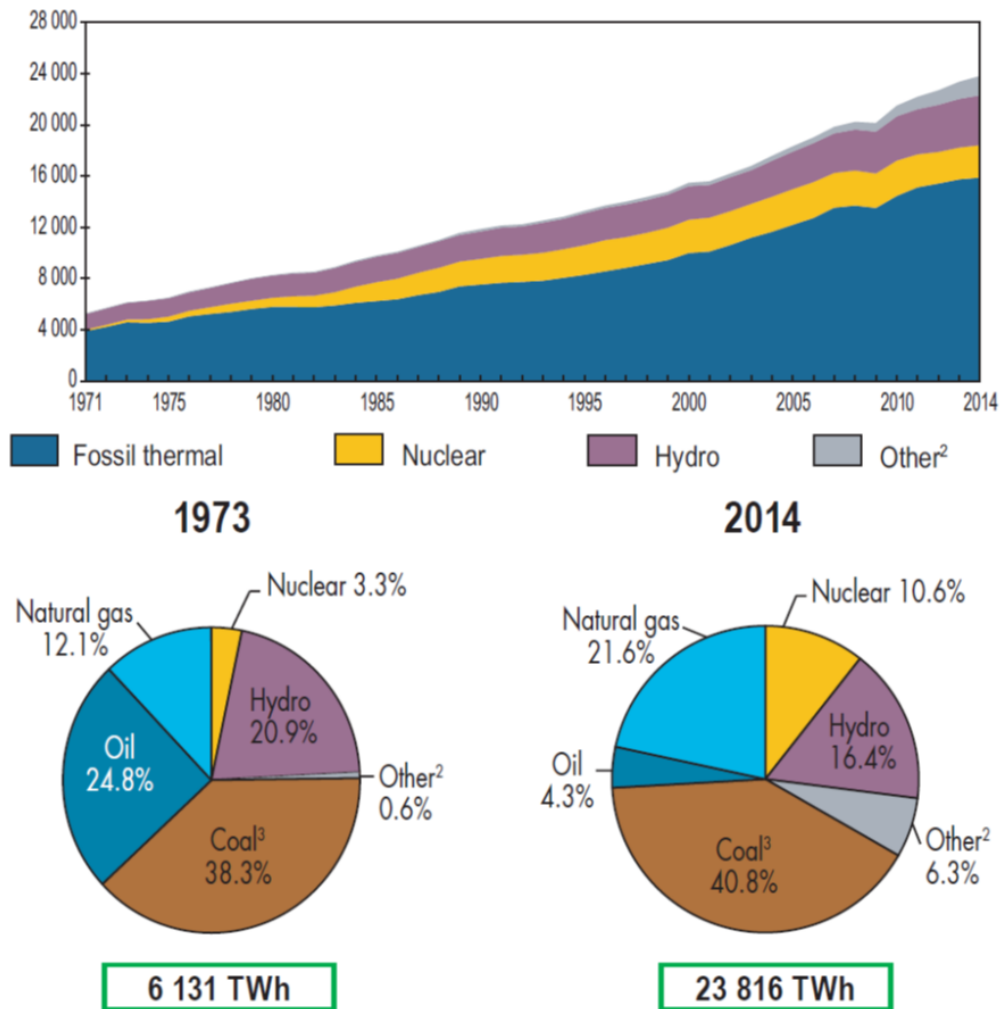


Figure 2: World electricity generation from 1971 to 2014 by fuel (TWh). ²“Other” includes geothermal, solar, wind, heat, etc. ³Peat and oil shale are indicated with coal. [International Energy Agency, Key world energy statistics[©], 2016, Pag. 24]

Between 1973 and 2014 the increment of more than 2% in the use of the coal to produce electricity is observed, due to the combined decrease in use of oil (about 20%) and the parallel increase of natural gas consumption (about 9%) and of coal (1.5%). In parallel, there was an enhancement in the generation of energy by natural gas ($\approx 10\%$), nuclear (7%) and renewables sources (about 6%). On the contrary, hydropower renewables decreased of more than 4%.

In **Figure 3** it is evident that the prevalent coal consumption derives from industrial applications, constantly growing, followed by commercial, agricultural and public activities.

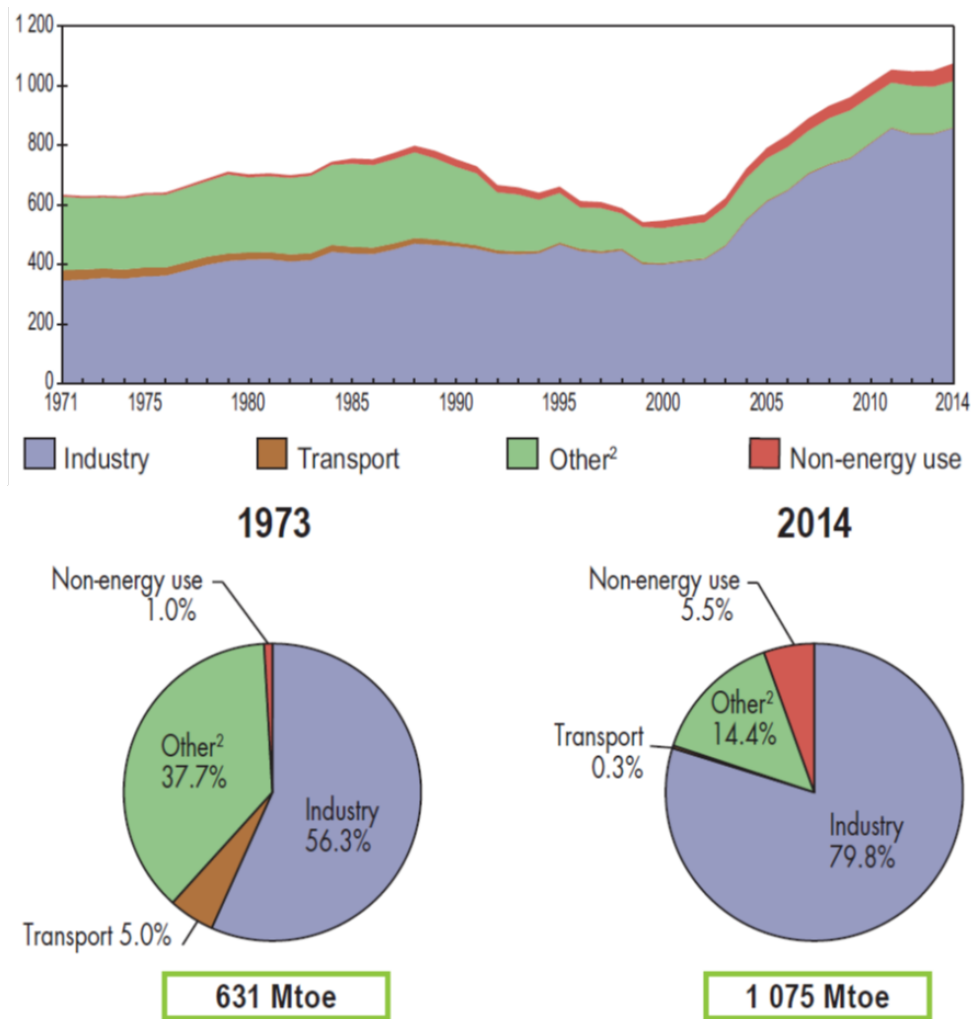


Figure 3: Total final consumption from 1971 to 2014 by sector. ²“Other” includes agricultural, commercial and public services.
 [International Energy Agency, *Key world energy statistics*®, 2016, Pag. 28]

The consequences of this trend are well-known: CO₂ emissions related to the energy consumption over the past decades have continuously increased (**Figure 4**).

Almost the 50% of the CO₂ emissions derives from the combustion of coal, followed by oil and natural gas.

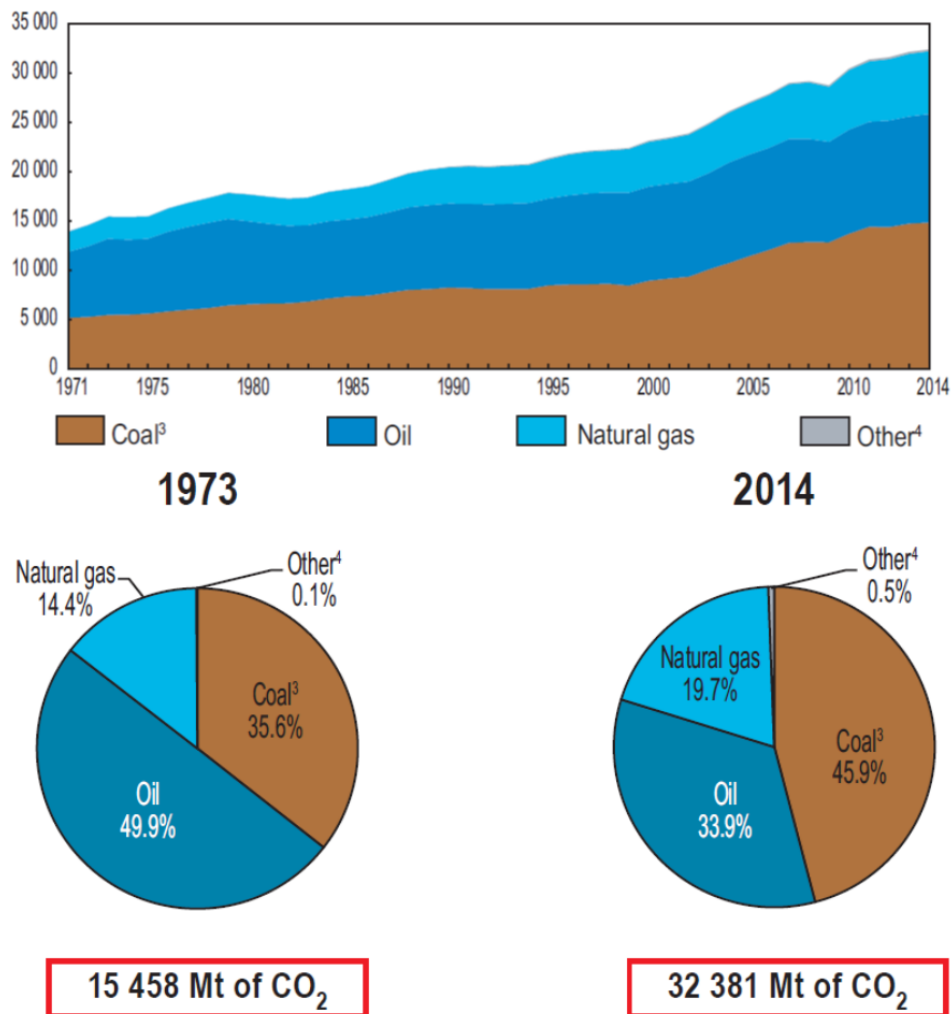


Figure 4: World CO₂ emissions from fuel combustion from 1971 and 2014 by fuel (Mt of CO₂).

³Peat and oil shale are indicated with coal; ⁴Included industrial waste and non-renewable municipal waste.

[International Energy Agency, Key world energy statistics[©], 2016, Pag. 44]

Within 2020, the European Union aims to reduce its greenhouse gas emissions by at least 20%, increase the share of renewable energy to at least 20% of consumption, and achieve energy savings of 20% or more. This is the set of measure to follow after the end of Kyoto Protocol.

The targets are of course hinder and combat the climate change and air pollutions and, at the same time, encourage the use of renewable energy sources, thus decreasing the dependence on fossil fuels.

The 2020 Energy Strategy priorities are schematically shown below [1]:

1. Review of the EU-ETS (European Union Emission Trading Scheme) System, able to limit the emissions from more than 11000 power stations and/or industrial plants and airlines operating between the member countries, covering around 45% of the EU's greenhouse gas emissions;

2. Promotion of the so-called “Effort sharing extra EU-ETS”, that provides to limit the emission coming from extra EU-ETS area (i.e. buildings, agriculture, transport). Different targets of emissions limitation are assigned to each member country (Italy: 13%);
3. Promotion of the CCS (Carbon Capture and Storage) process: it provides to capture waste CO₂ from large point sources, such as fossil fuel power plants, transport it to a storage site, and deposit it where it will not enter the atmosphere, normally an underground geological formation;
4. Energy coming from renewable sources: it aims to reach the production of more than 20% of energy needed for electric and thermal uses and for transport through renewable sources. To gain this value, some binding national targets are assigned (Italy: 17%). In particular, at least the 10% of the energy used in the transport has to come from renewable sources;
5. New CO₂ car emissions limits: by 2020 it will be 95 g CO₂/km;
6. Improvement of fossil fuels limitations: in their life cycle, the greenhouse gasses will be reduced of about 6%.

Renewable energy sources (RES) have an important role to play in combating climate change. Moreover, further deployment of renewable energy technologies has a potential to create hundreds of thousands of jobs in the EU.

Renewable energy production has grown rapidly in the last ten years, especially in a few key Member States with stable supportive policies. Over 1997 - 2007 the RES and waste generation park grew by around 80 GW whereas over 1990 – 1997 developments in this area represented just 15 GW. The RES and waste additionally installed capacity amounted to 64.4 GW over 2000-2007 while it was only 41.9 GW for thermal power plants. Wind power now forms the highest share of new production capacity and in 2007, it accounted for 25% of the net RES installed capacities.

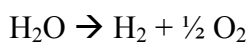
Currently, renewable sources are considered to be water (hydroelectric, wave, tidal), wind, sun (thermal and photovoltaics), biomasses and earth (geothermal). Some of them, such as wind power are available intermittently and often in remote locations, therefore the transmission and distribution network must be improved.

In this context, molecular hydrogen is progressively considered as one of the most effective environmentally friendly energy vectors. Indeed, at the moment it can be actually used as fuel in internal combustion engine built on the first car prototypes. Moreover, lots of efforts are continuously devoted to the development of fuel cells to produce electricity from hydrogen oxidation.

However, the main drawback of hydrogen is that it is not present on the earth as H_2 and thus must be obtained from other compounds, e.g. water.

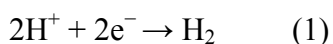
2. Water splitting

Water splitting is the general term for a chemical reaction in which water is separated into oxygen and hydrogen, for example by electrolysis, according to the following reaction:



Room-temperature water electrolysis is generally performed in aqueous acidic or alkaline electrolyte solutions. The water electrolysis under acidic condition is performed in a *Proton Exchange Membrane* (PEM) electrolyser.

At the cathode the reduction of protons to hydrogen (HER) takes place:



While at the anode the oxygen evolution reaction (OER) occurs:



Although PEM water electrolysis systems offers several advantages, like high energy efficiency, a fast, high-purity hydrogen (free from alkaline fogs) production rate and a compact design, their application remains hampered by the high cost of the catalysts and membranes [2, 3]. In particular, the U.S. Department of Energy (DOE) is working closely with its national laboratories, universities, and industry partners to overcome critical technical barriers to fuel cell commercialization [4].

Indeed, the development of efficient electrocatalysts for oxygen evolution reaction (OER) remains a key challenge in the water oxidation, since reaction (2) requires high overpotential on any electrode material.

Overpotential is the additional potential, beyond the thermodynamic requirement, needed to drive a reaction at a certain rate [5].

$$U = E_{rev} + \Sigma\eta$$

Where U is the electrode potential, E_{rev} the potential value under thermodynamically reversible conditions of the reaction occurring at the electrode and $\Sigma\eta$ the sum of the overpotentials related to the dissipative phenomena accompanying the reaction at the selected current density j .

The higher the overpotential, the higher the energy consumptions. The total overpotential is actually composed by different contributions:

$$\Sigma\eta = \Sigma\eta_{CT} + \Sigma\mu_{MT} + \Sigma\mu_{\Omega}$$

Where:

$\Sigma\eta_{CT}$ = sum of the overpotentials due to the electron transfer through the electrode (solid)/liquid interface;

$\Sigma\eta_{MT}$ = sum of the overpotentials due to the mass transfer of reactants and products to and from the reaction site;

$\Sigma\eta_{\Omega}$ = sum of the overpotentials due to the ohmic drops.

The acidic environment limits the catalysts for the oxygen-evolving reaction (OER) and hydrogen-evolving reaction (HER) to noble metals.

Indeed, on a bare metal (M), water adsorption and related oxygen species cover the surface before the liberation of O₂ and since the M-O bond strength is always stronger than the O-O dissociation energy, the OER always takes place at an oxide surface [6]. The role of the adsorbed intermediates is quite important. If the intermediate is weakly adsorbed, it is easily removed and cannot participate to the subsequent step. If otherwise it is too strongly bonded, it will hardly desorb, thus lowering the rate of the overall reaction.

This is the qualitative explanation of volcano plot proposed by Trasatti [6], based on Sabatier's principles, that consists on the correlation between the value of the enthalpy of atomic oxygen adsorption and the overpotential recorded (at constant current density) on several materials.

According to the volcano plot, suitable OER electrocatalysts in acidic media mainly involved materials on top of it and are represented by IrO₂, RuO₂, PtO₂, MnO₂ [7].

Among them RuO₂ is the more active one, followed by IrO₂, which in turn is ≈ 20 times more stable in acid media than RuO₂ [8].

Consequently, IrO₂ is considered as the benchmark material. Recent studies [9, 10] highlighted how it is still the most active OER electrocatalyst. However, given the high cost of the precious metal, large research efforts have been devoted to the development materials in which the IrO₂ was mixed with cheaper and more abundant elements.

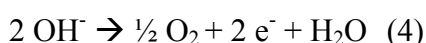
A few example of the Ir-based compositions are: IrO₂+SnO₂ [11, 12, 13, 14], IrO₂+Ta₂O₅ [15, 16, 17, 18, 19, 20, 21, 22, 23] and IrO₂+Sb₂O₅+SnO₂ [24, 25].

Compared with PEM water electrolysis, alkaline water electrolysis exhibits inherent low-cost characteristic because it can use a non-precious catalyst and a separator.

In alkaline water splitting, the reduction reaction can be written as:



While the OER is performed by an anodic oxidation of OH^- :



As for acidic media, also in alkaline solution the research for suitable electrocatalysts for both HER and OER is needed.

Of course, they also have to be low cost and made of highly abundant elements.

Jaramillo [9, 26] found that the IrO_2 remains the most active OER electrocatalysts also in alkaline media.

However, also other cheaper composite materials showed comparable, or even higher, activities, as shown in **Figure 5**:

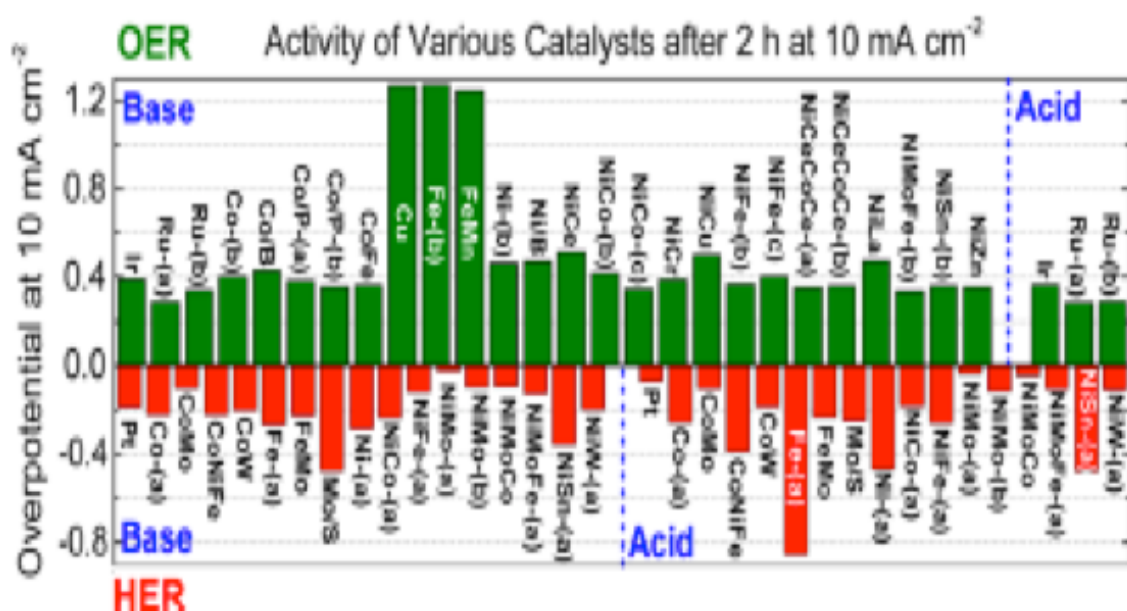


Figure 5: Activity of various HER and OER electrocatalysts both in acidic and alkaline media [9].

3. Photo Electrochemical Water splitting (PEC-WS)

The identification of efficient electrocatalysts comprised of earth-abundant materials for the oxygen evolution reaction (OER) and the hydrogen evolution reaction (HER) is crucial for the development of solar water-splitting devices [1–10].

The production of hydrogen represents one of the most attractive processes, able to conjugate the exploitation of the most popular intermittent, but never-ending source with the environmentally-oriented properties of hydrogen as an energy vector.

Notwithstanding the strong interest for PEC-WS, its development on an industrial scale is hindered by the high costs of the core materials, their low stability and the still inadequate efficiency.

Indeed, at present, the photoelectrochemical cells are based on photoelectrodes composed by a photoconverter, that typically is an n-/p-type semiconductor, in which the absorption of a photon produces an electron-hole couple. In the case of a p-type semiconductor (photocathode, PC) photogenerated electrons can be directly transferred into the electrolyte thus driving the reduction process, while concomitantly the holes are driven toward the anode for the oxidation reaction. In the case of an n-type semiconductor (photoanode PA), the opposite process occurs.

However, the exploitation of the photoconverter might be prevented by recombination phenomena and sluggish electron transfers (ETs), the latter being the key of any electrochemical reaction.

It is thus necessary to develop new photoelectrodes (PEs) that combine a semiconductor, able to generate electron-hole pairs, with a suitable electrocatalyst, able to increase the reaction rate (or reduce the energy requirements) and limit the internal recombination of charges.

In this way it is possible to increase the efficiency of the photoelectrodes using less expensive materials, at the same time.

However, as will be better explained later on, it was already demonstrated that the best electrocatalysts for oxygen evolution reaction are not necessarily the best photo-electrocatalysts (deposited onto the semiconductor) in photo-driven water oxidation. Indeed, according to [27], Pt and Co oxides, deposited onto W-doped BiVO₄, showed higher photocurrents with respect to IrO_x.

In addition, recent studies highlighted the ability of some electrocatalysts used as overlayers in inducing modification of the semiconductor electron density [28] or in storing the photogenerated holes, thus decreasing the probability of charge recombination [29, 30].

This greatly extends the possible candidates for photoelectrocatalysts and requires new efficient screening methods. To this end the scanning electrochemical microscopy (SECM), an optimal tool for the screening of electrocatalysts, e.g. for oxygen reduction [31] and evolution [32] reactions, and photocatalysts [38] was adopted.

3.1 Semiconductors

At present, the photoelectrochemical cells are based on photoelectrodes composed by a photo-converter, in which the absorption of a photon produces an electron-hole couple.

Figure 6 shows the semiconductor structure in the dark of (a) an n-type and (b) a p-type semiconductor when immersed in an electrolyte:

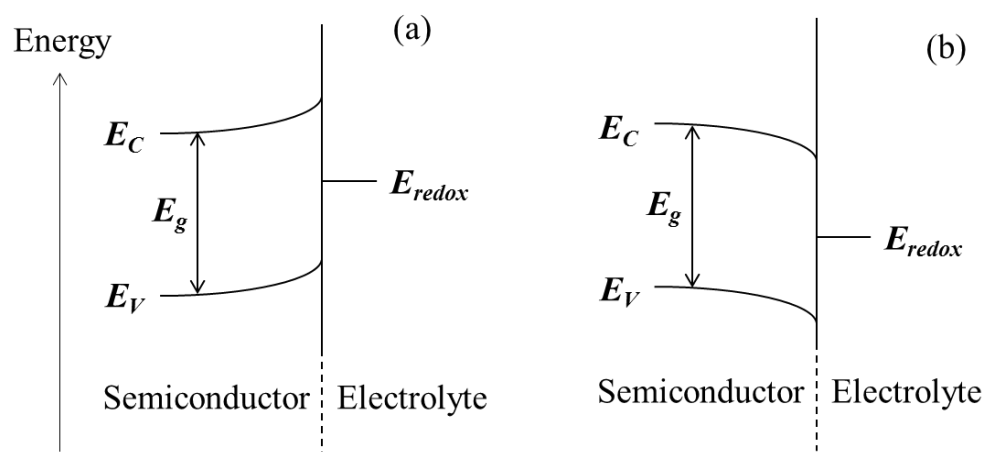


Figure 6: Semiconductor structure in the dark of (a) an n-type and (b) a p-type semiconductor. E_C = conduction band; E_V = valence band; E_{redox} = Fermi level of the redox couple in the electrolyte; E_g = band gap.

At equilibrium, the Fermi level of the semiconductor equalizes the Fermi level of the redox couple in solution (which is the Nernst potential).

This condition is attained thanks to a partial charge transfer between the semiconductor and the species in solution, thus inducing a gradient of the charge carriers in the semiconductor. This is at the bases of the formation of the so-called band bending with formation of a depletion or accumulation layer at the interface.

When the semiconductor is illuminated with an energy $h\nu$ equal or greater than the bandgap, E_g , electron-hole couples are generated, as shown in **Figure 7** in the case of a n-type semiconductor.

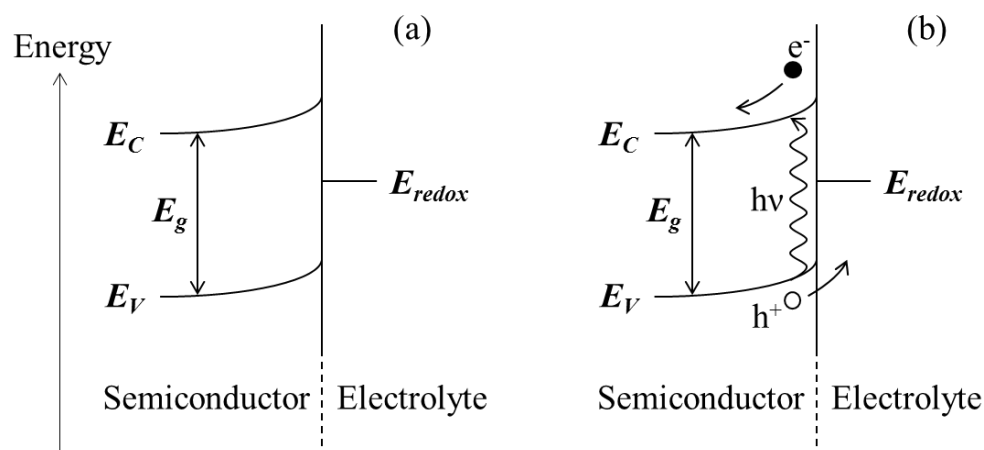
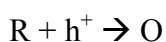


Figure 7: Semiconductor structure (a) in the dark and (b) under light. E_c = conduction band; E_v = valence band; E_{redox} = Fermi level of the redox couple in the electrolyte; E_g = band gap.

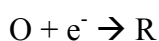
The electron-hole couples photogenerated in the depletion layer are induced from the electric field to move in opposite directions: thus, for a PA, electrons will move toward the semiconductor bulk and the holes toward the semiconductor surface.

This situation gives rise to a potential equal to the difference between the Fermi level of the illuminated semiconductor and that of the redox couple in solution.

When the circuit formed by the semiconductor and the counter electrode (typically made of metal or of conductive metal oxides) is externally closed, the minority charge carriers (i.e. the less abundant charge carriers) move toward the semiconductor surface and then in the electrolyte, in order to promote the reaction. For example, in the case of a n-type semiconductor, the minority charge carriers are the hole, that move in the electrolyte to carry out the oxidation of a R species:



On the contrary, the majority charge carriers (i.e. the more abundant charge carriers) move toward the semiconductor bulk and then to the counter electrode. In the end they go in the electrolyte to promote the reduction of an O species. In the case of a n-type semiconductor, the majority charge carriers are the electrons, that will carry out the reduction of an O species:



A photocurrent is thus generated, while the photopotential decreases, since Fermi levels tend to get closer.

The PEC cell is thus able to directly convert light into electricity and/or chemical energy.

The efficiency η of a PEC cell is given by the following equation:

$$\eta = \frac{E_g I_{CC} (FF) (VF)}{P_{in}} = \frac{P_{max}}{P_{in}}$$

Where:

E_g = band gap;

I_{CC} = the highest photocurrent under light;

FF = fill factor = $\frac{P_{max}}{P_{in}}$

VF = voltage factor, i.e. the ratio between the open circuit potential (V_{OC}) and E_g ;

$P_{in} = I_{CC} * V_{oc}$

E_g is thus a critical parameter. As we can see in **Figure 8**:

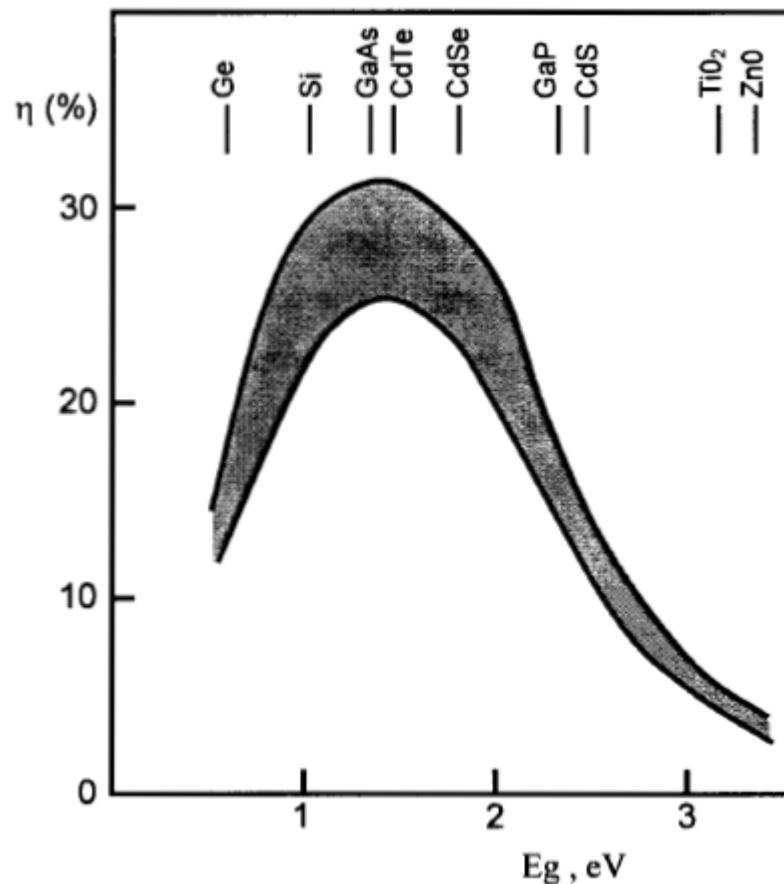


Figure 8: Theoric efficiency vs. band gap energy of different semiconductors [33].

Unfortunately, semiconductors characterized by a low band gap show also low stability in cell.

PEC cells can be used to convert solar energy in chemical products.

In particular, in the case of photoelectrochemical water splitting (PEC-WS), they use low cost and renewable energy source such as solar light and water to produce hydrogen, that can in turn be used as fuel.

Due to the presence of two redox couples in the electrolyte, the electrolyte Fermi level lies between the two redox levels according to the initial O₂ concentration (**Figure 9**):

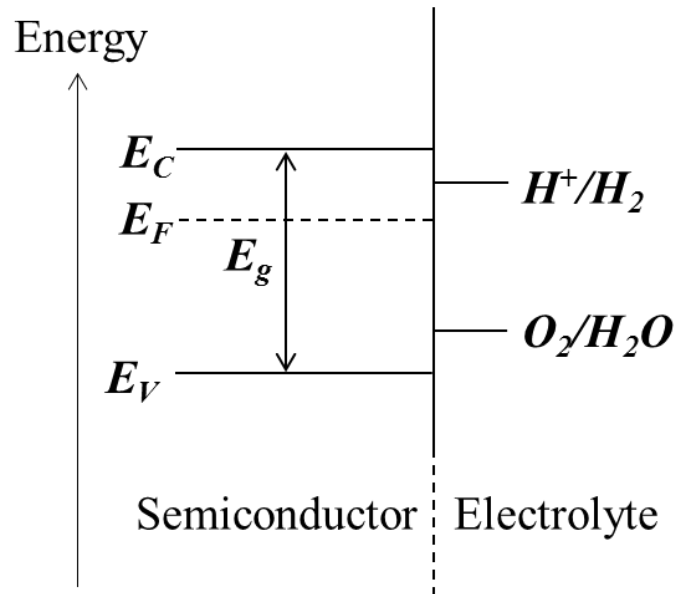


Figure 9: n-type semiconductor – electrolyte junction before the equilibrium. E_c = conduction band; E_v = valence band; E_F = Fermi level; E_g = band gap.

After that, the semiconductor Fermi level aligns with the electrolyte Fermi level, generating the depletion layer (**Figure 10**):

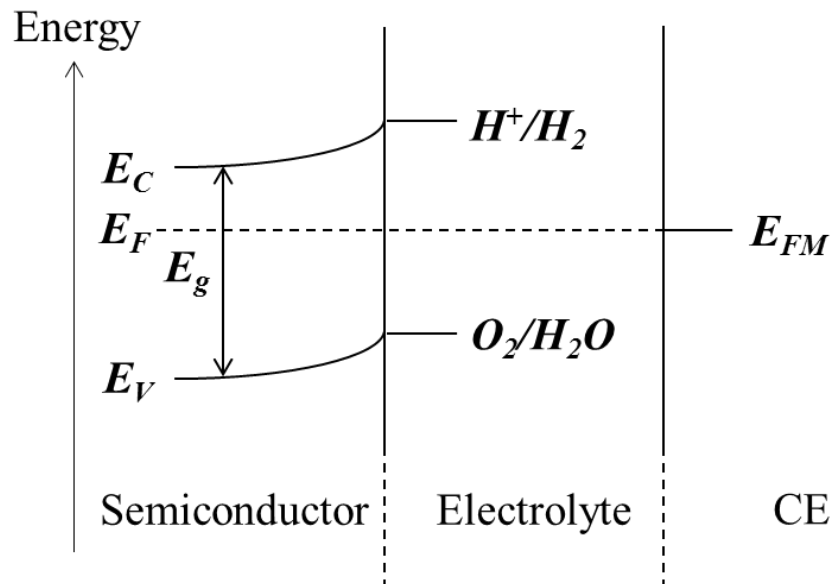


Figure 10: n-type semiconductor – electrolyte junction after the equilibrium in the dark. E_c = conduction band; E_v = valence band; E_F = Fermi level; E_g = band gap.

Under illumination, the semiconductor Fermi level enhances to the flat-band potential, E_{FB} , generating the photopotential (**Figure 11**):

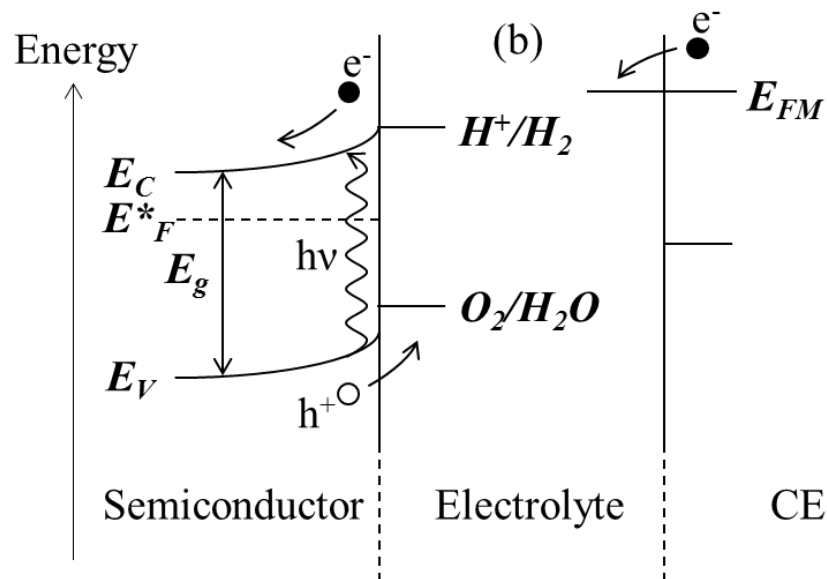


Figure 11: n-type semiconductor – electrolyte junction after the equilibrium in the light. E_c = conduction band; E_v = valence band; E^*_F = Fermi level under illumination; E_g = band gap.

The selected photoconverters should thus be made by highly abundant and thus not expensive elements and characterized by an appropriate electronic structure, e.g. suitable band gap and energy levels.

Since the semiconductor Fermi level under illumination stays under the redox potential of the H^+/H_2 couple, the energy coming from the illumination is not enough to flatten the bands, allowing the generation of hydrogen at the counter electrode.

For this reason, an external bias is needed.

Figure 12 shows the E_g values of the most studied, actual and innovative semiconductor materials for PEC-WS [34]:

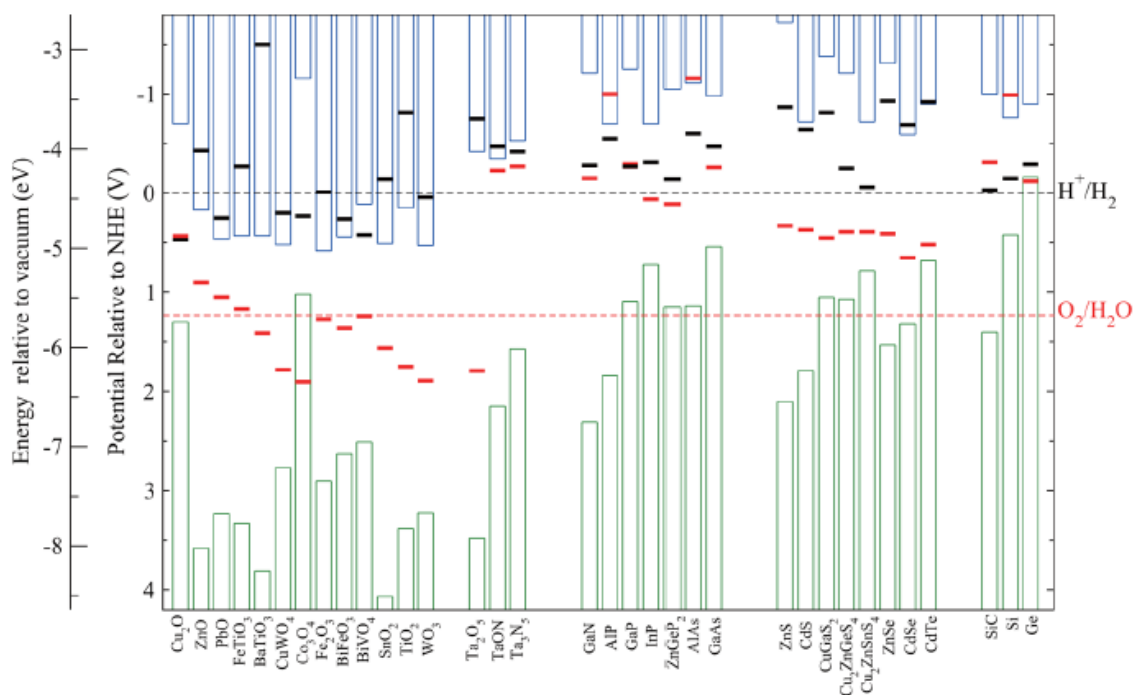


Figure 12: E_g values of different semiconductors [34].

An ideal material should combine some essential requirements:

- transfer efficiently the charge, carry out the reaction with competitive kinetic;
- be stable in aqueous electrolytes under solar illumination;
- be low cost;
- absorb the light very easily and with great intensity thanks to a narrow bandgap (1.3 – 1.4 eV).

It has also to be taken into account that for the photoelectrolysis of water the conduction band of the PC should be higher (more negative in potential) than the water reduction potential and the valence band of the PA lower (more positive in potential) than the water oxidation potential.

Until now, no material has been found to meet all the features listed above. Indeed, transition metal oxides, such as TiO₂ [35], possess an adequate stability but absorb only a small fraction of solar illumination, because of their large bandgap ($E_g = 3.2$ eV).

Many other semiconductors, such as InP ($E_g = 1.3$ eV), have smaller bandgaps and appropriate energy levels, but they are quite unstable in aqueous environment.

Also WO₃ ($E_g = 2.6$ eV) is not kinetically appropriate and is characterized by a large bandgap, however it is also inexpensive and stable. Some of the main methods for improving the PEC response of WO₃ have included morphological improvements and

the utilization of nanostructures, or the addition of a suitable photocatalyst for water oxidation [36].

Other materials identified as promising photoanode are TaON, Ta₃N₅ [37] and overall BiVO₄ [37,38,39] and hematite, previously presented, but some features, like efficiency and stability, have to be still improved.

This Ph.D. Thesis is mainly focused on the characterization of hematite (α -Fe₂O₃), synthesised in collaboration with the CNR-ISTM, but also WO₃, TiO₂ and BiVO₄, in the form of nanoparticles, were studied.

3.2 Hematite (α -Fe₂O₃) [40, 41]

Thanks to its chemical stability, widespread availability, and capability to absorb photons in the visible spectral range (band gap, $E_g = 2.0$ eV), hematite (α -Fe₂O₃) is a promising material to be used as photoanode for the production of hydrogen in the PEC-WS.

Indeed, iron is the fourth most common element in the earth's crust (6.3% by weight) and is also readily oxidized in air to the ferrous (+2) and ferric (+3) states.

Moreover, its red-brown colour is a precise suggestion that iron oxide is able to absorb solar light.

Last but not least, iron oxides are non-toxic.

All of these features make iron oxide a particularly attractive material for use as suitable photoanode (PA) in solar energy conversion.

Over the last decade, numerous reports were published describing continuing studies with pure and doped α -Fe₂O₃ made by various routes [41, 42, 43].

However, also many limitations of this material as suitable semiconductor for OER in photo-driven water electrolysis were discovered. The most important are the following:

- a flat band potential, E_{fb} , too low in energy for water reduction [44, 45] this requires the application of an external bias.
- a low activity towards water oxidation [44].
- a relatively low absorption coefficient, requiring 400–500 nm thick films for complete light absorption [46, 47];

- poor majority carrier conductivity [48, 49];
- a short diffusion length of minority carriers [50].

For these reasons, the improvement of $\alpha\text{-Fe}_2\text{O}_3$ performances is one on the main challenges nowadays.

In particular, it is generally accepted that [47, 51, 52] optimizing the electrode morphology can significantly increase the water splitting photocurrent density.

At the same time, further researches focused on reducing the bias required by employing various types of surface treatment.

By combining these two strategies it is possible to approach the performance of an ideal hematite photoanode, shown in **Figure 13**:

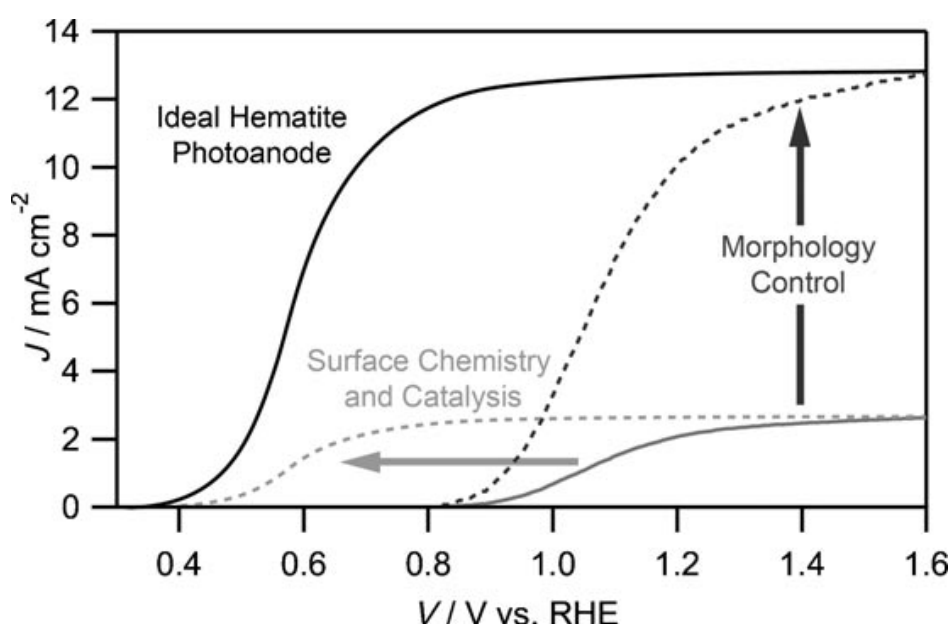


Figure 13: photocurrent density, J , vs. voltage behavior for an idealized hematite sample (solid black line) compared to the typical performance (solid grey trace). [40]

The latter aspect is overall of interest, as will explain in the next Chapter, and it represents the main aim of this Ph.D. Thesis.

For what concern the morphology control of hematite, different deposition techniques have been deeply investigated in the literature [51, 52], and in particular:

- Porous thin films from solution-based colloidal methods, with hematite nanoparticles of 5–10 nm in diameter, treated at high-temperature until obtaining nanoparticles of more than 50 nm diameter. However, a considerable anodic shift of the photocurrent onset potential was observed [40, 53];

- α -Fe₂O₃ nanowire arrays: hematite nanorods with diameters in the 10 nm range were deposited from the controlled precipitation of Fe³⁺ in aqueous solution [54]. These nanowires were characterized by an average diameter of 50 nm and a length of 0.1 to 1.5 μ m.
- Electrochemical Fe₂O₃ nanostructuring: potentiostatic anodization has provided another possible route to create structured hematite photoelectrodes [55]. However, even if different and interesting morphologies can be obtained with electrochemical deposition techniques, water splitting photocurrents have been limited by the quality of the material produced.
- Spray pyrolysis techniques: this synthesis way produces electrodes with superior performance, even without intentionally adding dopants to increase the conductivity of the Fe₂O₃.
- Atmospheric pressure chemical vapour deposition: Fe(CO)₅ vapours were transported, along with tetraethyl orthosilicate (TEOS) as a source of silicon dopant, by a carrier gas (dry air), and directed vertically onto a heated substrate. The poor thermal stability of the Fe(CO)₅ caused the homogenous nucleation of nanoparticles in the gas phase [56, 57]. However, even if this is a considerable step towards high performance hematite, the photocurrent density remains far from the 12.6 mAcm⁻² possible.
- Extremely thin absorber approach: this technique provides to cover the semiconductor with an extremely thin layer on a high-surface area. This method still has to be improved.
- Nanostructuring method comparison: this kind of materials can significantly increase the photocurrents, due, of course, to the nanostructuring, that can provide the absorption of the light.

3.3 Overlayers

Recent studies highlighted that a surface modification of a suitable semiconductor with different materials were able to reduce the overpotential for water photo-oxidation.

As already said, Bard [27] found that Pt and Co₃O₄ were effective electrocatalysts on BiVW-O films, while IrO_x showed really low photoactivity, even though IrO_x films showed the highest electrocatalytic activity for OER as a dark electrocatalyst.

Also the coating of nanostructured hematite photoanodes with a very thin layer (0.1 to 2 nm) of alumina by ALD provided a significant decrease (> 100 mV cathodic shift) in the overpotential required to photo-oxidize water [58]. This was due to the passivation of the hematite surface defects, that allowed to limit the charge recombination.

Moreover, in [28] the authors found that an Ir-based catalyst deposited onto Fe_2O_3 was able to enhance the charge separation and to store the photogenerated holes. This in turn allowed the water oxidation with lower charge recombination with respect to bare hematite.

On the contrary, the deposition of CoPi onto a BiVO_4 does not contribute significantly to the overall water oxidation current, nor to the anticipation of the reaction overpotential. This is probably due to the inability of the CoPi overlayer to transfer the holes from the semiconductor to the catalyst faster than the direct water oxidation on the semiconductor surface.

Other suitable materials to be used as overlayers include cobalt-based treatments [59], IrO_2 nanoparticles [60], and Ga_2O_3 overlayers [58].

Particular interest has recently focused upon in situ deposition of cobalt or nickel oxo/hydroxo-based overlayers on several water oxidation photoanodes [61].

Starting from these experimental evidences, different explanations were suggested:

- i. these materials are able to enhance the water oxidation kinetics or to reduce the overpotential required to drive water oxidation [62];
- ii. the overlayers photoactivities were connected to a passivation of the semiconductor surface, reducing the kinetics of surface recombination reactions [58];
- iii. overlayers reduces the electron density in the $\alpha\text{-Fe}_2\text{O}_3$ photoelectrode, thus preventing the electron/hole recombination and increasing the yield of long-lived holes at the electrode surface. [28] Consequently, the presence of high electron densities causes a decrease in the space charge layer width. The presence of the overlayers, on the contrary, will enhance electron depletion within the film. Surface treatments with suitable overlayers thus result in a cathodic shift of the photocurrent, not only by preventing the recombination phenomena or enhancing the kinetics of water photo-oxidation, like an electrocatalyst do, but rather by enhancing the spatial extent or magnitude of the space charge/electron depletion layer.

The same behavior was studied in presence on underlayers instead of overlayers. In a recent contribution, a Nb_2O_5 and a SiO_x underlayers were deposited under a hematite film and thus investigated. [40]. These resulted being responsible of an increase in n-doping in the hematite film. This was due to the increase in electron density, to a better charge separation and a reduced recombination at the hematite/electrolyte interface. This is in turn correlated to an increase in the photocurrent plateaus of the doped films. In this context, the photoactivity of the overlayer cannot anymore to be considered a pure catalytic effect.

As a consequence, the most know OER electrocatalysts cannot be considered the only materials able to shift the onset potential of the reaction under interest (reduced bias).

On the contrary, a wide range of materials can be suitable overlayers for the photo-driven water oxidation.

After these considerations, it should be evident that is necessary to find the perfect tool to rapidly screen big libraries of materials, without wasting time and material.

As already said, the scanning electrochemical microscopy (SECM) showed its features as optimal tool for the screening of electrocatalysts, e.g. for oxygen reduction [31] and evolution [32] reactions, and photocatalysts [38].

4. Work summary

This Ph.D. Thesis is divided into five main parts:

1. **Preliminary study of suitable OER electrocatalysts deposited onto titanium sheets by SECM:** in this part different suitable oxygen evolution reaction electrocatalysts are deposited onto a Ti sheet with a microliter piezo dispenser. After an activation step and a thermal treatment, the arrays were tested through the SECM in NaOH 0.1 M. The materials studied following this approach were not only Ir-based arrays, but also low-cost and abundant (respect to IrO_x) Co-, Fe-, Co- and Zn-based oxides. In order to solve the problem of the overlapping of oxygen profiles when the substrate is biased at an OER potential, the *double pulse method* has been applied, with reliable results.
2. **Study of different OER overlayers deposited onto hematite:** different OER electrocatalysts with different compositions of low-cost metals have been screened using the SECM. The deposited arrays were tested with two different approaches: the first one provides the replacement of the ultramicroelectrode tip with a 200 μm diameter white light optical fiber, that can locally generate electron-hole pairs; the second method involves the use of SECM in its conventional set-up, using a 25 μm Au tip as amperometric sensor and recording its current, that is directly proportional to the oxygen production rate at the substrate, in the dark and under visible light, the latter condition achieved thanks to a 523 nm green LED, in the SG/TC mode. As for the electrocatalysts deposited onto Ti sheets, the *double pulse method* has been applied to different spots and to the bare hematite.
A preliminary experiment involved the electrodeposition of amorphous IrO_x onto hematite by the so-called SECM direct mode. The composite was tested according to the previously explained conditions.
In the end, Co/Ni, Fe/Ni, Fe/Ni/Al, Fe/Ni/Mg and Fe/Ni/Ca arrays (for a total of almost 30 compositions) were dispensed and tested using the optical fiber as probe. In order to confirm the SECM results, the most photoactive compositions according to it were selected and deposited onto hematite as lab-scale electrodes. They were then tested during irradiation with a solar simulator.

3. **Study of TiO_2 , WO_3 and BiVO_4 nanoparticles prepared by cathodic corrosion methods:** this part of the Thesis has been performed at the laboratories of Professor Joaquin Rodríguez-López (University of Illinois at Urbana-Champaign UIUC, Urbana-Champaign, Illinois, USA).

This part of the work introduces the characterization of photocatalytic particles with well-defined and controllable morphology and composition, synthesised with a new, inexpensive and simple method.

They were then tested towards the photoelectrochemical oxidation of water in NaOH 0.1 M, where composites of these particles embedded in Nafion[®], displayed interesting photoanodic responses upon illumination with both UV and Visible light. Also some activation procedures were studied.

4. **The cavity-microelectrode (C-ME) as a tip for SECM:** this part explores the possible use of C-MEs as SECM tips to be used in different modes: *feedback*, *tip generation/substrate collection* (TG/SG) and *substrate generation/tip collection* (SG/TC).

Moreover, the possibility of conveniently studying parallel reactions occurring at a desired powder electrode material will also be introduced.

5. **Hematite/NiOOH architecture:** in this part of the Thesis, a detailed study on the photoactivity of hematite photoanodes covered with an amorphous Ni-oxyhydroxide layer is presented. In order to study the effect of this amorphous NiOOH layer on the photoanode performance, the SECM will be applied.

Indeed, the substrate photocurrents could be due not only to the actual activity of the semiconductor/overlayer architecture under light irradiation, but also to other parasite reaction. For this reason, the use of SECM in the *substrate generation/tip collection* (SG/TC) mode was needed.

This approach allows a fine determination of the reaction onset, ruling out any parasitic reactions (e.g., the oxidation of the electrode itself).

The experiments were repeated both in the dark and under solar simulation irradiation, on a bare hematite sample and one hematite/NiOOH photoelectrode.

-
- [1] European Commission's communication 'Energy 2020 - A strategy for competitive, sustainable and secure energy' - COM (2010) 639 final of 10 November 2010
- [2] Leng, Y.J. et al. *J. Am. Chem. Soc.* 134 (2012) 9054
- [3] Zeng, K.; Zhang, D.K. *Progr. Energy Combust. Sci.* 36 (2010) 307
- [4] https://www.hydrogen.energy.gov/fuel_cells.html
- [5] Bard, A.J.; Faulkner, L.R. *Electrochemical Methods: fundamentals and applications* (2001) John Wiley & Sons, Inc.
- [6] Trasatti S. *Electrochim. Acta* 29 (1984) 1503
- [7] Ardizzone, S.; Trasatti, S. *Adv. Coll. Interf. Sci.* 64 (1996)173
- [8] Alves, V. A.; da Silva, L.A.; Oliveira, E.D.; Boots, J.F.C. *Mater. Sci. Forum* 282 (1998) 655
- [9] Mc Crory, C.C.L.; Jung, S.; Ferrer, I.M.; Chatman, S.M.; Peters, J.C.; Jaramillo, T.F. *J. Am. Chem. Soc.* 137 (2015) 4347
- [10] Minguzzi, A.; Fan, F.F.; Vertova, A.; Rondinini, S.; Bard, A.J. *Chem. Sci.* 3 (2012), 217
- [11] Balko, E.N.; Nguyen P.H. *J. Appl. Electrochem.* 21 (1991) 678
- [12] De Pauli, C. P.; Trasatti, S. *J. Electroanal. Chem.* 396 (1995) 161
- [13] De Pauli, C. P.; Trasatti, S. *J. Electroanal. Chem.* 538 (2002) 145
- [14] Marshall, A.; Børresen, B.; Hagen, G.; Tsytkin, M.; Tunold, R. *Electrochim. Acta* 51 (2006) 3161
- [15] Comninellis, C.; Vercesi G. P. *J. Appl. Electrochem.* 21 (1991) 335
- [16] Comninellis, C.; Vercesi, P. *J. Appl. Electrochem.* 21 (1991) 139
- [17] Xu L, K.; Scantlebury, J. D. *J. Electrochem. Soc.* 150 (2003) B254
- [18] Xu L, K.; Scantlebury, J. D. *J. Electrochem. Soc.* 150 (2003) B288
- [19] Hu, J. M.; Zhang, J. Q.; Meng, H. M.; Cao C.N. *J. Mater. Sci.* 38 (2003) 705
- [20] Hu J. M.; Meng, H. M.; Zhang, J. Q.; Cao, C. N. *Corr. Sci.* 44 (2002) 1655
- [21] Hu, J. M.; Zhang, J. Q.; Cao, C. N. *Int. J. Hydrog. Energy* 29 (2004) 791
- [22] Morimitsu, M.; Otagawa, R.; Matsunaga, M. *Electrochim. Acta* 46 (2000) 401
- [23] Da Silva, L. M.; Franco, D. V.; De Faria, L. A.; Boodts, J. F. C. *Electrochim. Acta* 49 (2004) 3977
- [24] Chen, X.; Chen, G.; Yue, P. L. *J. Phys. Chem. B* 105 (2001) 4623
- [25] Chen, G.; Chen, X.; Yue, P. L. *J. Phys. Chem. B* 106 (2002) 4364
- [26] Mc Crory, C.C.L.; Jung, S.; Peters, J.C.; Jaramillo, T.F. *J. Am. Chem. Soc.* 135 (2013) 16977
- [27] Ye, H.; Park, H.S.; Bard, A.J. *J. Phys. Chem. C*, 115 (2011) 12464

-
- [28] Barroso, M.; Mesa, C.A.; Pendlebury, S.R.; Cowana, A.J.; Hisatomi, T.; Sivula, K.; Grätzel, M.; Klug, D.R.; Durrant J.R. *PNAS* 109 (2012) 15640
- [29] Badia-Bou, L.; Mas-Marza, E.; Rodenas P.; Barea, E.M.; Fabregat-Santiago, F.; Gimenez, S.; Peris, E.; Bisquert, J.J. *Phys. Chem. C* 117 (2011) 3826
- [30] Lin, F.; Boettcher, S.W.; *Nature Materials* 13 (2014) 81
- [31] Fernández, J.L.; Walsh, D.A.; Bard, A.J. *J. Am. Chem. Soc.* 127 (2005) 357
- [32] Minguzzi, A.; Alpuche-Aviles, M.A.; Rodríguez-López, J.; Rondinini, S.; Bard, A.J. *Anal. Chem.* 80 (2008) 4055
- [33] Scrosati, B.
- [34] Chen, S.; Wang, L-W *Chem. Mater.* 24 (2012) 3659
- [35] Fujishima, A.; Honda K. *Nature*, 238 (1972) 37
- [36] Leonard, K.C.; Nam, K.M.; Lee, H.C.; Kang, S.H.; Park, H.S.; Bard A. J. *J. Phys. Chem. C* 117 (2013) 15901
- [37] Cong, Y.; Park, H.S.; Wang, S.; Dang, H.X.; Fan, F.F.; Mullins, C.B.; Bard, A.J. *J. Phys. Chem. C* 116 (2012) 14541
- [38] Lee, J.; Ye, H; Pan, S.; Bard, A.J. *Anal. Chem.* 80 (2008) 7445
- [39] Ye, H.; Park, H.S.; Bard, A.J. *J. Phys. Chem. C* 115 (2011) 12464
- [40] Sivula, K.; Le Formal, F.; Grätzel, M. *ChemSusChem* 4 (2011) 432
- [41] Hardee, K.L.; Bard, A.J. *J. Electrochem. Soc.* 123 (1976) 1024
- [42] Quinn, R.K.; Nasby, R.D.; Baughman, R.J. *Mater. Res. Bull.* 11 (1976) 1011
- [43] Kennedy, J.H.; Anderman, M.; Shinar, R. *J. Electrochem. Soc.* 128 (1981) 2371
- [44] Dareedwards, M.P.; Goodenough, J.B.; Hamnett, A.; Trevellick, P.R. *J. Chem. Soc. Faraday Trans.* 79 (1983) 2027
- [45] Quinn, R.K.; Nasby, R.D.; Baughman, R.J. *Mater. Res. Bull.* 11 (1976) 1011
- [46] Itoh, K.; Bockris, J.O. *J. Appl. Phys.* 56 (1984) 874
- [47] Itoh, K.; Bockris, J.O. *J. Electrochem. Soc.* 131 (1984) 1266
- [48] Horowitz, G. *J. Electroanal. Chem.* 159 (1983) 421
- [49] Sanchez, C.; Sieber, K.D.; Somorjai, G.A. *J. Electroanal. Chem.* 252 (1988) 269
- [50] Kennedy, J.H.; Frese, K.W. *J. Electrochem. Soc.* 125 (1978) 709
- [51] Alexander, B.D.; Kulesza, P.D.; Rutkowska, L.; Solaraska, R.; Augustynski, J. *J. Mater. Chem.* 18 (2008) 2298
- [52] van de Krol, R.; Liang, Y.Q.; Schoonman, J. *J. Mater. Chem.* 18 (2008) 2311
- [53] Brilllet, J.; Grätzel, M.; Sivula, K. *Nano Lett.* 10 (2010) 4155
- [54] Moser, J.; Grätzel, M. *Helv. Chim. Acta* 65 (1982) 1436

-
- [55] Prakasam, H.E.; Varghese, O.K.; Paulose, M.; Mor, G.K.; Grimes, C.A. *Nanotechnology* 17 (2006) 4285
- [56] Cesar, I.; Kay, A.; J.A.G.; Grätzel, M. *J. Am. Chem. Soc.* 128 (2006) 4582
- [57] Wen, J.Z.; Goldsmith, C.F.; Ashcraft, R.W.; Green, W.H. *J. Phys. Chem. C* 111 (2007) 5677
- [58] Le Formal, F.; Tétreault, N.; Cornuz, M.; Moehl, T.; Grätzel, M.; Sivula, K. *Chem. Sci.* 2 (2011) 737
- [59] Kay, A.; Cesar, I.; Grätzel, M. *J. Am. Chem. Soc.* 128 (2006) 15714
- [60] Tilley, S.D.; Cornuz, M.; Sivula, K.; Grätzel, M. *Angew. Chem. Intl. Ed. Engl.* 49 (2010) 6405
- [61] Malara, F.; Minguzzi, A.; Marelli, M.; Morandi, S.; Psaro, R.; Dal Santo, V.; Naldoni, A. *ACS catalysis*, 5 (2015) 5292
- [62] Zhong, D.K.; Choi, S.; Gamelin, D.R. *J. Am. Chem. Soc.* 133 (2011) 18370

Experimental section

1. Electrochemical techniques

The electrochemical characterization of the electrodes was mainly performed by Scanning Electrochemical Microscopy (SECM). However, also other electrochemical techniques were used for other measurements, for example Cyclic Voltammetries (CVs), and Chronoamperometries.

In the following chapter will be briefly discussed the techniques used in this Ph.D. thesis.

1.1. Cyclic voltammetry [1]

Cyclic voltammetry (CV) is the most known and used electrochemical technique, since its high versatility allows its use in several areas of chemistry.

This comes from the possibility of rapidly provide a wide number of information on the thermodynamics of redox processes, the kinetics of heterogeneous electron-transfer reaction, coupled chemical reaction, adsorption processes, etc.

CV consists of the scanning of the potential of a working electrode, whose actual value is referred to the reference electrode, using a triangular potential waveform (**Figure 14**). The measurements are typically carried out in a supporting electrolyte of sufficiently high concentration (in order to un-favour mass transport due to ion migration), with three-electrode experimental set-up: the current flowing between the working and the counter electrode is measured as a function of the potential difference between the working and the reference electrode.

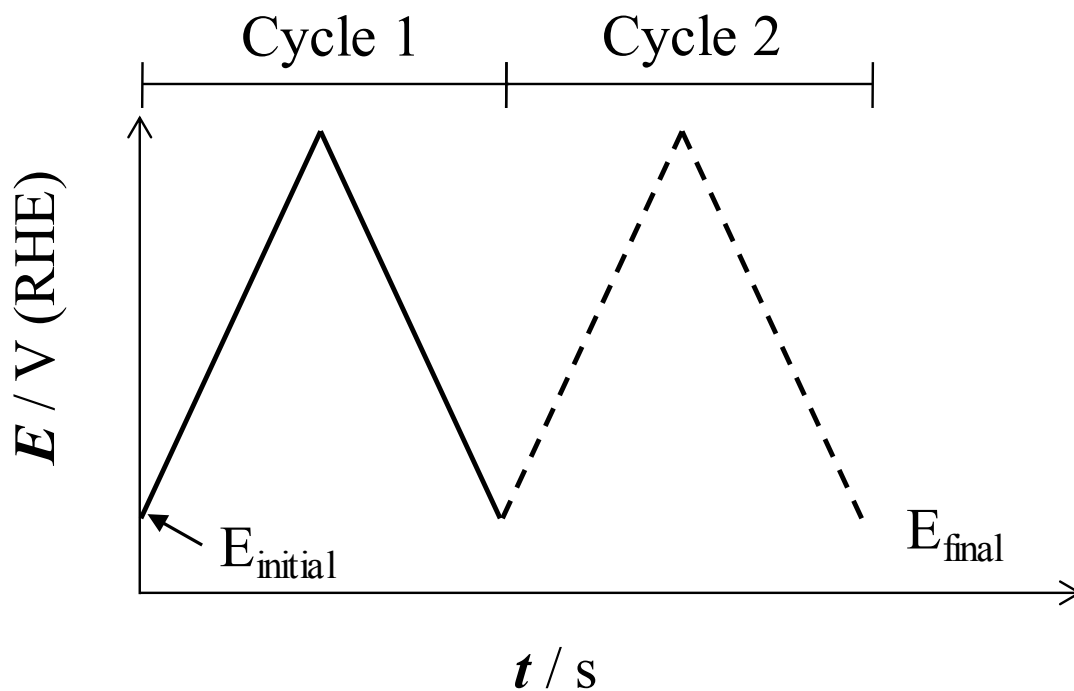


Figure 14: Potential-time variation in cyclic voltammetry.

The resulting plot of *current* versus *potential* is named cyclic voltammetry (**Figure 15**) and contains several information on the process occurring at the working electrode:

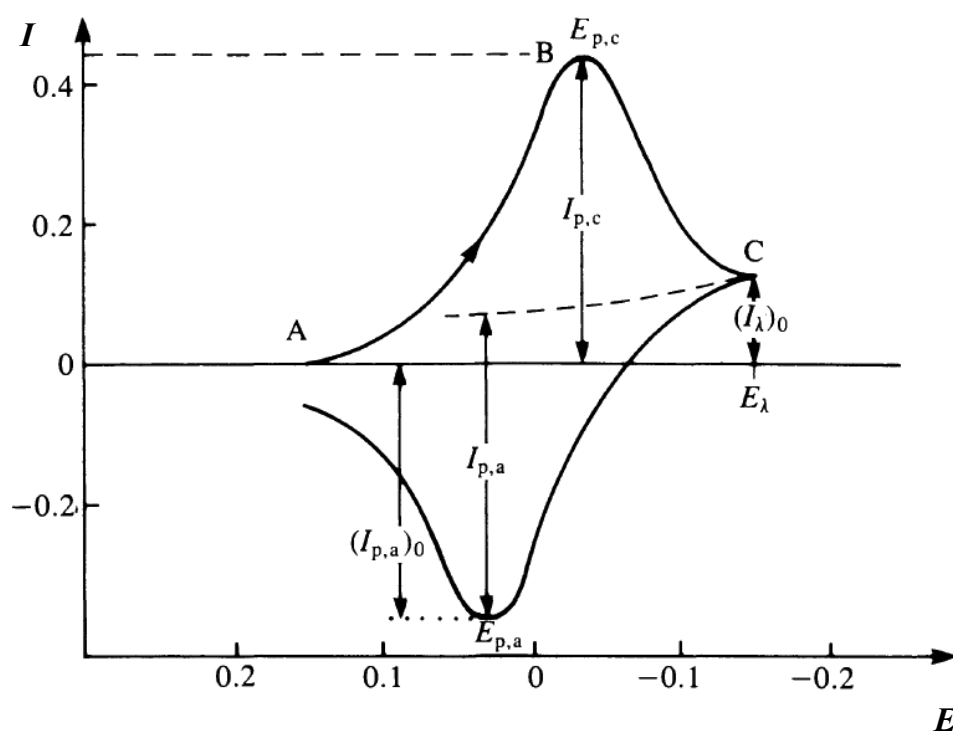


Figure 15: Cyclic voltammogram for a reversible system [2].

The recorded current intensity I (A) is given by:

$$I = I_c + I_f \quad (1)$$

Where I_f is the faradic current, due to the electrode reaction, which occurs when the appropriate potential is reached, while I_c is the capacitive current, due to the charging of the double layer near the electrode surface. The double layer at the electrode/solution interface can be related to a capacitor, which undergoes a charges redistribution according to:

$$dQ = C_{dl}dE = I_c dt \quad (2)$$

Where C_{dl} is the capacitance.

The capacitive current I_c is also proportional to v :

$$I_c = C_{dl}v \quad (3)$$

Being $v = \frac{dE}{dt}$.

Thus, a linear potential sweep produces a constant current proportional to C_{dl} and to v (**Figure 16**).

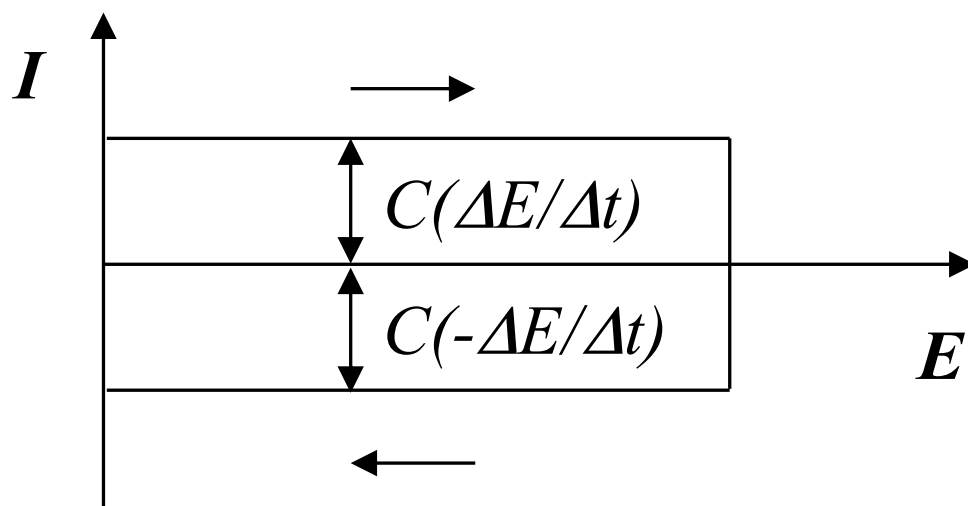


Figure 16: Potential-current variation of the capacitive part of a CV.

As already said, the faradaic current, I_f , is due to the reaction occurring at the electrode surfaces. These reactions involve a direct transfer of electrons via oxidation reaction at one electrode and a reduction at the other. Processes of this type are called faradaic processes because they are governed by faradaic laws, which state that an amount of chemical reaction at one electrode is proportional to the current:

$$Q = nFC$$

$$\frac{dQ}{dt} = i = nF \frac{dC}{dt}$$

Where n is the number of electrons involved in the process, F the Faraday constant and C is the concentration of the species.

1.2. Potentiostatic techniques

The study of the variation of the current response with the time when the potential is changed is called *chronoamperometry*.

Usually, the potential is stepped from a value at which no faradic reactions occur to a value at which the surface concentration is approximately zero.

The dependence of the current with the time is monitored, and reflects the change of the species concentration near the electrode surface if mass transport is diffusion-dependent (**Figure 17**):

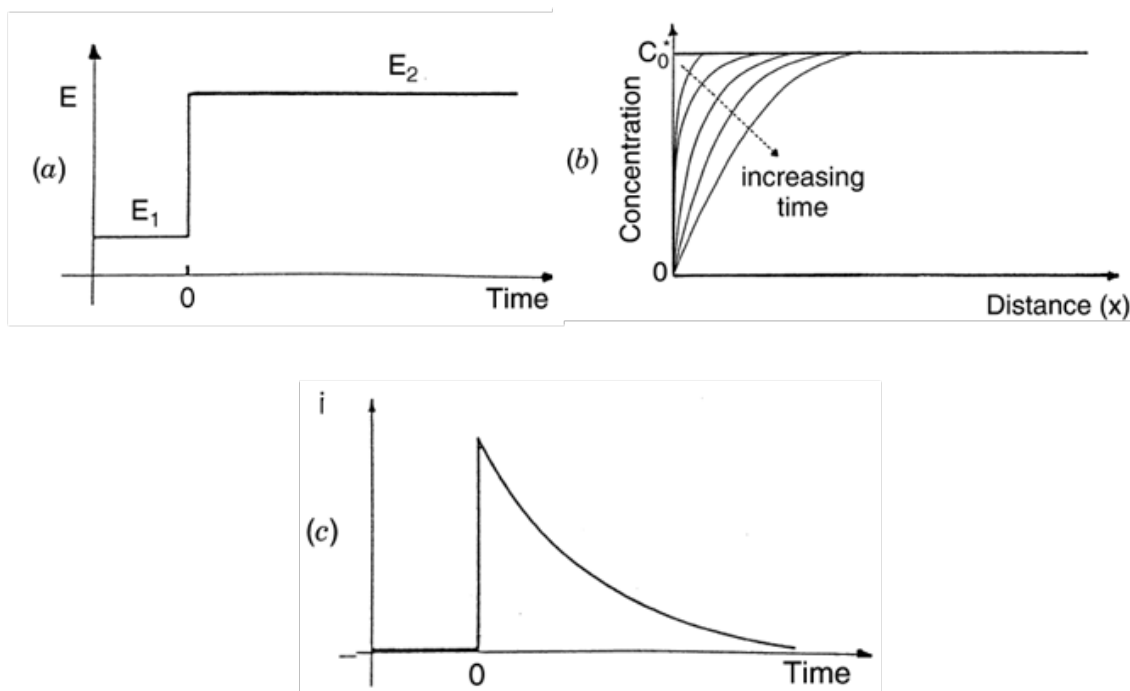


Figure 17: Chronoamperometry plots: (a) E vs t , (b) change of concentration vs distance and (c) I vs t [6].

The decay of the current respect to the time is given by the *Cottrell equation*:

$$i(t) = \frac{nFACD^{1/2}}{\pi^{1/2}t^{1/2}} = kt^{-1/2} \quad (4)$$

In this Ph.D. thesis, the potentiostatic techniques were performed as pulsed potential profile (double pulse method [3]), as explained in the “*Result and Discussion*” section.

1.3. Reference electrode: the calibration of saturated calomel electrode (SCE)

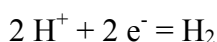
The thermodynamic potential of O_2/H_2O redox couple is:



the nernstian expression is then:

$$\begin{aligned} E_{O_2/H_2O/H^+} &= E_{O_2/H_2O/H^+}^\circ + \frac{RT}{4F} \ln(p_{O_2}) + \frac{RT}{4F} \ln\left(\frac{a_{H^+}}{a_{H_2O}^{1/2}}\right) \\ &= E_{O_2/H_2O/H^+}^\circ + \frac{k}{4} \ln(p_{O_2}) - k pH - \frac{k}{2} \ln(a_{H_2O}) \end{aligned}$$

Therefore, the O₂/H₂O redox potential under reversible thermodynamic conditions has the same pH dependence as the H⁺/H₂ couple:



$$E_{H^+} = \frac{RT}{2F} \ln(p_{H_2}) + \frac{RT}{F} \ln(a_{H^+}) = \frac{k}{2k} \ln(p_{H_2}) - k pH$$

Where:

R = gas constant;

T = absolute temperature;

F = 96485.309 C eq⁻¹;

p_{O_2}, p_{H_2} = oxygen and hydrogen partial pressures.

It is then convenient to use the Reversible Hydrogen Electrode (RHE) as the reference electrode, since it permits to quantify working electrode potentials independently from pH.

However, a RHE reference electrode requires experimental equipments which make the whole system difficult to handle. On the other hand, Saturated Calomel Electrode (SCE) is very easy to handle but its potential is independent on pH:

$$E_{SCE} = E^\circ - k \log(a_{Cl^-, sat})$$

SCE was therefore used as operational reference electrode, while the working electrode potentials are referred to RHE, by periodically calibrating SCE against RHE.

Figure 18 reports the experimental setup used for calibration procedure:

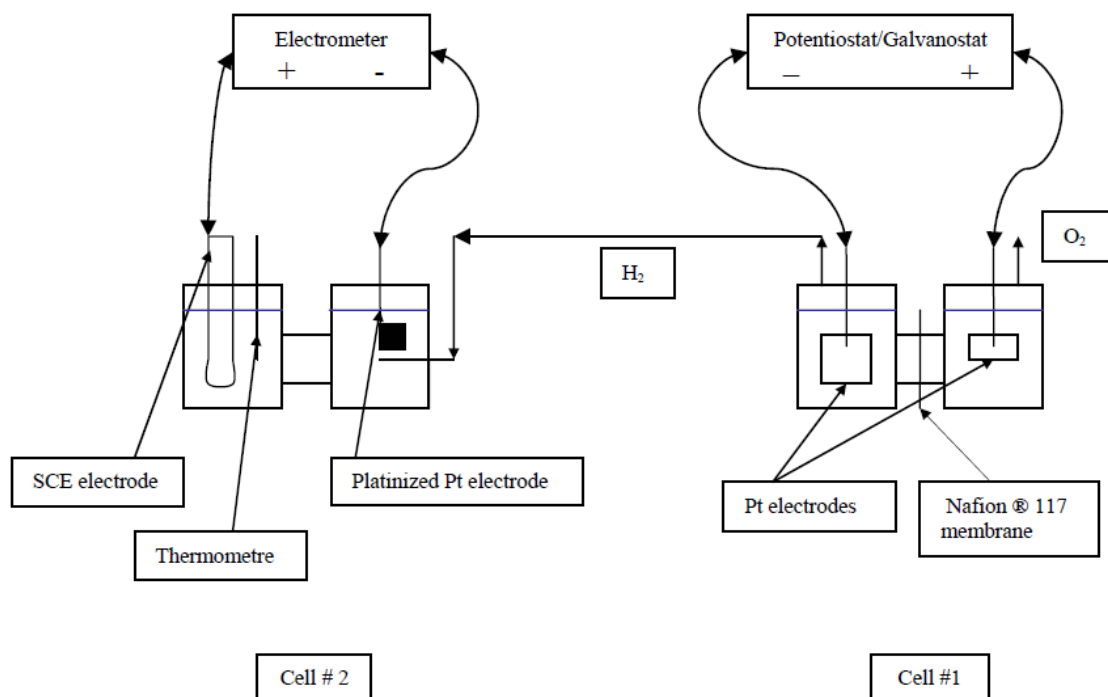


Figure 18: Experimental setup for the calibration procedure of SCE vs RHE at different pHs.

Hydrogen is produced in Cell #1 (a two compartment cell divided by a cationic membrane) by water electrolysis using aqueous HClO₄ 0.1 M as supporting electrolyte, and is fed to Cell #2. Cell #2 is composed by an SCE on one side and a half immersed platinized Pt foil.

In this way the following galvanic chain is obtained:



The cell potential is measured by an electrometer.

The procedure is repeated varying the electrolyte solution used the Cell #2. The following solutions, of different pH values, are used:

- HClO₄ 0.1 M
- NaClO₄ 0.1 M
- NaClO₄ 0.1 M adjusted to pH 9-10 by NaOH 0.1 M additions

The pH value is measured by using a glass electrode (with internal reference electrode: Ag/AgCl KCl 3 M) and a pH-meter.

The glass electrode and the pH-meter are calibrated by using pH 7 and pH 4 buffer solutions.

Operative Procedure

Hydrogen produced in Cell #1 is bubbled in the RHE compartment in Cell #2. Measurements are conducted at ambient temperature ($T \sim 22 \pm 2$ °C). Potential differences between SCE and RHE are recorded until a stable value is obtained (E_∞ at $\Delta E/\Delta t < 3$ mVs⁻¹). The values obtained must be reported to the standard conditions ($p_{H_2} = 101325$ Pa). This requires the determination of the actual p_{H_2} value within the cell, by applying the following equation:

$$p_{H_2} = P_{atm} + p_h - p_{vap}$$

Where:

P_{atm} = atmospheric pressure;

p_h = pressure due to the hydrostatic heads in the cell;

p_{vap} = vapor pressure of the solution.

Atmospheric pressure is measured by using an Hg barometer. p_h is null since the RHE chamber is in direct contact with the atmosphere, vapor pressure is obtained from the literature [4].

The correct value of the *d.d.p.* between SCE and RHE is then:

$$E_{corr} = E_\infty + \frac{RT}{2F} \ln \frac{1}{p_{H_2}}$$

The values $E_{corr} = E_{SCE} - E_{RHE}$ are linearly dependent on pH:

$$E_{corr} = E_{SCE} - E_{RHE} = m \cdot pH + q$$

1.4. Scanning Electrochemical Microscopy (SECM) [5, 6]

The majority of this Ph.D. thesis was focused on the use of Scanning Electrochemical Microscopy for the rapid screening of big libraries of suitable (photo)electrocatalysts.

Indeed, SECM showed quite recently its unique features in the screening of electrocatalysts for oxygen reduction [7] and evolution reactions [8], but also of

photocatalysts [9], in the fine determination of catalyzed reactions intermediates [10] and in the role of surface crystallographic orientation [11] and in biological field [12].

SECM provides information about the local topography of the examined substrates and also to study the local reactivity on the micrometer scale.

One of the most frequent uses consists in recording a current flowing in an ultramicroelectrode (UME), called the tip, positioned near a conductive, insulating or semiconductive substrate, immersed in solution.

The substrate perturbs the electrochemical response of the tip and this provides the desired information about the nature and the properties of the substrate. The tip and the substrate can be biased at the same time using only one counter and one reference electrode, thanks to a bipotentiostatic circuit, while the tip movements are controlled by a stepper or a piezoelectric motor (**Figure 19**).



Figure 19: Picture of a SECM apparatus.

The illustration of the motors and the cell of a SECM instrument is shown in **Figure 20**. The positioning system includes the positioning elements, a 3-axis positioner in which the tip is placed, the translator stage and the motor controller is able to accurately move

and position the probe in the three directions (x , y and z) and move it at a desired scan rate and over a given substrate area.

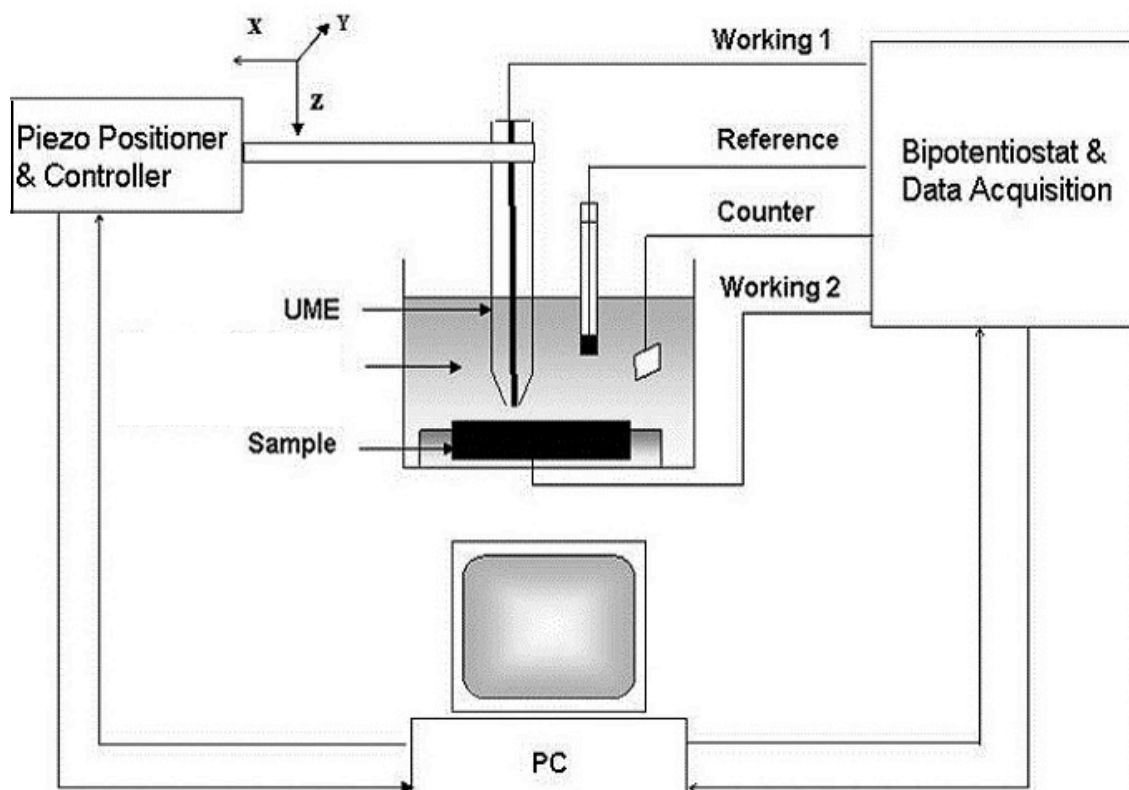


Figure 20: Illustration of the SECM instrument [5].

1.4.1. UME tip

An ultramicroelectrode is an electrode whose radius ranges between a few nm to 100 μm .

In SECM, a microdisc often constitutes the probe, i.e. the so-called tip.

An important parameter to be defined is the $RG = r_g / a$, where r_g is the radius of the tip electrode that includes both the insulating glass that covers the metal wire and the active part of the disc and a is the radius of the disc (**Figure 21**):

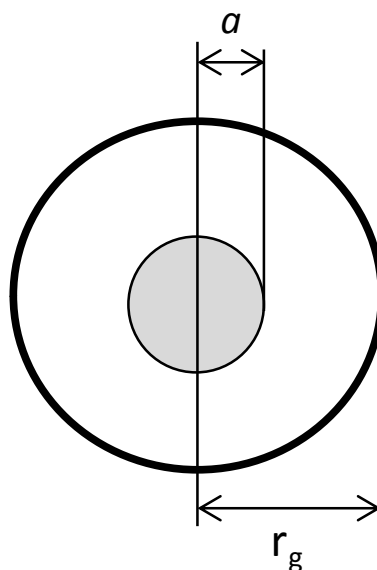


Figure 21: Size of a UME disc electrode with characteristic parameters: a = radius of the electroactive area; $r_g = a +$ radius of the insulating shell.

The selection of the RG value is a critical parameter: at high value of the RG, the collection efficiency is also high. However, a large RG makes the tip harder to use, because it becomes harder to reach short tip-substrate distances and easier to scratch the substrate during the test.

Thanks to the small size of the UME, the currents recorded are quite low (between 10^{-9} - 10^{-10} A). This means that the ohmic drop are negligible. Furthermore, thanks to the cylindrical diffusion profile typical of microdisk electrodes, the system reaches the steady state in the order of milliseconds.

1.4.2. Operational mode

There are different ways to operate with an SECM. One of the most commonly used is the *feedback mode*. This mode requires that the measurement is carried out in a solution containing an appropriate redox active species (O) and a supporting electrolyte that reduces the resistance of the solution and assures that the transport of the redox species to the tip occurs only by diffusion. To illustrate this mode, it is useful to consider a tip kept at a potential at which O is reduced to give R according to the reaction:



When the tip is away from the substrate, i.e. in the solution bulk, the reduction reaction occurs and a current flows. The current reaches a steady-state value ($i_{t\infty}$) that is governed by the rate of hemispherical diffusion of O from the bulk (**Figure 22**) and is equal to:

$$i_{t\infty} = 4nFDC^b a \quad (5)$$

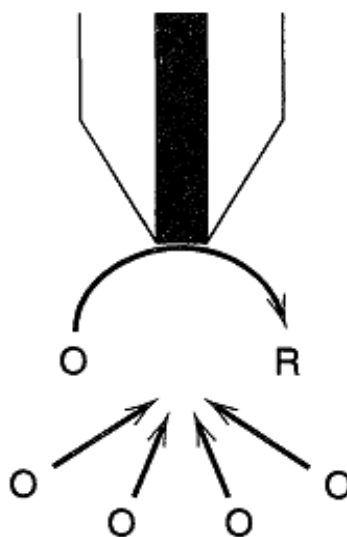


Figure 22: Basic principle of the feedback mode: away from the substrate the diffusion allows it to achieve the steady state ($i_{t\infty}$).

When the tip is approached to a substrate down to a distance comparable to the radius of the tip, the *feedback* occurs. In this case the current depends on the substrate nature and on the substrate-tip distance, d .

In the presence of a conductive substrate, the species R produced at the tip is oxidized again to O, thanks to the voltage created between the bulk solution and the layer close to the tip surface. The so-generated O species diffuses back to the tip. In this way, the flow of O to the tip increases, together with the tip current ($i_t > i_{t\infty}$).

This is the *positive feedback* (**Figure 23**):

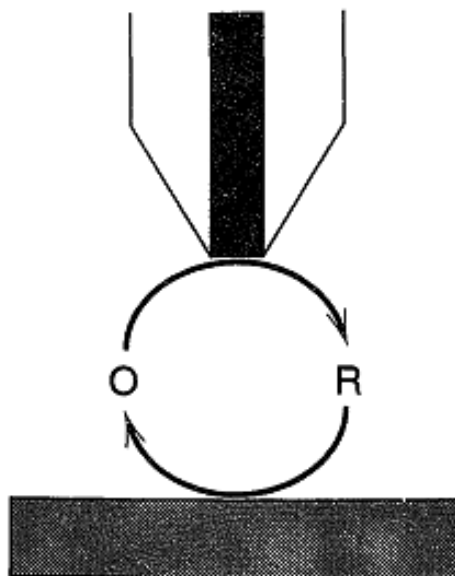


Figure 23: Positive feedback: the species R is regenerated from a conductive substrate.

On the other side, when the tip is approached to an insulating substrate, the latter partially blocks the flux of O at the tip. The current is therefore lower than in the bulk distance ($i_t < i_{\infty}$). This is the *negative feedback* (**Figure 24**):

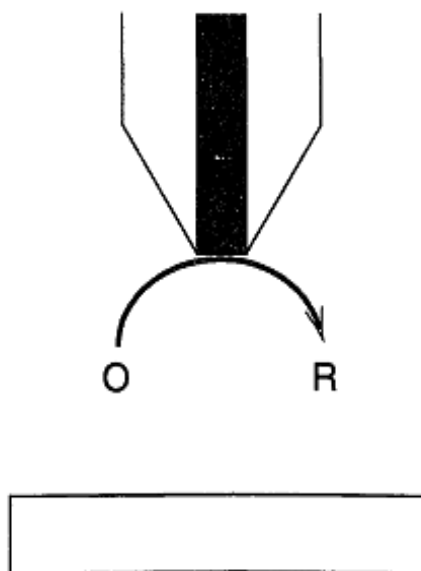


Figure 24: Negative feedback: the diffusion of R to the tip is prevented from the presence of an insulating substrate.

1.4.3. Approach curves

The approach curves related to a disc tip are calculated using digital simulation methods or numerical methods. Using these procedures empiric equations valid for both *negative feedback* (**Figure 25A**), and *positive feedback* (**Figure 25B**) have been obtained. These can be used to fit the experimental results:

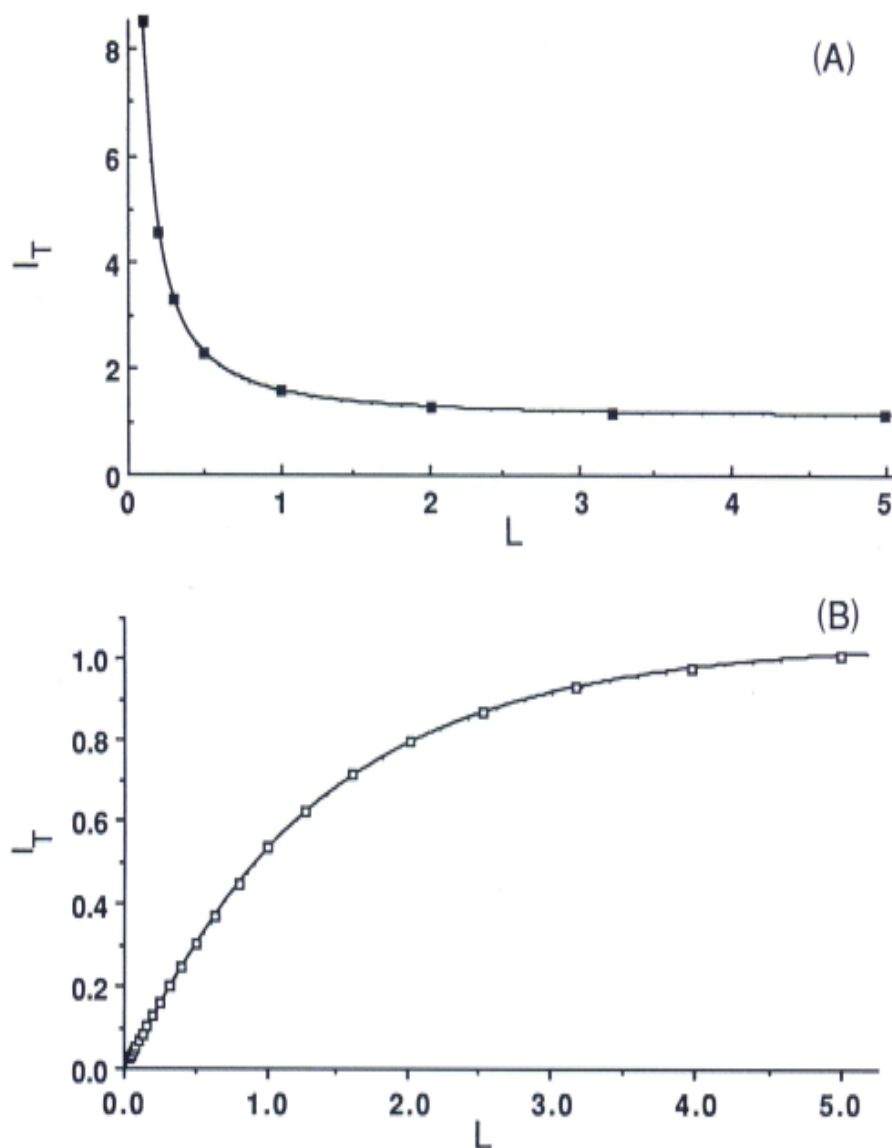


Figure 25: Approach curve of a conductive substrate (A) and insulator substrate (B).

Where $I_T = i_t / i_{t\infty}$ and $L = d / a$, to make the approach curves independent on the concentration and on the diffusion coefficient of the species R and on the electrode radius.

A typical use of approach curves is to set the position of the tip relative to the surface of the sample from i_t or to determine the tip radius graphically interpolating the empirical equation using a spreadsheet application.

Another typical use of approach curves is the tilt correction, the correction of the inclination of the platform where the SECM cell is placed: in order to prevent that the tip could scratch the substrate during the test, some approach curves are performed in different spots of the cell and the platform straightened.

1.4.4. Generation-collection mode

The *feedback mode* is extremely sensitive to the intrinsic activity of a material, but can be used only if the concentration of the reagent that is produced by the tip is sufficiently low to maintain the reaction at the tip itself under diffusive control. Furthermore, this method is strictly dependent on the distance between tip and substrate.

If all these conditions are not fully satisfied, then the *feedback mode* cannot be used.

There are two different *Generation-Collection modes*: TG/SC (tip generation/substrate collection) and SG/TC (substrate generation/tip collection).

In SG/TC (**Figure 26A**) the tip acts as a sensor, measuring the concentration of the product generated at the substrate. The latter is biased at the appropriate potential that allow the reaction, while at the tip the reaction is kept under diffusive control. Under this condition, the tip current is proportional to the concentration of the species produced at the substrate after equation (5). Note that the concentration of the species produced depends on the rate of its production that in turn depends on the substrate activity. Although the concentration changes with time, it reaches the steady state in a short time when the substrate is sufficiently small.

In the TG/SC (**Figure 26B**), the tip is biased to a potential suitable to generate a reagent while substrate consumes it. It is then possible to measure the substrate current i_s , which is strictly bound to the activity of the area over which the tip is located.

Usually, if the substrate is much larger than the tip, the heterogeneous electron transfer is in steady state conditions and there are no concurrent chemical reactions, the two currents are nearly equal, and then the collection efficiency, given by the ratio i_s / i_t , tends to 1. If these conditions are not satisfied or if the species generated reacts in the

space between tip and substrate, i_t and i_s will be different, the collection efficiency will decrease and will change in function of the distance d between tip and substrate.

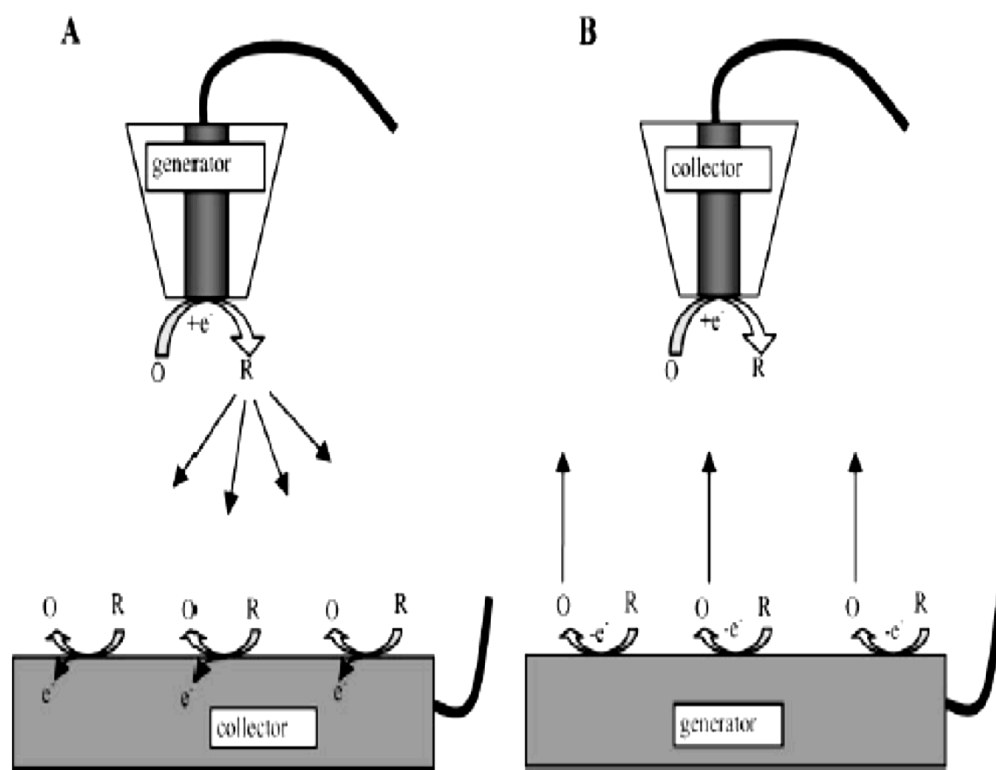


Figure 26: Scheme of (A) TG/SC mode and (B) SG/TC mode. In (A) the tip reduces the species O to R, which diffuses toward the substrate [5].

1.4.5. Imaging

A very important feature in SECCM is the possibility of recording images, that are the representation of the dependence of tip (or substrate) current as a function of the tip x-y position.

In this case, the current is dependent on both the substrate geometry and its electrochemical properties.

Considering the tip scanning a surface of homogeneous composition in the x-y plane while tip height is kept constant, if substrate surface present a certain roughness degree (with a mesh size comparable to or higher than the tip dimension), tip (and substrate) current changes during the scan, since tip-substrate distance changes. In this case, because of feedback phenomena, tip (substrate) current represents the surface morphology.

If, otherwise, the substrate composition is not homogeneous, for example presenting both insulating and conductive regions, tip current variations during the scan are mainly due to the presence of *positive feedback* or *negative feedback* areas.

In this case, the image is a representation of the electrochemical properties of the different regions of the surface.

The same approach can be repeated in the *generation/collection* mode. In this case, both tip and substrate are biased at a potential suitable to allow the reactions under interest.

In the case of catalysts screening, the substrate presents spots with different activity respect to the desired reaction, the tip current changes during the scan, enhancing in presence of highly active spots.

The tip current recorded in absence of active spots is called background current.

An example of the resulting image obtained both through the *feedback* and the *generation/collection* modes is shown in Figure 27:

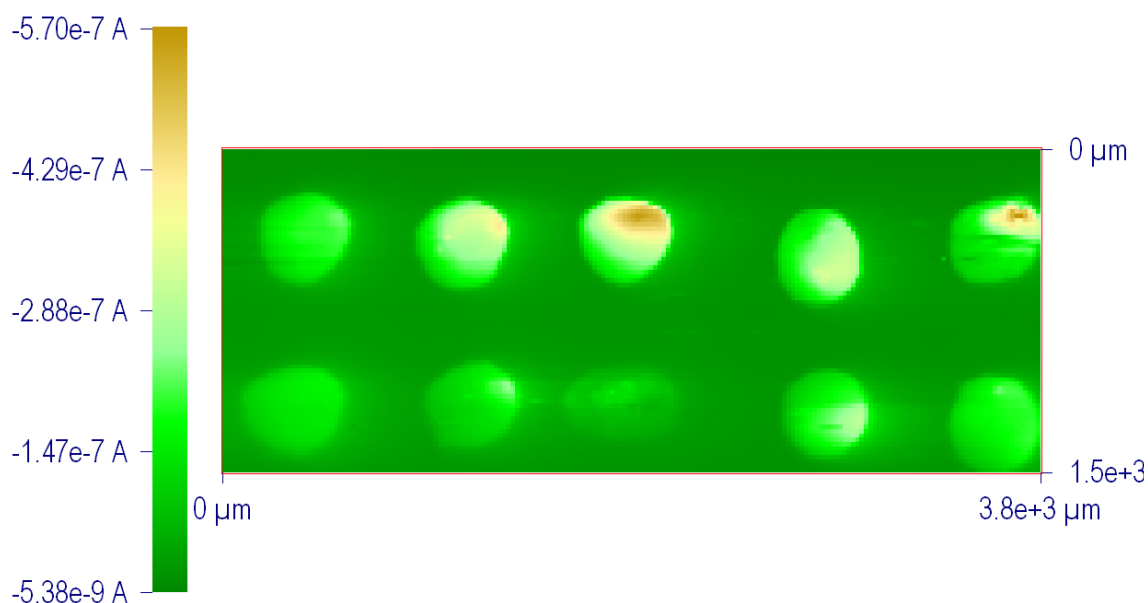


Figure 27: SG/TC image of 10 Co/Ni mixed oxides spots deposited onto a Ti sheet with a $25 \mu\text{m}$ diameter Au tip. $E_{\text{sub}} = 1.4 \text{ V (RHE)}$. $E_{\text{tip}} = 0 \text{ V (RHE)}$.

2. Chemical-physical techniques

2.1 Scanning Electron Microscopy (SEM)

Electron microscopes are useful techniques for the analysis of the morphology of solids. In particular, in order to study the shape, the size and the structure of nanoparticles, electron microscopies are the most suitable techniques. Indeed, thanks to the short wavelength of electrons, and to the possibility, by using a magnetic field, of build an electron lens, they can analyse the samples to the nanometer scale.

The primary electron beam is emitted from a metal cathode, and is focused onto the sample surface.

In the case of scanning electron microscopy (SEM), secondary electrons, produced after the interaction of the primary beam with the matter, are collected by an analyser placed on the top of the sample at a given angle with respect to the incident beam, as shown in **Figure 28**:

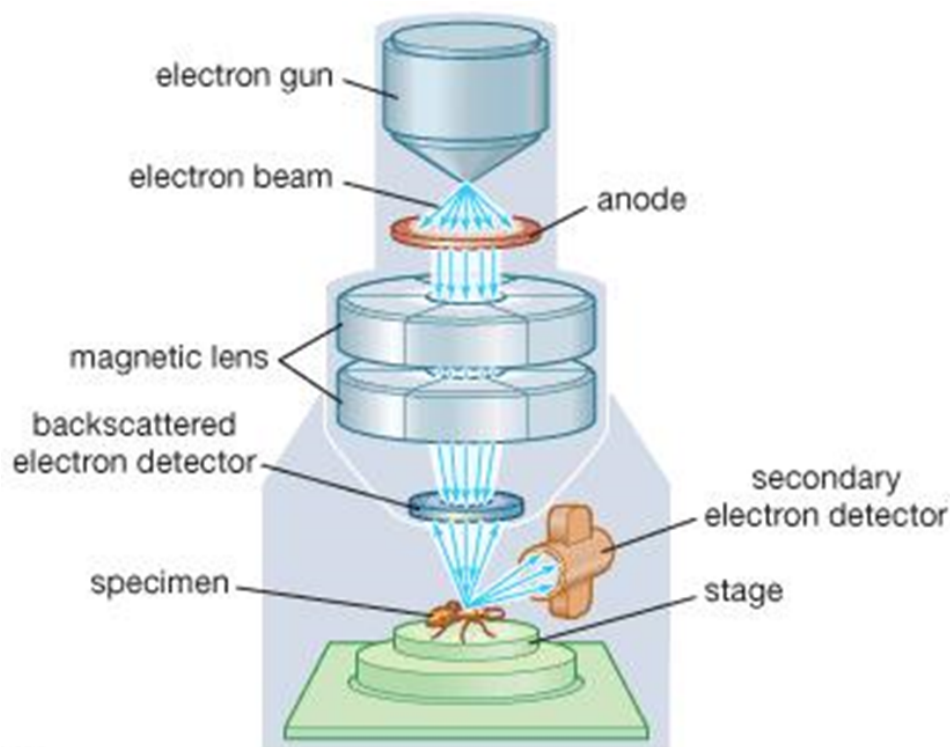


Figure 28: scheme of a SEM instrument.

Since only the sample surface is the source of secondary electrons, and since the emission coefficient depends on the angle between the incident beam and the surface, this technique gives an image of the sample surface.

2.2 Transmission Electron Microscopy (TEM)

Otherwise, in TEM techniques, electrons are emitted from a metal cathode, and are focused onto the sample surface. The electron beam is then scanned over a desired portion of the sample. This technique is characterized by very low resolution limits: usually 0.5 \AA .

It is thus very useful for the analysis of the structures of thin samples through which electrons are transmitted. **Figure 29** shows a scheme of a TEM instruments:

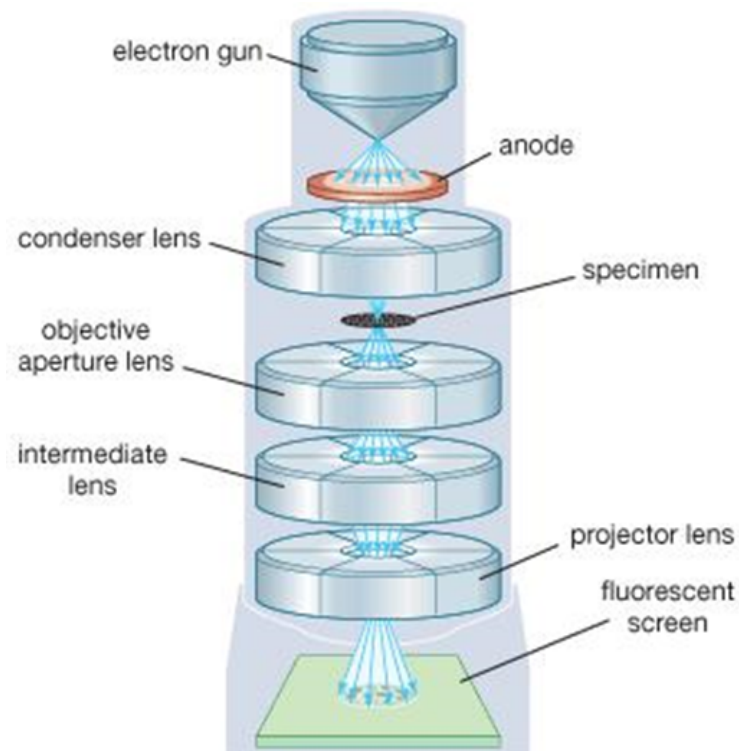


Figure 29: scheme of a SEM instrument.

In TEM the electrons are accelerated to 100 keV or higher (up to 1 MeV) and then focused onto a thin sample (less than 200 nm) by means of a condenser lens system. Accelerated electrons can then penetrate the sample.

The greatest advantages that TEM offers are the high magnification factor ranging from 50 to 10^6 and its ability to provide morphology images, diffraction patterns, and elemental analysis during the same working session.

By selecting between direct electrons (brightfield, BF) or scattered one (dark field, DF), different information can be obtained. Elastic scattering does not provoke energy losses and gives rise to diffraction patterns. Inelastic interaction between incident beam and sample electrons occur in the presence of heterogeneities such as grain boundaries, dislocations, second-phase particles or defects, thus leading to a spatial variation in the intensity of transmitted electrodes.

It is also very useful, in terms of morphological and structural investigations, to tilt the sample in a particular angle, in order to produce many diffraction beams. In this case, a structural image is produced, showing dark column corresponding to atoms that form fringes. This kind of technique is called *high resolution TEM* (HRTEM). In addition, electrons are diffracted by the sample and the diffraction pattern can be recorded in order to obtain a complementary information about the sample structure. This technique is called *selected-area electron diffraction* (SAED).

3. Working electrodes for the electrochemical analysis

3.1 Tip preparation

The tip used in the Scanning Electrochemical Microscopy may have different geometries: disc, semi-spherical, cylindrical and planar. The tips used in this Ph.D. thesis are disc electrodes.

The materials used to prepare them were:

- Glass capillaries with outer diameter 1.5 mm, internal diameter 0.75 mm, length 100 mm;
- Gold wire (GoodFellow): diameter between 0.025 mm and 0.1 mm, 0.05 mm and 0.025 mm, 99.99% purity;
- Copper wires;
- Silver paste (Fluka).

The first step for the preparation of an UME consists in cutting the capillary in two halves, to obtain two portion of about 5 cm in length. In order to avoid a poor seal of the glass and the formation of bubbles inside the capillary it is necessary to remove moisture and dust, as well as other polluting substances or water. These conditions are obtained by washing the capillaries with acetone and immersing them in ultrasounds for about 5 minutes. After being dried in an oven, the capillaries are sealed using a flame at a not too high temperature, to avoid the excessive curvature of the glass tip. The capillary is rotated continuously over the flame until a conical shape is obtained.

At this point a portion of the gold wire (about 2 cm), previously washed with acetone and cleaned in ultrasound for about 5 minutes and dried, is introduced inside the capillary. It is essential that the wire is straight before being inserted inside the capillary. Finally, the gold wire is sealed: the open end of the capillary is connected to the vacuum line to prevent the formation of bubbles while the close one is placed in the center of a metal spiral, that is heated for about 10 minutes to remove moisture and impurities on the wire or on the internal glass walls. The wire heating is then raised up to melt the glass around the Au wire, thanks also to the application of vacuum. Then, the non-welded wire is connected to a copper wire by silver paste. The other end the

golden wire is exposed using abrasive papers with different grit (180, 1000, 2400, 4000), proceeding from the coarsest to the finest. The last step consists in sharpening the capillary to obtain the desired value of $RG = (r_g/a)$. The tips used in the present work have $RG \approx 10$.

Figure 30 represents the finished tip:



Figure 30: Picture of an Au UME tip.

3.2 Arrays preparation

SECM arrays consists in Ti sheets ($1.5 \times 1.5 \text{ cm}^2$) or hematite samples ($1 \times 1 \text{ cm}^2$) covered by small oxide spots of different composition. The selected materials are low-cost and high abundant elements.

The creation of oxide arrays starts dispensing the suitable precursor solution. Since spots must be as small as possible (in order to decrease SECM imaging time), a very small amount of precursors must be deposited, and a picoliter dispenser is then used. The latter consists in a small quartz pipette by which the solution is pumped out by mean of a piezoelectric system. The pipette position is determined by motors moving in three dimensions and is controlled by a computer.

It is possible to dispense one or more solutions, and the relative amount of the precursors on each spot can be determined by modulating the number of drops. For example, keeping constant the total number of drops for each spot and the concentration of each precursor solution, the ratio between the number of drops is equal to the molar ratio.

The Ti sheets were previously cleaned using abrasive papers with two different grits (2400, 4000). After that, the solutions with a 0.1 M concentration of precursor salt

dissolved in a water/glycerol (3:1) were deposited using a CHI 1550 picoliter dispenser (CH Instruments, Austin, Texas) was used. The deposition parameters were the following: pulse amplitude: pulse amplitude: 80 V; pulse width: 40 μ s; pulse period: 1000 s., centre to centre distance: 800 μ m.

The samples were then vortexed and activated by the exposition to gaseous NH_3 atmosphere for 1 hour.

In the end, the arrays were dried for 1 h at 180 $^\circ\text{C}$ (after a 5 $^\circ\text{C}/\text{min}$ ramp) under a N_2 flow and annealed at 500 $^\circ\text{C}$ for 2 h in air. This procedure yielded 500 μm diameter spots (**Figure 31**).

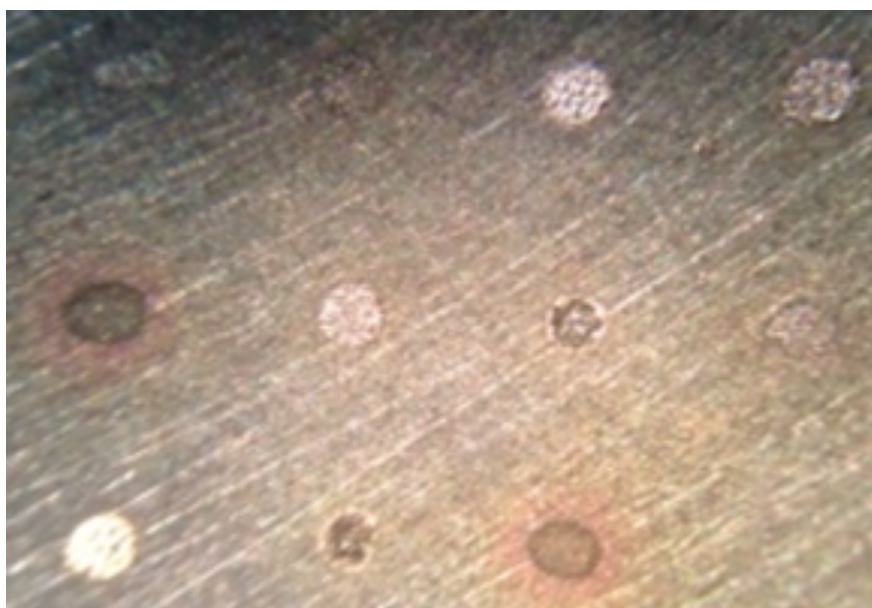


Figure 31: Image obtained with a metallographic microscope of an array deposited onto a Ti sheet.

For what concern the deposition onto hematite samples, the precursor solutions were diluted to 1 mM dissolved in a water/glycerol (3:1).

The substrate was previously cleaned 30 minutes in acetone, 30 minutes in ethanol and 30 seconds in water. After that, the solutions were deposited with the piezo-dispenser with the same parameters used for Ti sheets.

This kind of substrate were not activated in NH_3 flux, but were dried for 1 h at 180 $^\circ\text{C}$ (after a 5 $^\circ\text{C}/\text{min}$ ramp) under a N_2 flow and annealed at 300 $^\circ\text{C}$ for 2 h in air. This procedure yielded 500 μm diameter spots, made of amorphous metal oxides (**Figure 32**).

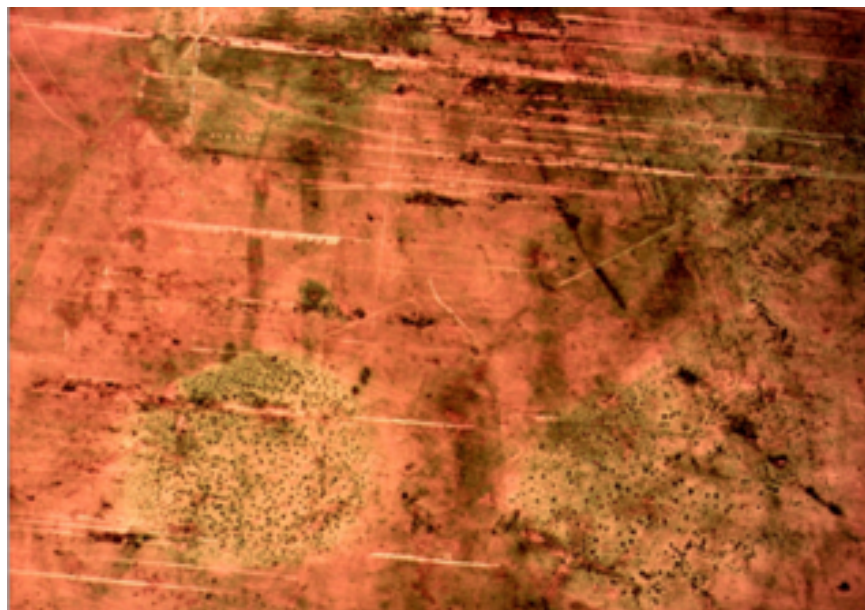


Figure 32: Image obtained with a metallographic microscope of an array deposited onto a hematite sample.

3.3 Lab-scale electrodes preparation

As for the arrays, also the lab-scale electrodes were created starting from solution of precursor metal salts with a concentration of 1 mM dissolved in a water/glycerol (3:1) mixture. The precursor solutions were then mixed in different ratios, according to the desired compositions.

These mixtures were dispensed onto hematite samples (1 cm²), previously cleaned sonicating them 30 minutes in acetone, 30 minutes in ethanol and 30 minutes in water. The deposition occurred by drop-casting and different amount of solutions were tested, in order to study the influence of the overlayer loading.

All the samples were then dried for 1 h at 150 °C in an oven and then annealed for 2 h in air at 500 °C (after a 5 °C/min ramp).

3.4 Cavity-Microelectrodes (C-MEs)

The cavity microelectrode is an innovative tool for the study of finely dispersed electrode materials to be adopted in several electrochemical systems [13, 14]. in fact, the

benefits introduced by the use of C-ME, compared to more classical powder supports are manifold. The C-ME allows to:

1. Minimize the ohmic drop effect thanks to the micrometric size and therefore to the low associated current intensities;
2. Not to use a gluing agent on the electrochemical response;
3. Not to have a contribution from the current collector (the microdisk at the base of the cavity) since its surface area is negligible in comparison with the one of the hosted material.

A schematic representation of a C-ME is shown in **Figure 33**:

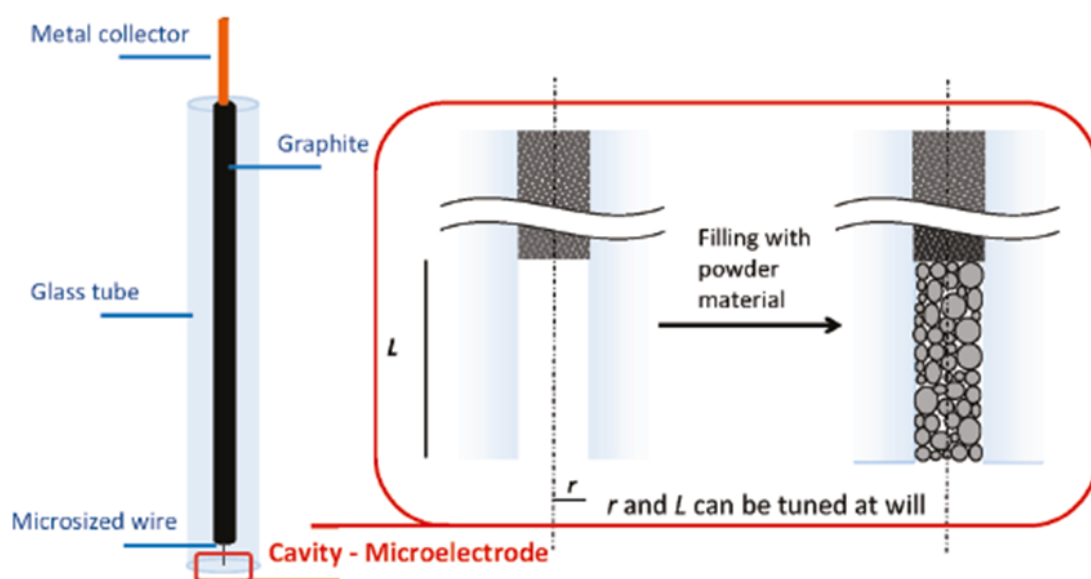


Figure 33: Schematic representation of a C-ME, the red insert represent the cavity magnification.

Quite recently, it was proved that C-MEs allow to carry out a rapid screening of electrochemical behaviour of different materials thanks of the possibility of a quick and reliable electrode preparation [15, 16].

Moreover, it is possible to accurately know the cavity diameter and depth, and thus the volume. This implies that an analysis carried out by a C-ME can be considered as quantitative [17] and that it is possible to evaluate and know the amount of the powder under investigation.

In addition, other quantitative information can be derived from the voltammetric data obtained using C-MEs of know volume.

However, the possible presence of irregularities in the cavity bottom can make the determination of the cavity volume difficult, thus leading to an inaccurate quantification of the amount of powder under study. This represents the main limitation of C-MEs.

Gold-based cavity microelectrodes are usually prepared as follows:

- an Au wire (Goodfellow, 99,9% purity, temper hard, $\varnothing = 25, 50, 63 \mu\text{m} \pm 10\%$) was sealed into a glass tube by means of an air/liquid petroleum gas flame;
- the Au disk was first exposed and then polished by using abrasive papers of 400-800-1000-2400-4000 mesh and alumina powders (mean particle size 0.3 and 0.05 μm);
- the contact between the Au wire and the external Cu wire connector was made with graphite powder;
- the upper end of the glass tube is finally sealed by a silicon paste.

The electrode was then electrochemically cleaned by repeatedly cycling between 0 and 1.5 V (SCE) at 500 mV s^{-1} . The CVs were repeated for 270 cycles.

The experimental radius, r_e , was determined via the steady state current recorded in aqueous KNO_3 0.1 M in the presence of 1 mM $\text{Fe}(\text{CN})_6^{3-}$ or 1mM $\text{Ru}(\text{NH}_3)_6\text{Cl}_3$ in KCl 0.1 M at 1 mV s^{-1} in the 0.6/-0.4V (SCE) potential window, at 25 °C, according to the following equation:

$$I_{ss} = 4nFc_bDr_e$$

where:

r_e = geometric metallic disk radius;

I_{ss} = steady state current intensity;

c_b = concentration of the redox mediator;

D = diffusion coefficient of the redox mediator;

n = number of electrons;

F = Faraday constant.

The etching of the Au wire was performed according to the following procedures:

1. galvanostatic dissolution at 2 mA cm^{-2} in aqueous HCl 0.5 M + H_2SO_4 0.5 M. The Au dissolution is followed by cycling the potential between 0 and 1.1 V (SCE), for 500

cycles at 500 mV s^{-1} , in the same solution used for the galvanostatic dissolution, to smooth the Au surface via reconstruction;

- galvanostatic square wave current profile between $+1.5$ and $-0.074 \text{ mA cm}^{-2}$ at a frequency of 0.0025 s^{-1} , in aqueous $\text{HCl } 0.5 \text{ M} + \text{H}_2\text{SO}_4 \text{ } 0.5 \text{ M}$.

This last procedure likely couples the galvanostatic dissolution of Au with the removal of dissolution products from the Au surface and the incipient recess by H_2 evolution.

After the etching, the depth of the recess, L , is determined *via* the steady state limiting current of the ruthenium-hexamine complex, as above, according to the following equation [18]:

$$I_{\text{ss}} = \frac{4\pi n F c_b D r_e^2}{4L + \pi r_e}$$

where L is the only unknown quantity.

In addition, the cavity bottom surface area (and thus its equivalent radius, r_b .) is evaluated by integration of the gold oxide reduction peak of the CV recorded in HClO_4 0.1 M between 0.5 and 1.7 V (SCE) at 20 mV s^{-1} . This method, that follows the guidelines reported by [19] leads to the conversion factor of $937.8 \text{ } \mu\text{C cm}^2$, obtained according to reference. The surface area of the Au disk at the cavity bottom obtained by this method value is compared with the value measured before the etching to evaluate the performance of the etching procedure.

The cavity is now ready to be filled with the investigated powder using the electrode as a pestle.

In this Ph.D. Thesis, cavity microelectrodes were prepared starting from an ultramicroelectrode (UME), in order to use them as SECM tip, as will explain in the *Results and Discussion* part.

Thus, the possibility to use C-MEs as SECM tips in different modes, *feedback*, *tip generation/substrate collection (TG/SG)* and *substrate generation/tip collection (SG/TC)*, will be explored in more details.

Moreover, the possibility of conveniently studying parallel reactions occurring at a desired powder electrode material is also here introduced.

In this case, the Au C-ME were prepared with the following procedure: a galvanostatic square wave current profile between $+1.5$ and -7 mA cm^{-2} was applied to the tip in

aqueous NaCl 0.5 M + HCl 0.5 M + H₂SO₄ 0.5 M. The anodic step lasted twice than the cathodic one and the cycle frequency was 0.00028 s⁻¹.

After the etching, the cavity bottom was homogenized by cycling its potential (500 cycles at 500 mV s⁻¹) in the same solution between 0 and 1.1 V (Ag|AgCl 3 M KCl).

After the etching, the depth of the recess was determined as previously explained.

3.5 Synthesis of hematite ($\alpha - \text{Fe}_2\text{O}_3$)

Hematite was synthesised in collaboration with the LABCAT group of the Istituto di Scienze e Tecnologie Molecolari –Consiglio Nazionale delle Ricerche (ISTM-CNR) and in particular thanks to Dr. Francesco Malara and Dr. Alberto Naldoni.

Hematite was deposited on fluorine-doped tin oxide (FTO)-coated glass substrates (Solaronix, 10 Ω /sq) previously cleaned by sonicating them in acetone and then in water.

The synthesis took place at 70 °C for 3 h using a precursor aqueous solution of FeCl₃·6H₂O 0.15 M (Sigma-Aldrich) and NaNO₃ 1 M (Sigma-Aldrich), at pH 1.5 optimized with HCl [20]. After the deposition the samples were rinsed with deionized water and then calcinated at 500 °C for 1 h, followed by 20 min at 800 °C [21].

In the case of $\alpha - \text{Fe}_2\text{O}_3$ modified with NiOOH, hematite photoelectrodes were immersed in a Ni(NO₃)₂ 0.1 M solution with a pH 6.6 obtained by the addition of NaOH. The solution was then purged with nitrogen gas for 1 h.

The NiOOH was deposited by photodeposition: an open circuit voltage was applied to the sample and different photodeposition times were tested: 60, 300, 600, and 1200 s. The best results were obtained applying the potential for 600 s.

This step was then followed by an electrodeposition at 1.2 V (Ag|AgCl 3 M) for 60 s.

-
- [1] Wang, J. *Analytical Electrochemistry*, 2nd edition (2000) Wiley-VCH.
- [2] Brett, C.M.A.; Oliveira Brett, A.M. *Electrochemistry, principles, methods, and application* (1994) Oxford University Press
- [3] Minguzzi, A.; Battistel, D.; Rodríguez López, J.; Vertova, A.; Rondinini, S.; Bard, A.J.; Daniele, S. *J. Phys. Chem. Sci.*, 119 (2015) 2941
- [4] Perry's Chemical Engineers' sixth edition (Robert H. Perry, Don Green, McGraw-Hill International editions, Chemical Engineering Series)
- [5] Bard, A.J.; Mirkin, M.V. *Scanning Electrochemical Microscopy*, (2001) Marcel Dekker.
- [6] Bard, A.J.; Faulkner, L.R. *Electrochemical methods: Fundamentals and Applications*, John Wiley and Sons, Inc.
- [7] Fernández, J.L.; Walsh, D.A.; Bard, A.J. *J. Am. Chem. Soc.*, 127 (2005) 357
- [8] Minguzzi, A.; Alpuche-Aviles, M.A.; Rodríguez López, J.; Rondinini, S.; Bard, A.J. *Anal. Chem.*, 80 (2008) 4055
- [9] Lee, J.; Ye, H.; Pan, S.; Bard, A.J. *Anal. Chem.*, 80 (2008) 7445
- [10] Rodríguez-López, J.; Minguzzi, A.; Bard, A.J. *J. Phys. Chem. C*, 114 (2010) 18645
- [11] Sánchez-Sánchez, C.M.; Solla-Gullón, J.; Vidal-Iglesias, F.J.; Aldaz, A.; Montiel, V.; Herrero E., *J. Am. Chem. Soc.*, 132 (2010) 5622
- [12] Wittstock, G.; Schumann, W. *Anal. Chem.* 69 (1997) 5059
- [13] Cachet-Vivier, C.; Keddad, M.; Vivier, V.; Yu, L.T. *J. Electroanal. Chem.* 688 (2013) 12
- [14] Li, C.M.; Hu, W. *J. Electroanal. Chem.* 688 (2012) 20
- [15] Minguzzi, A.; Locatelli, C.; Cappelletti, G.; Scavini, M.; Vertova, A.; Ghigna, P.; Rondinini, S. *J. Phys. Chem. A* 116 (2012) 6497
- [16] Minguzzi, A.; Locatelli, C.; Cappelletti, G.; Bianchi, C.L.; Vertova, A.; Ardizzone, S.; Rondinini, S. *J. Mater. Chem.* 22 (2012) 8896
- [17] Locatelli, C.; Minguzzi, A.; Vertova, A.; Cava, P.; Rondinini, S. *Anal. Chem.* 83 (2011) 2819
- [18] Bond, A.M.; Luscombe, D.; Oldham, K.; Zoski, C.G. *J. Electroanal. Chem.* 249 (1988) 1
- [19] Trasatti, S.; Petrii, O.A. *Pure & Appl. Chem.* 63 (1991) 711
- [20] Kim, J.Y.; Magesh, G.; Youn, D.H.; Jang, J.-W.; Kubota, J.; Domen, K.; Lee, J.S. *Sci. Rep.*, 3 (2013) 2681.
- [21] Sivula, K.; Zboril, R.; Le Formal, F.; Robert, R.; Weidenkaff, A.; Tucek, J.; Frydrych, J.; Grätzel, M. *J. Am. Chem. Soc.*, 132 (2010) 7436

Results and discussion

1. Rapid screening of oxygen evolution reaction electrocatalysts deposited onto titanium sheets by SECM

1.1. Introduction

As preliminary study, electrocatalysts for the oxygen evolution reaction (OER) with different compositions of low-cost metals (Ni, Al, Fe, Co, Mg, Ca, etc.) have been screened using the Scanning Electrochemical Microscopy (SECM), in the substrate generation/tip collection (SG/TC) mode.

As deeply explained in the *Introduction*, in the electrochemical water splitting, the overall reaction is physically separated into its half reactions, water oxidation (at the anode) and water reduction (at the cathode). Nonetheless, the pathways for the reduction of water have been elucidated and the relevant catalytic materials assessed. Vice versa, the water oxidation is a four-electron and four-proton process and leads to the formation of an oxygen-oxygen bond, thus requiring rather high overpotentials even in presence of good electrocatalysts. For this reason, the development of efficient electrocatalysts for oxygen evolution reaction (OER) remains a key challenge.

Noble metal oxides have been mainly considered being the best materials for electrocatalysts. For example, RuO₂ and IrO₂ are considered the most active compounds in acidic environment, with the first presenting the highest activity and the second a ≈ 20 times higher stability. Unfortunately, they are also very expensive. Even in alkaline media, IrO₂ shows high performances, that are however comparable to those referred to other low cost materials, e.g. Co oxide, CoFe, NiCo, etc.

Consequently, it is necessary to find new catalysts showing the same activity and low OER overpotentials showed by RuO₂ or IrO₂, but with a lower cost, as well.

Arrays of small spots (≈ 500 μm diameter) of different compositions are prepared over a supporting metal. An ultramicroelectrode (UME), the tip, positioned close to a substrate immersed in an electrolyte moves over the sample thanks to x-y-z stepper motors.

The amount of oxygen produced by the substrate spots is reduced at the tip, in the so-called *substrate generation/tip collection (SG/TC)* mode. The tip can thus be used as local oxygen sensor, providing the desired information about the activities and the properties of the substrate itself.

The experimental scheme of the SECM substrate generation/tip collection mode is shown in **Figure 34**.

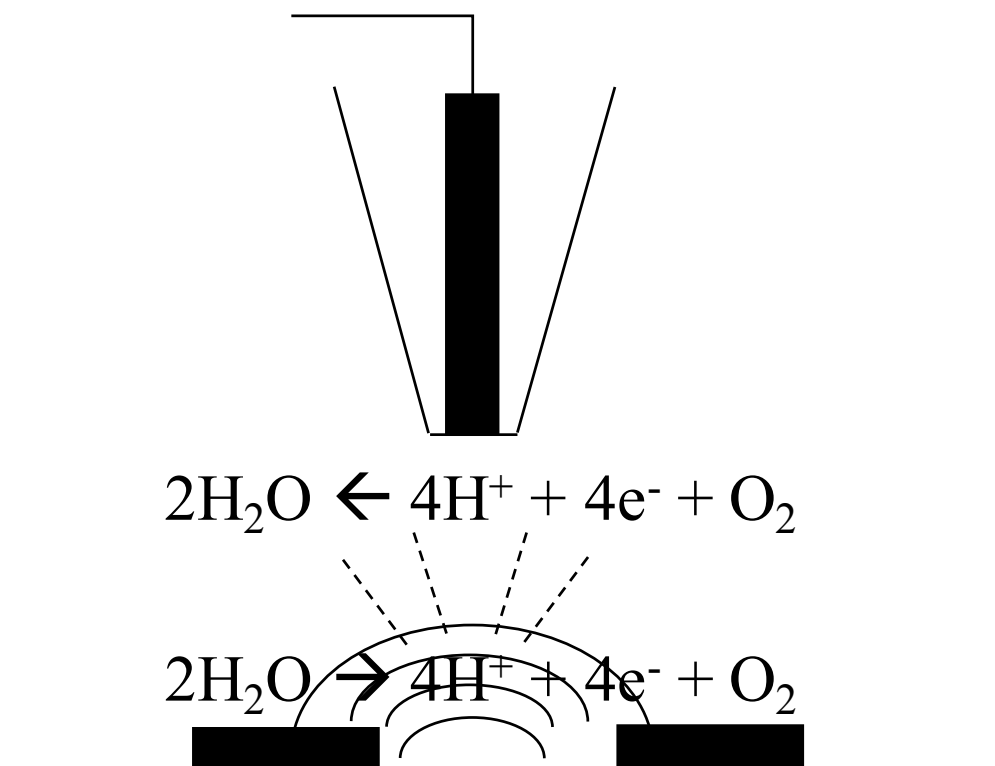


Figure 34: Pictorial scheme of a SG/TC experiment: the array spots produce O_2 , while the tip reduces it.

The recorded tip current as a function of its position is represented by a color-coded image that gives information about the local topography of the examined substrates and/or on their local reactivity at a given potential.

In this section, we will show the results obtained using a 25 μm diameter Au tip and its application to the preliminary characterization of mixed oxide electrocatalysts for OER.

Unfortunately, when the substrate is placed under oxygen evolution conditions, all the spots are able to oxidize water to oxygen at a rate dependent on their intrinsic characteristics. Consequently, the current recorded at the tip will be due to the cumulative amount of oxygen produced not only by the spot under examination, but also from the neighbour ones, as shown in **Figure 35**:



Figure 35: Overlapping of oxygen diffusion profiles of different spots, when they are all biased at an E_{OER} at the same time [1].

Therefore, tip current cannot be univocally associated with the activity of the spot under investigation. This also causes the increase of tip current at the background level, thus reducing the image contrast.

To minimize this drawback, two solutions are possible: the first is the *shielded tip approach* [2**Errore. Il segnalibro non è definito.**], consists in depositing a gold metal layer on the tip walls, polarised at the same potential of the tip, to reduce the O_2 produced by the neighbouring spots and hence shield the tip. The wall is biased at a potential negative low enough to guarantee mass transport-limited oxygen reduction and allows to shield the tip from the oxygen coming from the neighbouring spots.

An alternative method, based on the substrate potential *double pulse* [¹], can be used. This involves a measure of the tip current during the application of a pulsed potential profile to the substrate, done by placing the tip at a desired and constant distance from the substrate ($< 20 \mu\text{m}$). The potential profile applied to the substrate is pulsed between two values: $E_{sub,OER}$, which corresponds to a potential of oxygen evolution, and $E_{sub,rest}$, which corresponds to a value at which the substrate cannot evolve oxygen. The applied potential profile are graphically described in **Figure 36**:

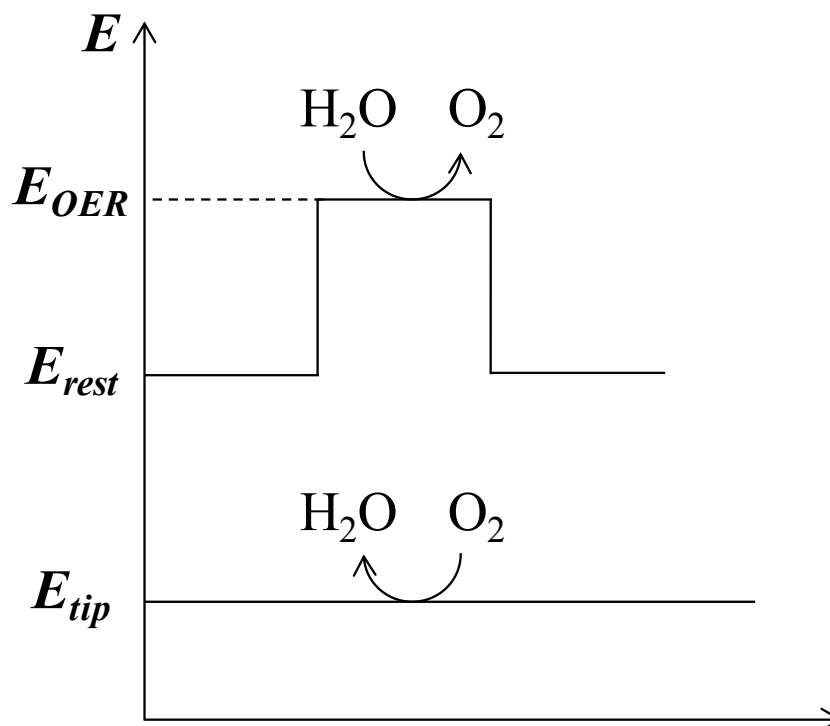


Figure 36: Double pulse potential profile applied both to the substrate and the tip.

This method presents the following advantages:

1. It is not necessary to finely correct the substrate tilt;
2. The potential step is applied for a relatively short time, so that the growth of the reaction product concentration profiles from different spots in the array do not overlap;
3. Each spot of material in the array is examined independently and at constant distance and this allows in principle a more detailed analysis of each material;
4. A normal tip is used, thus making it more suitable for the following investigation of electrocatalysts deposited onto a photoconverter.

On the other hand, with this method no images are recorded and so the results are not of immediate visual inspection. In addition, the final results are obtained after the raw signal treatment and interpretation.

This last method was initially adopted for an Ir-Sn mixed oxide array, tested in H_2SO_4 0.5 M, used as standard array. Then, different Co-based mixed oxides arrays were prepared: each spot is composed by 90% Co and 10% of other metals, e.g. Ni, Fe, Cu and Zn. Also the 100% Co was tested. The experiments were performed in NaOH 0.1 M

All the spots were prepared starting from chloride or nitrate salts and were deposited onto Ti sheets (previously cleaned) with a piezo-dispenser.

1.2. Experimental

All chemicals were used as received. Aqueous solutions were prepared with water from a Millipore purification system. All the experiments cited were performed at room temperature.

1.2.1. Sample preparation

For array based on $\text{Sn}_{1-x}\text{Ir}_x\text{O}_2$ mixed oxides in the nominal composition range from 0 to 100% of IrO_2 have been prepared in 10% increment. A solution of 0.1 M $\text{IrCl}_3 \cdot 3\text{H}_2\text{O}$ (99.8% purity, Alfa Aesar, Ward Hill, MA) in water/glycerol (3:1) was firstly dispensed onto a Ti sheet (1.5×1.5 cm, 0.75 mm thickness, Aldrich 99.7% purity), previously washed in water and sonicated in acetone, using a CHI 1550 picoliter dispenser (CH Instruments, Austin, Texas) with spot deposition parameters of pulse amplitude: 50 V, pulse width: 15 μs , pulse period: 500 ms, centre to centre distance: 500 μm . Successively, a 0.1 M solution of $\text{SnCl}_4 \cdot 5\text{H}_2\text{O}$ (98% purity, Alfa Aesar, Ward Hill, MA) in water/glycerol (3:1) was dispensed in the same way as for the Ir precursor. To keep the total moles of the two components constant on every spot, the number of drops is varied between 0 and 10. In this way 11 $\text{Sn}_{1-x}\text{Ir}_x\text{O}_2$ spots were obtained with compositions ranging from 100% IrO_2 to 100% SnO_2 with steps of 10%. The array was composed of a 3 three equivalent spot lines, in order to study the reproducibility, as shown in **Figure 37**:

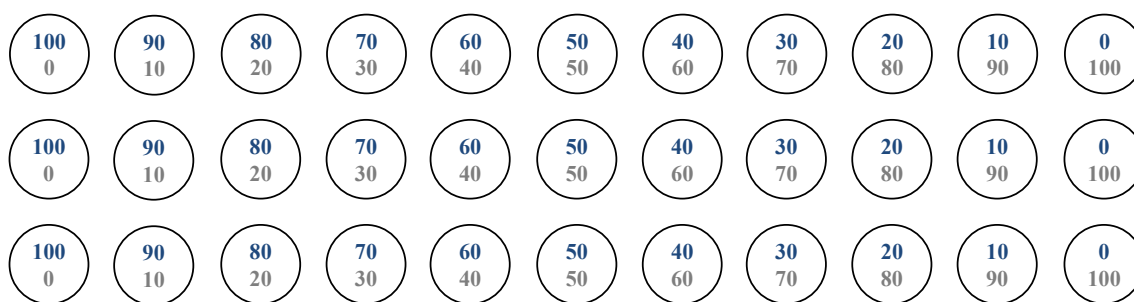


Figure 37: 3-rows array composed of Ir (blue) and Sn (grey) oxides in different ratios.

The sample was then vortexed for 10 minutes and immediately exposed to gaseous NH_3 (1 atm) atmosphere for 1 hour. The sample was aged in air for 24 hours, then dried for 1 hour at 180 °C (after a 5 °C/min ramp) in a tube furnace under an Ar flow. They were

annealed at 500 °C for two hours in oxygen (1 atm). This procedure yielded 300 µm diameter spots.

For Co-based array, instead, each spot was composed of 90% Co oxide and 10% of the second element (Ni, Fe, Zn, Cu) oxide. A solution of 0.1 M $\text{Co}(\text{NO}_3)_2 \cdot 6\text{H}_2\text{O}$ (98% purity, Sigma-Aldrich) was dissolved in a water/glycerol (3:1) mixture and deposited onto a titanium sheet ($1.7 \times 1 \text{ cm}^2$, 0.5 mm thick, 99% purity, Alfa Aesar), previously cleaned using abrasive papers with two different grits (2400, 4000). The parameters used for the array creation were the following: pulse amplitude: 80 V; pulse width: 40 µs; pulse period: 1000 s. The spots centre-to-centre distance was set at 800 µm. Successively, 0.1 M solutions of $\text{FeSO}_4 \cdot 7\text{H}_2\text{O}$ (99.5% purity, Carlo Erba), ZnCl_2 (97% purity, Sigma-Aldrich), $\text{Ni}(\text{NO}_3)_2 \cdot 6 \text{H}_2\text{O}$ (99% purity, Alfa Aesar) and $\text{Cu}(\text{NO}_3)_2 \cdot 2\frac{1}{2}\text{H}_2\text{O}$ (98% purity, Sigma-Aldrich) in water/glycerol (3:1) were dispensed in the same way as for the Co precursor. In this way a 3x11 array was obtained. In order to check the reproducibility, a pure 100% CoO_2 spot was deposited in each row. The array is shown in **Figure 38**:

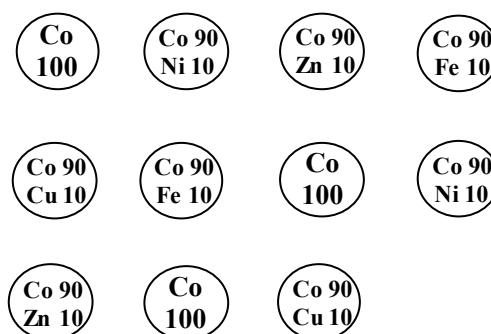


Figure 38: 3-rows array composed of Co and other oxides (Fe, Zn, Ni and Cu), with Co kept fixed at 90%.

The sample was then vortexed and exposed to gaseous NH_3 atmosphere for 1 hour. The sample is then dried for 1 h at 180 °C (after a 5 °C/min ramp) under a N_2 flow and annealed at 500 °C for 2 h in air. This procedure yielded 500 µm diameter spots.

1.2.2. Tip preparation

The tip procedure is deeply explained in the Experimental Part. In tip part of the Thesis, a 25 µm diameter Au tip was used as core material.

1.2.3. Arrays characterization by SECM

All measurements were carried out using the CHI920C bipotentiostat (CH Instruments, Austin, Texas, USA). The tip was placed in an appropriate movable support, which can be moved in the three dimensions X, Y, Z by stepper motors for relatively large distances (from a few mm to a few μm) or by piezoelectric ones down to nanometric resolution. A graphite tip and an Ag|AgCl (3 M KCl) electrodes were used as counter and reference electrodes respectively. The reference electrode was separated from the solution using a double bridge containing a solution of KNO_3 0.1 M avoiding interferences caused from Cl^- contained in the reference electrode solution and to separate the last one from the alkaline solution adopted in most experiments. The substrate was placed in a SECM Teflon[®] cell with an O-ring (exposed area: about 1 cm^2) and fixed onto a platform whose inclination is variable. The substrate contact was made thanks to a Cu plate.

In order to correct the substrate tilt and to place the tip at a fixed and desired distance from the sample, negative feedback approach curves were performed. These curves represent the tip current, i_t , as a function of d , tip-substrate distance, and are obtained when the tip is moved toward the substrate in the z direction. The tip-substrate distance was set at $\approx 50 \mu\text{m}$.

After that, the samples were firstly screened in the SG/TC mode, biasing the tip at an E_{ORR} and the substrate at an E_{OER} .

The images were gained using a $100 \mu\text{m}$ diameter Au tip

1.2.4. Arrays characterization by SECM double pulse method

To carry out these experiments, the same set-up previously described in 1.2.3 was used. After that, the tip was moved over a spot, and the tip-substrate distance was set at $20 \mu\text{m}$, by performing *negative feedback* approach curves, as explained before.

After that, the substrate potential was pulsed by applying a square wave potential signal (200 mV amplitude, 6 s period) to cycle the substrate between the oxygen evolution conditions (E_{OER}) and a rest potential (E_{rest}), at which no electron transfer reaction could take place. At the same time the tip was positioned over the selected spot and kept at constant oxygen reduction potential, while measuring the relevant I_{tip} .

Figure 39 **Errore. L'origine riferimento non è stata trovata.** represents a collection of tip current transients recorded over one spot of the $\text{Sn}_{1-x}\text{Ir}_x\text{O}_2$ mixed oxides array:

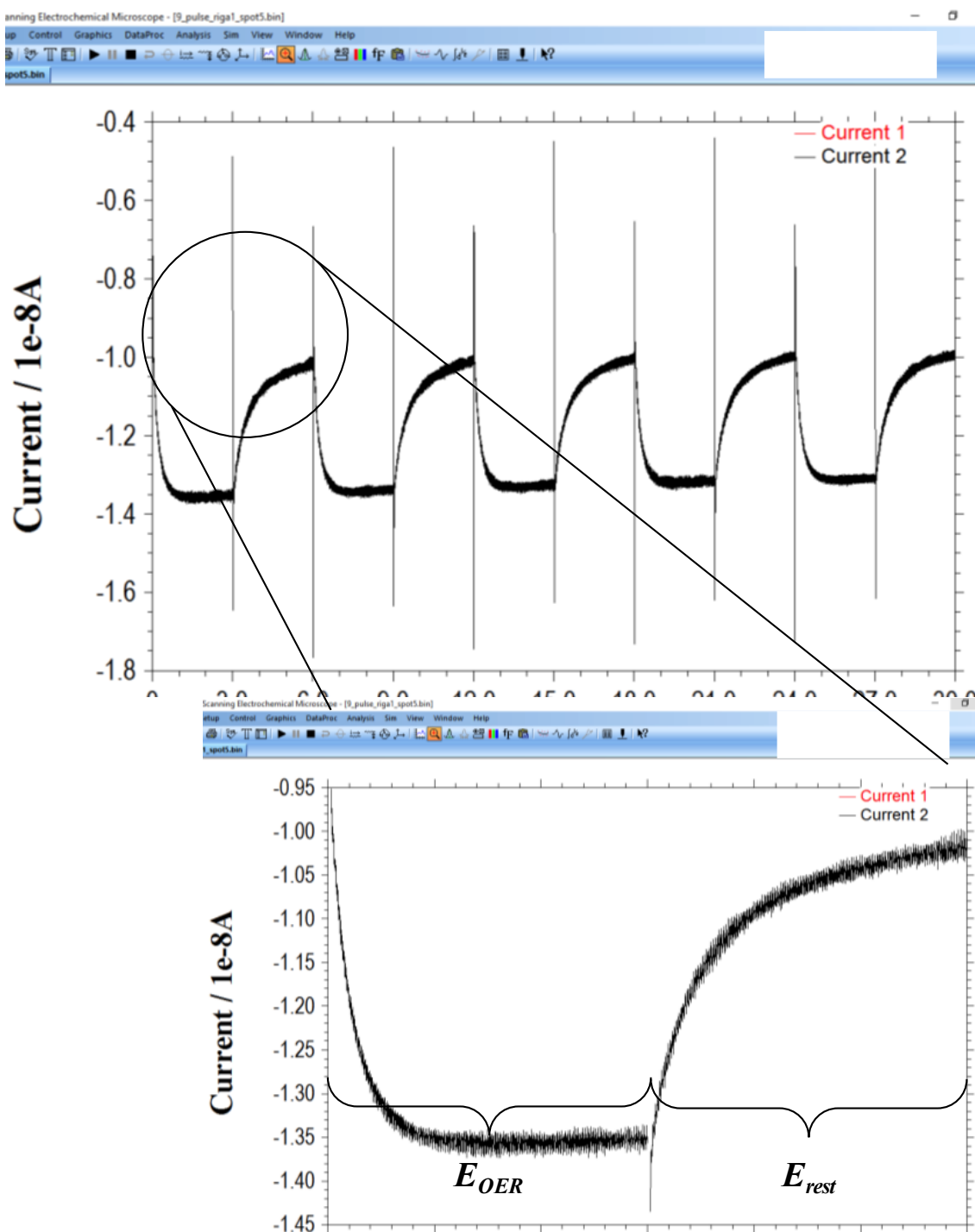


Figure 39: I_{tip} trend while a pulsed potential profile is applied to the substrate.

Remember that the tip current is proportional to the quantity of oxygen produced by the substrate:

$$i_{tip} \div C_{O_2} \div j_{spot}$$

Thus, the spot activity might be directly bound to the tip current.

1.3. Result and discussion

1.3.1. Oxygen evolution electrocatalysts SECM screening

The array based on $\text{Sn}_{1-x}\text{Ir}_x\text{O}_2$ mixed oxides was then screened with the SECM in H_2SO_4 0.5 M at $250 \mu\text{m s}^{-1}$. The tip was biased at 0.09 V (RHE), while the substrate potential was set at 1.4 V (RHE).

The $\text{Sn}_{1-x}\text{Ir}_x\text{O}_2$ mixed oxides array was firstly imaged in the SG/TC mode, as shown in **Figure 40**. This array was screened with the SECM in H_2SO_4 0.5 M at $250 \mu\text{m s}^{-1}$, using a $25 \mu\text{m}$ diameter Au tip. As already said, the tip was biased at 0.09 V (RHE) and the substrate at 1.4 V (RHE).

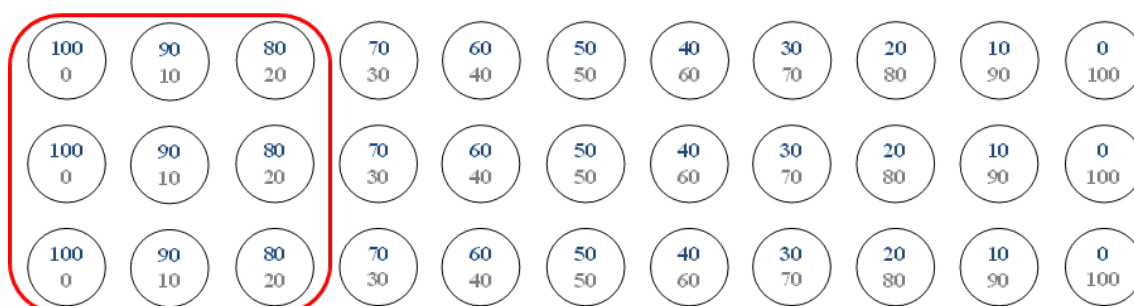
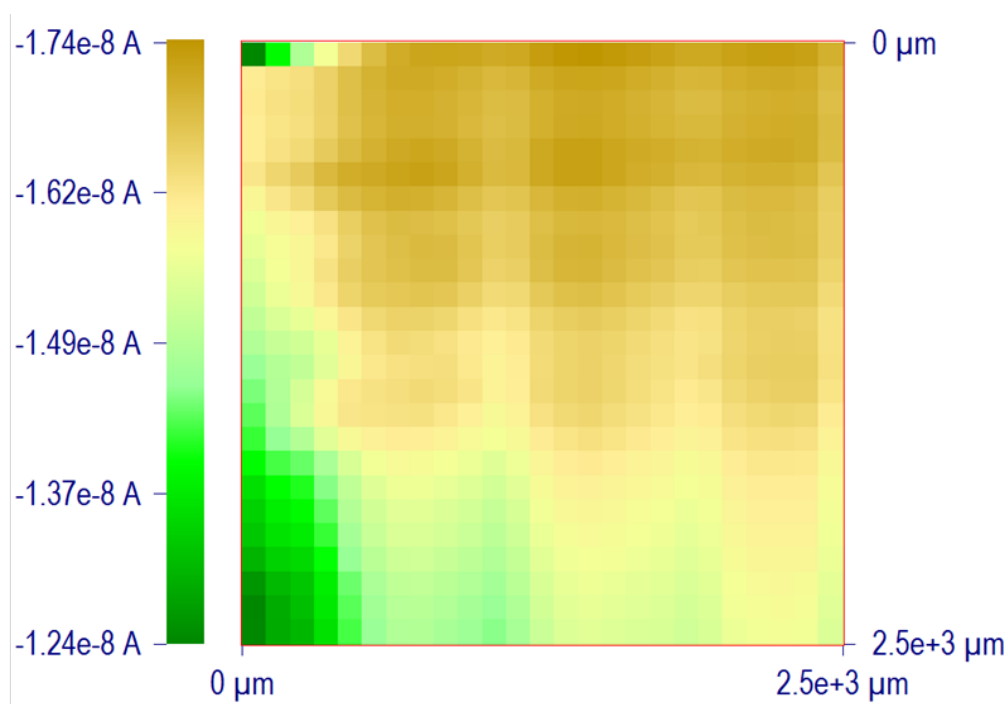


Figure 40: SECM image of the $\text{Sn}_{1-x}\text{Ir}_x\text{O}_2$ mixed oxides array with different Sn/Ir ratios at $250 \mu\text{m s}^{-1}$. $E_{\text{sub}} = 1.4 \text{ V (RHE)}$ in H_2SO_4 0.5 M with a $25 \mu\text{m}$ diameter Au tip. $E_{\text{tip}} = -0.09 \text{ V (RHE)}$.

Figure 40 shows 9 of the 33 spots (11 spots 3 rows) composing the array. Note that despite the quite high distances between spots (about $500 \mu\text{m}$ from center to center), the image is very confused, and the spots cannot be distinguished. Indeed, since all the spots are biased at the same time, they produce oxygen simultaneously. This means that, the time it takes to obtain the image is enough to reach a steady state and an oxygen concentration between spots relatively high, thus causing the overlapping of oxygen diffusion profiles. The resulting image is thus very confused. However, the main drawback is that the oxygen diffusing from the neighboring spots superimposes to the one produced by the spot under investigation, giving not reliable results.

Moreover, it is not possible to exactly know each spot position. For this reason, the tip was moved along the x axis, as it will be explained later.

On the contrary, the Co-based array was tested in NaOH 0.1 M, at $400 \mu\text{m s}^{-1}$, with the tip biased at 0 V (RHE) and the substrate at 1.7 V (RHE).

Figure 41 shows an image of the Co-based mixed oxides array, obtained in the SG/TC mode. The substrate was screened in NaOH 0.1 M at $400 \mu\text{m s}^{-1}$, using a $25 \mu\text{m}$ diameter Au tip, as previously said. This time, the tip was biased at 0 V (RHE) and the substrate at 1.7 V (RHE).

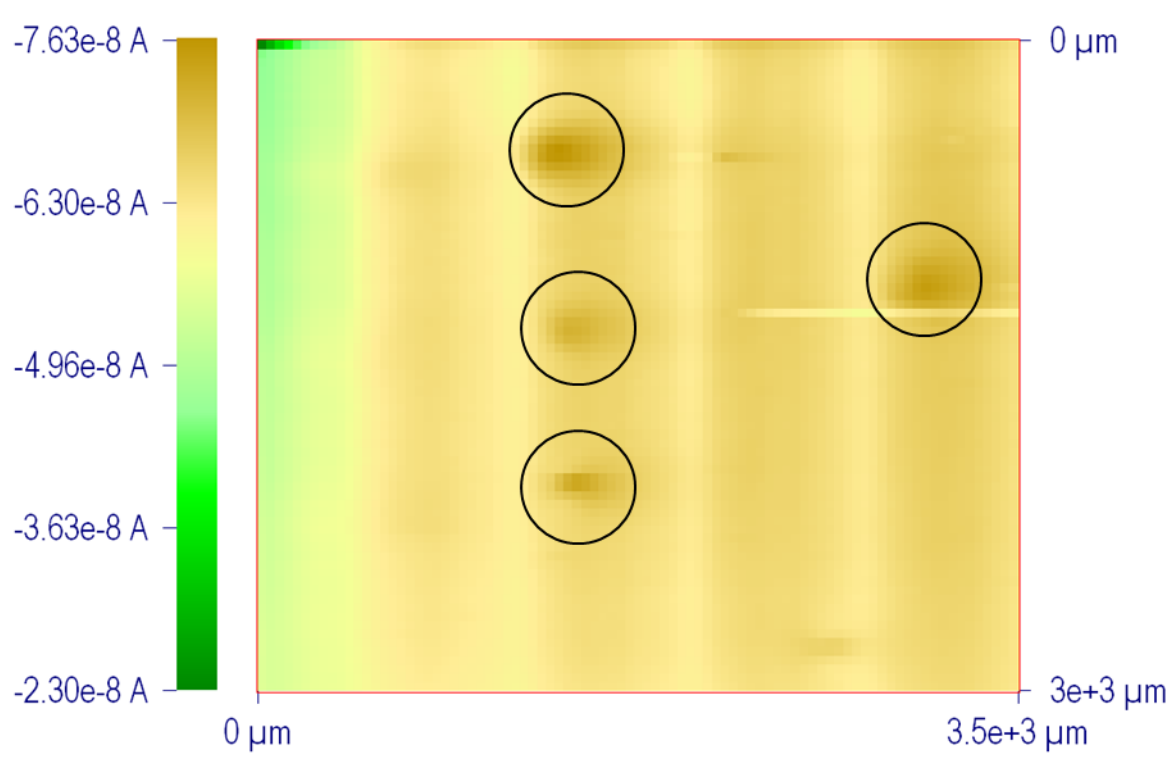


Figure 41: SECM image of the Co-based mixed oxides array with fixed 90%CoO₂ and 10% of Zn, Fe, Cu, Ni oxides in NaOH 0.1 M. Image speed: $250 \mu\text{m s}^{-1}$ with a $25 \mu\text{m}$ diameter Au tip. $E_{sub} = 1.7 \text{ V (RHE)}$. $E_{tip} = 0 \text{ V (RHE)}$.

As we can see, also in this case the image is very confused, even if the spots composing the array were quite far one to each other (about $800 \mu\text{m}$ from center to center). Only 4 of the 11 spots composing the array are evident.

1.3.2. Evaluation of oxygen evolution electrocatalysts by double pulse method

The method implies that the x-y position of each spot is known. To do that, the same conditions adopted for the images acquisitions were adopted but for the recording of x or y scans. In a typical scan (see **Figure 42**), the presence of each spot caused a peak of tip current, due to the production of oxygen at the different spots. The eight peaks

shown correspond to eight of the eleven spots of the array. Since the array is biased at oxygen evolution potential, an enhancement of the current in presence of the spots with respect to the background occurs. This in turn causes also an enhancement of the tip current while it is moving over the array, being the first biased at an oxygen reduction potential.

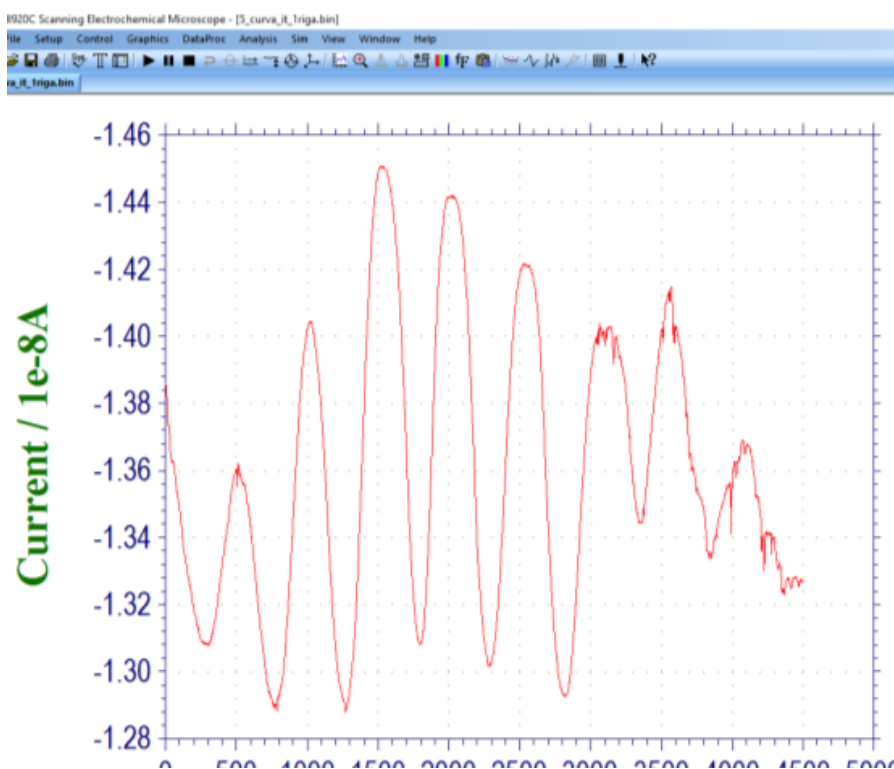


Figure 42: I_{tip} vs. x curve.

The eight peaks shown correspond to eight of the eleven spots of the array. Since the array is biased at oxygen evolution potential, an enhancement of the current in presence of the spots with respect to the background occurs. This in turn causes also an enhancement of the tip current while it is moving over the array, being the first biased at an oxygen reduction potential.

The scan is then repeated in the other direction. In this way, the first row and line of the arrays are identified. The procedure is repeated to individuate the spots center coordinates.

After that, the tip was moved over a spot, and the tip-substrate distance was set at 20 μm , by performing negative feedback approach curves, as explained before.

The substrate potential was pulsed between oxygen evolution conditions, $E_{OER} = 1.4$ V (RHE), and a rest potential at which no oxygen was produced, $E_{rest} = 1.2$ V (RHE). 10 periods are typically recorded.

At the same time the tip was kept at constant potential $E_{tip} = -0.04$ V (RHE). The resulting I_{tip} was recorded.

The experiment was repeated for all the spots.

Figure 43 shows a series of tip current profiles thus obtained: after the application of the potential step, the current rises sharply, and then it rapidly decays to almost the background level after the square pulse ends.

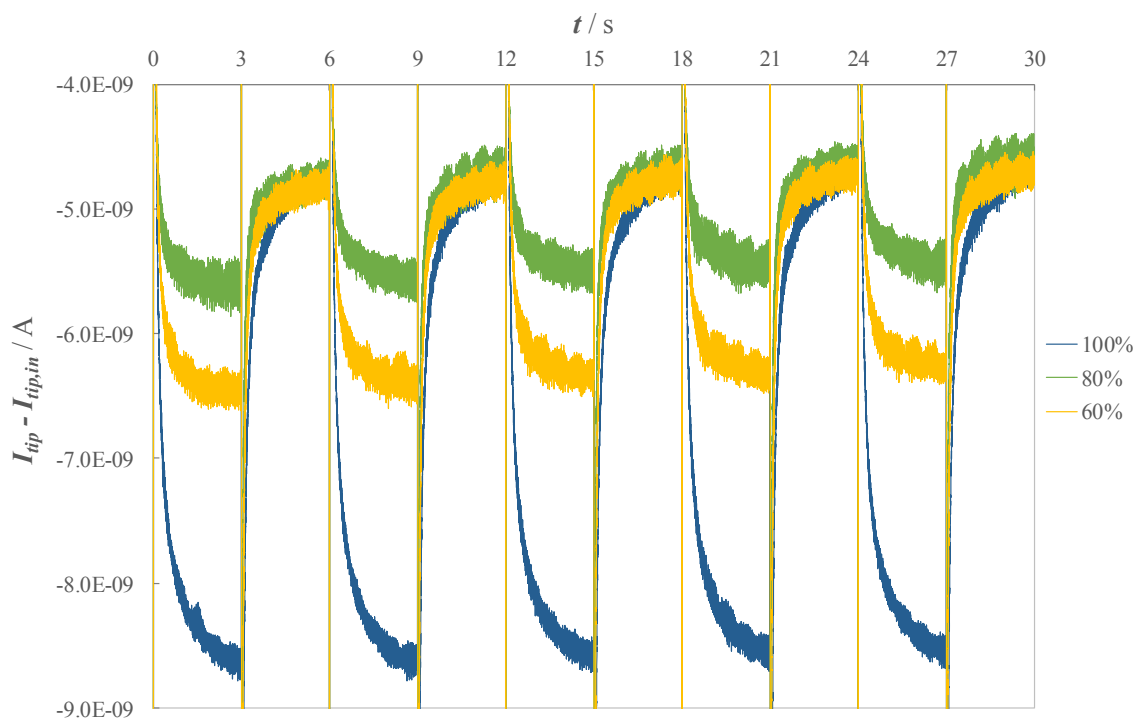


Figure 43: SG/TC double-pulse method applied to three spots in the Ir/Sn array in H_2SO_4 0.5 M. $E_{rest} = 1.2$ V and $E_{OER} = 1.4$ V (RHE) and tip-to-spot distance $d = 20$ μ m.

The results are summarized in **Figure 44** and clearly identify an increase in %IrO₂ with an increase in spots activity, but for what concern 70% and 80% IrO₂, probably due to the aging or degradation of the sample:

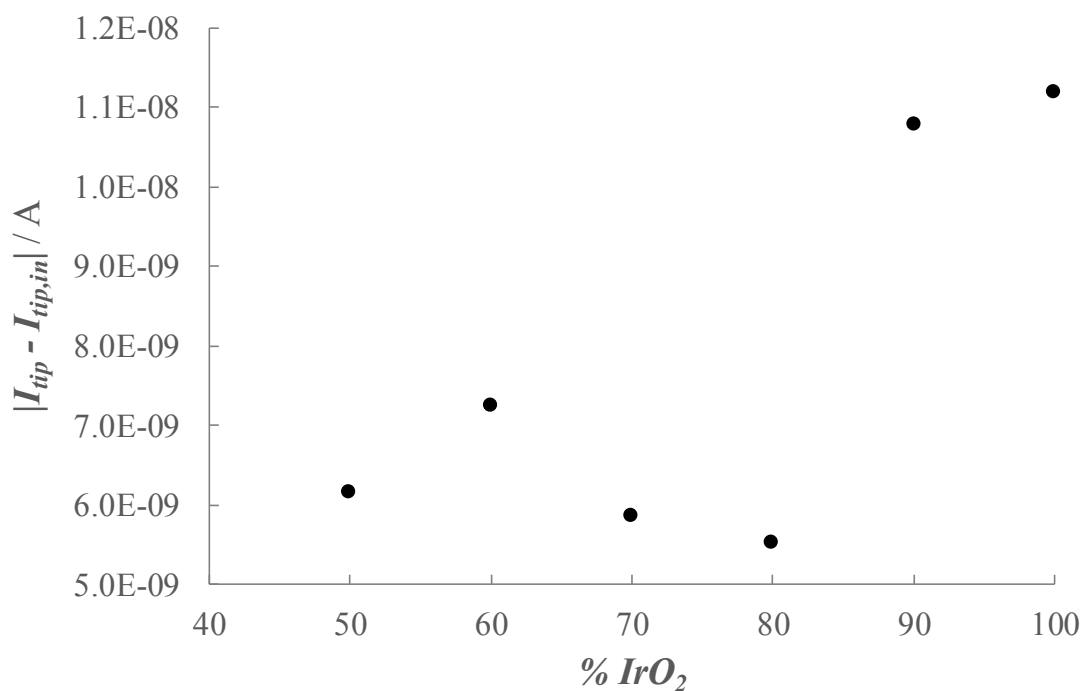


Figure 44: I_{tip} versus %IrO₂ content.

Except for these two spots, this trend is consistent with previously reported in papers [1] and [2].

The same procedure used for the Sn_{1-x}Ir_xO₂ mixed oxides array was repeated also with the Co-based array, in NaOH 0.1 M. The tip was thus moved over the selected spot and then approached toward it. The tip-substrate distance was set at $\approx 5 \mu\text{m}$.

After that, the *double pulse method* was applied: as explained in the *Experimental Section*, the substrate potential was pulsed by applying a square wave potential signal (500 mV amplitude, 6 s period) between oxygen evolution conditions, $E_{OER} = 1.7 \text{ V}$ (RHE), and a rest potential at which no oxygen was produced, $E_{rest} = 1.2 \text{ V}$ (RHE). This square wave profile was repeated 10 times.

At the same time the tip was kept at constant potential $E_{tip} = 0.2 \text{ V}$ (RHE). The resulting I_{tip} was recorded. As previously explained, the spot activity is directly connected to the tip current.

The tip was then moved over another spot and the experiment was repeated.

Figure 45 shows a series of tip current profiles thus obtained: after the application of the potential step, the current rises sharply, and then it rapidly decays to almost the background level after the square pulse ends, as shown also in **Figure 43**.

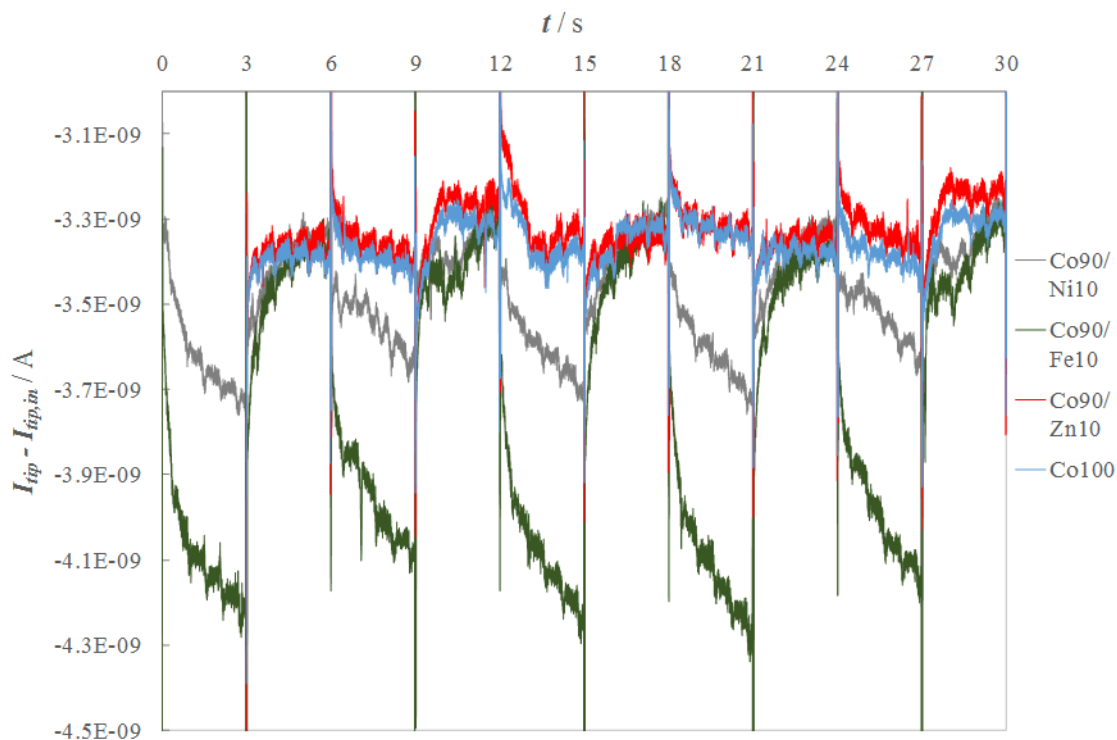


Figure 45: SG/TC double-pulse method applied to two spots in the Co oxide array in NaOH 0.1 M. $E_{rest} = 1.2$ V and $E_{OER} = 1.7$ V (RHE) and tip-to-spot distance $d = 5$ μm .

The results are summarized in **Figure 46**:

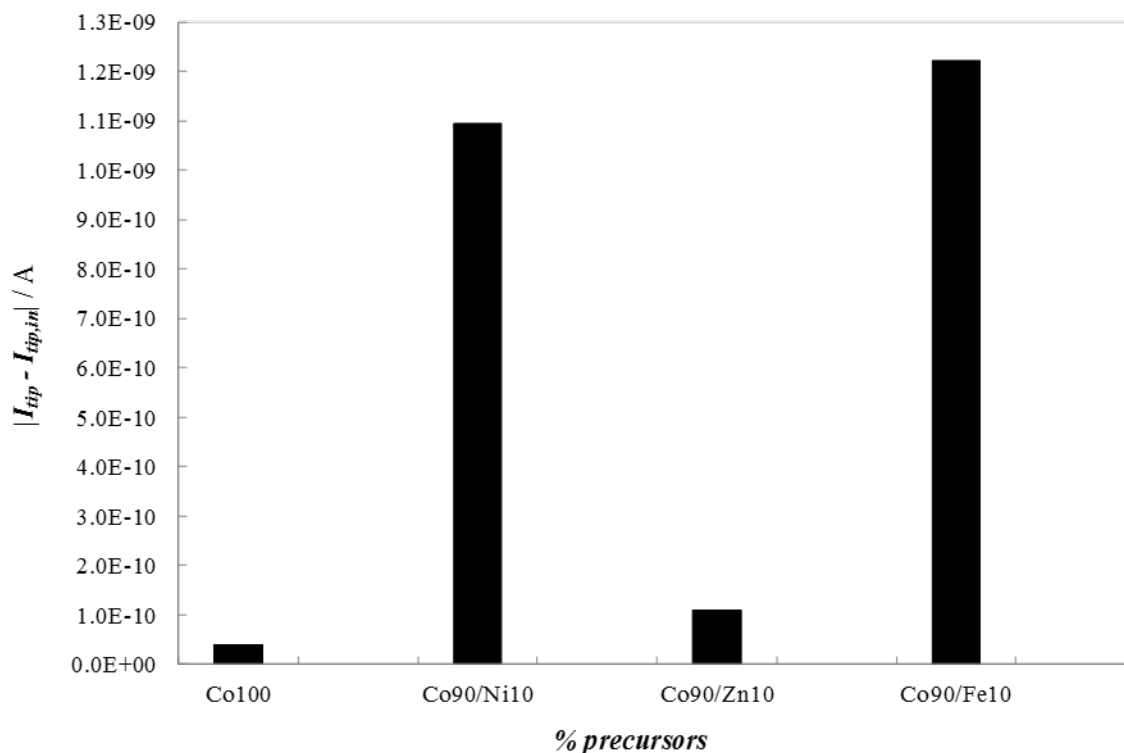


Figure 46: I_{tip} versus %metal precursor content.

As we can see, according to the results obtained with the *double pulse method*, the most active OER electrocatalyst seems to be the Co90%/Fe10%, followed by Co90%/Ni10%. Co90%/Zn10% and pure Co oxide show very low currents.

This results are in agreement with a paper written by Jaramillo et al. [3], according to whom CoO_x , $CoPi$, $CoFeO_x$, NiO_x , $NiCeO_x$, $NiCoO_x$, $NiCuO_x$, $NiFeO_x$, and $NiLaO_x$, tested in NaOH 1 M, achieved 10 mA cm^{-2} current densities at similar operating overpotentials between 0.35 and 0.43 V.

1.4. Conclusions

In this section, the *double pulse method* was successfully applied to low-cost and abundant materials.

This method provides the application of a square wave signal to the sample under investigation: the substrate potential is pulsed between a rest potential, at which the electrocatalysts cannot produce oxygen, and a OER potential.

This method is useful when the spots composing the substrate can produce oxygen at the same time. Indeed, obtaining an SECM image with the SG/TC mode takes enough time to let the spots reach a steady-state condition. The oxygen diffusion profiles thus overlap, producing a cloud that in turn generates a confused SECM image. The activity showed by a spot could thus be related not only to the spot under investigation, but also to the neighbour ones.

With the *double pulse method*, on the contrary, the spots produce oxygen just for few seconds, thus never allowing the oxygen profiles overlapping.

This method was applied to two different arrays deposited onto a titanium sheet, previously cleaned: one $\text{Sn}_{1-x}\text{Ir}_x\text{O}_2$ mixed oxides and one Co-second metal mixed oxides.

The first one was tested only as “standard” array, while the second showed interesting features: the spots composed of 100% of the pure Co oxide are not as active as the spots composed of mixtures. The most active one seemed to be the one composed by 90% Co and 10% Fe, followed by the one composed by 90% Co and 10% Ni.

This trend can be easily found also in the literature, confirming the results obtained with the *double pulse method*.

2. Study of different OER overlayers deposited onto hematite

2.1. Introduction

After different OER electrocatalysts with different compositions of low-cost metals have been screened using the SECM, some mixtures were selected to be deposited onto hematite.

As already said, it was demonstrated that the best electrocatalysts for oxygen evolution reaction are not necessarily the same for the photo-driven water oxidation. Indeed, according to ^[1], Pt and Co oxides, deposited onto W-doped BiVO₄, showed higher photocurrents with respect to IrO_x.

In *Chapter 1.1*, we demonstrated the application of SECM for the rapid screening of different materials onto a metal (Ti) sheet.

In this part of the Thesis, arrays of small spots ($\approx 500 \mu\text{m}$ diameter) of different compositions were dispensed over hematite. Then, they were tested with two different approaches: the first one provides the replacement of the ultramicroelectrode tip with a $200 \mu\text{m}$ diameter white light optical fiber, that can locally generate electron-hole pairs (**Figure 47**):

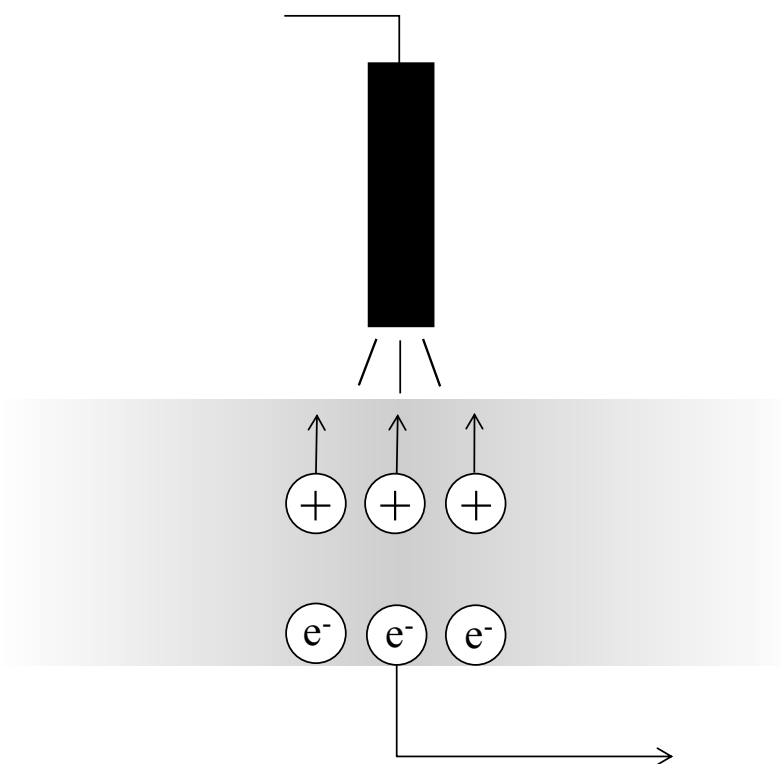


Figure 47: Pictorial scheme of the locally electron/hole separation due to the use of an optical fiber as probe.

With this set-up, the substrate potential was biased to allow the OER and the photocurrents recorded during the fiber scan allowed the generation of a color-coded two-dimensional image, as already described in several papers [1],^{4,5}].

However, the substrate photocurrents could be due not only to the actual activity of the semiconductor/overlayer architecture under light irradiation, but also to parasitic reactions. For this reason, the rapid screening using the optical fiber as probe outputs preliminary results that require further studies.

The second method involves the use of SECM in its conventional set-up, using a 25 μm Au tip as amperometric sensor and recording its current, that is directly proportional to the oxygen production rate at the substrate, in the dark and under visible light, the latter condition achieved thanks to a 523 nm green LED.

In this case the amount of oxygen produced by the substrate spots is detected by the tip, according to the *substrate generation/tip collection (SG/TC)* mode, as described in the *Experimental* chapter.

In order to solve the problem of the overlapping of oxygen profiles when the substrate is biased at an OER potential, the *double pulse method* has been applied to different spots and to the bare hematite. Thus, it was possible to evaluate the activity of the tested materials both in terms of photocurrents and anticipation of the OER onset potential.

The first material tested onto hematite was an amorphous Ir oxide. Indeed, it is considered the most active OER electrocatalyst, and thus we decided to use it as “standard” material.

The *SECM direct mode* [⁶] was applied to electrodeposit hydrous iridium oxide onto hematite. In the *direct mode* the substrate acts as WE, while the UME tip acts as counter electrode (**Figure 48**). Since the tip is brought close to the substrate (few micrometers), the electron transfer is limited to a small area on the surface and the deposition of the material is geometrically limited by the current distribution.

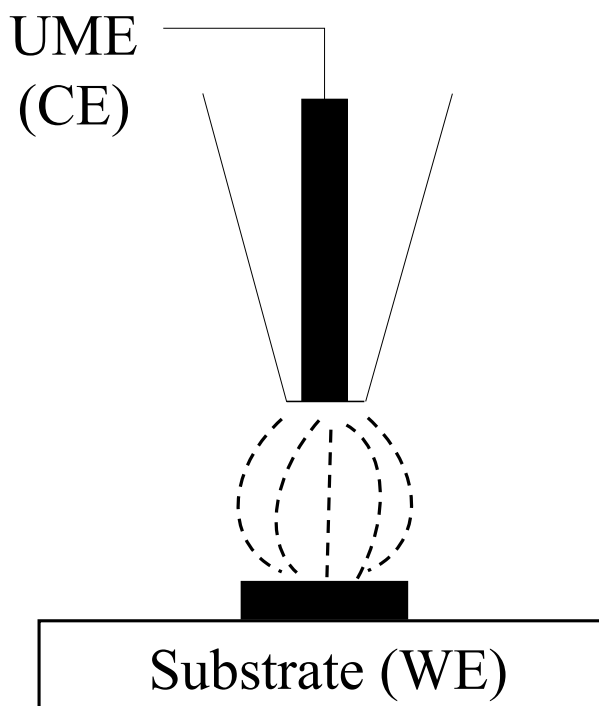


Figure 48: Pictorial scheme of a SECM *direct mode* experiment: the substrate acts as CE while the tip (WE) is placed close to it. The deposition is geometrically limited by the current distribution.

This is very effective if we want to electrodeposit small spots of materials and thus create spots and arrays directly in the SECM cell.

After that, different mixtures of various low-cost and abundant elements were tested: the first array consisted of Co/Ni mixed oxides. However, Co is relatively expensive, so we decided to replace it with Fe, that is a cheaper and more abundant element.

The first Fe/Ni mixed oxides array gave very interesting results.

Moreover, according to [7], Ca^{2+} is well-known to be an important ion in the oxygen-evolving complex of Photosystem II. This raised the possibility that metal ions (e.g., Ca^{2+} , Mg^{2+} , Al^{3+}) could enhance catalyst activity, for example, by facilitating deprotonation of a reactive water molecule or formation of the O-O bond. Otherwise, such metal ions could have a beneficial structural role in the oxide material.

For this reason, the most active composition was selected and a third element (Al, Mg and Ca) was added in different ratios.

Aluminium is well known in the literature [8] as thin coating (0.1 to 2 nm) for nanostructured hematite photoanodes and can lead to a significant decrease in the OER overpotential (100 mV cathodic shift).

Moreover, ternary Al-based oxides like Al/Ni/Co, Al/Co/Fe and Al/Fe/Ni were well studied [9] as OER electrocatalysts, giving promising results.

On another side, Ca was selected since it is a key element in the photosynthesis, as part of the oxygen-evolving complex that is the site of water oxidation of plants, together with Mn. It was thus probable a key role of Ca also in photoelectrochemical oxygen evolution.

In order to confirm the SECM results, the most photoactive compositions according to it were selected and deposited onto hematite as lab-scale electrodes. They were then tested during irradiation with a solar simulator.

However, since the nanopatterns composing the hematite can have different orientations and thus different active surface areas, it was necessary normalize the obtained photocurrents for the actual electrode surface area, that is proportional to its double layer capacitance.

Being the materials and the preparation of the electrodes the same, we can assume that the capacitance of an electrode is proportional to its surface area.

2.2. Experimental

All chemicals were used as received. Aqueous solutions were prepared with water from a Millipore purification system. All the experiments cited were performed at room temperature.

2.2.1. Synthesis of hematite

Hematite was synthesised in collaboration with Doctor Alberto Naldoni of CNR-INSTM.

Hematite was deposited on fluorine-doped tin oxide (FTO)-coated glass substrates (Solaronix, 10 Ω /sq) previously cleaned.

The synthesis took place at 70 °C for 3 h using a precursor aqueous solution of $\text{FeCl}_3 \cdot 6\text{H}_2\text{O}$ 0.15 M (Sigma-Aldrich) and NaNO_3 1 M (Sigma-Aldrich), at pH 1.5 optimized with HCl [10]. After the deposition the samples were rinsed with deionized water and then calcined at 500 °C for 1 h, followed by 20 min at 800 °C [11].

2.2.2. Amorphous IrO_x deposition through SECM direct mode

Amorphous Ir oxide was electrodeposited onto hematite starting from a suitable solution introduced for the first time by Yamanaka [12]. This bath provides the addition of oxalic acid and potassium carbonate, in order to bring the pH to 10.5, to an iridium chloride solution.

The deposition was performed through the SECM direct mode with two different approaches: a first preliminary test was carried out using a 100 μm diameter Au tip as WE and a screen printed carbon electrode (DropSense[®], Metrohm) as substrate (exposed area: 0.196 cm^2).

After that, a hematite sample was used as CE and spiral Au wire (1 cm length) as WE, in order to completely cover the exposed area of the substrate (1 cm^2).

In both the cases, the substrate was placed in a SECM Teflon[®] cell with an O-ring and fixed onto a platform whose inclination is variable. The hematite contact was made thanks to a Cu plate, while the DropSense[®] one was made with a small piece of aluminium foil.

The two WE were placed in the movable support, in order to be moved along the three axes X, Y, Z by stepper motors for relatively large distances (from a few mm to a few μm) or by piezoelectric ones down to nanometric resolution.

In order to place the WE at a fixed and desired distance from the sample, negative feedback approach curves were recorded. As already explained, these curves show the tip current, i_t , as a function of d , the tip-substrate distance, and are obtained when the WE is moved toward the substrate in the vertical z direction. Thanks to the comparison with empirical models, it is possible to correlate the tip distance to d . The final tip-substrate distance was set at $\approx 5 \mu\text{m}$.

The deposition occurred through the application of a chronoamperometric curve to the WE. The applied current density was set at $j = 0.1 \text{ mA cm}^{-2}$.

Also different deposition times were tested (10 min, 1h and 5h), but the best performances were obtained after 1h.

2.2.3. Sample preparation (array)

All the arrays were dispensed starting from solutions of precursor metal salts with a concentration of 0.1 M dissolved in a water/glycerol (3:1) mixture.

The following metal salts were used: $\text{FeSO}_4 \cdot 7\text{H}_2\text{O}$ (99.5% purity, Carlo Erba), $\text{Ni}(\text{NO}_3)_2 \cdot 6 \text{H}_2\text{O}$ (99% purity, Alfa Aesar), $\text{Mg}(\text{NO}_3)_2 \cdot 6\text{H}_2\text{O}$ (97% purity, Sigma-Aldrich), $\text{Al}(\text{NO}_3)_3 \cdot 9\text{H}_2\text{O}$ (99% purity, Carlo Erba) and $\text{Ca}(\text{NO}_3)_2 \cdot 4\text{H}_2\text{O}$ (98%, BDH).

These mixtures were dispensed onto hematite samples (1 cm^2), previously cleaned by sonication for 30 minutes in acetone, 30 minutes in ethanol and 30 minutes in water. The deposition occurred using a CHI 1550 picoliter dispenser (CH Instruments, Austin, Texas) with spot deposition parameters of pulse amplitude: 80 V; pulse width: 40 μs ; pulse period: 1000 s. The spots centre-to-centre distance was set at 800 μm .

The precursor solutions were deposited one after the other in different amounts according to the desired array composition.

All the samples were then dried for 1 h at 180 $^\circ\text{C}$ (after a 5 $^\circ\text{C}/\text{min}$ ramp) under a N_2 flow and annealed at 500 $^\circ\text{C}$ for 2 h in air. This procedure yielded 500 μm diameter spots.

After have found the proper conditions, different array with different precursors were dispensed.

The first one was a Co/Ni mixed oxide array, obtained with compositions ranging from 100% Co to 100% Ni with steps of 20%.

Then the Fe was introduced: as for the Co/Ni array, compositions ranged from 100% Fe to 100% Ni with steps of 20%.

Once the most photoactive composition was selected, a third element was added in different ratios, with the aim of enhancing the composite photocurrents.

The three selected materials were Al, Mg and Ca, for the reasons previously explained.

For what concern the Fe/Ni/Al array, the amount of Al was ranged from 0% to 50% with steps of 10%.

For what concern the Fe/Ni/Mg and Fe/Ni/Ca arrays, the amounts of Mg and Ca were ranged from 0% to 20% with steps of 5%.

2.2.4. Sample preparation (lab-scale electrodes)

As for the arrays, also the lab-scale electrodes were prepared starting from solution of precursor metal salts with a concentration of 1 mM dissolved in a water/glycerol (3:1) mixture. The precursor solutions were then mixed in different ratios, according to the desired compositions. The synthetic pathway reflects the one adopted for the preparation of the arrays.

The following metal salts were used: $\text{FeSO}_4 \cdot 7\text{H}_2\text{O}$ (99.5% purity, Carlo Erba), $\text{Ni}(\text{NO}_3)_2 \cdot 6\text{H}_2\text{O}$ (99% purity, Alfa Aesar), $\text{Mg}(\text{NO}_3)_2 \cdot 6\text{H}_2\text{O}$ (97% purity, Sigma-Aldrich), $\text{Al}(\text{NO}_3)_3 \cdot 9\text{H}_2\text{O}$ (99% purity, Carlo Erba) and $\text{Ca}(\text{NO}_3)_2 \cdot 4\text{H}_2\text{O}$ (98%, BDH).

These mixtures were dispensed onto hematite samples (1 cm^2), cleaned as previously explained. The deposition was carried out by drop-casting and different amount of solutions were tested to study the influence of the overlayer loading: 50 μl , corresponding to $5 \cdot 10^{-5}\text{ mmol cm}^{-2}$ and 5 μl , corresponding to $5 \cdot 10^{-6}\text{ mmol cm}^{-2}$.

All the samples were then dried for 1 h at 150 °C and then annealed for 2 h in air at 500 °C (after a 5 °C/min ramp).

2.2.5. Tip preparation

The tip used in the SECM may have different geometries: disc, semi-spherical, cylindrical and planar. The tips used in this Ph.D. thesis were microdisc electrodes.

The materials used to prepare them were:

- Glass capillaries with outer diameter 1.5 mm, internal diameter 0.75 mm, length 100 mm;
- Gold wire (GoodFellow): diameter 0.025 mm, 99.99% purity;
- Copper wires;
- Silver paste (Fluka).

The first step for the preparation of an UME consists in cutting the capillary in two halves, to obtain two portions of about 5 cm in length. In order to avoid a poor seal of the glass and the formation of bubbles inside the capillary it is necessary to remove moisture and dust, as well as other polluting substances or water. These conditions are obtained by washing the capillaries with acetone and immersing them in ultrasounds for about 5 minutes. After being dried in an oven, the capillaries are sealed using a flame at a not too high temperature, to avoid the excessive curvature of the glass tip. The capillary is rotated continuously over the flame until a conical shape is obtained.

At this point a portion of the gold wire (about 2 cm), previously washed with acetone and cleaned in ultrasound for about 5 minutes and dried, is introduced inside the capillary. It is essential that the wire is straight before being inserted inside the capillary. Finally, the gold wire is sealed: the open end of the capillary is connected to the vacuum line to prevent the formation of bubbles while the closed one is placed in the center of a metallic spiral, that is heated for about 10 minutes to remove moisture and impurities on the wire or on the internal glass walls. The wire heating is then raised up to melt the glass around the Au wire, thanks also to the application of vacuum. Then, the non-welded wire is connected to a copper wire by silver paste. The other end the golden wire is exposed using abrasive papers with different grit (180, 1000, 2400, 4000), proceeding from the coarsest to the finest. The last step consists in sharpening the capillary to obtain the desired value of $RG = (rg / a)$. The tips used in the present work have $RG \approx 10$.

2.2.6. Arrays characterization by SECM

All measurements were carried out using the CHI920C bipotentiostat (CH Instruments, Austin, Texas, USA). The tip was placed in an appropriate movable support, which can be moved in the three dimensions X, Y, Z by stepper motors for relatively large distances (from a few mm to a few μm) or by piezoelectric ones down to nanometric

resolution. A graphite tip and an Ag|AgCl (3 M KCl) electrodes were used as counter and reference electrodes respectively. The reference electrode was separated from the solution using a double bridge containing a solution of KNO₃ 0.1 M avoiding interferences caused from Cl⁻ contained in the reference electrode solution and to separate it from the alkaline solution adopted in most experiments. The substrate was placed in a SECM Teflon[®] cell with an O-ring (exposed area: about 1 cm²) and fixed onto a platform whose inclination is variable. The hematite contact was made thanks to a Cu plate, while the DS one was made with a small piece of aluminium foil.

All the arrays were tested in NaOH 0.1 M.

The amorphous Ir oxide spot deposited on the screen printed carbon electrode was firstly screened in the SG/TC mode. The tip-substrate distance was set at $\approx 5 \mu\text{m}$ and the sample was imaged with a 100 μm diameter Au tip.

The same procedure was repeated using a hematite sample as substrate. In this case, the sample was irradiated from the bottom using a green LED (523 nm).

When the tip was replaced by a 200 μm diameter white light optical fiber (Thorlabs[®]), it was placed in the same movable support, in order to move it in the three axes X, Y, Z through the stepper motors, over the substrate. As always, a graphite tip and an Ag|AgCl (3 M KCl) electrodes were used as counter and reference electrodes respectively and the substrate was placed in a SECM Teflon[®] cell with an O-ring (exposed area: about 1 cm²). The substrate contact was made thanks to a Cu plate.

In order not to ruin the fiber, this kind of experiments were carried out ~~in~~ at pH 11 phosphate buffer.

The fiber-substrate distance was set to approximately 100 μm .

2.2.7. Lab-scale electrodes characterization

SECM images are very useful to obtain preliminary results about the photoactivity of different materials. However, it is also necessary to confirm these data synthesizing lab-scale electrodes to be tested under solar simulator irradiation.

In this case, all measurements were carried out using an Autolab (Metrohm) PGSTAT. The photoelectrode was placed in a quartz cell, with a Pt wire and an Ag|AgCl (in 3 M KCl) electrodes as counter and reference electrodes respectively. The reference

electrode was separated from the solution using a double bridge containing a solution of KNO_3 0.5 M.

The used electrolyte was NaOH 1 M.

The samples were irradiated with a 300 W xenon arc lamp (calibrated at 100 mW/cm^2) coupled to an AM 1.5 G filter. The light source-sample distance was constant and fixed at 15 cm.

2.2.8. Evaluation of active surfaces through the study of electrode capacitances

As explained in the *Introduction*, it was necessary to normalize the photocurrents with respect to their active surface areas, directly connected to capacitance of the double-layer generated on the electrode surface.

To measure the capacitance, CVs at different scan rates were performed in a potential range where no faradaic processes are present.

Indeed, when the potential is swept linearly in time:

$$vt = R_s \left(\frac{dq}{dt} \right) + \frac{q}{C_d} \quad (1)$$

Where:

R_s = resistor;

q = charge;

C_d = capacitor.

If $q = 0$ at $t = 0$:

$$i = vC_d \left[1 - e^{\left(-\frac{t}{R_s C_d} \right)} \right] \quad (2)$$

The current rises from zero and attain a steady-state value:

$$i = vC_d \quad (3)$$

This steady-state current can then be used to estimate C_d :

$$C_d = \frac{i}{v} \quad (4)$$

All measurements were carried out using a CHI920C bipotentiostat (CH Instruments, Austin, Texas, USA).

The solution used for these experiments was NaOH 1 M as explained for the other experiments.

Five different samples of α -Fe₂O₃ and three Fe_{0.6}Ni_{0.4}/ α -Fe₂O₃ photoanodes were tested, carrying out CVs at four different scan rate: 10 mV s⁻¹, 50 mV s⁻¹, 100 mV s⁻¹ and 500 mV s⁻¹.

2.3. Result and discussion

2.3.1. Amorphous Ir oxide

The deposition of one amorphous Ir oxide spot was performed on a screen printed carbon electrode in the SECM direct mode with a 100 μm diameter Au tip as explained in the *Experimental Section*.

In order to verify the real occurrence of the deposition, the spot was imaged in H_2SO_4 0.5 M at 100 $\mu\text{m s}^{-1}$ with a 100 μm Au tip in the SG/TC mode, as shown in **Figure 49**. The tip was biased at 0 V (RHE), while the substrate at 1.4 V (RHE).

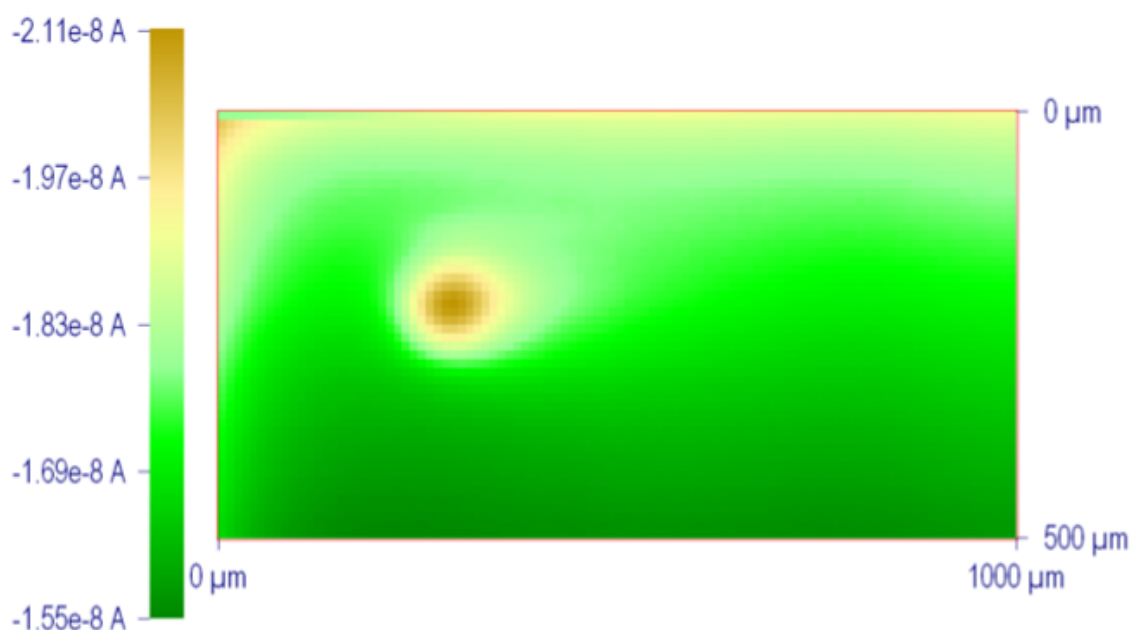


Figure 49: SECM image at 100 $\mu\text{m s}^{-1}$ of an amorphous IrO_x spot obtained after 1h deposition. $E_{\text{sub}} = 1.4$ V (RHE), $E_{\text{tip}} = 0$ V (RHE) in H_2SO_4 0.5 M with a 100 μm diameter Au tip.

The spot is clearly visible, meaning that the deposition properly occurred.

Moreover, its diameter is approximately 100 μm , like the Au tip used as WE, and with a very regular morphology, meaning that the deposition is actually limited by the current distribution.

This experimental evidence confirms the advantages of SECM *Direct Mode* to obtain small and regular spots of materials under interest directly in the SECM cell.

The electrolyte was thus changed in order to study their activities in the selected conditions.

Moreover, this avoids the deposition of the spots through the piezo-dispenser, their activation and annealing, thus removing steps in the array preparation and simplifying the procedure.

The same procedure was repeated using a $\alpha\text{-Fe}_2\text{O}_3$ sample as WE and an Au wire (length = 1 cm), put parallel to the substrate, as CE.

Indeed, it was of our interest to screen the edge of iridium oxide overlayer under light irradiation, in order to study the differences of performances in its presence.

Thus, the screening was performed in the SG/TC mode irradiating the sample from the bottom with a green LED (523 nm) in NaOH 0.1 M at $100 \mu\text{m s}^{-1}$, using a $100 \mu\text{m}$ diameter Au tip. The latter was biased at 0 V (RHE), while the substrate at four different potentials: 0.5 V, 1 V, 1.1 V and 1.4 V (RHE).

Figure 50 schematically shows the sample and the investigated area:

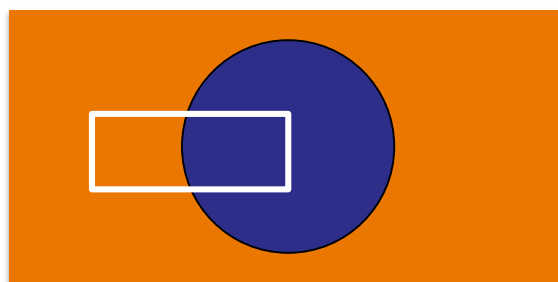


Figure 50: Pictorial scheme of an hematite sample (orange) covered with one big spot of amorphous IrO_x (blue). The white square limits the scanned area.

Figure 51 show the SECM images obtained in these conditions, applying three different potentials to the substrate (0.5, 1 and 1.4 V RHE):

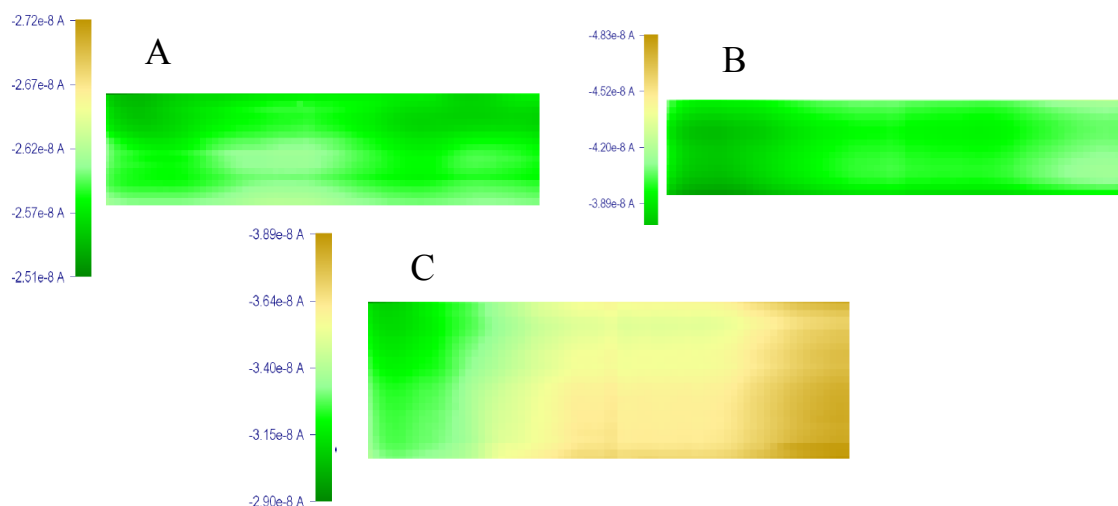


Figure 51: SECM image at $100 \mu\text{m s}^{-1}$ of an amorphous IrO_x spot obtained after 1h deposition. $E_{\text{sub}} = 0.5 \text{ V}$ (A), 1.4 V (B) and 1 V (C), $E_{\text{tip}} = 0 \text{ V}$ (RHE) in NaOH 0.1 M with a $100 \mu\text{m}$ diameter Au tip.

Note that in **Figure 51A**, $E_{\text{sub}} = 0.5 \text{ V}$ (RHE), too low to produce oxygen even in presence of the overlayer; this provides low photocurrents and no differences between bare and covered hematite. In **Figure 51B**, $E_{\text{sub}} = 1.4 \text{ V}$ (RHE), and the potential is high enough to allow the production of oxygen even by the uncovered semiconductor. For this reason, we recorded high photocurrents, but no differences between uncovered and covered hematite. In the end, in **Figure 51C** $E_{\text{sub}} = 1 \text{ V}$ (RHE): the border between $\alpha\text{-Fe}_2\text{O}_3$ and $\alpha\text{-Fe}_2\text{O}_3/\text{IrO}_x$ is clearly visible and the enhancement of the photocurrents related to the presence of the overlayer suggests that the oxygen can be produced only in presence of the catalyst.

This verifies that the presence of an overlayer deposited onto a semiconductor can actually anticipate the onset potential of the OER.

In order to better show the SECM images of **Figure 51**, the same results are shown as 3D image (**Figure 52**):

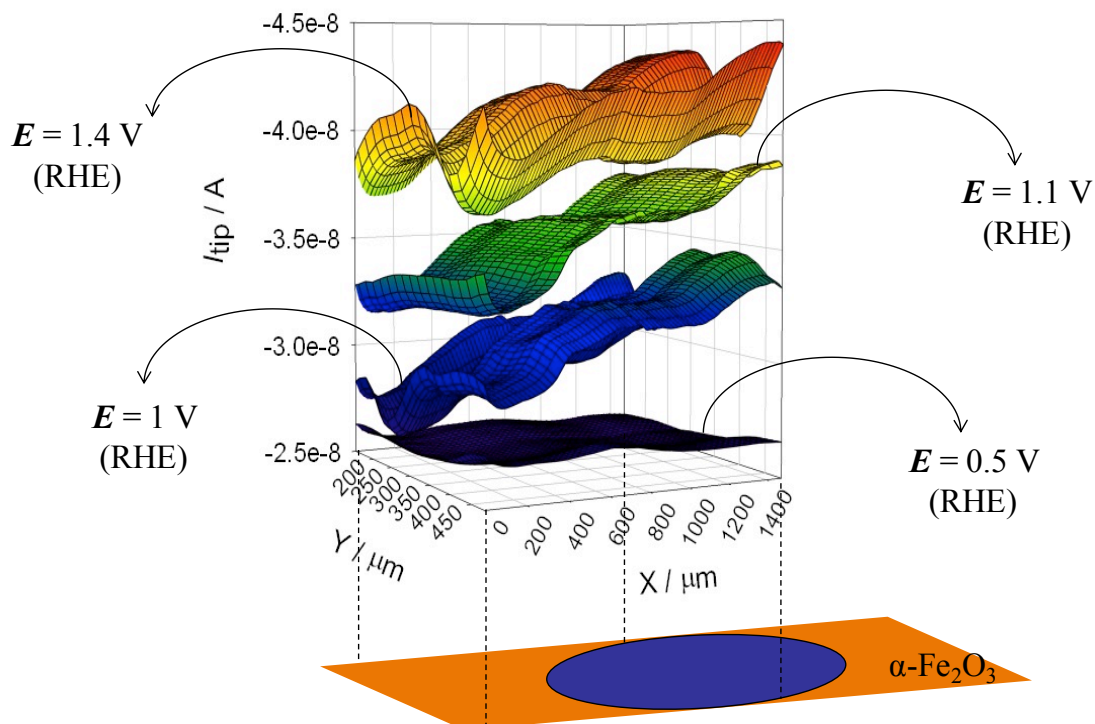


Figure 52: 3D representation of four SECM images carried out at $100 \mu\text{m s}^{-1}$ of an amorphous IrO_x spot deposited onto hematite after 1h. $E_{\text{tip}} = 0 \text{ V (RHE)}$ in $\text{NaOH } 0.1 \text{ M}$ with a $100 \mu\text{m}$ diameter Au tip.

Note that the same screening was repeated also applying $E_{\text{sub}} = 1.1 \text{ V (RHE)}$ to the substrate: the differences between bare and covered hematite are even more highlighted respect to the image obtained at $E_{\text{sub}} = 1 \text{ V (RHE)}$.

2.3.2. Oxygen evolution photoelectrocatalysts SECM screening by a white light optical fiber

The first array screened using a white light optical fiber as probe, was the one of **Figure 53**. The substrate was biased at 1.6 V (RHE) .

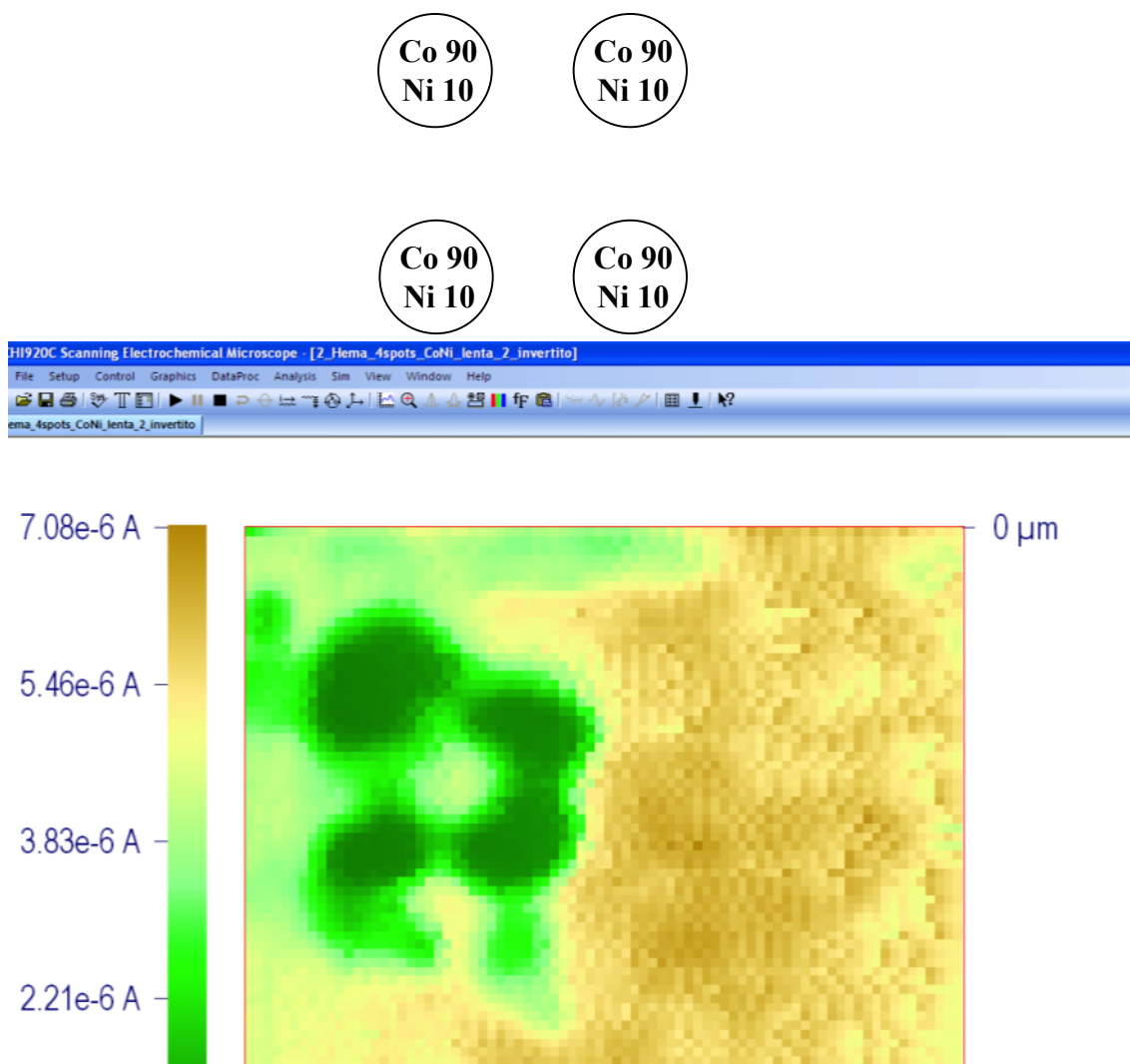


Figure 53: SECM image of the 4-spots $\text{Co}_{0.9}/\text{Ni}_{0.1}$ mixed oxides array obtained with a white light optical fiber at $500 \mu\text{m s}^{-1}$ in $\text{NaOH } 0.1 \text{ M}$. $E_{\text{sub}} = 1.6 \text{ V (RHE)}$.

As we can see the four spots are clearly visible, but their photocurrents are lower with respect to those related to $\alpha\text{-Fe}_2\text{O}_3$.

This was probably due to the concentration of the precursor solutions, that produced a deposit that is thick enough to partially absorb the light.

For this reason, we decided to dilute the metal precursor solutions at two lower concentrations: 0.01 M and 1 mM.

A 4-spots array with these compositions was screened with the fiber at three different potentials: 0.85 V, 1 V and 1.4 V (RHE).

As we can see in **Figure 54**, spots with these lower concentrations led to higher photocurrents than those shown by the 0.1 M precursor concentration array.

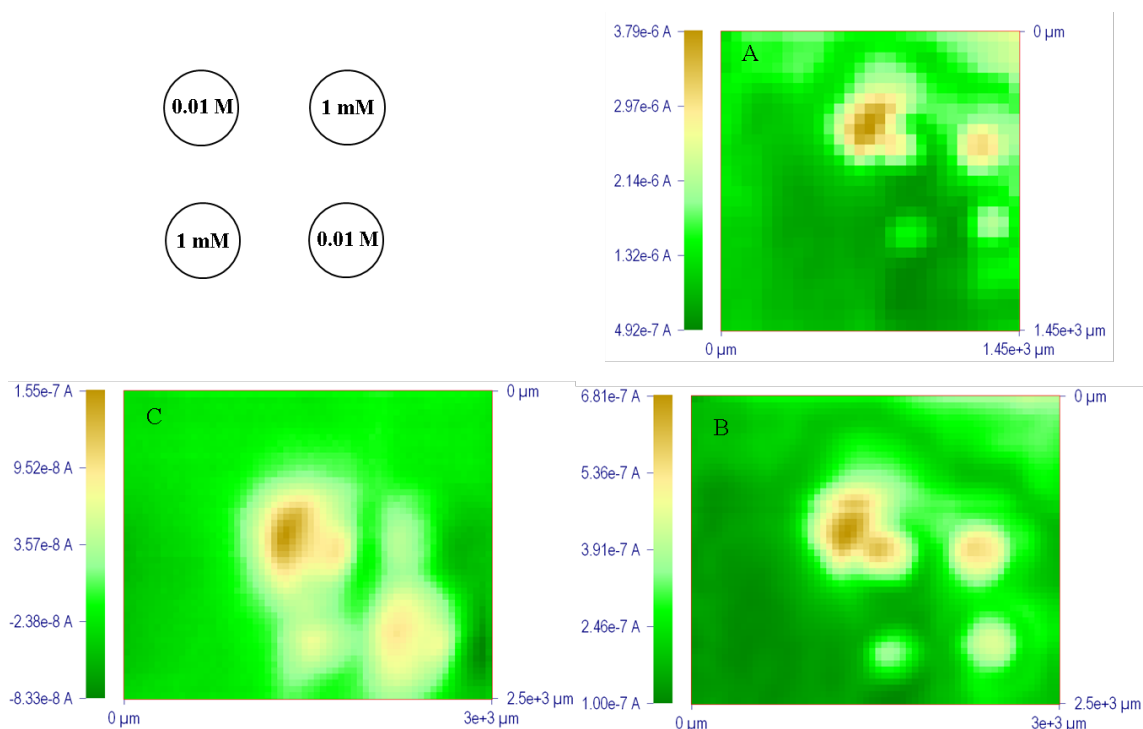


Figure 54: SECM image the 4-spots $\text{Co}_{0.9}/\text{Ni}_{0.1}$ mixed oxides array at different metals precursor solution concentrations. The image was obtained with a white light optical fiber at $500 \mu\text{m s}^{-1}$ in $\text{NaOH } 0.1 \text{ M}$. $E_{\text{sub}} = 1.4 \text{ V}$ (A), 1 V (B) and 0.85 V (C).

Since the spots made starting from 1 mM solution concentration showed the same photocurrents obtained with the 0.01 M one and more regular spot morphologies, we decided to adopt the former value.

In all the three images, the first row shows higher photocurrents probably because of small tilting issues.

After that, several different arrays made of different metal precursors were dispensed as explained in the *Experimental Section* and screened with the white light optical fiber in $\text{NaOH } 0.1 \text{ M}$.

The first array was a Co/Ni mixed oxide one shown in **Figure 55**. The substrate was biased at 1 V (RHE):

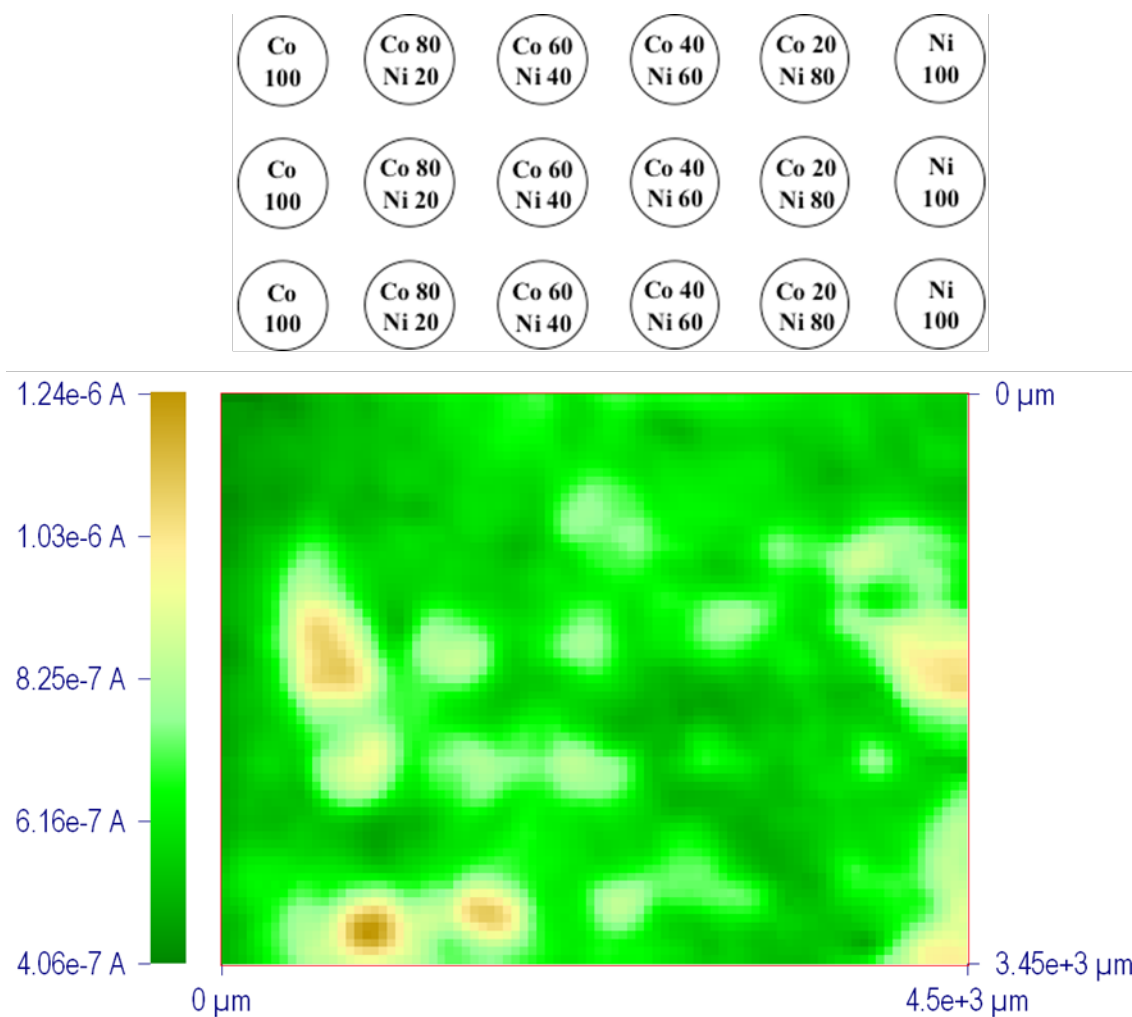


Figure 55: SECM image of a Co/Ni mixed oxides array obtained with a white light optical fiber at $500 \mu\text{m s}^{-1}$ in NaOH 0.1 M. $E_{sub} = 1 \text{ V (RHE)}$.

Almost all the spots are recognisable, even if it is clear that higher amount of Co leads to higher photocurrents. Indeed, Co oxide is the most active spot.

On the contrary, large amounts of Ni do not actually enhance the spots performances. Note that some areas of the substrate seem to be photoactive even in absence of the overlayers. This is probably due to the poor homogeneity of the hematite layer thickness.

Since the Co is an expensive element, we decided to replace it with Fe, that is a cheaper and more abundant element.

The dispensed Fe/Ni mixed oxides array was screened in the same previous conditions:

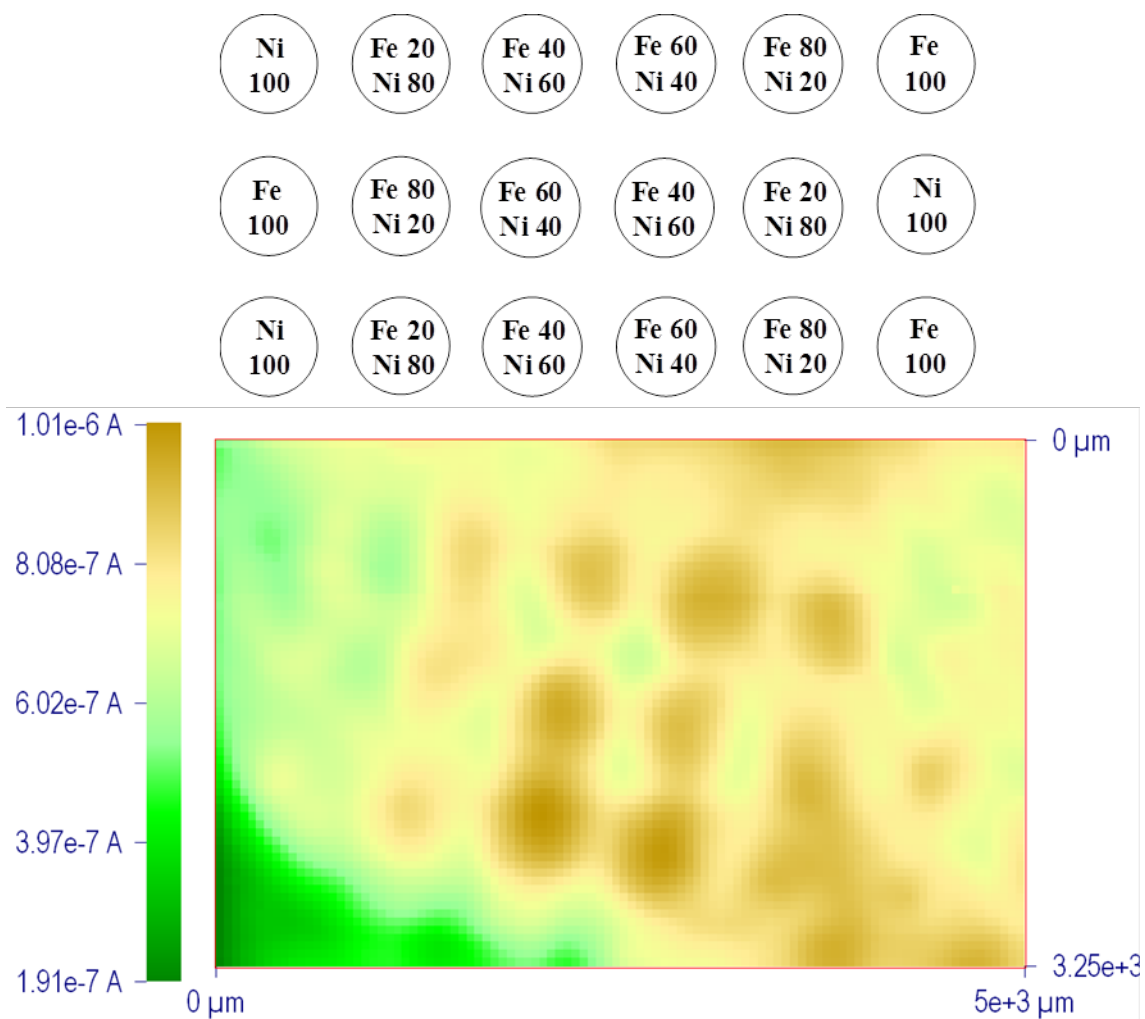


Figure 56: SECM image of a Fe/Ni mixed oxides array obtained with a white light optical fiber at $500 \mu\text{m s}^{-1}$ in NaOH 0.1 M. $E_{sub} = 1 \text{ V (RHE)}$.

As **Figure 56** shows, the simultaneous presence of both Ni and Fe in similar amount leads to higher photocurrents. In particular, the spot made of 60% Fe and 40% Ni is the most active one. Also the 40% Fe and 60% Ni one shows high performances.

On the contrary, the pure Fe and Ni oxides show photocurrents close to the bare hematite.

Unfortunately, the non-homogeneities of hematite here are even more visible and make the SECM image contrast more confused and complicated to investigate.

Probably, since the nanopatterns composing the hematite can have different orientations and thus different local morphology. This in turn causes a non-homogeneity in the substrate activity and thus in the hematite photocurrents. Thus, the SECM image is characterized by non-constant currents that limit the image contrast.

We then decided to further enhance the performances of the $\text{Fe}_{0.6}\text{Ni}_{0.4}$ mixture, by the addition of a third element.

The Fe/Ni/Al array (**Figure 57**) was screened with the fiber in same condition used for the other arrays:

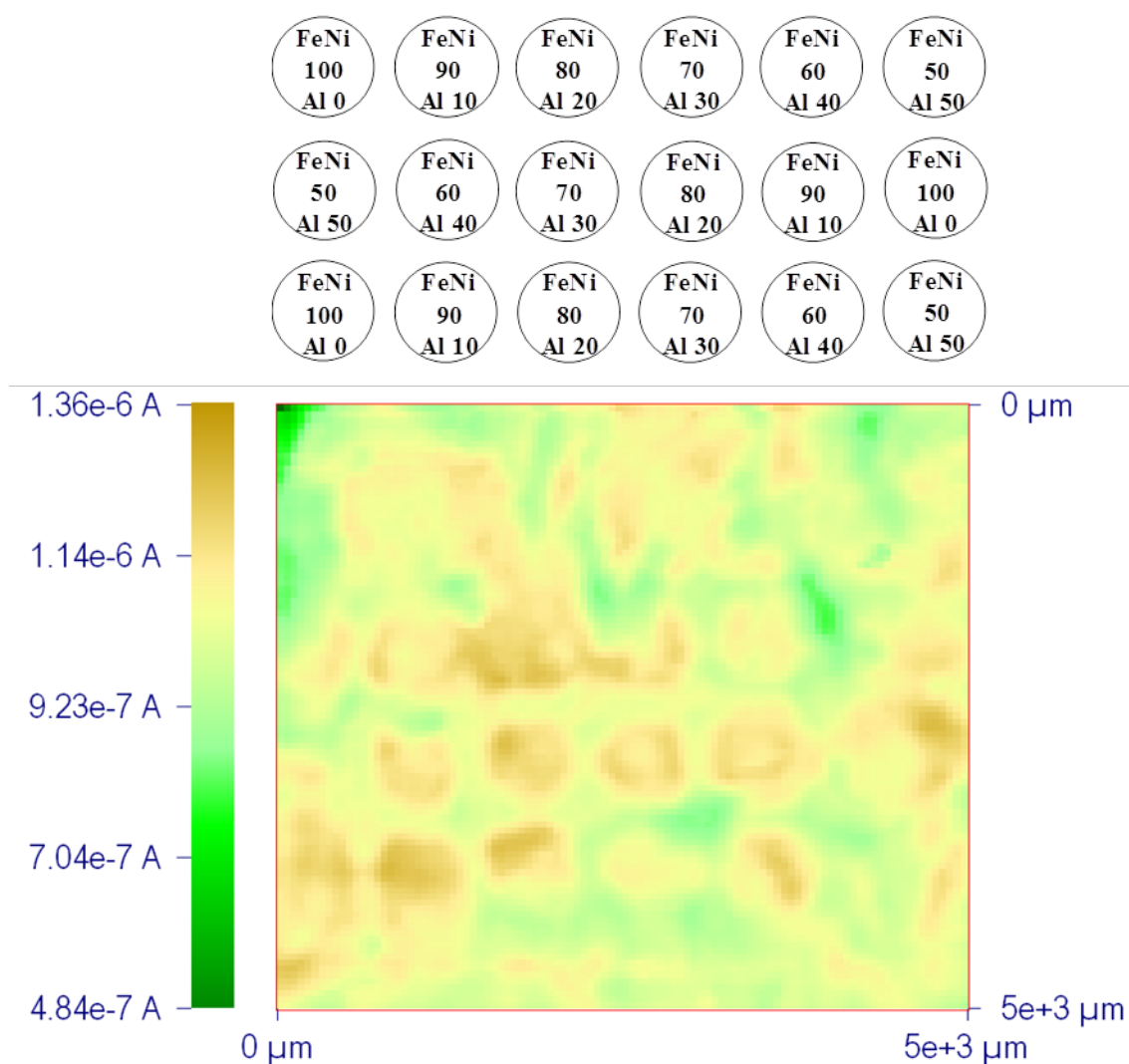


Figure 57: SECM image of a Fe/Ni/Al mixed oxides array obtained with a white light optical fiber at $500 \mu\text{m s}^{-1}$ in NaOH 0.1 M. $E_{sub} = 1 \text{ V (RHE)}$.

As **Figure 57** shows, almost all the spots are clearly evident. However, the addition of different amount of Al to the mixed $\text{Fe}_{0.6}\text{Ni}_{0.4}$ composition does not enhance the activity of the mixture.

As an alternative to the Al, also Ca and Mg were added, separately.

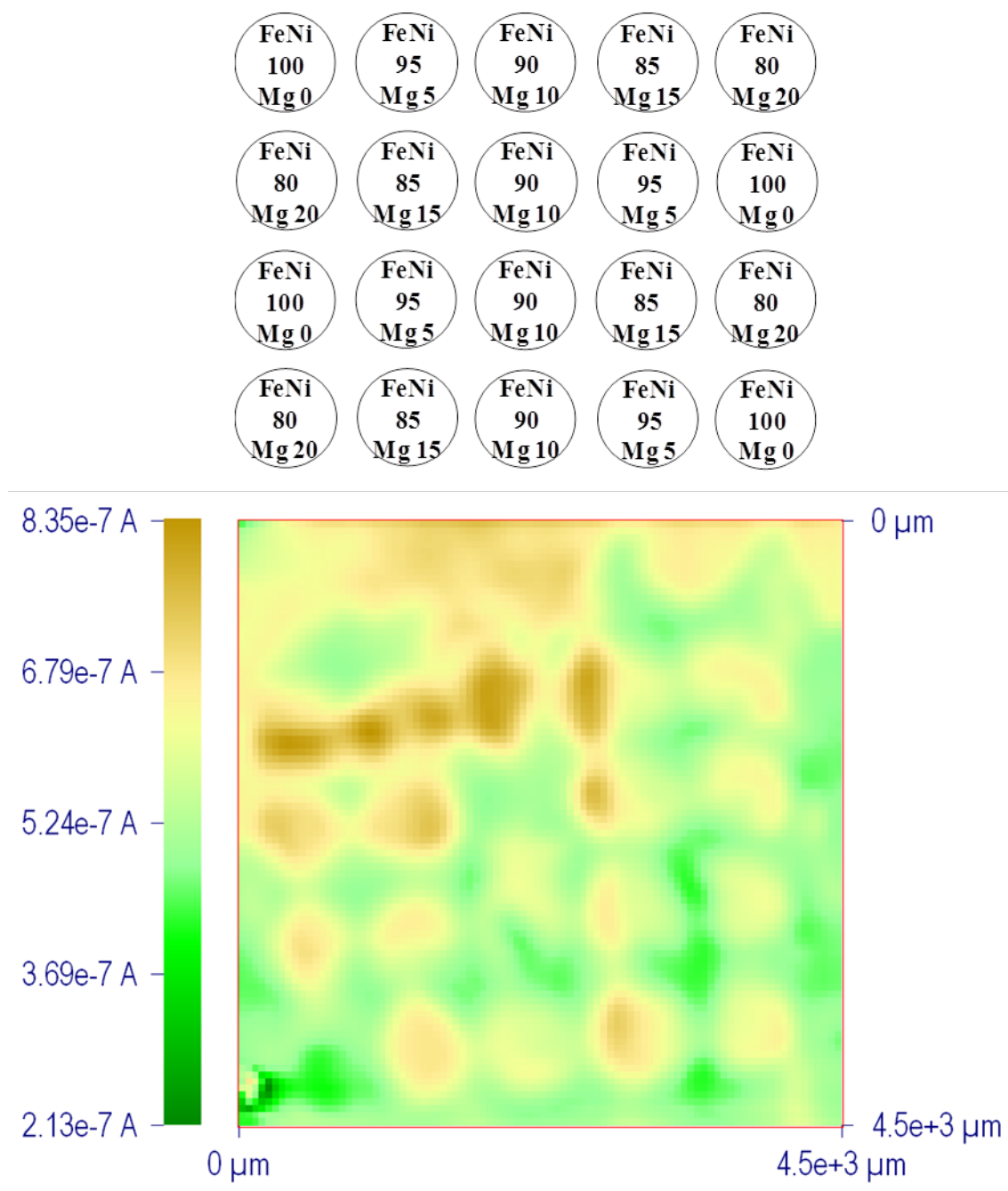


Figure 58: SECM image of a Fe/Ni/Mg mixed oxides array obtained with a white light optical fiber at $500 \mu\text{m s}^{-1}$ in NaOH 0.1 M. $E_{\text{sub}} = 1$ V (RHE).

As we can see in **Figure 58**, almost all the spots are clearly evident. The first and the second rows show higher photocurrents probably because of some inhomogeneity of the hematite layer, as previously explained. All the other spots have higher photoactivities with respect to the semiconductor, however the performances of the $\text{Fe}_{0.6}\text{Ni}_{0.4}$ composition are not enhanced, exactly as happened with the addition of Al.

Finally, different amounts of Ca were added (**Figure 59**).

The array was then screened with the white light optical fiber in NaOH 0.1 M.

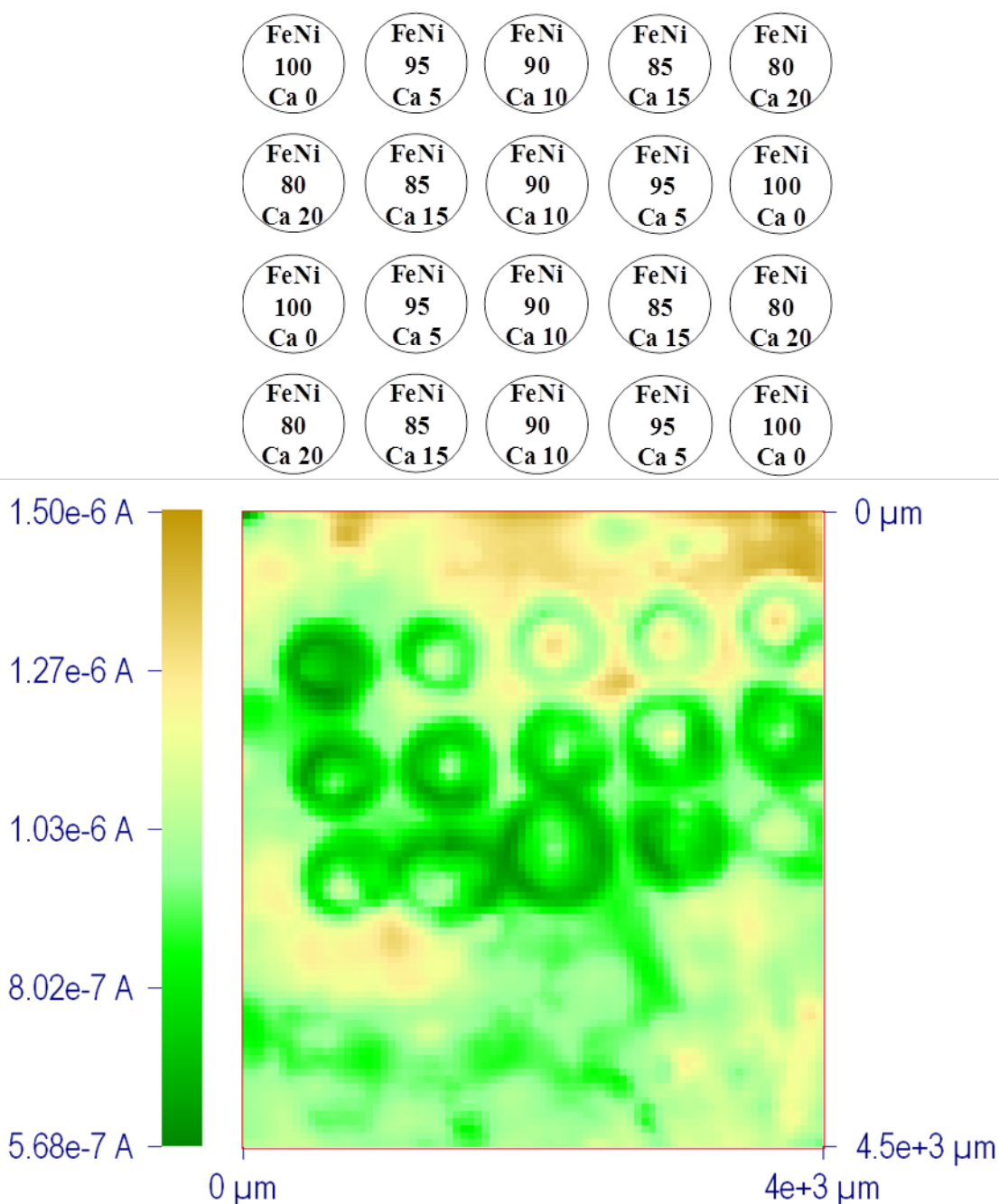


Figure 59: SECM image of a Fe/Ni/Ca mixed oxides array obtained with a white light optical fiber at $500 \mu\text{m s}^{-1}$ in NaOH 0.1 M. $E_{\text{sub}} = 1 \text{ V (RHE)}$.

As we can see, all the spots are visible, however the presence of Ca produces a drop in the array photocurrents.

In order to verify the results obtained through the SECM, the most photoactive materials were selected and deposited onto hematite as lab-scale electrodes, as will explain in *Section 2.3.4*.

2.3.3. Evaluation of $\text{Co}_{0.9}\text{Ni}_{0.1}$ photoelectrocatalyst by SECM images and double pulse method

As explained in Chapter 1, before recording out a SECM image of an array and its evaluation in terms of activity, it is necessary to correct the substrate tilt and to place the tip at a fixed and desired distance from the sample. To do that, negative feedback approach curves were performed.

The tip used as probe was a 25 μm diameter Au one, and the tip-substrate distance was set at $\approx 5 \mu\text{m}$.

The 4-spots $\text{Co}_{0.9}\text{Ni}_{0.1}$ mixed oxides array was firstly imaged in the SG/TC mode, as shown in **Figure 60**, in NaOH 0.1 M at $200 \mu\text{m s}^{-1}$, irradiating it with a 523 nm green LED (LEDEngine) from the bottom. The tip was biased at 0.05 V (RHE) while three different potentials were applied to the substrate: 0.5V, 1 V and 1.4 V (RHE).

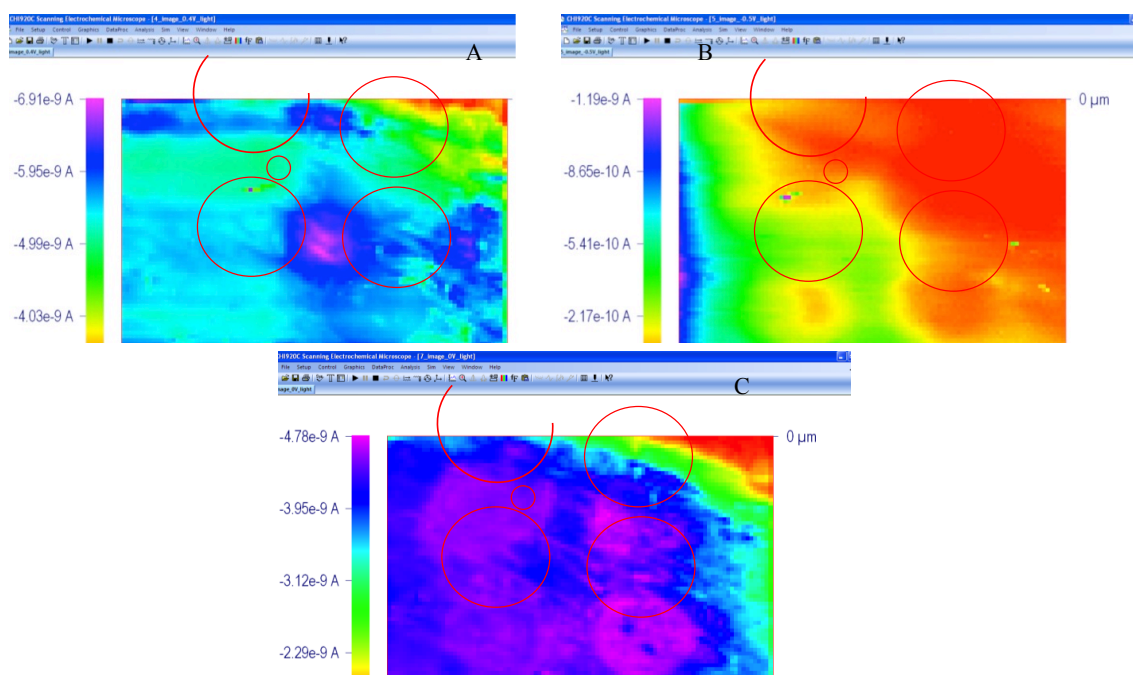


Figure 60: SECM image the 4-spots $\text{Co}_{0.9}\text{Ni}_{0.1}$ mixed oxides array at $200 \mu\text{m s}^{-1}$ in NaOH 0.1 M with a 25 μm diameter Au tip. $E_{\text{sub}} = 1.4 \text{ V}$ (A), 0.5 V (B) and 1 V (C). $E_{\text{tip}} = 0.05 \text{ V}$ (RHE).

The various images are recorded at different applied potentials.

In **Figure 53A**, $E_{\text{sub}} = 1.4 \text{ V}$ (RHE), and the potential is high enough to allow the production of oxygen even by the uncovered semiconductor. For this reason, we recorded high photocurrents, but the spots were not observable. In **Figure 53B**, $E_{\text{sub}} = 0.5 \text{ V}$ (RHE), too low to produce oxygen even in presence of the overlayer; this

provides low photocurrents and no differences between bare and covered hematite. In the end, in **Figure 53C** $E_{sub} = 1$ V (RHE): all the four spots are clearly visible and the enhancement of the photocurrents related to the presence of the overlayer suggests that the oxygen can be produced only in presence of the catalyst.

This verifies that the presence of an overlayer deposited onto a semiconductor can actually anticipate the onset potential of the OER.

After that, the tip was moved over a spot, and the tip-substrate distance was set at 5 μm , by means of approach curves.

After that, the substrate potential was pulsed by applying a square wave potential signal (200 mV amplitude, 6 s period) to cycle the substrate between the oxygen evolution conditions (E_{OER}) and a rest potential (E_{rest}), at which no electron transfer reaction could take place. At the same time the tip was positioned over the selected spot and kept at constant oxygen reduction potential, while measuring the relevant I_{tip} .

The substrate potential was pulsed between $E_{rest} = 0.7$ V (RHE) and different oxygen evolution conditions, changed from 0.8 V to 1.4 V (RHE). This square wave profile lasted 6 seconds and was repeated 10 times.

At the same time the tip was kept at constant potential $E_{tip} = 0$ V (RHE). The resulting I_{tip} was recorded.

It worthy to remind that the tip current is proportional to the quantity of oxygen produced by the substrate:

$$i_{tip} \div C_{O_2} \div j_{spot}$$

Thus, the spot activity is directly related to the tip current.

The experiment was repeated for 2 $\text{Co}_{0.9}\text{Ni}_{0.1}$ spots and the uncovered hematite.

Figure 61 shows the tip current profiles obtained at different E_{OER} applied to the substrate: after the application of the potential step, the current rises sharply, and then it rapidly decays to almost the background level after the square pulse ends.

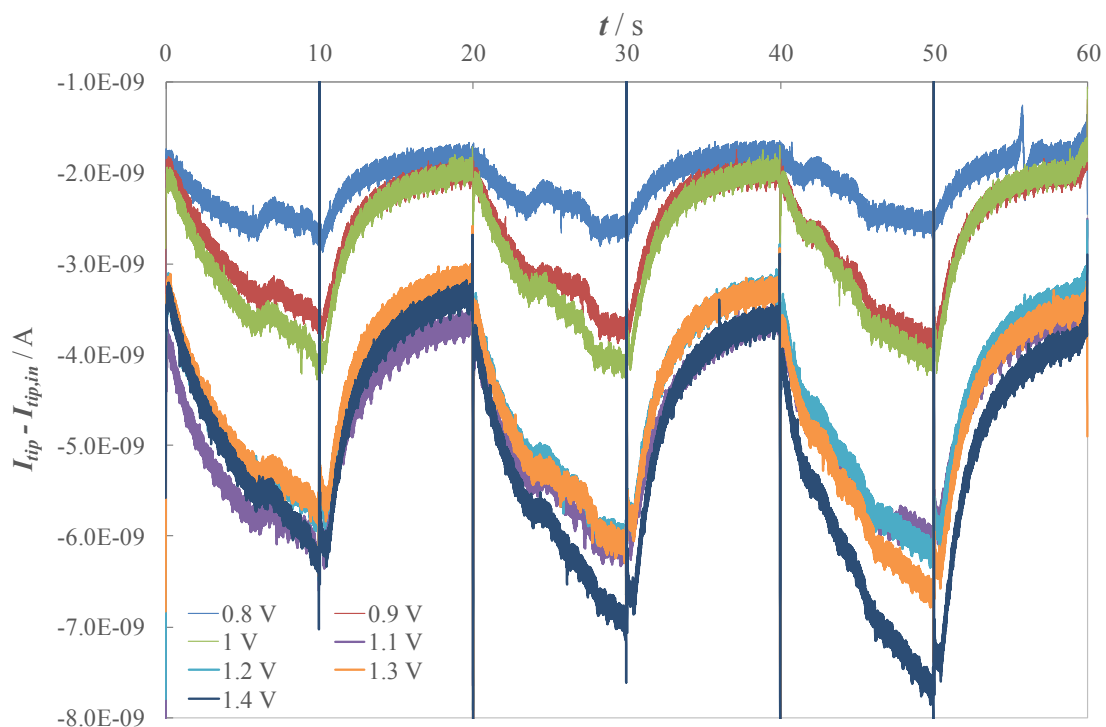


Figure 61: SG/TC double pulse method applied to a $\text{Co}_{0.9}\text{Ni}_{0.1}$ spot in NaOH 0.1 M. $E_{rest} = 0.7$ V and E_{OER} from 0.8 V to 1.4 V (RHE). Tip-to-spot distance $d = 5$ μm . $E_{tip} = 0$ V (RHE)

It is clearly evident that an enhancement in the substrate currents leads to an even higher production of oxygen by the spot. This in turn leads to an increase in the tip currents. The rise is already evident when $E_{sub} = 0.8$ V (RHE) (light blue line), even if a more evident difference between E_{rest} and E_{OER} is obtained starting from $E_{sub} = 0.9$ V (RHE) (red line). This response is even more clear increasing the substrate potential.

The analysis was then repeated on another $\text{Co}_{0.9}\text{Ni}_{0.1}$ spot and on the bare hematite.

The results are summarized in **Figure 62** and clearly identify an increase in the tip current in presence of the spots, starting to produce oxygen at 0.8 V (RHE). Its production is higher with respect to the bare hematite.

The trend is confirmed by the second spot, even if its currents are lower with respect to the first one, probably due to the aging or degradation of the sample:

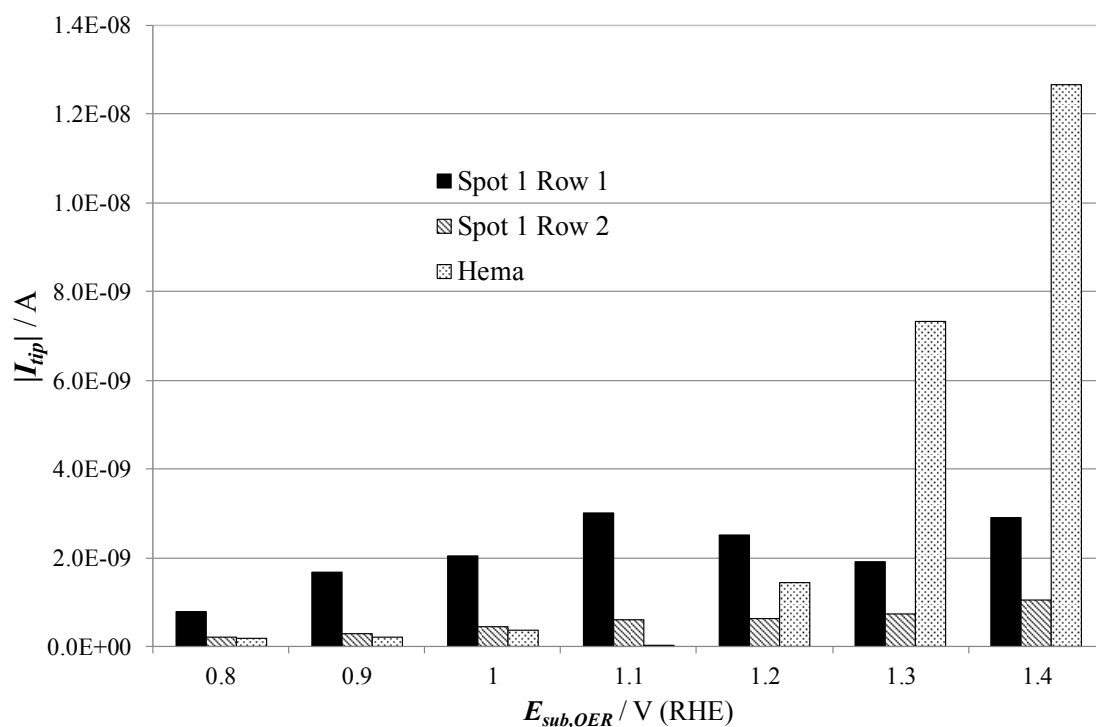


Figure 62: Response of the I_{tip} when the SG/TC double pulse method is applied to two different $Co_{0.9}Ni_{0.1}$ spots and bare hematite in NaOH 0.1 M irradiating with a green LED.

It is evident that the OER onset potential is anticipated of about 400 mV when the hematite is covered with an overlayer.

2.3.4. Evaluation of $Fe_{0.6}Ni_{0.4}$ -based photoelectrocatalysts as lab-scale electrodes

As previously said in *Section 2.3.2*, the most photoactive compositions according to SECM preliminary images were deposited and tested as lab-scale electrodes under solar simulator irradiation in NaOH 1 M.

First of all, the dependence of the electrode photoactivity with the overlayer loading was tested (**Figure 63**): two different amounts of the $Fe_{0.6}Ni_{0.4}$ composition were deposited onto hematite and tested, carrying out CVs of the samples between 0.4 V and 1.6 V (RHE) at 10 mV s^{-1} .

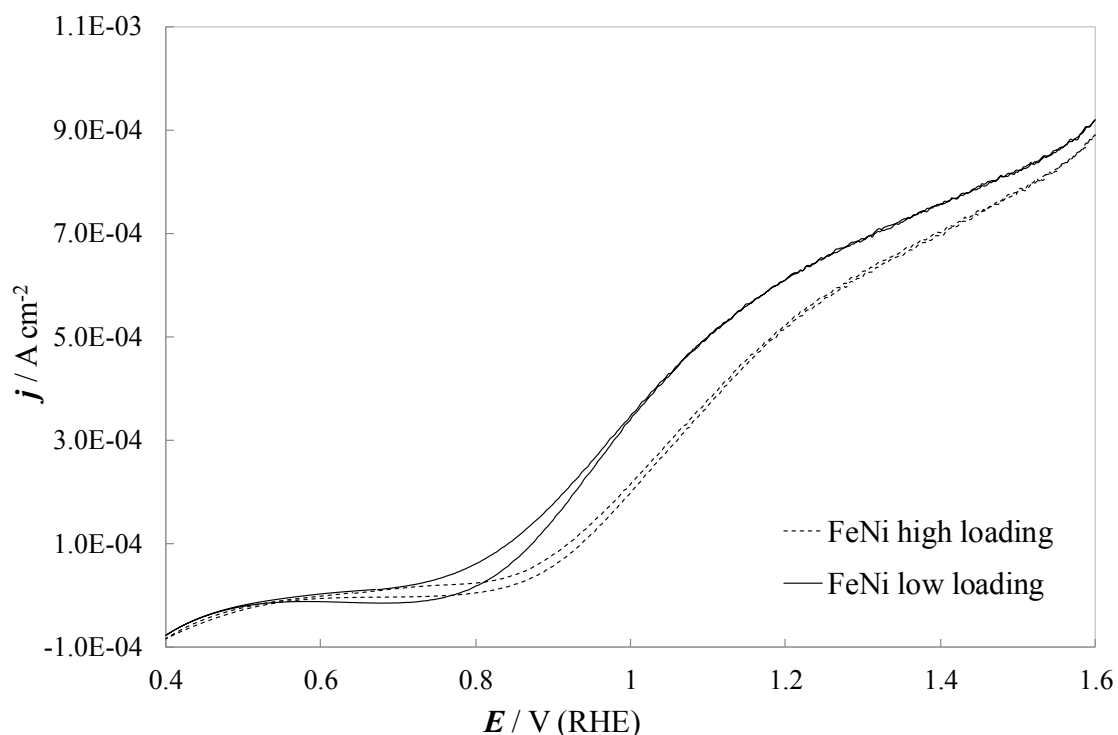


Figure 63: CVs of two hematite/ $\text{Fe}_{0.6}\text{Ni}_{0.4}$ photoanode with two different overlayer loadings ($5 \cdot 10^{-5} \text{ mmol cm}^{-2}$ and $5 \cdot 10^{-6} \text{ mmol cm}^{-2}$) performed in NaOH 1 M under solar simulator irradiation.

It is clear that thinner overlayer loading leads to better performances. One hypothesis that can explain this behaviour is that the material layer is thinner and thus more transparent, allowing the light to easily irradiate the photoanode.

In the end, four different compositions were deposited as lab-scale electrodes. The selected mixtures, according to SECM, were: $\text{Fe}_{0.6}\text{Ni}_{0.4}$, $(\text{FeNi})_{0.8}\text{Al}_{0.2}$, $(\text{FeNi})_{0.95}\text{Mg}_{0.05}$ and $(\text{FeNi})_{0.95}\text{Ca}_{0.05}$. They were also compared with respect $\alpha\text{-Fe}_2\text{O}_3$. Here the spots compositions are normalized

CVs were carried out in NaOH 1 M at 10 mV s^{-1} under solar simulator irradiation.

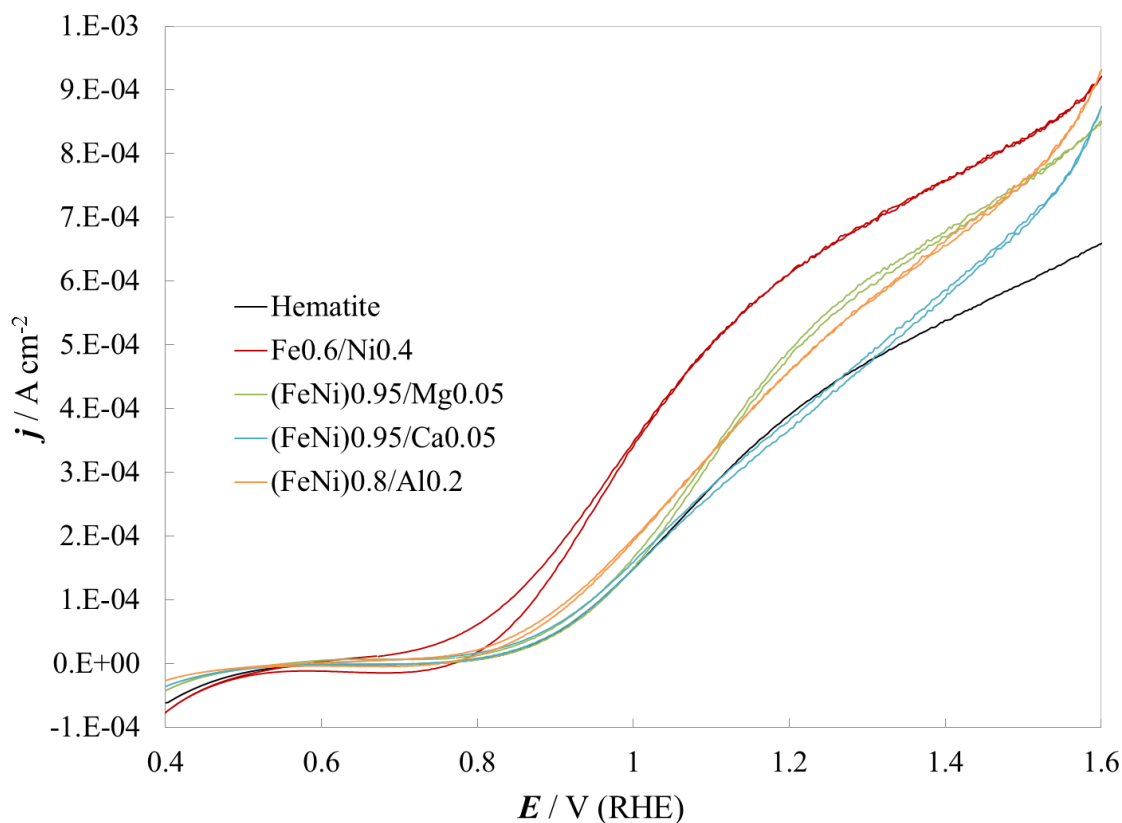


Figure 64: CVs of four different hematite/overlayer photoanodes in NaOH 1 M under solar simulator irradiation.

Figure 64 summarizes the results obtained: the most photoactive composition is the $\text{Fe}_{0.6}\text{Ni}_{0.4}$ one, reaching a photocurrent of almost 1 mA cm^{-2} , while the addition of a third element does not actually lead to an improvement in the mixture performances. However, all the electrodes give higher photocurrents with respect to the bare hematite, except for what concerns the Fe/Ni/Ca composition, which shows worst performances. We can thus totally confirm the results obtained with the SECM.

Moreover, the $\text{Fe}_{0.6}\text{Ni}_{0.4}$ composition is the best one not only in terms of photocurrents, but also of onset potential. Indeed, it is cathodically shifted of $\approx 200 \text{ mV}$ with respect to the bare hematite. The Fe/Ni/Al is not a good overlayer, while Fe/Ni/Ca and Fe/Ni/Mg show the same onset of the semiconductor.

2.3.5. Evaluation of active surfaces through the study of electrode capacitances

CVs at four different scan rates (10 mV s^{-1} , 50 mV s^{-1} , 100 mV s^{-1} and 500 mV s^{-1}) were performed between $E_{in} = 0.9 \text{ V}$ and $E_{fin} = 1.1 \text{ V}$ (RHE), in the dark.

This procedure was applied to five hematite and three $\text{Fe}_{0.6}\text{Ni}_{0.4}$ samples, in order to verify the reproducibility of the results.

Figure 65 shows an example of capacitances study on a hematite sample:

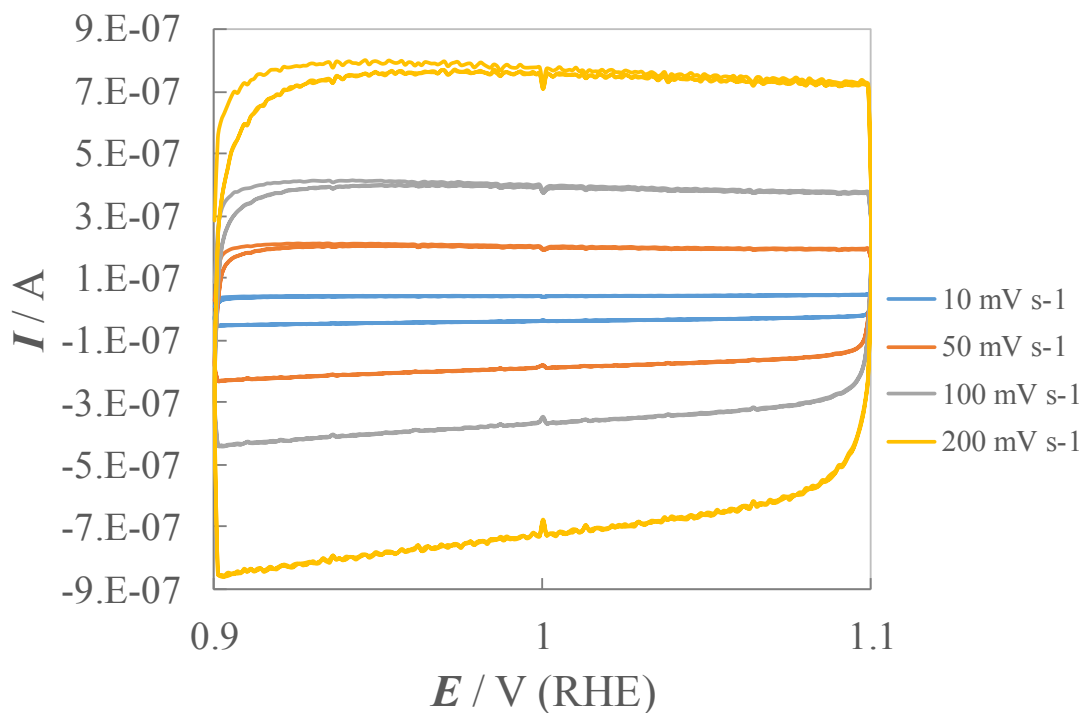


Figure 65: CVs of a hematite sample carried out in the dark between $E_{in} = 0.9$ V and $E_{fin} = 1.1$ V (RHE) at four different scan rates (10 mV s^{-1} , 50 mV s^{-1} , 100 mV s^{-1} and 500 mV s^{-1}).

Values of current at a same fixed potential have been then plotted against the scan rates, as shown in **Figure 66** after the relation:

$$C_d = \frac{I}{v}$$

Where:

C_d is the capacitance, I the current read at a common potential value, v the potential scan rate.

Here, the chosen potential is $E = 1.01$ V (RHE).

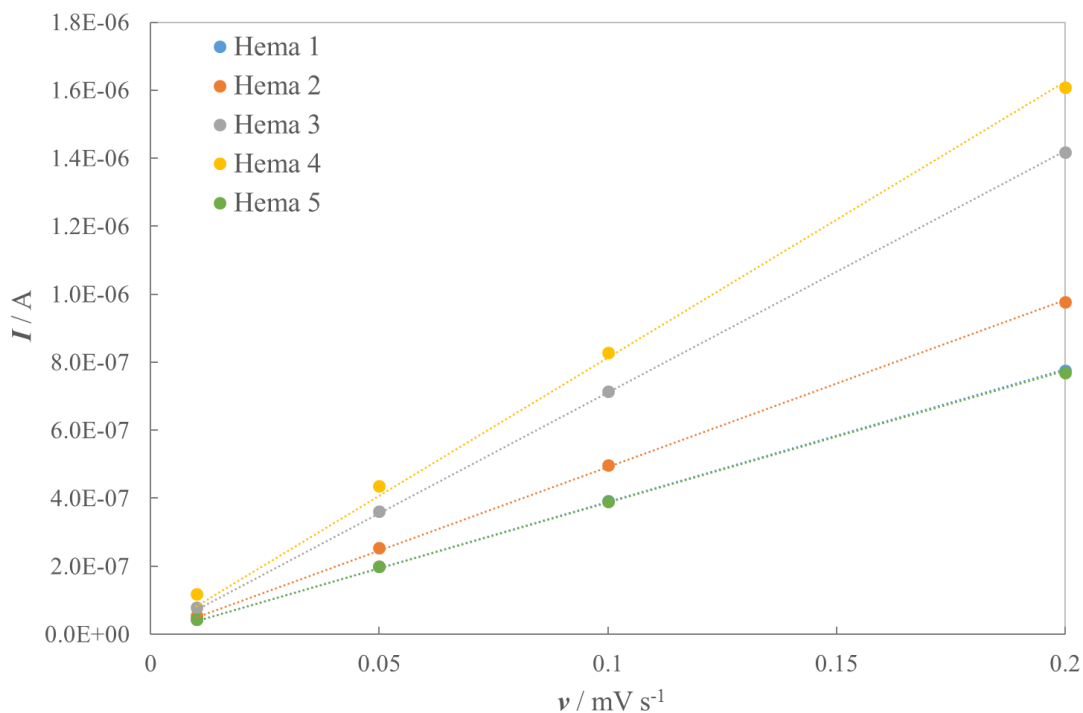


Figure 66: Plot of I recorded at $E = 1.01$ V (RHE) vs. scan rate of five hematite samples.

The slope of these lines gives the value of the capacitances of each sample.

It is clearly deducible that each hematite electrode is characterized by its own active surface area, having also different capacitances. This is probably due to the different orientation of the hematite nanocrystals.

However, normalizing the photocurrents recorded applying the same conditions explained in *Chapter 2.2.8*, it is possible to verify the reproducibility of the activity of the tested photoelectrodes.

For this kind of normalization, the capacitances were obtained from the following equation:

$$\frac{(I_A - I_C)}{2} \cdot \nu$$

Where:

I_A and I_C are the anodic and cathodic current respectively and ν is the potential scan rate.

The two current values are read at $E = 1.01$ V (RHE).

Figure 67 shows the photocurrents of three different $\text{Fe}_{0.6}\text{Ni}_{0.4}$ samples and five hematite, normalized for their capacitances:

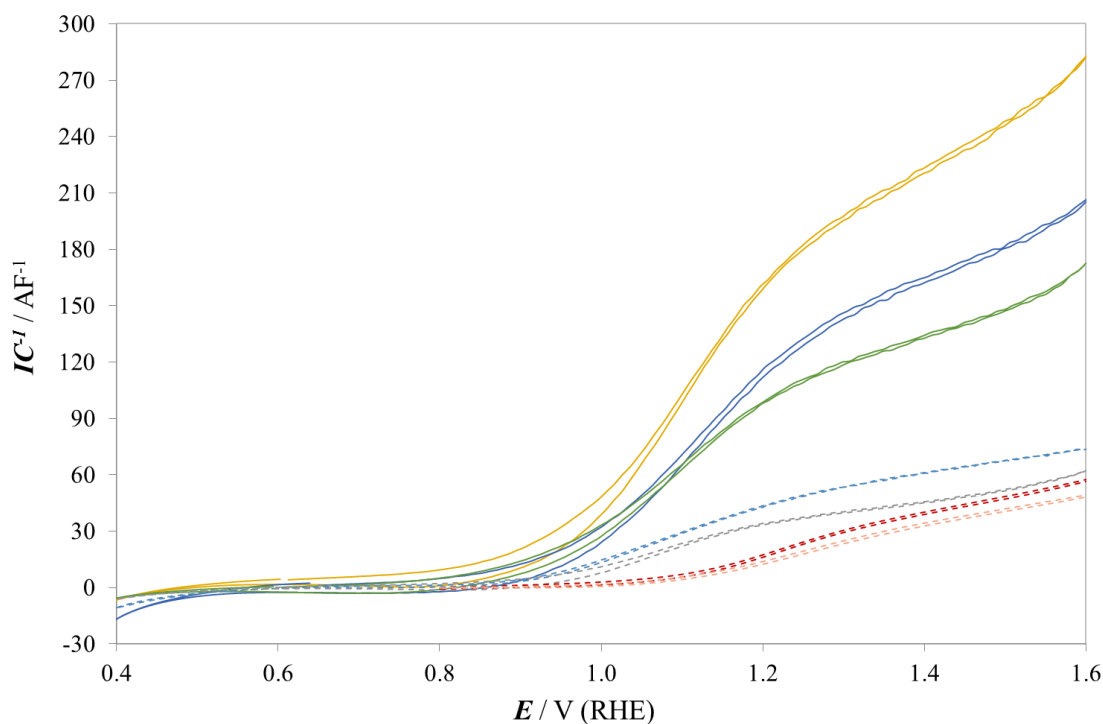


Figure 67: Photocurrents of three $\text{Fe}_{0.6}\text{Ni}_{0.4}$ samples (solid lines) and five hematite (dashed lines) normalized for their capacitances.

It is clearly evident that the three $\text{Fe}_{0.6}\text{Ni}_{0.4}$ photoanodes show the highest photoactivities, having the higher currents also after normalization.

The actual effect of the overlayers on the architecture performances is thus confirmed.

Moreover, the set of hematite samples are close one to each other, meaning that the reproducibility of the results is good. The same conclusion can be reached also for the three $\text{Fe}_{0.6}\text{Ni}_{0.4}$ photoelectrodes.

In the end, the $\text{Fe}_{0.6}\text{Ni}_{0.4}$ composition is the best one not only in terms of photocurrents, but also of onset potential. Indeed, it is cathodically shifted of ≈ 200 mV with respect to the bare hematite.

We can thus conclude that the results obtained in *Section 2.3.4* are here confirmed.

2.4. Conclusions

Arrays of different materials composition were deposited onto hematite.

At the end, almost 30 different compositions were screened and studied through the SECM using only four hematite samples. This confirms the usefulness of this tool when big libraries of different materials have to be tested.

The arrays were tested applying two different approaches: the first one provides the replacement of the ultramicroelectrode tip with a 200 μm diameter white light optical fiber, that can locally generate electron-hole pairs. The second approach provides the use of SECM in its classical set-up, using a 25 μm diameter Au tip as amperometric sensor and recording its current in the SG/TC mode. It is important to remember that the tip current is directly connected to the oxygen produced by the substrate. The experiments were repeated in the dark and under visible light, thanks to a 523 nm green LED.

In order to solve the problem of the overlapping of oxygen profiles when the substrate is biased at an OER potential, the *double pulse method* has been applied to different spots and to the bare hematite, confirming a cathodic shift of the OER onset potential.

In order to confirm the SECM results, the most photoactive compositions according to it were selected and deposited onto hematite as lab-scale electrodes. They were then tested irradiating them with a solar simulator.

The most photoactive composition is the $\text{Fe}_{0.6}\text{Ni}_{0.4}$ one, reaching a photocurrent of almost 1 mA cm^{-2} , while the addition of a third element does not actually lead to an improvement in the mixture performances. However, all the electrodes give higher photocurrents with respect to the bare hematite, except for what concern the Fe/Ni/Ca composition, which shows at least the same behavior, or even worst.

The results obtained with the SECM are thus completely confirmed.

Moreover, the $\text{Fe}_{0.6}\text{Ni}_{0.4}$ composition is the best one not only in terms of photocurrents, but also of onset potential. Indeed, it is cathodically shifted of $\approx 200 \text{ mV}$ with respect to the bare hematite. The Fe/Ni/Al is not so performing, while Fe/Ni/Ca and Fe/Ni/Mg show the same onset of the semiconductor.

In the end, the photocurrents of three $\text{Fe}_{0.6}\text{Ni}_{0.4}$ samples and five hematite photoelectrodes were normalized for their active surface areas.

The three $\text{Fe}_{0.6}\text{Ni}_{0.4}$ photoanodes show the highest photoactivities, having the higher normalized currents.

On the contrary, the five hematite samples have very low normalized photocurrents.

The actual effect of the overlayers on the architecture performances is thus confirmed.

Also the results reproducibility is confirmed.

In the end, the $\text{Fe}_{0.6}\text{Ni}_{0.4}$ composition is the best one not only in terms of photocurrents, but also of onset potential. Indeed, it is cathodically shifted of about 200 mV with respect to the bare hematite.

3. Study of TiO_2 , WO_3 and BiVO_4 nanoparticles prepared by cathodic corrosion methods

*The following part of the Thesis has been performed at the laboratories of Professor Joaquin Rodríguez-López (University of Illinois at Urbana-Champaign UIUC, Urbana-Champaign, Illinois, USA).

** All the data are represented with negative currents and potentials in the first quarter.

*** Based on the paper in preparation: Matthew L. Kromer, Zachary T. Gossage, Burton H. Simpson, Sara Morandi, Paramaconi Rodríguez, Joaquín Rodríguez-López *Synthesis of Photocatalytically Active TiO_2 , WO_3 and BiVO_4 Microparticles from Metal Wires through a Simple Cathodic Corrosion Method*, in preparation.

3.1. Introduction

This part of the work is devoted to the characterization of photocatalytic particles with well-defined and controllable morphology and composition, synthesised with a new, inexpensive and simple method.

This innovative method described in [13], and based on a cathodic corrosion process, is a facile synthesis way of metal oxide nano- and micro-particles, including TiO_2 , BiVO_4 and hydrated WO_3 . It only requires a metal substrate, and upon the use of a well-defined cathodic waveform, generates particles of well-defined composition, crystallinity, and shape. Furthermore, these particles are synthesized in matters of minutes and they do not require a chemical capping agent and time-consuming cleaning procedures.

The factors that impact on the morphology and electrochemical activity of particles obtained *via* cathodic corrosion are discussed.

TiO_2 , BiVO_4 and WO_3 were synthesised.

Despite the simple preparation route (explained later in *Experimental Part*), the obtained particles show a moderate activity towards the photoelectrochemical oxidation of water in basic medium (NaOH 0.1 M). As described in the following, composites of these particles embedded in 5 wt% Nafion[®] perfluorinated resin solution (Sigma-Aldrich) displayed interesting photoanodic responses upon illumination with both UV and Visible light.

3.2. Experimental

All chemicals were used as received. Aqueous solutions were prepared with water from a Millipore® purification system. All the experiments presented were performed at room temperature.

3.2.1. NPs synthesis

The semiconductor nanoparticles were prepared by Prof. Paramaconi Rodriguez group (University of Birmingham).

BiVO₄ particles were synthesised using a mixture (1:1 by volume) of saturated CaCl₂ solution and MilliQ water as electrolyte. Then, 750 µl of a saturated solution of Bi₂O₃ were added. After that, a vanadium wire with diameter of 0.15 mm (99.8% Alfa Aesar) was immersed in the electrolyte and a square wave voltage between -8 V and 2 V was applied (**Figure 68**).

For what concern the synthesis of WO₃ particles, a tungsten wire (diameter of 0.127 mm, Rembar Co. LLC, USA) was immersed in a KHSO₄ 1 M solution. A Pt foil was used as CE.

In this case, the square wave voltage was applied in two different ranges:

- Method 1: from -5 V to 5 V, resulting in a more concentrated suspension;
- Method 2: from -2 V to 3 V, resulting in a more diluted suspension.

All of the resulting suspensions were collected by centrifugation and suspended in with MilliQ water to remove the excess of the reactants.

The same procedure was applied to synthesise the TiO₂ nanoparticles.

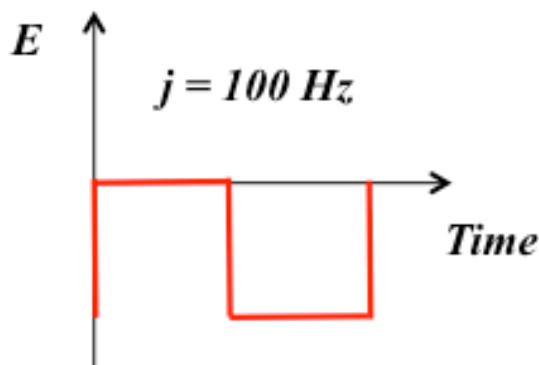


Figure 68: Scheme of the cathodic corrosion.

Figure 69 shows SEM images of the nanoparticles:

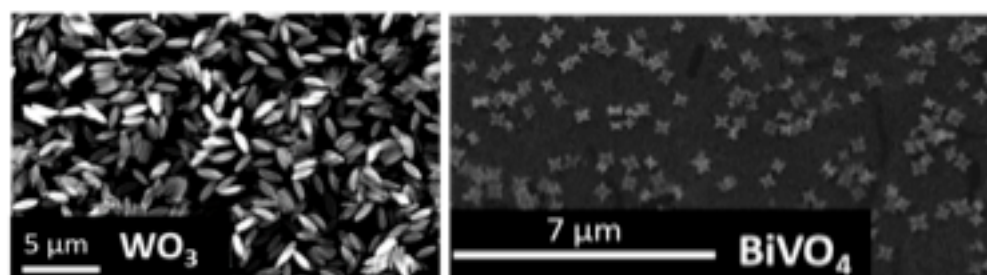


Figure 69: SEM images of WO₃ and BiVO₄ particles.

3.2.2. Sample preparation

The samples were prepared in three different ways:

- 1) Nanoparticles mixed with Nafion[®] dispersion deposited onto FTO:

FTO substrates were firstly cleaned by sonication for 30 minutes in acetone, 30 minutes in ethanol and 30 minutes in deionized water.

50 μl of the nanoparticle suspensions in water previously sonicated at least 10 minutes were deposited as prepared on an FTO by drop-casting. After that, the Nafion[®] dispersion was added on the dried sample, with a NPs / Nafion[®] ratio of 1:50, in order to promote the adhesion of the NPs to the substrate. The samples were then tested by back-irradiation.

- 2) Nanoparticles mixed with Nafion[®] deposited onto Glassy Carbon (GC) electrodes:

Unfortunately, FTO electrodes are moderately photoactive, and could affect the results of the semiconductors under study. For this reason, it was decided to deposit the nanoparticles also onto a non-photoactive support, like GC electrode.

In this case, 20 μm of sonicated nanoparticle suspensions were deposited as prepared by drop-casting. The Nafion[®] dispersion was then added on the dried sample, with a NPs / Nafion[®] ratio of 1:50.

Of course, in this case it was not possible to illuminate the sample from the bottom, and it was thus irradiated from the top.

These tests were carried out using SECM, as explained below.

3) Nanoparticles:

Since the nanoparticles did not show significant photocurrents, different kind of activation were applied.

The first activation method provided the deposition of 100 μl of each type of nanoparticle suspensions previously sonicated at least 10 minutes onto a cleaned FTO by drop-casting, followed by the activation of the materials by annealing them at 500 $^{\circ}\text{C}$ (after a 5 $^{\circ}\text{C}/\text{min}$ ramp) for 3h in air.

4) Hydrogen activation:

In the end, TiO_2 nanoparticles were activated with hydrogen. Indeed, the chemical or electrochemical reduction of TiO_2 provides the formation of new defects in the material responsible of the increase of the photoactivity under visible light [¹⁴].

Thus, two activation ways were followed: according to the first, 100 μl of previously sonicated TiO_2 nanoparticles were deposited on cleaned FTO by drop-casting and then activated by annealing the sample at 500 $^{\circ}\text{C}$ under a flux of H_2 and Ar (5% of H_2).

The second way provided the activation of the TiO_2 nanoparticles by keeping the sample biased at a hydrogen evolution potential for 30 minutes.

This activation was applied to the TiO_2 nanoparticles and to two different (0.1 M and 1 mM) commercially available anatase TiO_2 nanoparticles suspension (Sigma-Aldrich, nanopowder, < 25 nm particle size, 99.7%).

All the experiments were carried out in NaOH 0.1 M, both in the dark and under irradiation of a white light. In some experiments a 400 nm cut-off light was used, in order to exclude the UV-light contribution. A classical three-electrode cell configuration was used, in which the substrate covered by NPs was the WE, a platinum wire the counter electrode (CE) and an Ag|AgCl (3 M KCl) the reference electrode (RE). The latter was separated from the solution by a salt bridge consisting of a glass pipette filled with agar, containing 0.1 M aqueous KClO_4 .

One of the main limits of a conventional photocurrent measurement is that the latter includes both the contributions of water electrolyses and photocorrosion.

Here, Scanning ElectroChemical Microscopy (SECM) was used in the substrate generation / tip collection (SG/TC) mode to attain a (tip) current/ substrate potential characteristics that is related to the sole contribution of water oxidation at the substrate, being the tip potential biased to a potential at which it reduces oxygen under mass-transport control.

In this case the tip was a platinum disc electrode fabricated using a 25 μm wire.

SECM experiments were carried out in a four-electrode cell configuration using the substrate as WE1, the SECM tip as the WE2, a platinum wire CE and an Ag|AgCl (3 M KCl) as RE, separated from the solution by an agar in 0.1 M KClO_4 salt bridge.

The electrolyte was NaOH 0.1 M.

Figure 70 schematically shows the cell setup.

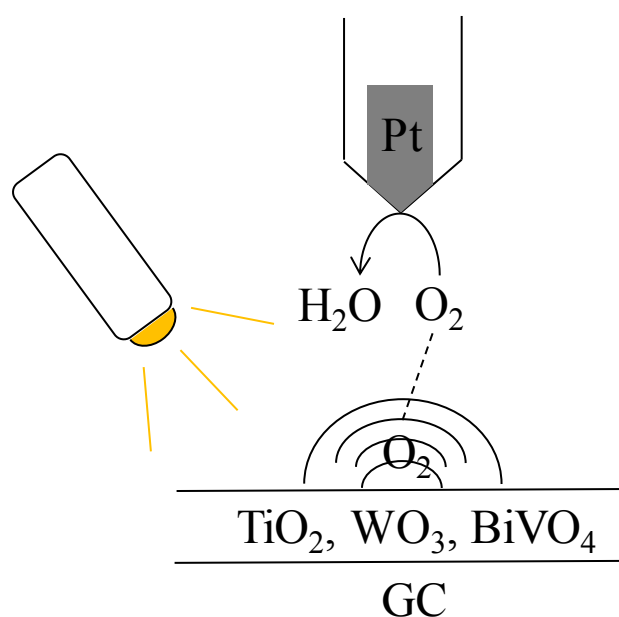


Figure 70: SECM experiment set-up.

In order to place the tip at a fixed and desired distance from the sample, negative feedback approach curves were recorded. These curves represent the tip current, i_t , as a function of d , tip-substrate distance, and are obtained when the tip is moved toward the substrate in the z direction, recorded at $1 \mu\text{m s}^{-1}$. The tip-substrate distance was set at $\approx 5 \mu\text{m}$.

The tip was biased at a constant potential of 0.1 V (RHE), while a cyclic voltammetry between 0.6 and 1.7 V (RHE) was applied to the substrate. The tip potential was selected in order to reduce O_2 to water under mass transport control.

Figure 71 shows the potential profiles applied to both tip and substrate:

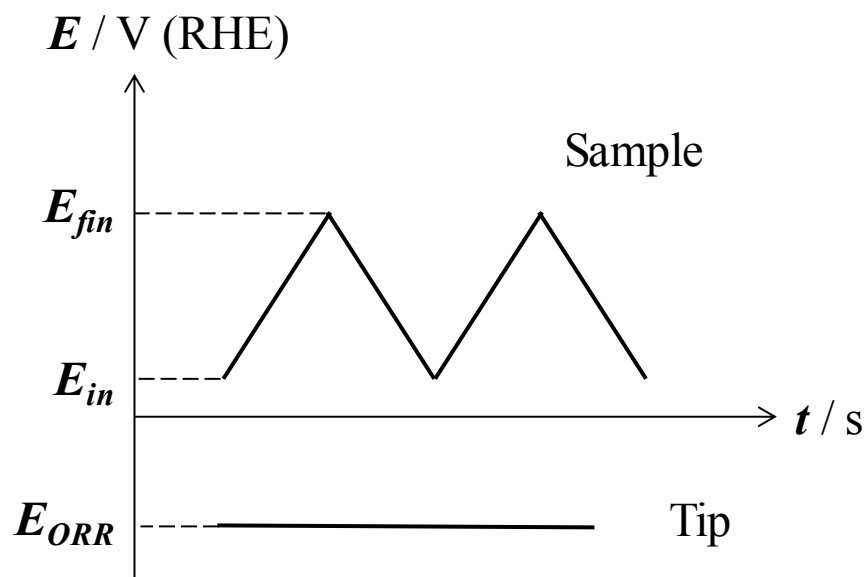


Figure 71: Potential profile applied both to the substrate and the tip.

3.2.3. Tip preparation

The tip used in the SECM experiment was made according to the procedure already discussed in the Experimental Section. A 0.025 mm Pt wire was used as core material.

3.3. Result and discussion

3.3.1. Nanoparticles mixed with Nafion[®] deposited onto FTO

As already said in the *Experimental Section*, 50 μl of nanoparticle suspensions were deposited as prepared on an FTO by drop-casting and tested in NaOH 0.1 M. They were then irradiated from the bottom.

Unfortunately, the photocurrents recorded under these conditions were too low or even zero, meaning that no photoactivity was observed, probably because of the low cohesion of these materials on the FTO. Indeed, after the tests were performed, no more nanoparticles were present onto the support.

For this reason, in order to promote the adhesion of the NPs to the substrate, a Nafion[®] polymer was added on the dried sample, with a NPs / Nafion[®] ratios of 1:50

The samples were then cycled between 0.5 V and 1.8 V (RHE) in the dark, under white light and using a 400 nm cut-off.

The CV scan rate was 20 mV s^{-1} .

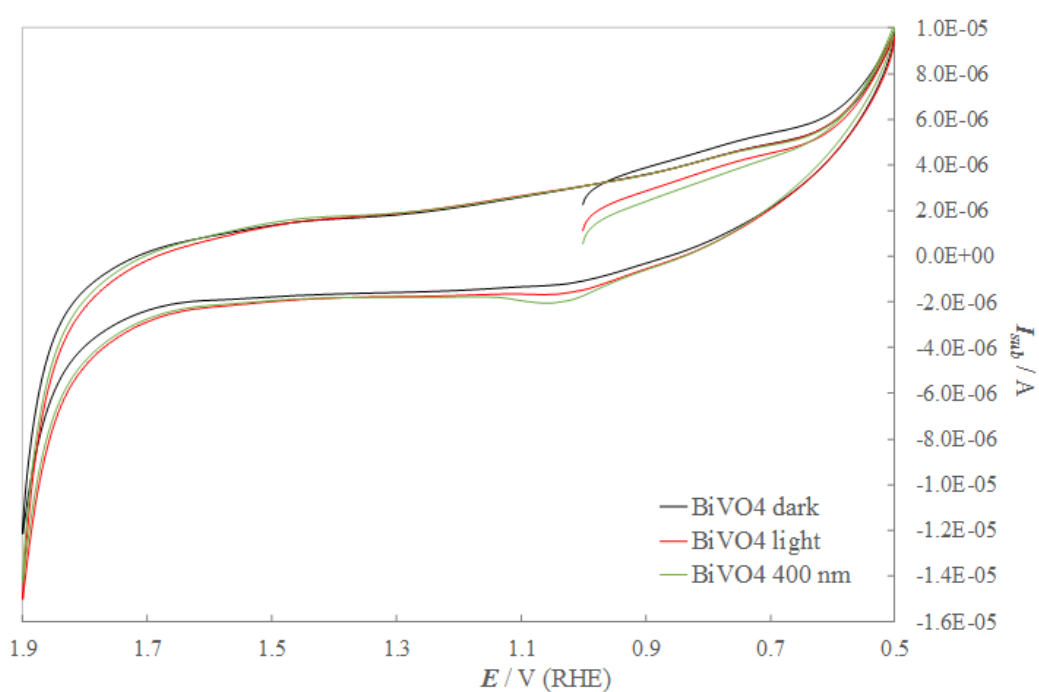


Figure 72: Cyclic voltammetry of BiVO₄ nanoparticles suspension / Nafion[®] 1:50 in NaOH 0.1 M in the dark (black line), under white (red line) and 400 nm cut-off light (green line). Scan rate: 20 mV s^{-1} .

BiVO_4 nanoparticles show a significant photocurrent both under white (red line) and 400 nm cut-off light (green line), meaning that the material is photoactive also in the visible region.

At the same time, the OER onset potential is cathodically shifted of ≈ 100 mV.

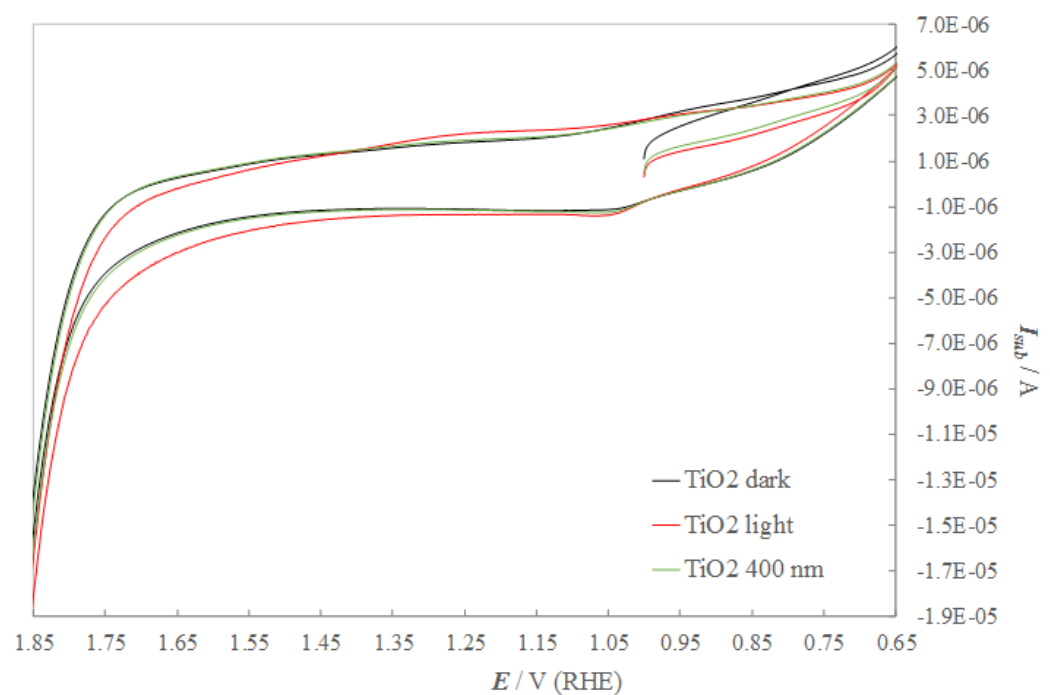


Figure 73: Cyclic voltammetry of TiO_2 nanoparticles suspension / Nafion[®] 1:50 in NaOH 0.1 M in the dark (black line), under white (red line) and 400 nm cut-off light (green line). Scan rate: 20 mV s^{-1} .

On the contrary, TiO_2 nanoparticles show a significant photocurrent only when irradiated by a white light, while no photoactivity is evident when a 400 nm cut-off is used. Indeed, as it is well known, TiO_2 band-gap is too high to allow the generation of electron-hole couples when the semiconductor is irradiated by visible light.

As for what concerned the BiVO_4 nanoparticles, also the TiO_2 OER onset potential is cathodically shifted of ≈ 100 mV.

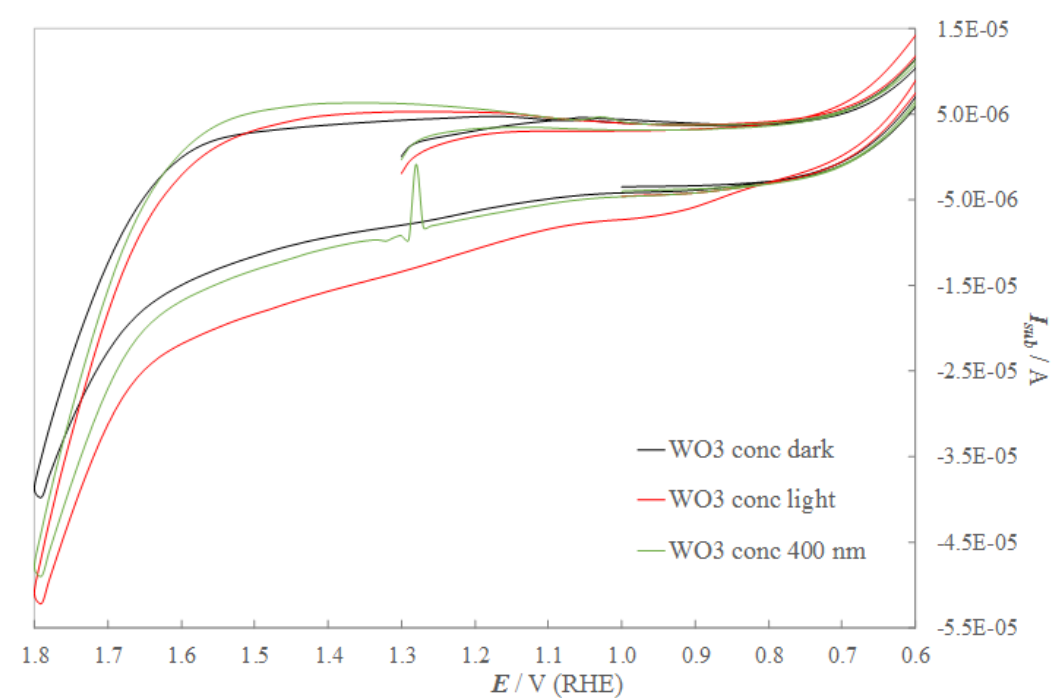


Figure 74: Cyclic voltammetry of more concentrated WO_3 nanoparticles suspension / Nafion[®] 1:50 in NaOH 0.1 M in the dark (black line), under white (red line) and 400 nm cut-off light (green line). Scan rate: 20 mV s^{-1} .

The WO_3 nanoparticles dispensed starting from a more concentrated suspension show a significant photocurrent both under white (red line) and 400 nm cut-off light (green line), meaning that the material is photoactive also in the visible region. However, when irradiated by a white light, WO_3 photocurrents start rising at very low potential ($\approx 1 \text{ V}$ vs. RHE), while in presence of the 400 nm cut-off the OER onset potential is cathodically shifted of only $\approx 50 \text{ mV}$.

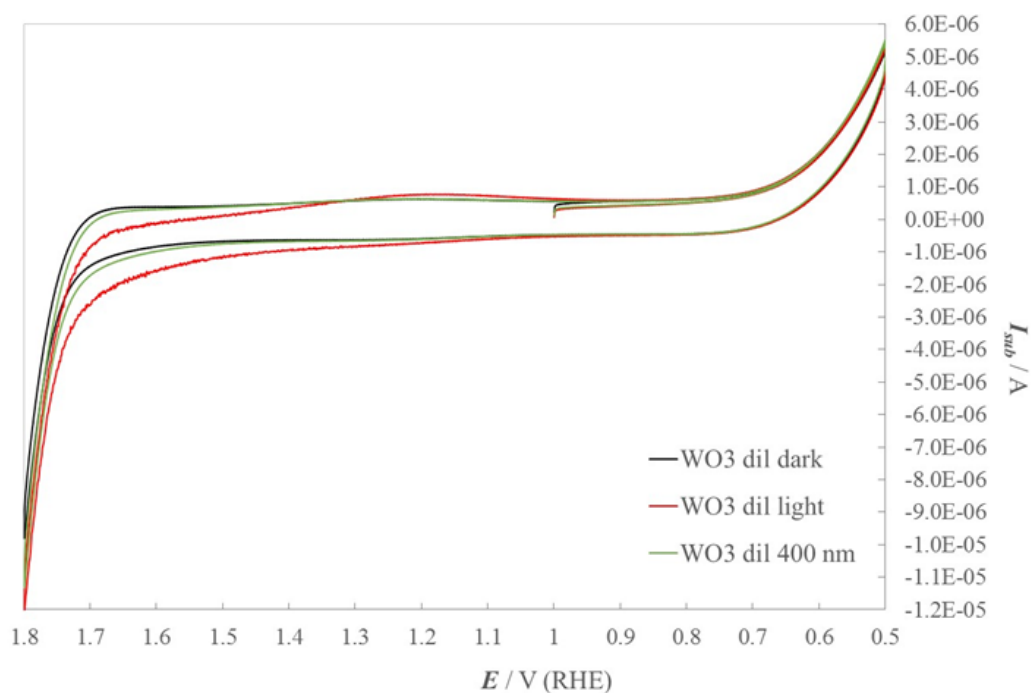


Figure 75: Cyclic voltammetry of more diluted WO_3 nanoparticles suspension / Nafion[®] 1:50 in NaOH 0.1 M in the dark (black line), under white (red line) and 400 nm cut-off light (green line). Scan rate: 20 mV s^{-1} .

In the end, also the WO_3 nanoparticles dispensed starting from a more diluted suspension show a significant photocurrent both under white (red line) and 400 nm cut-off light (green line) at very anodic potential ($\approx 1.8 \text{ V}$ vs. RHE). This means that the material is photoactive also in the visible region. However, when irradiated by a white light, WO_3 photocurrents start rising at lower potential ($\approx 1.5 \text{ V}$ vs. RHE), while in presence of the 400 nm cut-off the OER onset potential is not anticipated.

In order to evaluate the increase of photocurrent under strong oxygen evolution conditions, chronoamperometries were carried out while the light was chopped, as shown in **Figure 76**.

During these experiments, all the samples were biased at an oxygen evolution potential, $E = 1.8 \text{ V}$ (RHE), for about two minutes. In the meantime, the light was switched on and off after 20 seconds.

Moreover, the Nafion[®] dispersion was added on the dried sample, with a NPs / Nafion[®] ratio of 1:50.

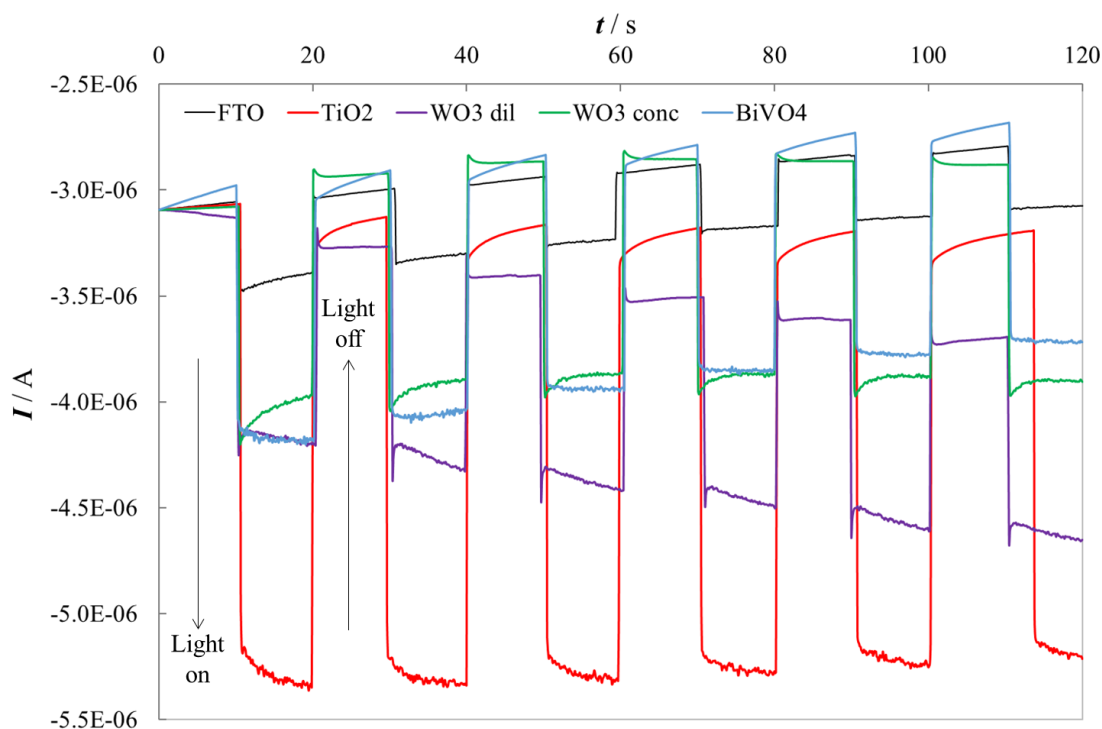


Figure 76: Chronoamperometries under OER conditions of FTO (black line), BiVO₄ (blue line), TiO₂ (red line), concentrated WO₃ (green line) and diluted WO₃ (purple line) nanoparticles suspensions / Nafion[®] 1:50 in NaOH 0.1 M under chopped white light.

As we can see in **Figure 76**, the most active material is TiO₂, followed by the less concentrated WO₃, suspension than the more concentrated WO₃ one and BiVO₄.

Moreover, BiVO₄ and concentrated WO₃ currents showed low stability, since their photocurrents decreased during the experiment. On the contrary, the more diluted WO₃ photocurrents show an increase, meaning that they probably needed some time to be completely activated. In the end, the TiO₂ was the most stable sample.

Also FTO showed a small photoactivity, even if very low if compared to that of the nanoparticles.

For this reason, it was necessary to repeat the study of these nanoparticles also with a not photoactive support, i.e. a Glassy Carbon (GC) electrode.

In the end, the same experiment was repeated not at a constant potential, but performing CVs between 1.25 V and 1.65 V (RHE) under chopped light (**Figure 77**).

The CV scan rate was 20 mV s⁻¹.

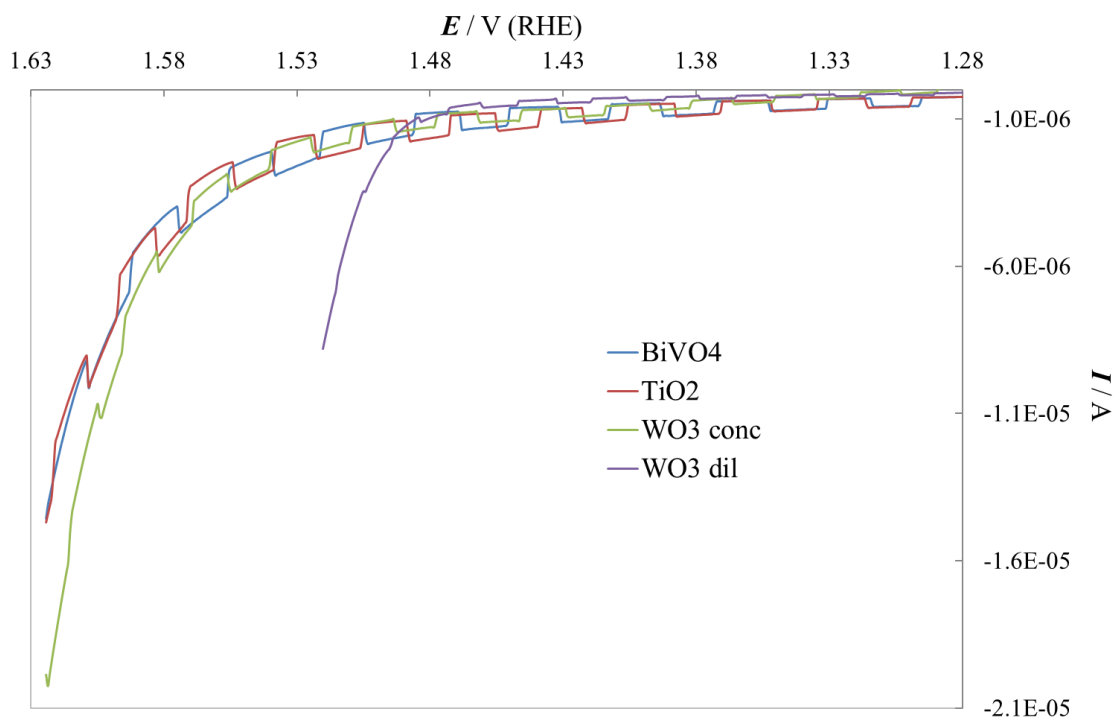


Figure 77: Cyclic voltammeteries under OER conditions of BiVO₄ (blue line), TiO₂ (red line), concentrated WO₃ (green line) and diluted WO₃ (purple line) nanoparticles suspensions / Nafion[®] 1:50 in NaOH 0.1 M under chopped white light. Scan rate: 20 mV s⁻¹.

As we can see, all the materials show a clear photoactivity.

If we consider the currents recorded while the light was on, the TiO₂ nanoparticles are the most active, followed by BiVO₄.

The most concentrated WO₃ are a little bit less photoactive than TiO₂ and BiVO₄, while the more diluted WO₃ show really low photocurrents under illumination.

On the contrary, the most diluted WO₃ nanoparticles have an OER onset potential about 5 mV lower with respect to the other three materials, which are very similar.

As previously observed, FTO showed a small photoactivity, even if it is much lower those related to nanoparticles.

For this reason, it was necessary to repeat the study of these materials also with a not photoactive support, i.e. a Glassy Carbon (GC) electrode.

1.3.2 Nanoparticles mixed with Nafion[®] deposited onto Glassy Carbon (GC) electrodes

Instead of an FTO, a Glassy Carbon (GC) support was used.

Also in this case, the SECM was used, as previously explained.

The electrolyte was NaOH 0.1 M, again.

The samples were then cycled between 0 V and 1.9 V (RHE), with the Pt tip kept fixed at 0.1 V (RHE). The CV scan rate was 20 mV s^{-1} .

The CVs were performed both in the dark and under with light.

Figure 78 shows both the substrate and tip response of BiVO_4 nanoparticles suspension:

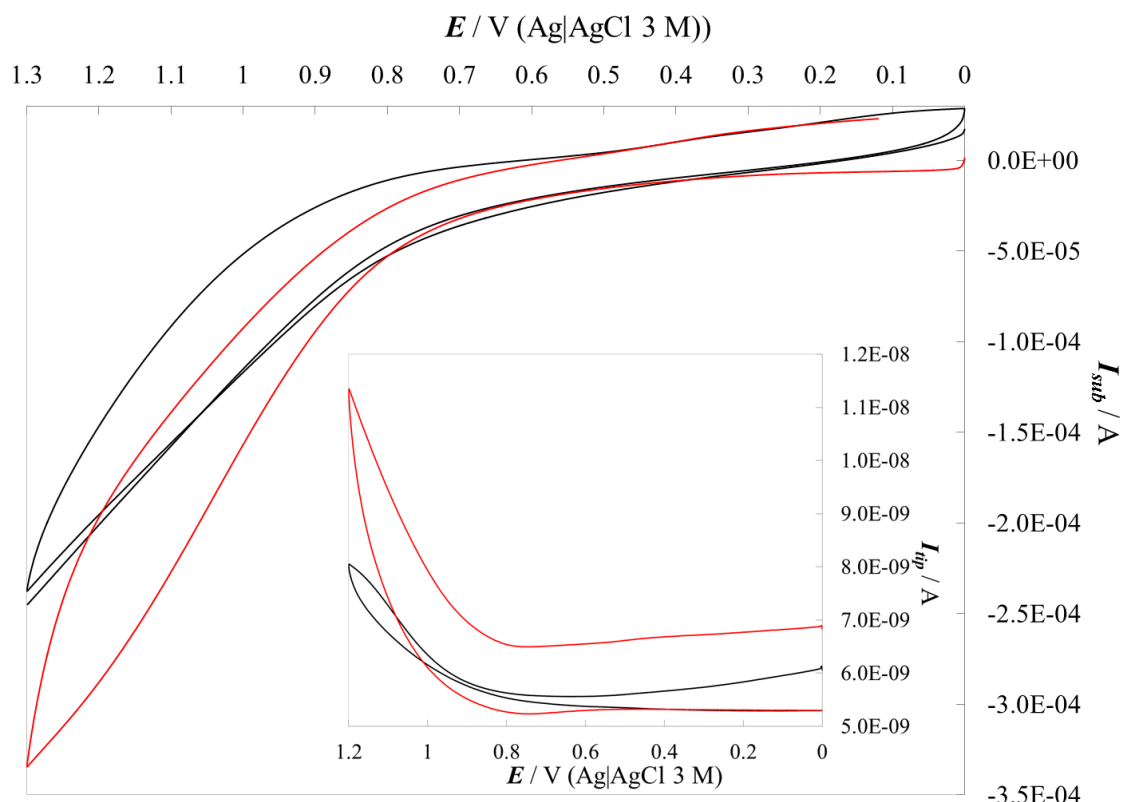


Figure 78: Cyclic voltammeteries of BiVO_4 , nanoparticles suspension / Nafion® 1:50 in NaOH 0.1 M in the dark (black line) and under white light (red line). Insert: tip current at $E_{tip} = 0.1 \text{ V}$ (RHE). Scan rate: 20 mV s^{-1} .

As we can see, BiVO_4 nanoparticles show photoactivity under white irradiation (red line). Also the tip current was higher when the substrate was illuminated, due to the higher amount of oxygen produced by the sample under light. This confirms that the substrate photocurrents are related to the oxygen production and not to other parasite reactions.

The OER onset potential of both the substrate and tip does not change significantly under light irradiation.

Figure 79 shows both the substrate and tip response of TiO_2 nanoparticles suspension:

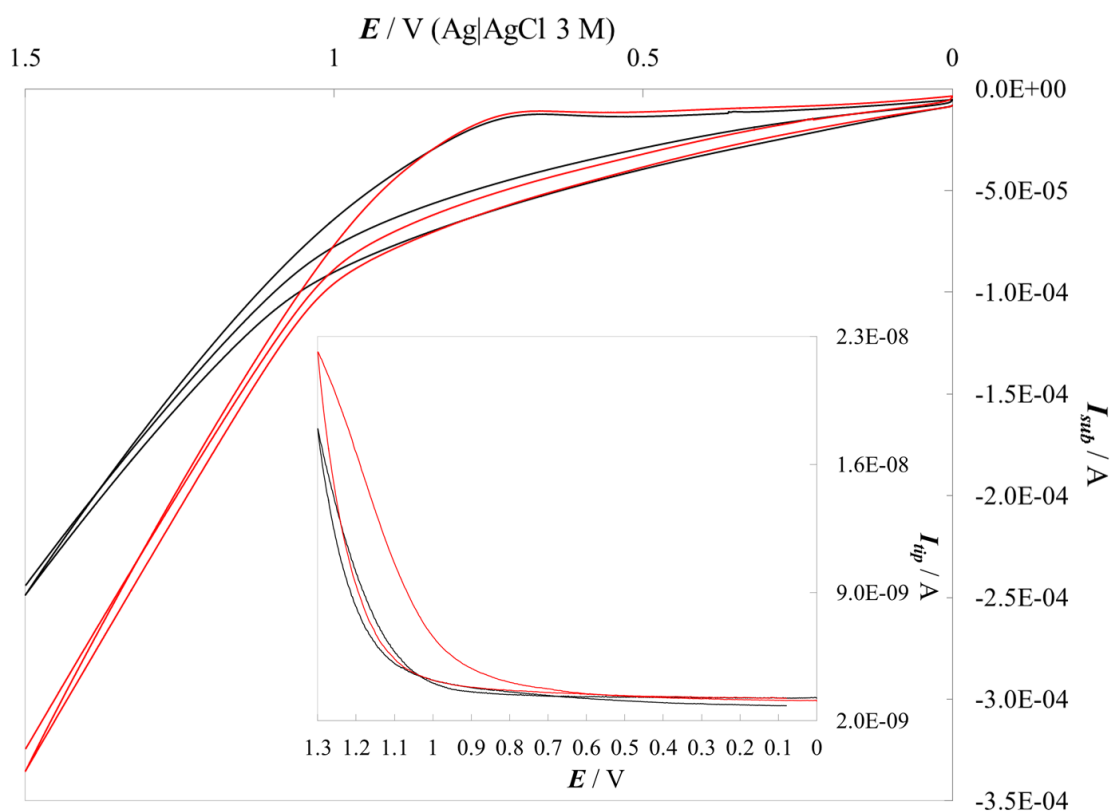


Figure 79: Cyclic voltammeteries of TiO_2 nanoparticles suspension / Nafion[®] 1:50 in NaOH 0.1 M in the dark (black line) and under white light (red line). Insert: tip current at $E_{tip} = 0.1$ V (RHE). Scan rate: 20 mV s^{-1} .

Also TiO_2 nanoparticles show a huge photoactivity under white irradiation (red line). However, the tip current does not show such difference between dark and light. This probably means that the substrate photocurrents are not related only to the oxygen production, but also to other parasite reactions.

For what concern the OER onset potential, both substrate and tip don't show significant shifts under light irradiation.

Figure 80 shows both the substrate and tip response of the more concentrated WO_3 nanoparticles suspension:

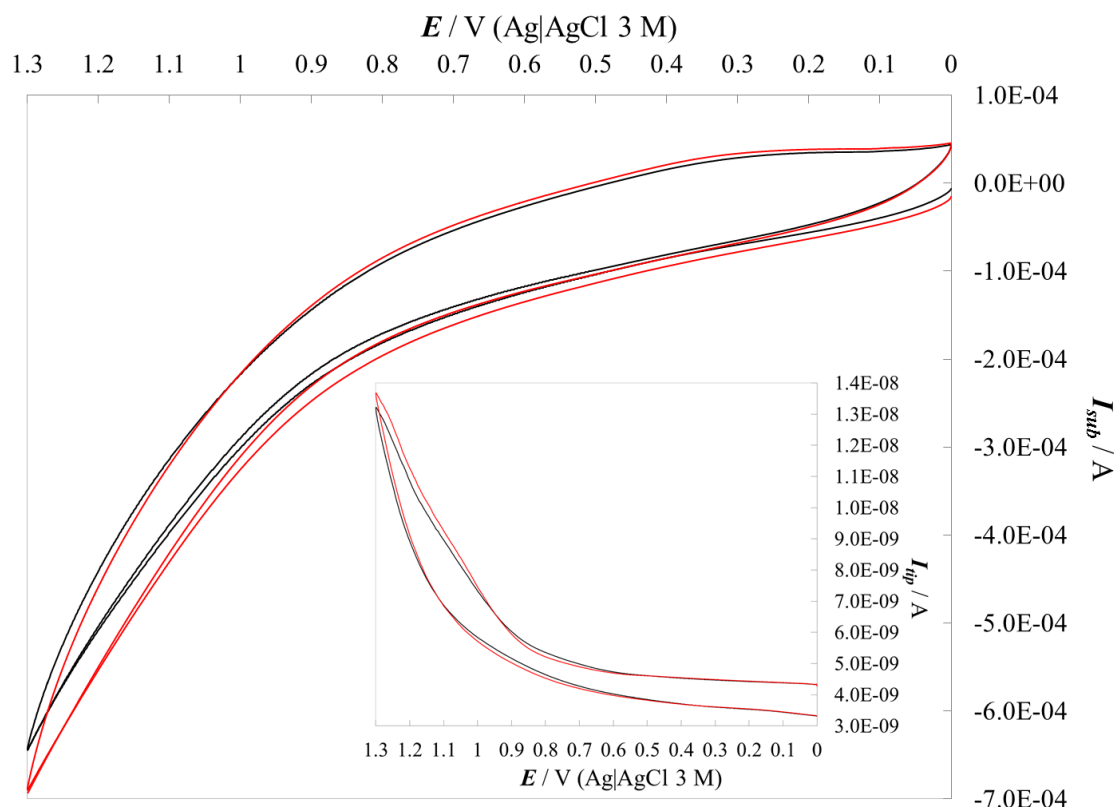


Figure 80: Cyclic voltammeteries of the more concentrated WO_3 nanoparticles suspension / Nafion[®] 1:50 in NaOH 0.1 M in the dark (black line) and under white light (red line). Insert: tip current at $E_{tip} = 0.1$ V (RHE). Scan rate: 20 mV s^{-1} .

The more concentrated WO_3 nanoparticles suspension show photoactivity under white irradiation (red line), even if low. Also the tip current was higher when the substrate was illuminated, due to the amount of oxygen produced by the sample under light. This confirms that the substrate photocurrents are related to the oxygen production, even if not huge, and not to other parasite reactions.

For what concern the OER onset potential, both substrate and tip don't show significant shifts under light irradiation.

In the end, **Figure 81** shows both the substrate and tip response of the more diluted WO_3 nanoparticles suspension:

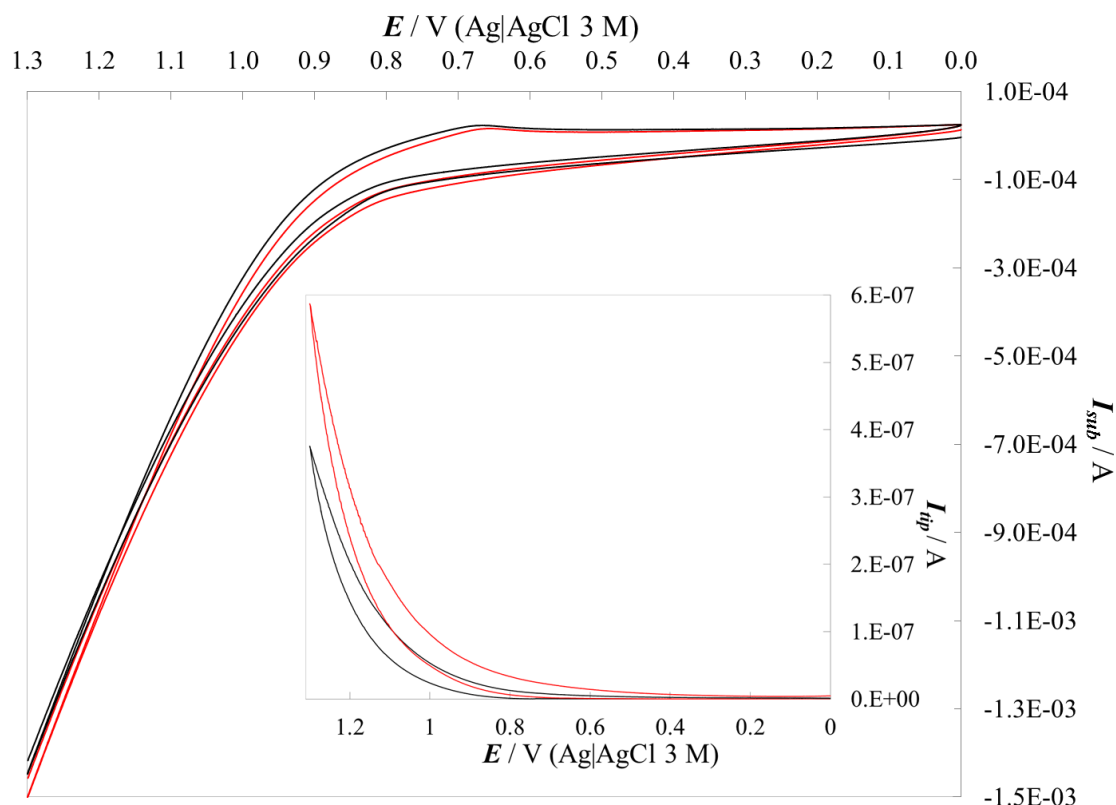


Figure 81: Cyclic voltammeteries of the more diluted WO_3 nanoparticles suspension / Nafion[®] 1:50 in NaOH 0.1 M in the dark (black line) and under white light (red line). Insert: tip current at $E_{tip} = 0.1$ V (RHE). Scan rate: 20 mV s^{-1} .

The more diluted WO_3 nanoparticles suspension show the lowest photoactivity under white irradiation (red line). However, the tip current was higher when the substrate was illuminated: this means that the substrate photocurrents, even if low, are actually due to the amount of oxygen produced by the sample under light. This confirms that the substrate photocurrents are related to the oxygen production, even if not huge, and not to other parasite reactions.

For what concern the OER onset potential, the substrate one does not show any significant shifts. On the contrary, the tip current shows a shift of ≈ 100 mV.

1.3.3 Effect of Nafion[®] on nanoparticles photoactivity

20 μl of previously sonicated nanoparticles were deposited onto cleaned GC, and dried. After that, Nafion[®] polymer was added in a different nanoparticles / Nafion[®] ratios: 4:1. The materials were then tested in NaOH 0.1 M, again.

Figure 82 show the results obtained in presence of BiVO_4 nanoparticles in excess with respect to Nafion[®] 4:1. In the insert, the tip response is shown:

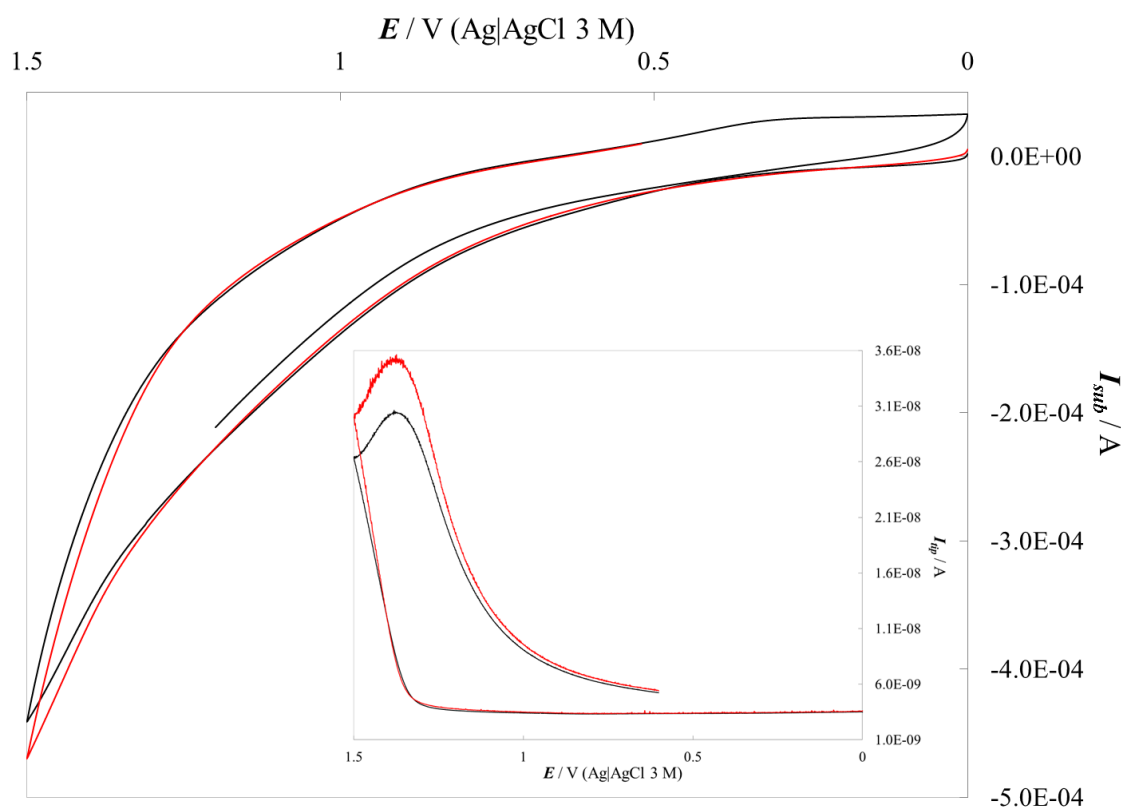


Figure 82: Cyclic voltammeteries of BiVO_4 , nanoparticles suspension / Nafion[®] 4:1 in NaOH 0.1 M in the dark (black line) and under white light (red line). Insert: tip current at $E_{tip} = 0.1$ V (RHE). Scan rate: 20 mV s^{-1} .

As we can see, BiVO_4 nanoparticles show photoactivity under white irradiation (red line), even if very low. Also the tip current was higher when the substrate was illuminated, due to the higher amount of oxygen produced by the sample under light. This confirms that the substrate photocurrents are related to the oxygen production and not to other parasite reactions.

The OER onset potential of both the substrate and tip does not change significantly under light irradiation.

Figure 83 show the results obtained in presence of TiO_2 nanoparticles in excess with respect to Nafion[®] 4:1. In the insert, the tip response is shown:

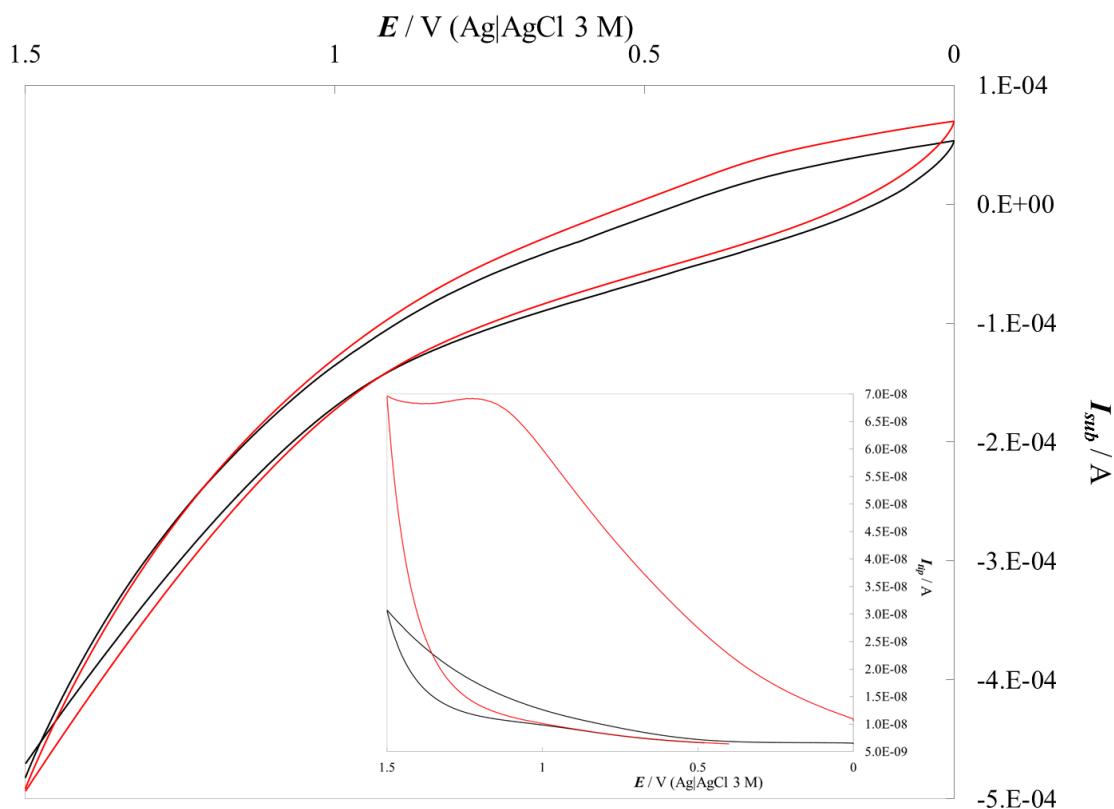


Figure 83: Cyclic voltammeteries of TiO_2 , nanoparticles suspension / Nafion[®] 4:1 in NaOH 0.1 M in the dark (black line) and under white light (red line). Insert: tip current at $E_{tip} = 0.1$ V (RHE). Scan rate: 20 mV s^{-1} .

TiO_2 nanoparticles show really low photocurrents under white irradiation (red line). On the contrary, the differences of the tip current in the dark and under light show a huge enhancement in the production of oxygen when the substrate is irradiated. This confirms the convenience in using an UME as oxygen sensor to collect the oxygen actually produced by the semiconductor.

For what concern the OER onset potential, the tip shows a shift under light irradiation of ≈ 100 mV.

Figure 84 show the results obtained in presence of the most concentrated WO_3 nanoparticles in excess with respect to Nafion[®] 4:1. In the insert, the tip response is shown:

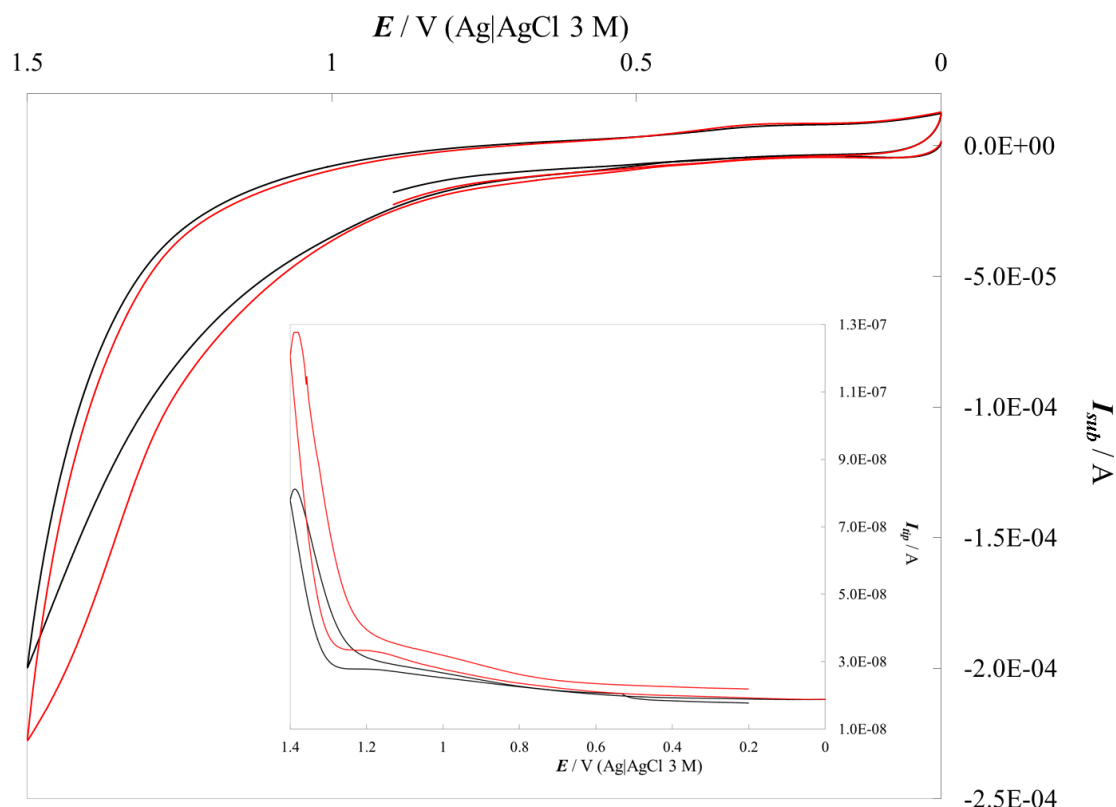


Figure 84: Cyclic voltammeteries of the more concentrated WO_3 nanoparticles suspension / Nafion[®] 4:1 in NaOH 0.1 M in the dark (black line) and under white light (red line). Insert: tip current at $E_{tip} = 0.1$ V (RHE). Scan rate: 20 mV s^{-1} .

The more concentrated WO_3 nanoparticles suspension show photoactivity under white irradiation (red line). Also the tip current was higher when the substrate was illuminated, due to the amount of oxygen produced by the sample under light. This confirms that the substrate photocurrents are related to the oxygen production, even if not huge, and not to other parasite reactions.

Moreover, it is evident that an excess of nanoparticles with respect to the Nafion[®] leads to an enhancement in the material photoactivity.

For what concern the OER onset potential, both substrate and tip don't show significant shifts under light irradiation.

In the end, **Figure 85** show the results obtained in presence of the most diluted WO_3 nanoparticles in excess with respect to Nafion[®] 4:1. In the insert, the tip response is shown:

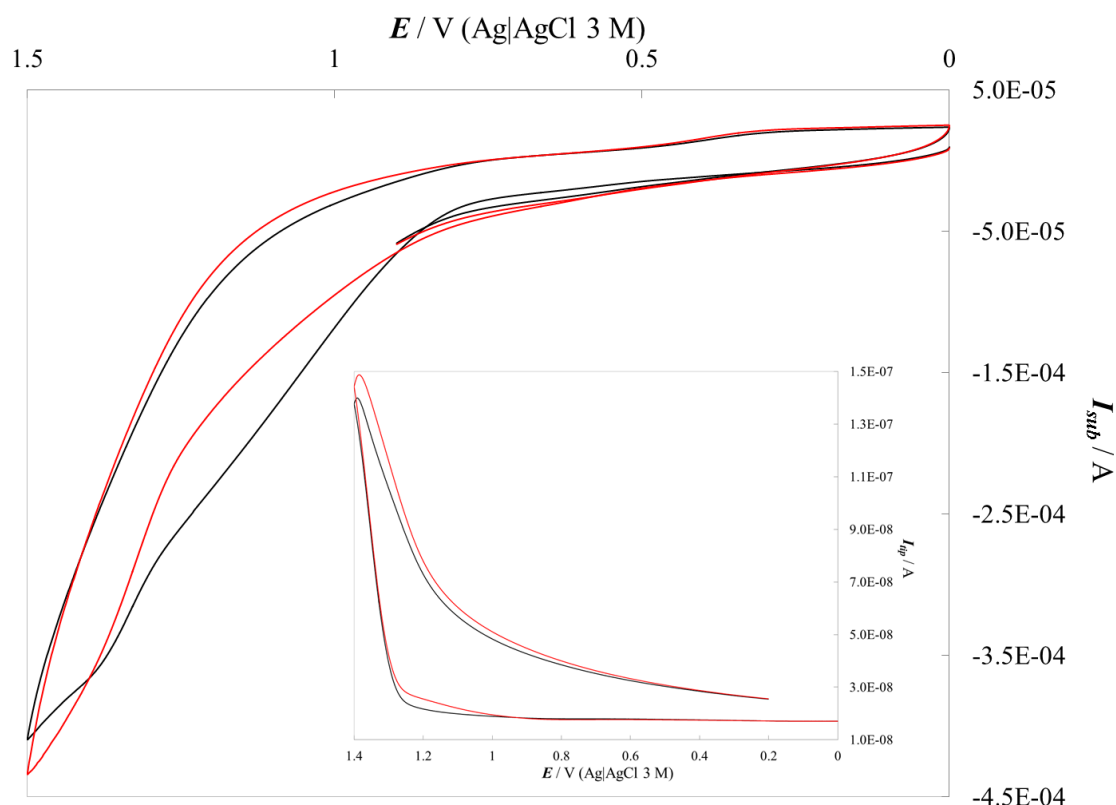


Figure 85: Cyclic voltammeteries of the more diluted WO_3 nanoparticles suspension / Nafion[®] 4:1 in NaOH 0.1 M in the dark (black line) and under white light (red line). Insert: tip current at $E_{tip} = 0.1$ V (RHE). Scan rate: 20 mV s^{-1} .

Also the more diluted WO_3 nanoparticles suspension show photoactivity under white irradiation (red line). The tip current was higher when the substrate was illuminated, due to the amount of oxygen produced by the sample under light. This confirms that the substrate photocurrents are related to the oxygen production, even if not huge, and not to other parasite reactions.

Moreover, even these nanoparticles show an enhancement in the photoactivity when they are in excess with respect to the Nafion[®].

For what concern the OER onset potential, both substrate and tip don't show significant shifts under light irradiation.

After that, we focused on TiO_2 nanoparticles, both since they were the most photoactive ones and with the aim of comparing them to commercially available TiO_2 nanoparticles. $20 \mu\text{l}$ of previously sonicated nanoparticles were deposited onto cleaned GC and dried. After that, Nafion[®] suspension was added in a different nanoparticles / Nafion[®] ratios: 5:1, 10:1 and 50:1.

Figure 86, **Figure 87** and **Figure 88** show the behaviour of both the samples and the tip in the dark and under white light.

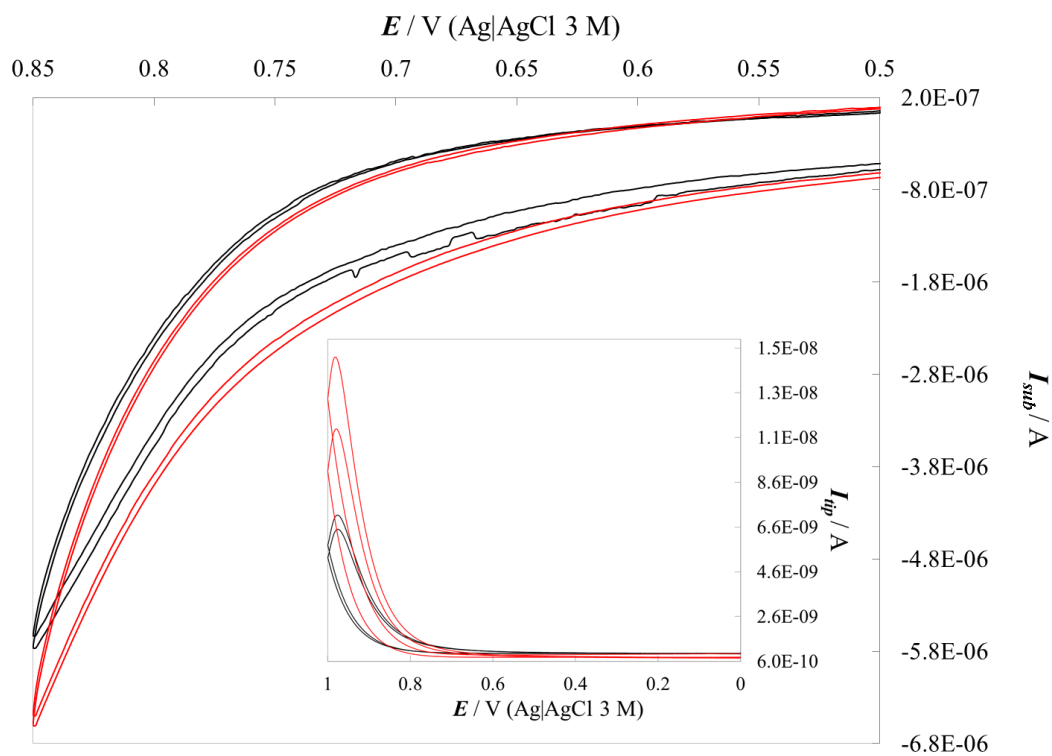


Figure 86: Cyclic voltammeteries of TiO_2 nanoparticles / Nafion[®] 5:1 in NaOH 0.1 M in the dark (black line) and under white light (red line). Insert: tip current at $E_{tip} = 0.1$ V (RHE). Scan rate: 20 mV s^{-1} .

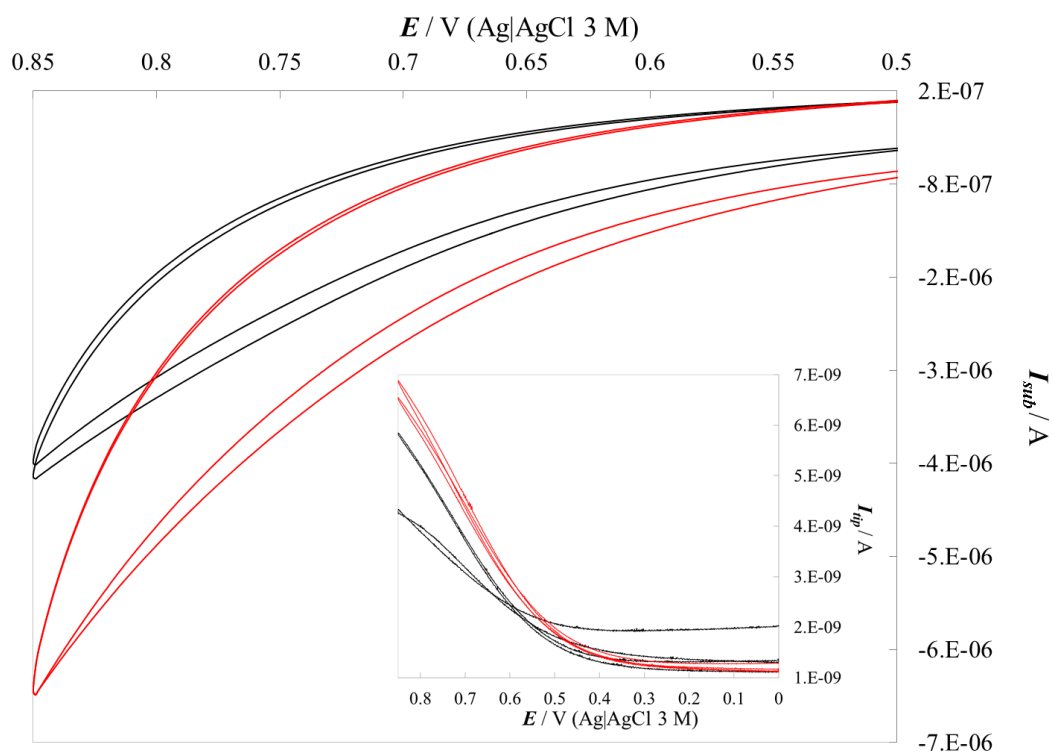


Figure 87: Cyclic voltammograms of TiO_2 nanoparticles / Nafion[®] 10:1 in NaOH 0.1 M in the dark (black line) and under white light (red line). Insert: tip current at $E_{tip} = 0.1$ V (RHE). Scan rate: 20 mV s^{-1} .

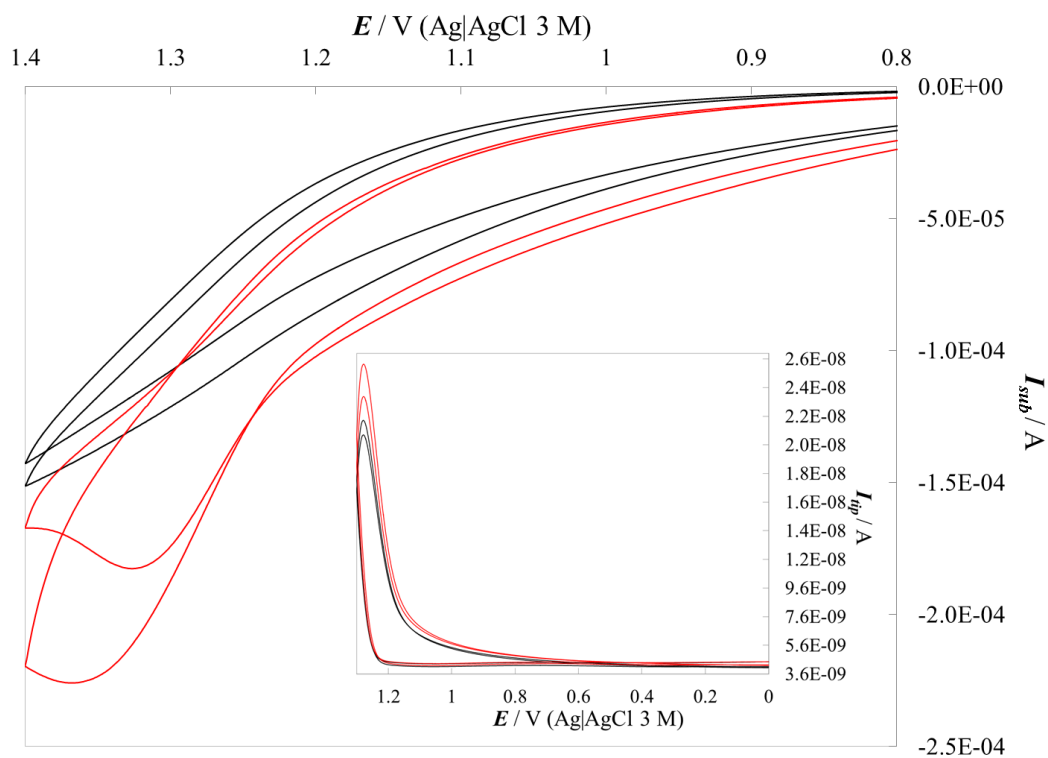


Figure 88: Cyclic voltammograms of TiO_2 nanoparticles / Nafion[®] 50:1 in NaOH 0.1 M in the dark (black line) and under white light (red line). Insert: tip current at $E_{tip} = 0.1$ V (RHE). Scan rate: 20 mV s^{-1} .

As we can see, the higher nanoparticles/Nafion[®] ratio, the higher the difference between dark and light, i.e photocurrent.

The tip responses are comparable to those of the samples.

However, when the white light was chopped, no differences between dark and light were evident.

Figure 89 shows the trend of the TiO₂ photocurrent with respect to the different nanoparticles loading at different applied potentials:

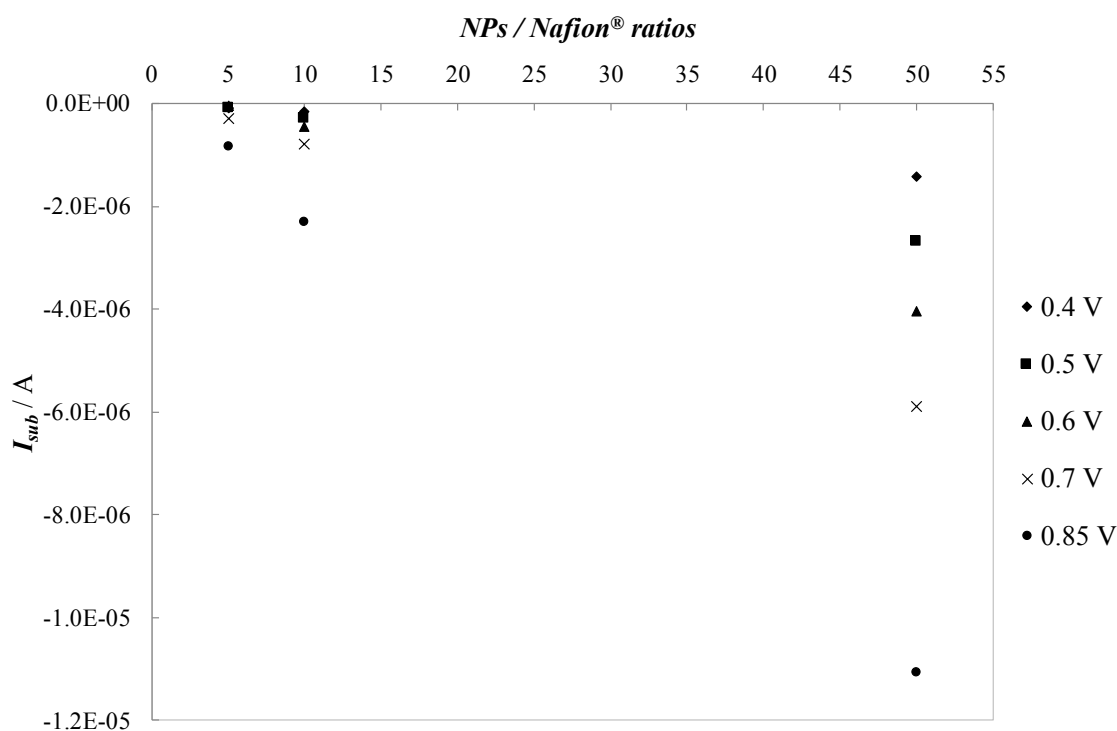


Figure 89: TiO₂ photocurrent with respect to the different nanoparticles loading at different applied potentials.

Figure 89 evidences that photocurrents recorded at different potentials and different nanoparticles / Nafion[®] show linearity in the considered loading range.

1.3.4 Nanoparticles annealed at 500 °C

In order to enhance the too-low photoactivity of the synthesized nanoparticles, different activation strategies were adopted: the first provided the annealing of the samples at 500 °C (after a 5 °C/min ramp) for 3 h in air. With this approach it was possible to enhance the crystallinity of the materials and reduce the contact resistance.

Figure 90, Figure 91, Figure 92 and Figure 93 shows the cyclic voltammeteries of substrate and tip carried out both in the dark and under white light irradiation of all the samples:

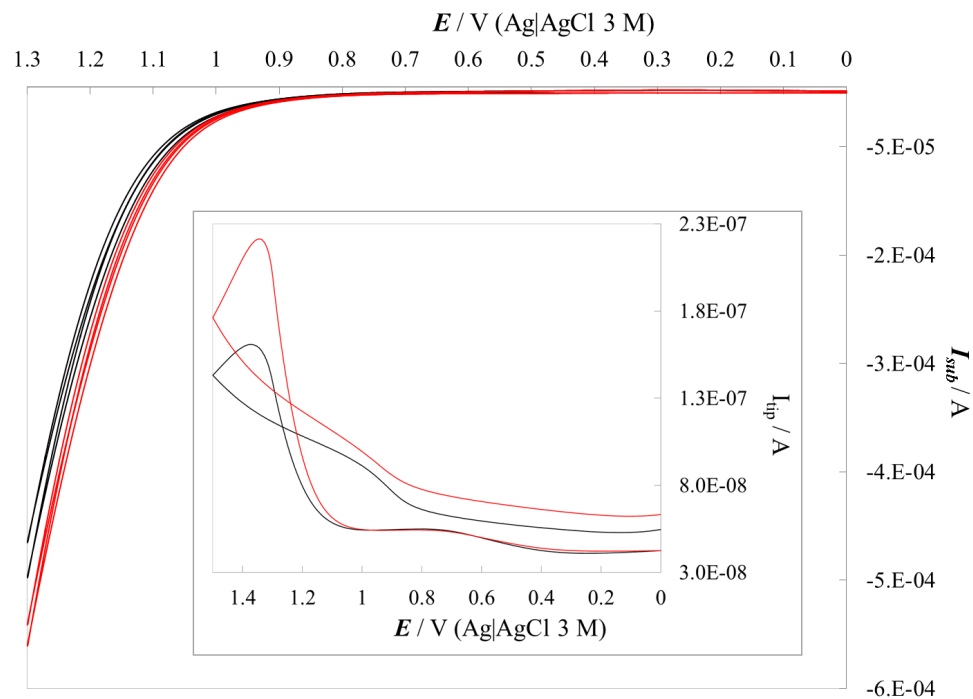


Figure 90: Cyclic voltammeteries of annealed BiVO₄ nanoparticles in NaOH 0.1 M in the dark (black line) and under white light (red line). Insert: tip current at $E_{\text{tip}} = 0.1 \text{ V}$ (RHE). Scan rate: 20 mV s^{-1} .

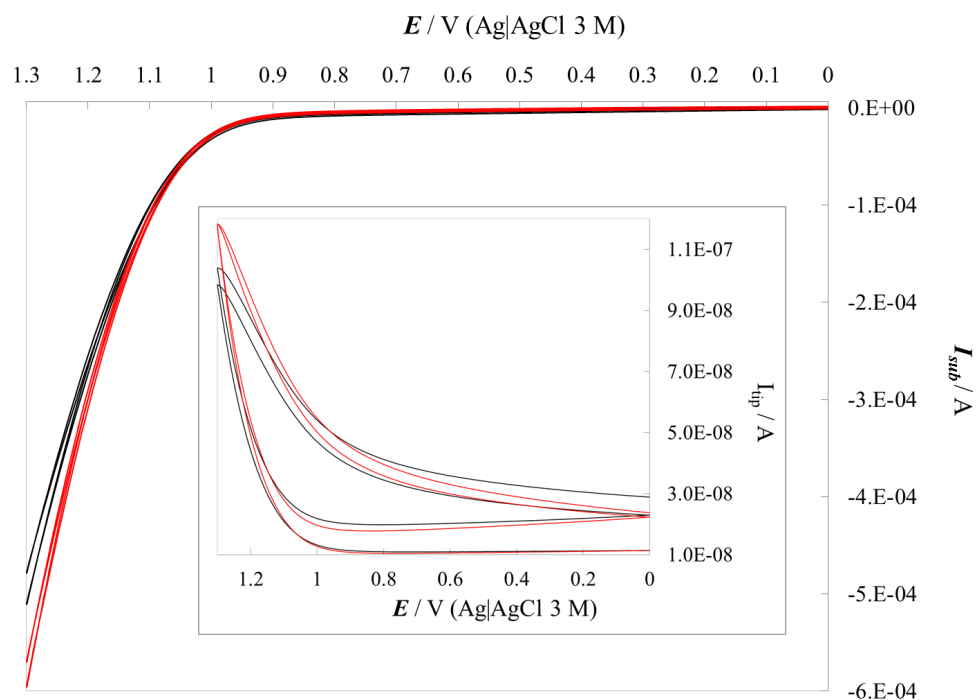


Figure 91: Cyclic voltammeteries of annealed TiO_2 nanoparticles in NaOH 0.1 M in the dark (black line) and under white light (red line). Insert: tip current at $E_{tip} = 0.1$ V (RHE). Scan rate: 20 mV s^{-1} .

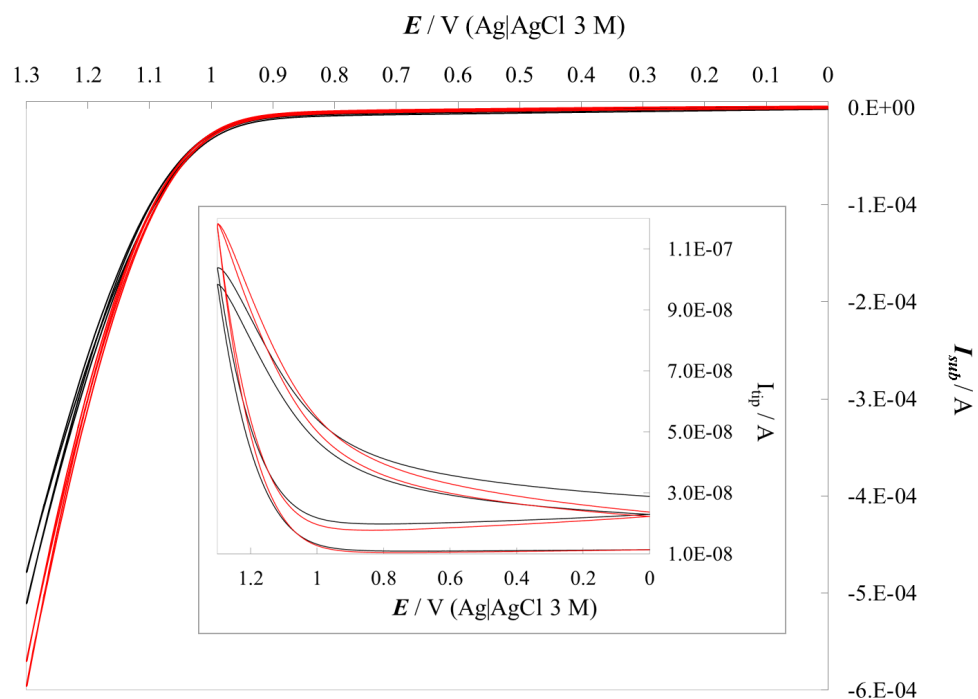


Figure 92: Cyclic voltammeteries of annealed most concentrated WO_3 nanoparticles in NaOH 0.1 M in the dark (black line) and under white light (red line). Insert: tip current at $E_{tip} = 0.1$ V (RHE). Scan rate: 20 mV s^{-1} .

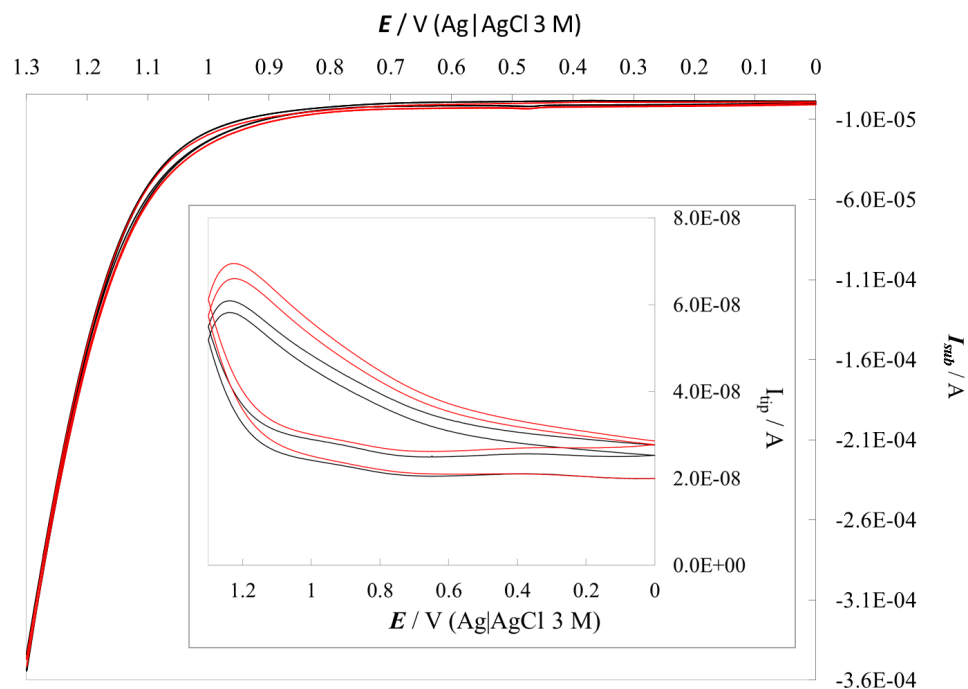


Figure 93: Cyclic voltammeteries of annealed most diluted WO_3 nanoparticles in NaOH 0.1 M in the dark (black line) and under white light (red line). Insert: tip current at $E_{tip} = 0.1$ V (RHE). Scan rate: 20 mV s^{-1} .

As we can see, all the semiconductors show a higher photocurrent under light irradiation after the activation, but the most diluted WO_3 nanoparticles.

On the contrary, the tip currents confirms the photoactivity of all the four materials. Unfortunately, no samples showed a lower onset oxygen evolution potential.

After that, the same samples were tested under chopped light, as shown in **Figure 94**.

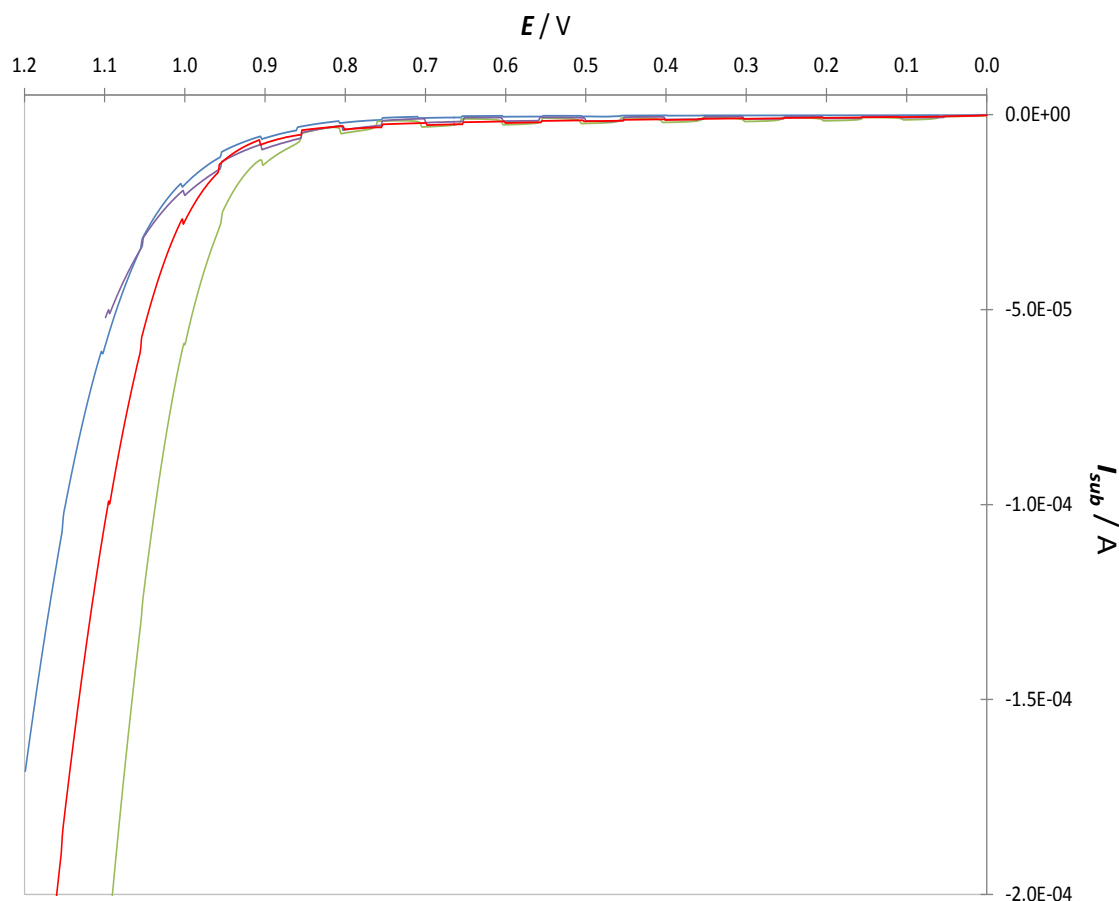


Figure 94: Cyclic voltammeteries under OER conditions of BiVO₄ (blue line), TiO₂ (red line), concentrated WO₃ (green line) and diluted WO₃ (purple line) nanoparticles in NaOH 0.1 M under chopped white light. Scan rate: 20 mV s⁻¹.

As we can see, all the samples show the same photoactivity under chopped white light. On the contrary, the OER onset potentials changes: BiVO₄ (blue line) and diluted WO₃ (purple line) have the same higher onset potential, while the TiO₂ (red line) cathodically shifts it of ≈ 50 mV. Finally, the concentrated WO₃ (green line) shows the lowest onset potential, ≈ 100 mV before BiVO₄ and diluted WO₃ and ≈ 50 mV before TiO₂.

Figure 95 shows the behaviour of the tip under the same conditions, with $E_{tip} = 1$ V (RHE).

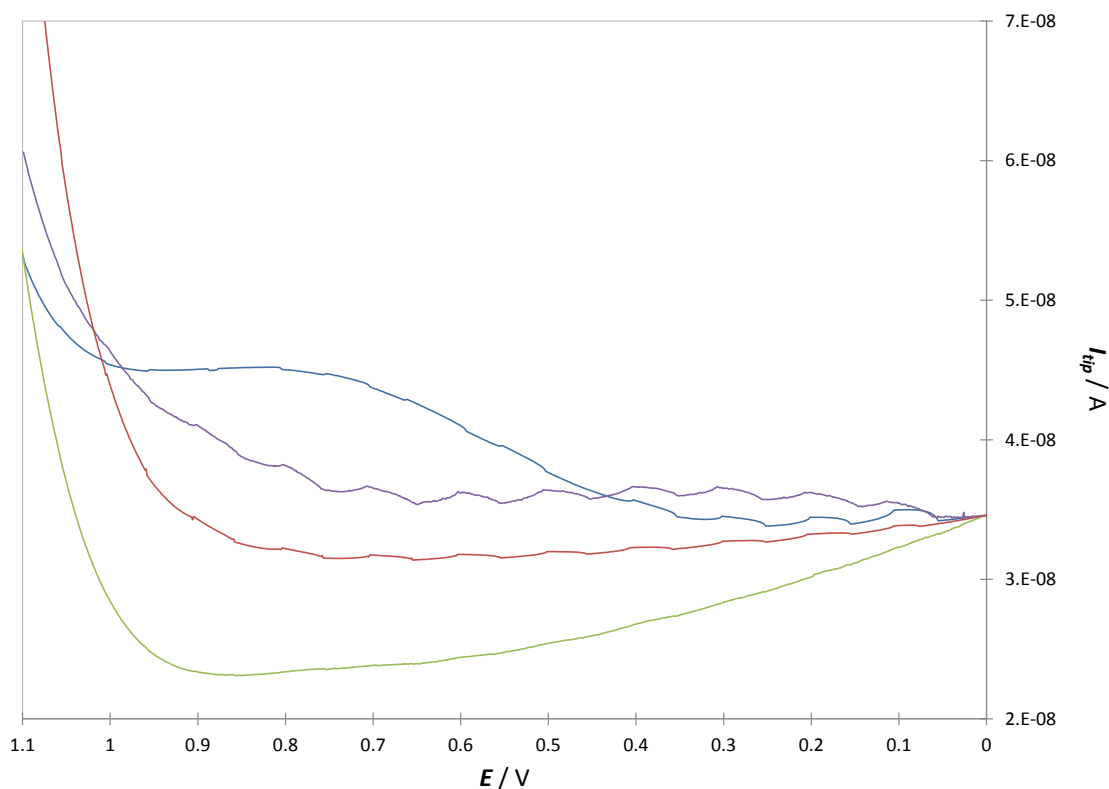


Figure 95: Tip cyclic voltammeteries under OER conditions of BiVO₄ (blue line), TiO₂ (red line), concentrated WO₃ (green line) and diluted WO₃ (purple line) nanoparticles in NaOH 0.1 M under chopped light. Scan rate: 20 mV s⁻¹.

The tip currents show quite different results with respect to the substrate: first of all, the semiconductors don't have the same photoactivity, but are completely different. The most active is the diluted WO₃ (purple line), followed by TiO₂ (red line). On the contrary, concentrated WO₃ (green line) and BiVO₄ (blue line) don't have any photoactivity.

This means that the photocurrents shown by the substrates, are not probably related to the actual photoactivity of the materials, but to other parallel reactions (photodegradation of the nanoparticles, presence of some impurities, etc.). Only the diluted WO₃ can be considered actually photoactive.

1.3.5 Hydrogen activation

The second strategy adopted to enhance the semiconductors photoactivity is to activate them with hydrogen. Indeed, several paper recently focused on the chemical or electrochemical reduction of the TiO₂, creating new defects in the material responsible of the increase of the photoactivity under visible light [15].

In this case, the attention was focused onto commercial and homemade TiO₂ nanoparticles and two activation ways were followed: according to the first, 100 μ l of previously sonicated TiO₂ nanoparticles were deposited on cleaned FTO by drop-casting and then activated by annealing the sample at 500 °C under a flux of H₂ and Ar (5% of H₂).

The second way provided the activation of the TiO₂ nanoparticles by keeping the sample biased at a hydrogen evolution potential for 30 minutes.

Two different suspensions of commercial TiO₂ nanoparticles were prepared, with two different concentrations: 0.1 M and 1 mM.

Figure 96 shows the cyclic voltammeteries of the commercially available TiO₂ 0.1 M suspension tested both in the dark and under white light illumination (chopped or not), after the activation by annealing it at 500 °C under a flux of H₂ and Ar (5% of H₂):

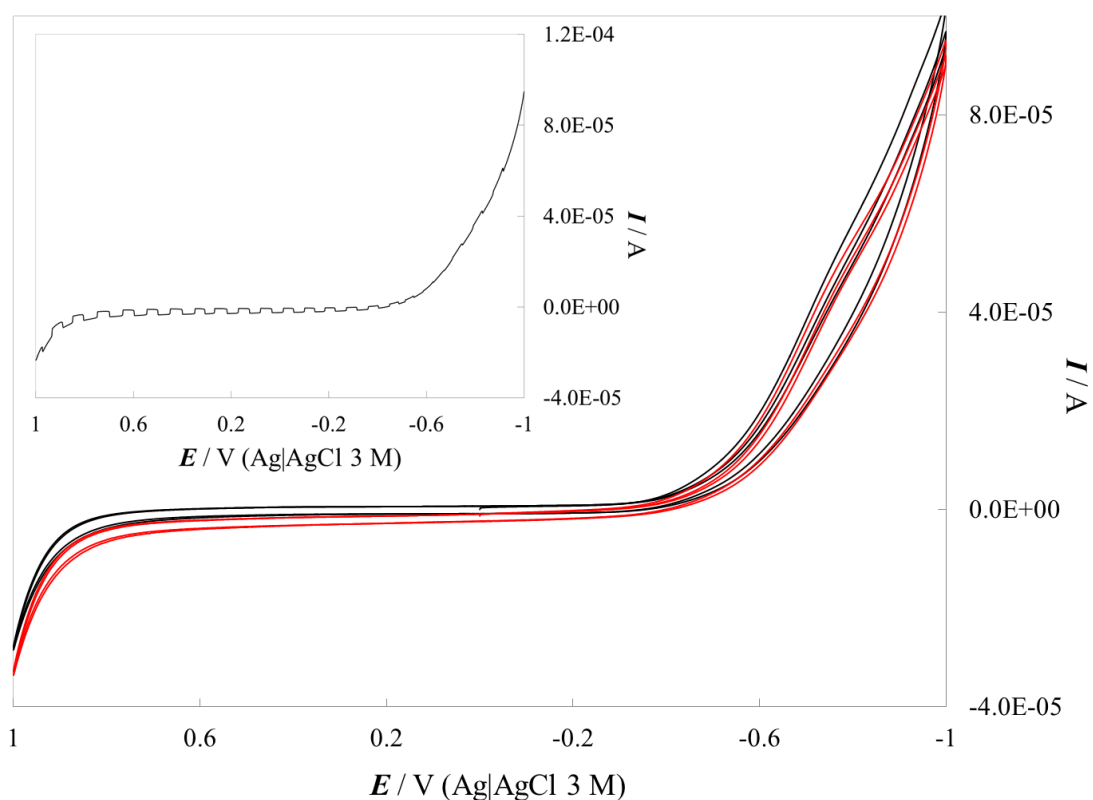


Figure 96: Cyclic voltammeteries of a commercially available TiO₂ 0.1 M sample in the dark and under white light irradiation in NaOH 0.1 M. Inset: tip current under chopped light. Scan rate: 20 mV s⁻¹.

As we can see, there is a substantial difference between dark and light when the light was chopped, meaning that the activation was efficient.

Also the tip current was higher when the substrate is irradiated, and this was due to the higher amount of oxygen produced by the sample under light.

Figure 97 shows the results obtained for the commercial TiO_2 1 mM suspension, prepared and tested as the previous sample:

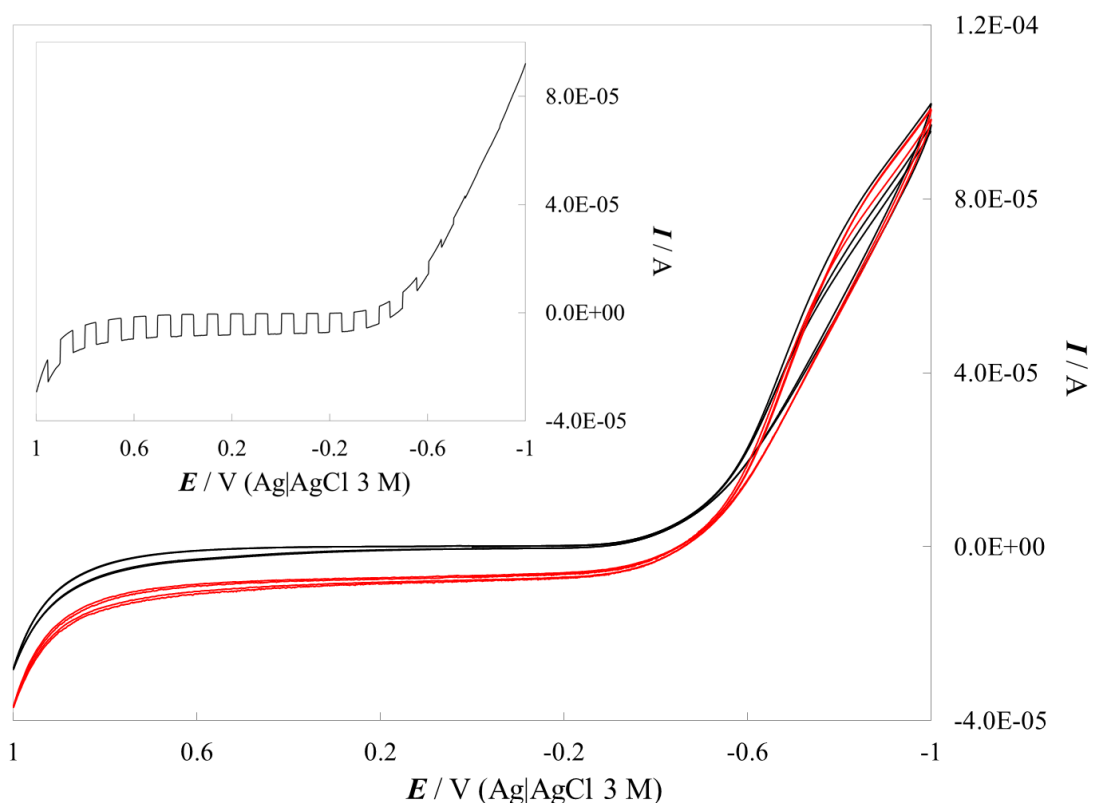


Figure 97: Cyclic voltammeteries of a commercially available TiO_2 1 mM sample in the dark (black line) and under white light irradiation (red light) in NaOH 0.1 M. Insert: tip current under chopped light. Scan rate: 20 mV s^{-1} .

As we can see, the photoactivity resulted to be higher even though the concentration was two orders of magnitude lower.

Also in this case, as for the 0.1 M TiO_2 suspension, the tip current was higher when the substrate was irradiated, meaning that higher amount of oxygen produced by the sample was higher under light.

In the end, the same experiment was carried out on the synthesized TiO_2 nanoparticles. **Figure 98** shows the cyclic voltammeteries of this sample in the dark and under white light irradiation (both chopped or not), after the activation in hydrogen.

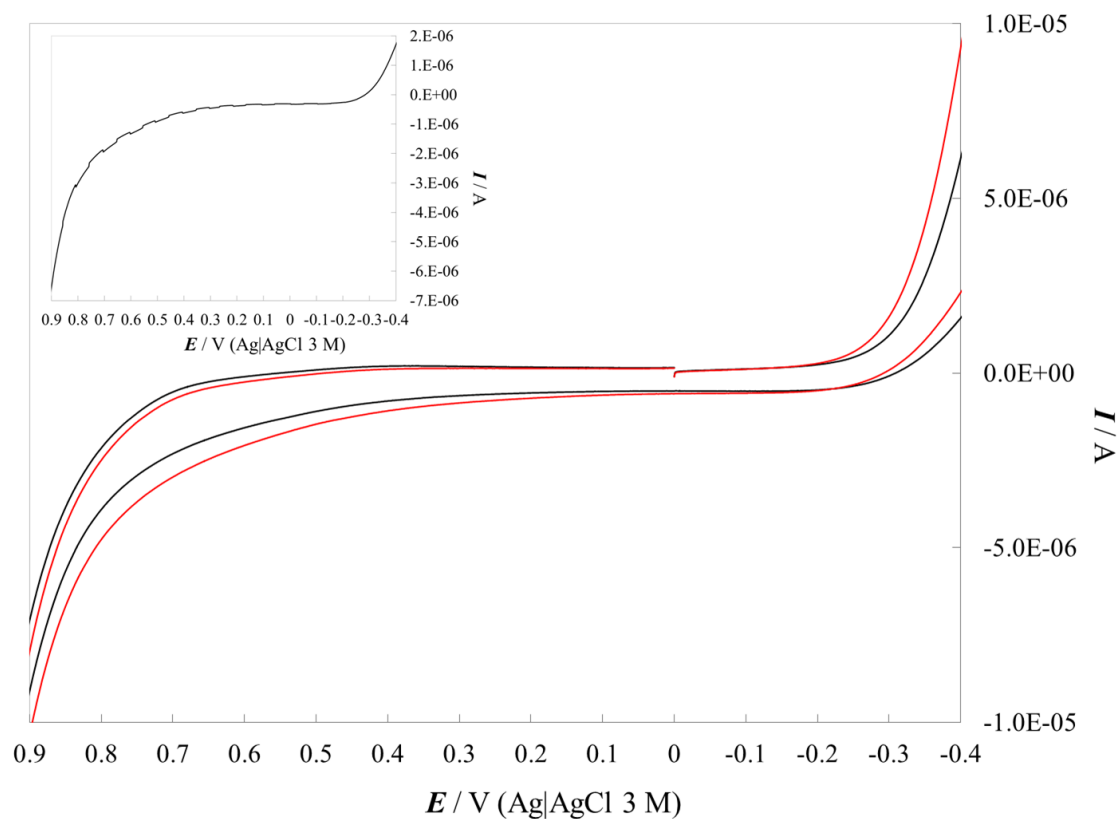


Figure 98: Cyclic voltammeteries of a homemade TiO₂ sample in the dark (black line) and under white light irradiation (red light) in NaOH 0.1 M. Insert: tip current under chopped light. Scan rate: 20 mV s⁻¹.

As we can see, the difference between dark and light when the light was chopped was very low and not clearly visible.

Nevertheless, even with this sample the tip current was monitored (**Figure 99**):

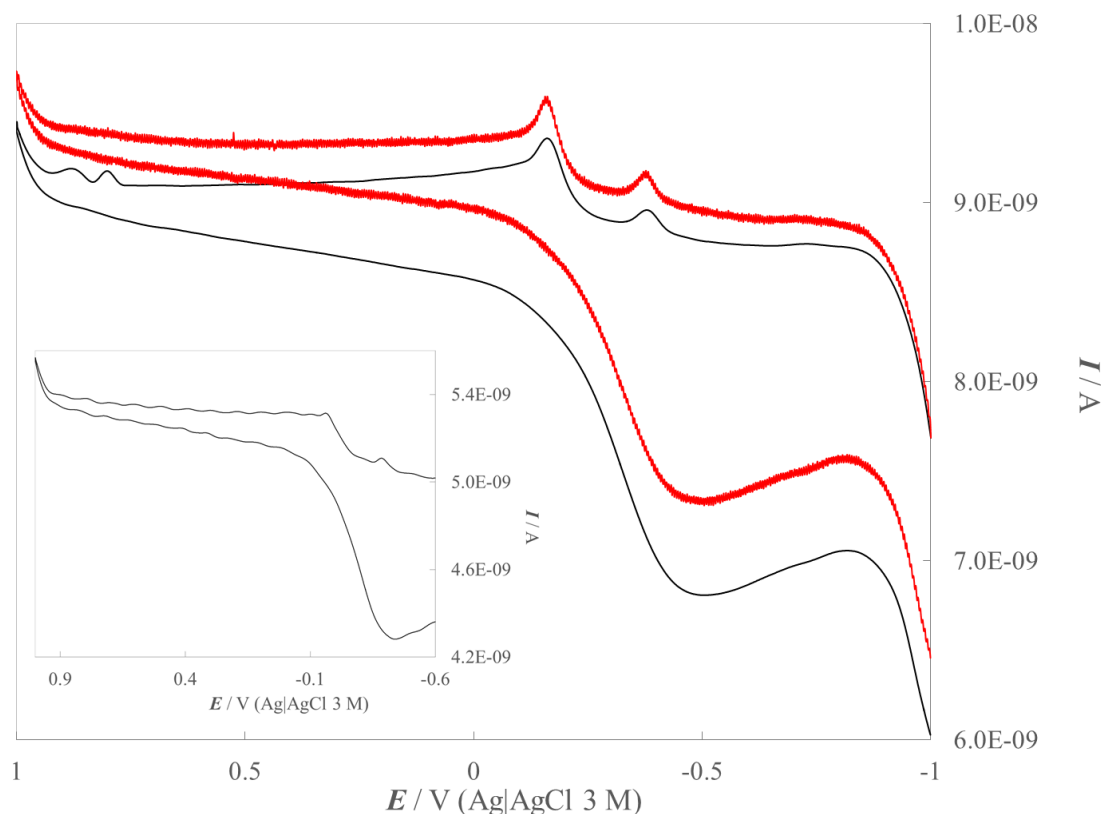


Figure 99: Tip cyclic voltammeteries of a homemade TiO_2 sample in the dark (black line) and under white light irradiation (red light) in NaOH 0.1 M. Insert: tip current under chopped light. Scan rate: 20 mV s^{-1} .

Here, a higher, even if small, difference between dark and light is evident, meaning that an amount of oxygen, even if small, was produced.

The tip shows some peaks between 0 V and 0.5 V (Ag|AgCl 3 M) probably due to the presence of small impurities.

Finally, an electrochemical activation was applied: 100 μl of TiO_2 nanoparticles were deposited on cleaned FTO by drop casting and activated by keeping the sample biased at a hydrogen evolution potential, $E_{\text{HER}} = 0 \text{ V}$ (RHE), for 30 minutes.

In this case, in order to promote a correct adhesion of the nanoparticles to the FTO, the Nafion[®] solution was added with a ratio of nanoparticles suspension/ Nafion[®] 50:1.

Also this kind of activation was applied to two different suspensions of commercial TiO_2 nanoparticles, 0.1 M and 1 mM, and to the homemade ones.

Figure 100 shows the cyclic voltammeteries of the sample in the dark and under white light irradiation, before the electrochemical activation:

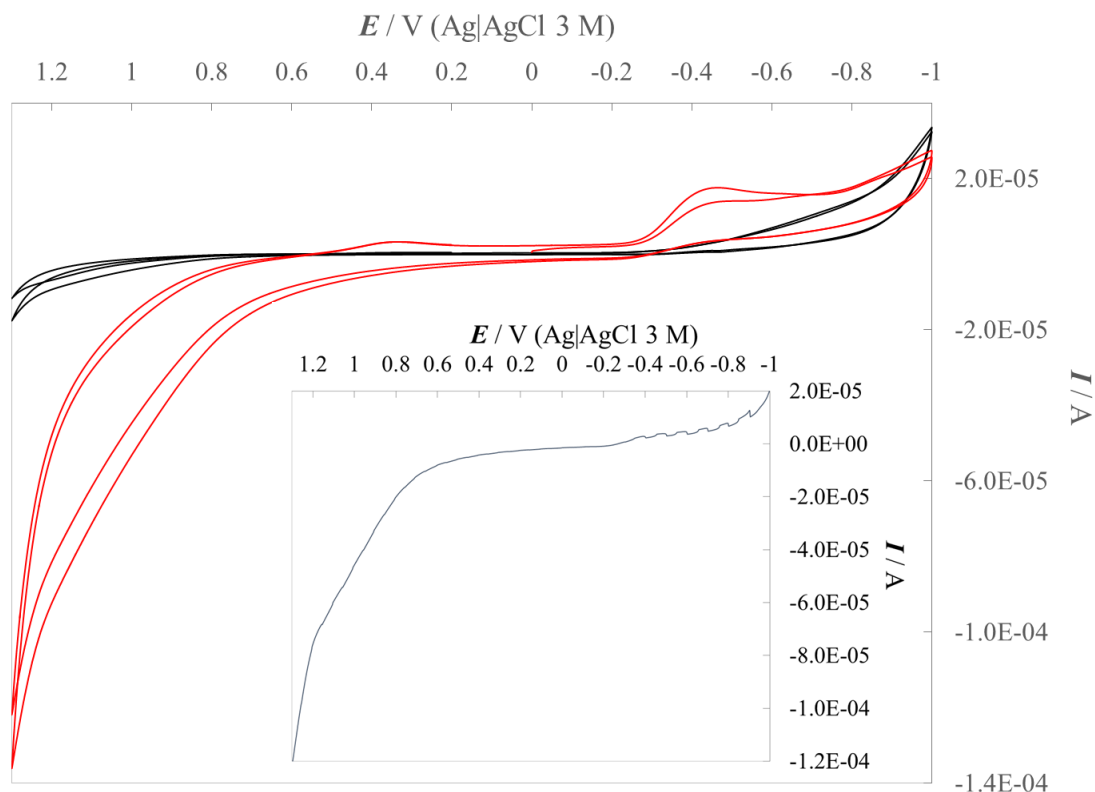


Figure 100: Cyclic voltammeteries of a commercially available TiO_2 0.1 M / Nafion[®] 1:50 sample in the dark (black line) and under white light (red line) in NaOH 0.1 M. Insert: tip current under chopped light. Scan rate: 20 mV s^{-1} .

As we can see, there is a huge difference between dark and light, but this photoactivity is not clearly evident chopping the light.

Only between -0.9 V and -0.1 V (Ag|AgCl 3 M) a small difference is visible.

Then, the sample were activated by applying some chronoamperometries at a fixed hydrogen evolution potential, $E_{HER} = 0 \text{ V (RHE)}$.

Figure 101 shows the comparison between the cyclic voltammeteries carried out both in the dark and under white light irradiation before and after 30 minutes hydrogen evolution potential activation and the same cyclic voltammeteries recorded while chopping the light:

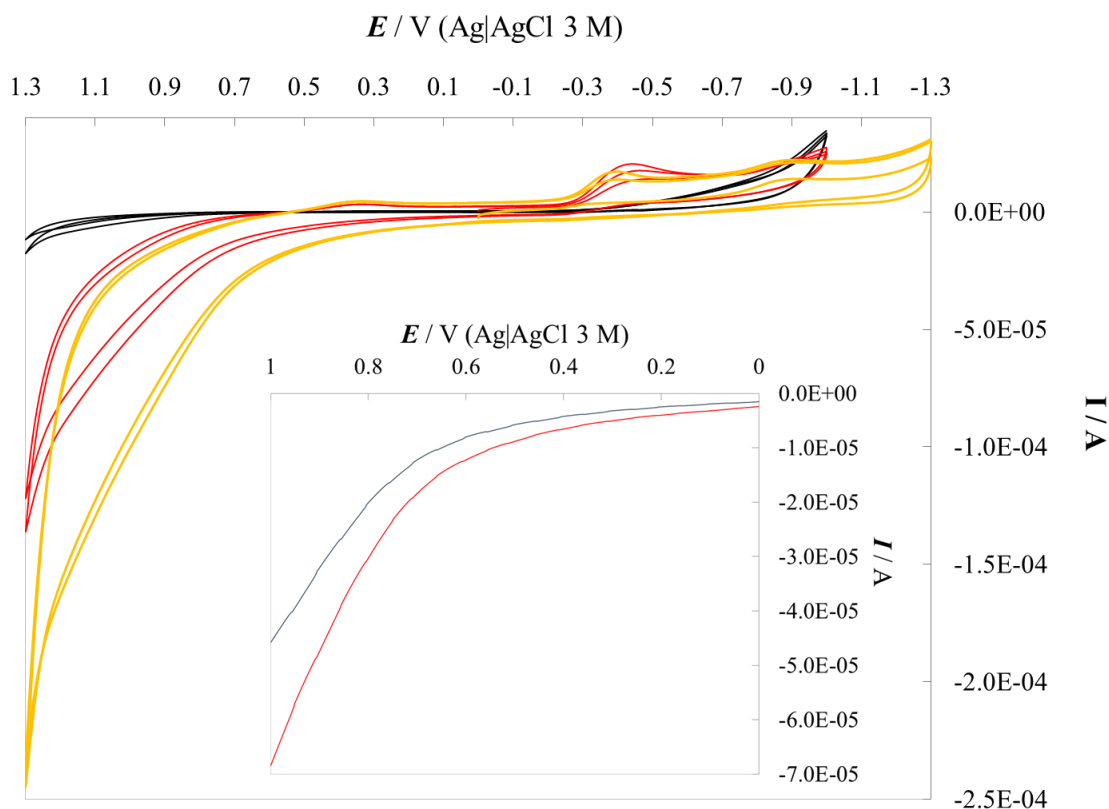


Figure 101: Cyclic voltammeteries of a commercial TiO_2 0.1 M / Nafion[®] 1:50 sample in the dark (black line) and under white light irradiation before the activation (red line) and under light after 30 minutes activation (yellow line). Insert: cyclic voltammetry under chopped white light before (blue line) and after (red line) activation. All the experiments were carried out in NaOH 0.1 M. Scan rate: 20mV s^{-1} .

As we can see, the photocurrents are clearly enhanced after a 30 minutes activation. However, when the light was chopped the difference between dark and light was negligible.

The same experiments were carried out with a sample of commercially available TiO_2 nanoparticles 1 mM / Nafion[®] 50:1.

Figure 102 shows cyclic voltammeteries of the sample in the dark and under white light irradiation, before the electrochemical activation, while **Figure 103** shows the comparison between the cyclic voltammeteries obtained before and after 30 minutes activation, both in the dark and under light:

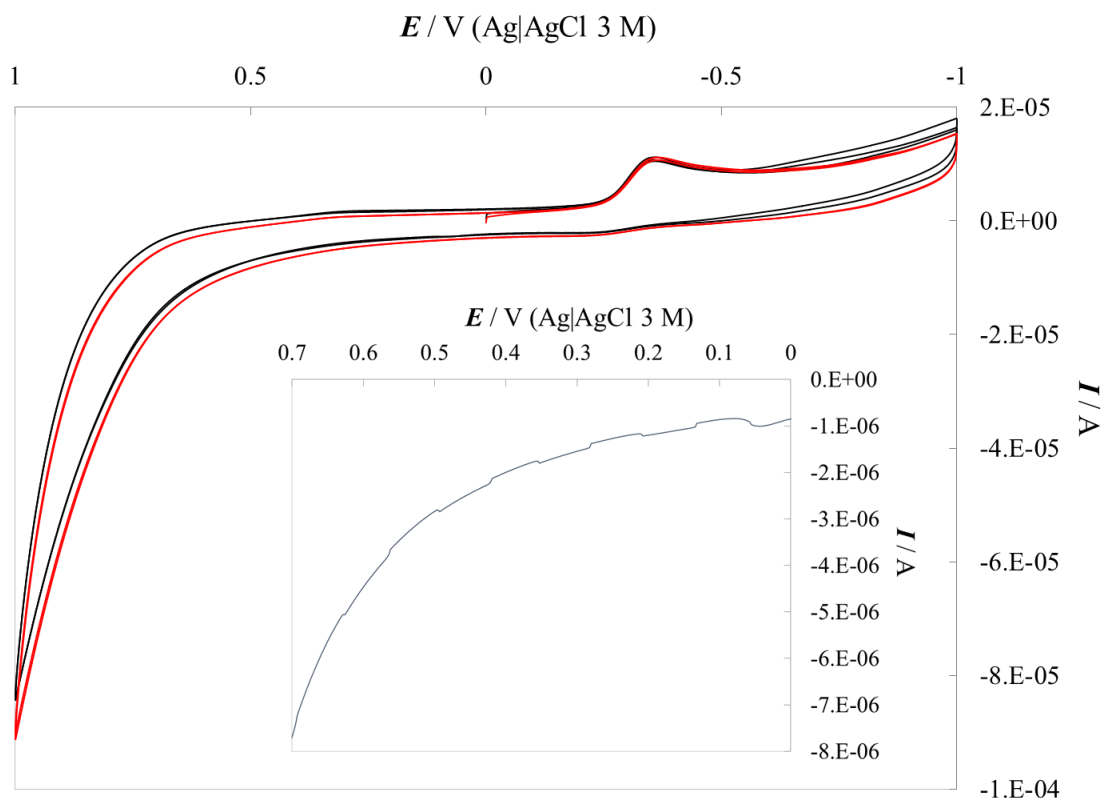


Figure 102: Cyclic voltammeteries of a commercially available TiO_2 1 mM / Nafion[®] 1:50 sample in the dark (black line) and under white light irradiation (red light) in NaOH 0.1 M. Insert: tip current under chopped light. Scan rate: 20 mV s^{-1} .

As we can see in **Figure 102**, there is a small difference between dark and light. When the light was chopped, the difference between dark and light was evident, even if poor.

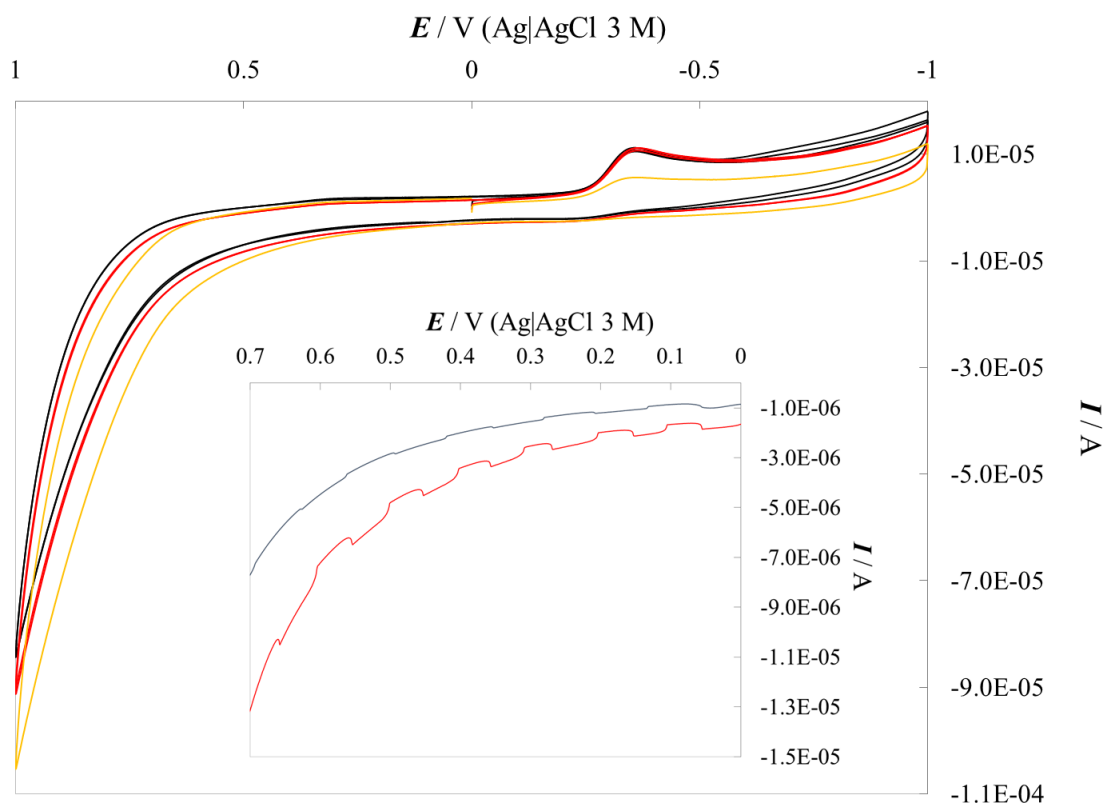


Figure 103: Cyclic voltammeteries of a commercial TiO₂ 1 mM / Nafion[®] 1:50 sample in the dark (black line) and under white light irradiation before the activation (red light) and under light after 30 minutes activation (yellow line). Insert: cyclic voltammetry under chopped white light before (blue line) and after (red line) activation. All the experiments were carried out in NaOH 0.1 M. Scan rate: 20mV s⁻¹.

On the contrary, according to **Figure 103** the photocurrent was enhanced after 30 minutes activation. Also under chopped light the effect of illumination is clearly evident, meaning that the electrochemical activation actually enhanced the photocurrents of the substrate.

Finally, the same tests were repeated with the TiO₂ homemade nanoparticles / Nafion[®] 50:1.

In **Errore. L'origine riferimento non è stata trovata.** are shown the results of the same experiment previously explained:

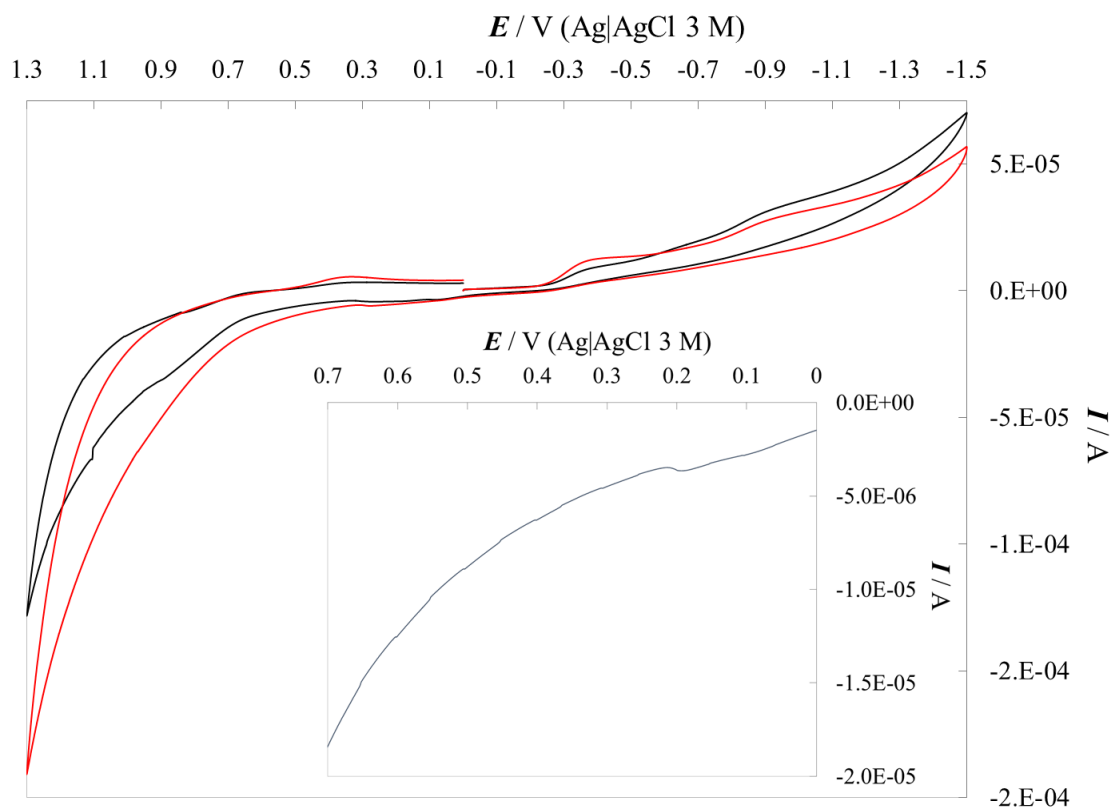


Figure 104: Cyclic voltammeteries of TiO₂ nanoparticles / Nafion[®] 1:50 sample in the dark (black line) and under white light irradiation (red light) in NaOH 0.1 M. Insert: tip current under chopped light. Scan rate: 20 mV s⁻¹.

As we can see, there is a clearly evident difference between dark and light, but this photoactivity is not visible when the light was chopped, exactly as for the other samples.

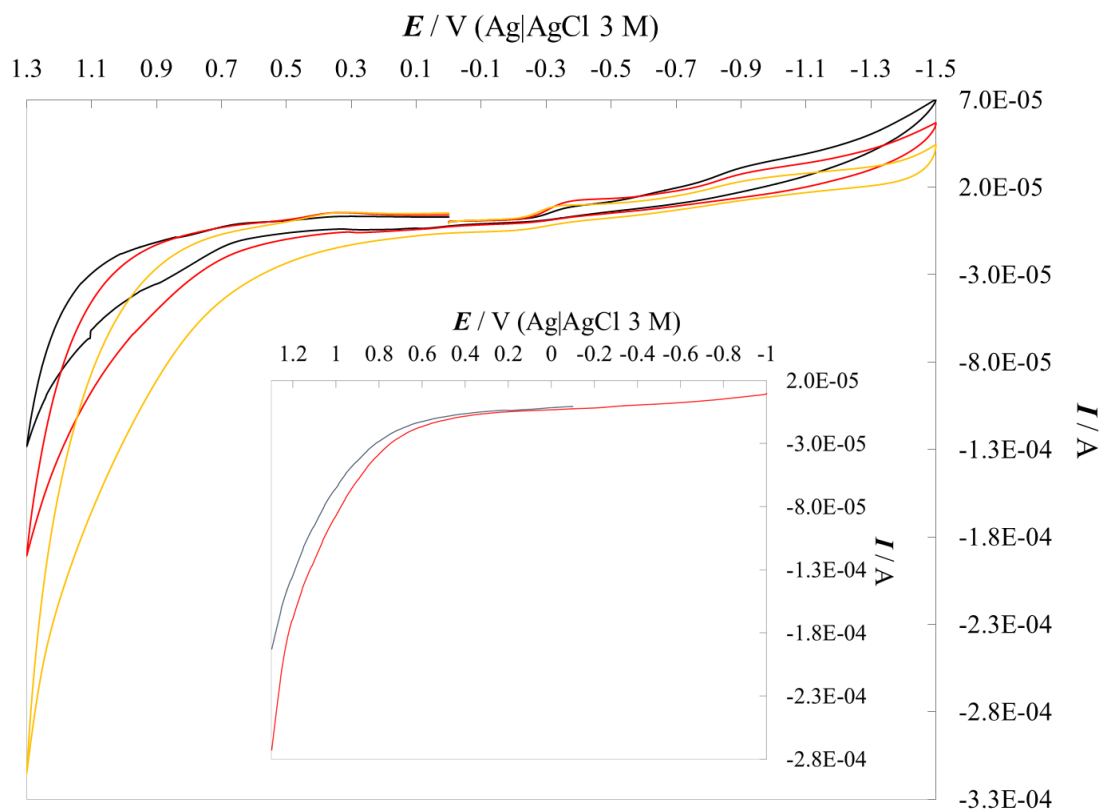


Figure 105: Cyclic voltammeteries of TiO_2 nanoparticles / Nafion[®] 1:50 sample in the dark (black line) and under white light irradiation before the activation (red line) and under light after 30 minutes activation (yellow line). Insert: cyclic voltammetry under chopped white light before (blue line) and after (red line) activation. All the experiments were carried out in NaOH 0.1 M. Scan rate: 20mV s^{-1} .

As we can see, the photocurrent clearly enhanced after 30 minutes activation (yellow line). However, when the light was chopped no difference in the dark and under light is evident, meaning that this nanoparticles were not active not even after the electrochemical activation.

3.4. Conclusions

The use of an innovative method based on the cathodic corrosion has been presented as facile synthesis way of metal oxide nano- and microparticles. In particular, TiO_2 , BiVO_4 and hydrated WO_3 nanoparticles have been synthesized.

Despite the simple preparation route, the obtained particles photoactivity towards the photoelectrochemical oxidation of water in NaOH 0.1 M was determined.

Composites of these particles were also covered by Nafion[®], in order to enhance their adhesion to the current collector.

Interesting photoanodic responses upon illumination with both UV and Visible light have been obtained for most of the semiconductors, even if lower with respect to commercially available materials.

However, this synthesis method is very innovative and promising.

4. The cavity-microelectrode (C-ME) as a tip for SECM

*Based on the published paper: S. Morandi, A. Minguzzi, *The cavity-microelectrode as a tip for scanning electrochemical microscopy*, *Electrochem. Comm.*, 59, 2015, 100-103

4.1 Introduction

As already explained in the *Experimental Section*, the most typical SECM configuration provides the use of a disk microelectrode, the tip, positioned in the solution in parallel to the sample of interest, the substrate. The tip can be moved in three dimensions thanks to the use of stepper or piezoelectric motors.

Unfortunately, several factors limit the possibilities of the SECM:

1. The preparation of tips is time consuming and handmade;
2. The nature of the metal wires useful to build tips is limited to a few metals (Au, Pt, Ag...) and carbon fibers;
3. Tips need to be cleaned before each use.

The limitation in the nature of the metal wires is the most important drawback in many fields. To give a few examples, in the screening of oxygen reduction reaction catalysts most researches adopted Au tips to locally produce oxygen at a constant rate while the tip screens the catalysts libraries [¹⁶]. However, Au dissolves under oxygen evolution reaction (OER) conditions and the catalyst library likely covers with a layer of Au, modifying the materials features.

In another case, a Mn tip was desired but Mn wires are not commercially available.

This is why a more versatile version of tip is needed [¹⁷].

The Cavity-microelectrode (C-ME) is an optimal tool in this sense. It consists in a micrometer-sized empty cylinder with glass walls and metallic bottom and can be easily and quickly filled with any powder.

C-MEs present the following advantages:

1. They are easily prepared;
2. They are low-cost tools;
3. Their geometric parameters (radius and depth) can be accurately determined;

4. Due to their small dimensions, they contain only a small amount of powder (typically $10^{-7} - 10^{-8}$ g).
5. The effect of ohmic drops on electrochemical signals is minimized;
6. They don't need gluing agents (for example polymers) for the adhesion of the material onto the support;
7. The contribution of the microdisk at the base of the cavity is negligible since its surface area is at least two order of magnitude lower than the one of the amount of powder;
8. The used powder can be replaced with a new amount and this allows to have a "fresh" electrode.

Cycles of CME filling/emptying with the same powder lead to highly reproducible results [18].

For these reason, C-MEs have been used in the last years to study materials in a wide range of applications: catalysts, batteries, enzymes, supercapacitors and so on [19].

Recently, the possibilities of C-MEs have been widened by showing that they can easily lead to quantitative analysis [20], for quantitative rapid screening [18] and for fine electrochemical characterization [21] thanks to the knowledge of the amount of material inserted in the cavity.

C-MEs are typically prepared by recessing a metallic microdisk. The most commonly used materials are Pt, that is etched by hot aqua regia and Au, that can be etched by electrochemical dissolution in Cl^- or CN^- baths. The quality of C-ME geometry is improved using Au and the electrochemical dissolution that guarantees the dissolution kinetics.

In turn, Au C-MEs led to a more precise and accurate quantitative analysis [22] and allowed electrochemical noise measurements on oxygen evolution reaction electrocatalysts [23]. Very recently, double barrel C-MEs have been used to contain a catalyst sample and a reference one to precisely compare water oxidation onset potentials [24]. About the use of cavity-microelectrodes in SECM, Bard's group has already shown the preparation and use of etched microelectrodes as support to create carbon paste SECM tips [25].

Therefore, this work aims to explore in more details the possible use of C-MEs as SECM tips to be used in different modes: *feedback*, *tip generation/substrate collection* (TG/SG) and *substrate generation/tip collection* (SG/TC). The possibility of

conveniently studying parallel reactions occurring at a desired powder electrode material is also here introduced.

4.2 Experimental

All chemicals were used as received. Aqueous solutions were prepared with water from a Millipore purification system. All the experiments cited were performed at room temperature.

4.2.1 C-MEs preparation

C-MEs were realized starting from a UME.

The recess was obtained using a potentiostat/galvanostat CHI 633d (CH Instruments, Austin, Texas) following the procedure reported in literature (16): a galvanostatic square wave current profile (double step, DS) between +1.5 and -7 mA cm^{-2} was applied to the tip in aqueous NaCl 0.5 M + HCl 0.5 M + H₂SO₄ 0.5 M. The anodic step lasted twice than the cathodic one and the cycle frequency was 0.00028 s^{-1} .

After the etching, the cavity bottom was homogenized by cycling its potential (500 cycles at 500 mV s^{-1}) in the same solution between 0 and 1.1 V (Ag|AgCl in 3 M KCl).

After the etching, the depth of the recess, l , was determined, as described in the literature [20,22,26], from the steady state limiting current obtained changing the potential between 1.011 V and 1.461 V (RHE) at 2 mV s^{-1} in Fc(MeOH), according to the following equation:

$$l = \frac{4\pi n F c D r^2}{4I_l} - \frac{\pi r}{4}$$

Where:

n = number of electrons = 1;

F = Faraday constant = 96485 C mol^{-1} ;

D = Fc(MeOH) diffusion coefficient = $7.10 \cdot 10^{-6} \text{ cm}^2 \text{ s}^{-1}$;

c = electrolyte concentration;

r = radius (previously determined on the original UME).

In the case of the C-ME tips presented in this Section, $l = 25.3 \text{ }\mu\text{m}$ and $l = 60.0 \text{ }\mu\text{m}$ (**Figure 106**):

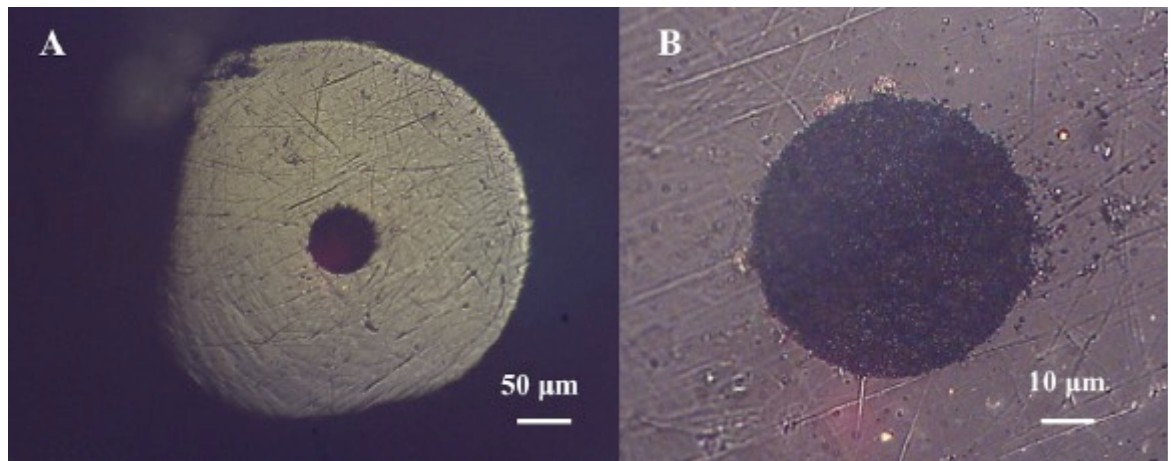


Figure 106: Optical images of a 25 μm radius Au cavity-microelectrode filled with Pt/C at two different magnitudes.

The cavity was then filled with the desired material by using the former as a pestle and then cleaning the glass surface from the powder excess with a piece of paper.

From **Figure 106** we can note that the cavity filling does not extend beyond the cavity edge and this is likely at the bases of the filling reproducibility [21]. Observing the tip at the microscope after each filling guarantees that the powder does not protrude from the cavity.

At the end of each experiment, cavity is emptied by keeping the electrode in an ultrasound bath and then dried in an oven at 80 °C.

4.3 Result and discussion

4.3.1 Feedback mode

To evaluate if a C-ME could be used as probe for SECM technique, the electrode should fulfil the expected behaviour of positive/negative *feedback* approach curves.

Therefore, a C-ME tip was filled with Vulcan[®] XC72R (Cabot), immersed in a KClO₄ 0.1 M aqueous solution containing Fc(MeOH) 1 mM and approached it towards a substrate, consisting in a Pt disk (exposed area = 0.196 cm²) embedded into Teflon[®].

In this case the potential applied to the C-ME was $E_{tip} = 0.4$ V (Ag|AgCl in KCl 3 M).

Figure 107A and **B** show the obtained experimental approach curves and compare them to the relevant fitting curves calculated using the conventional empirical equations [27]:

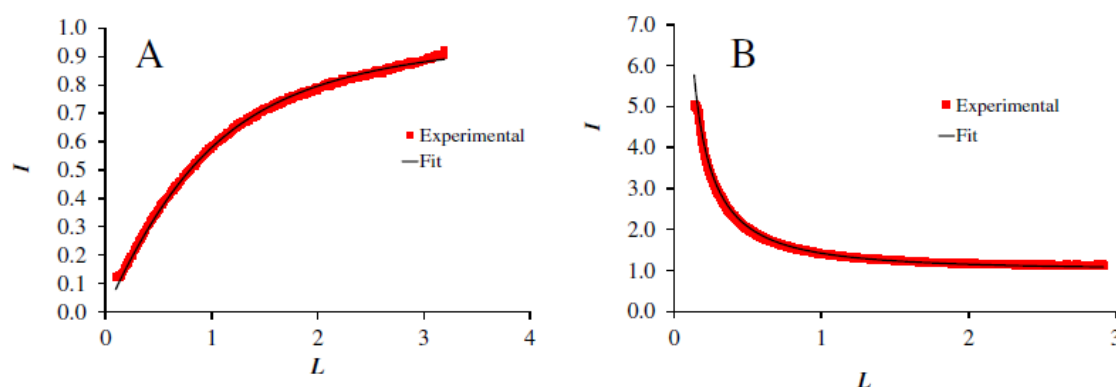


Figure 107: Approach curves of a C-ME tip filled with Vulcan[®] XC72R recorded in KClO₄ 0.1 M containing 1 mM Fc(MeOH) over a (A) plastic or (B) Pt substrate [28].

As deeply explained in the *Experimental Section*, the good correspondence of experimental and theoretical curves suggests that C-ME tips can be used in SECM for positioning and feedback experiments.

However, this is possible until tip and substrate reactions are controlled by mass transport. Indeed, after an initial period in which thin layer diffusion within the layer sums to planar/semi-infinite one, the reagent within the porous media is consumed, and the porous bed behaves like a planar electrode (following Cottrell equation). Thus, the electroactive species reacts exclusively at the outer surface of the tip, as a conventional SECM disk electrode.

The same behaviour is confirmed even changing the C-ME filling with another sufficiently high conductivity material like Co_3O_4 (Sigma Aldrich, $\sigma=10^{-3}\text{--}10^{-4} \Omega^{-1} \text{cm}^{-1}$ [29]).

Indeed, a feedback image was recorded at the Pt/ Teflon[®] boundary in Fc(MeOH) as shown in **Figure 108**:

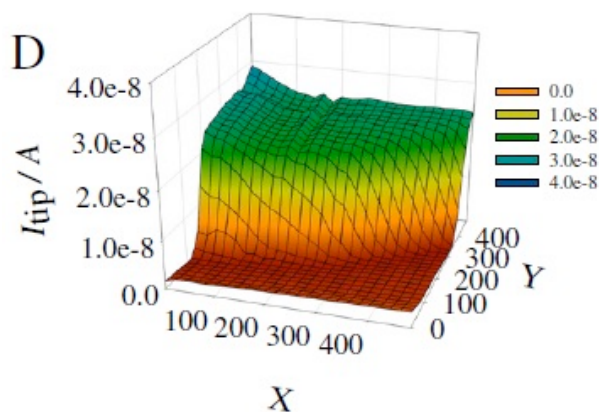


Figure 108: 3D SECM image recorded with the C-ME filled with Co_3O_4 recorded in KClO_4 0.1 M containing Fc(MeOH) 1 mM over a Pt/ Teflon[®] substrate [28].

As we can see, the conductive area (Pt, green) and the insulating one (plastics, red) are clearly recognisable, confirming that C-ME can be used as tip in one of the most conventional SECM experiments: a *feedback* image.

The choice of Co_3O_4 comes also from the need of having a good oxygen evolving catalyst as will be discussed in the following.

On the other hand, in the case of charge transfer controlled reaction at the tip, the C-ME likely behaves as a three-dimensional electrode, with the reacting species allowed to partially penetrate inside the cavity. This implies that the empiric equations used to fit approach curves for diffusion controlled systems are no longer useful and a new empirical equation is needed, as shown in **Figure 109**.

This is the case of a tip (with $l = 60 \mu\text{m}$) filled with Co_3O_4 approached towards a Pt substrate in NaOH 0.1 M using dissolved oxygen as the redox mediator.

$$E_{tip} = -1.0 \text{ V (Ag|AgCl in KCl 3 M)}.$$

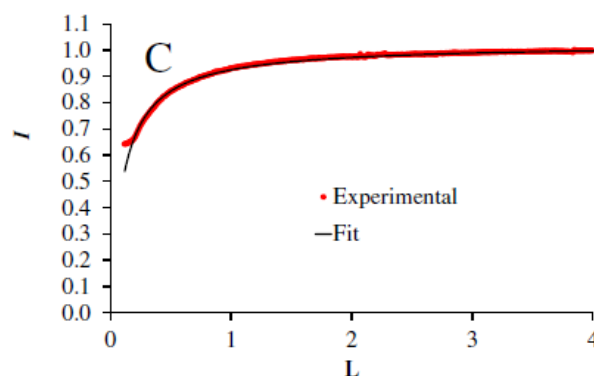


Figure 109: Approach curves of a C-ME tip filled with Co_3O_4 in NaOH 0.1 M towards a Pt substrate [28]

The approach curve shown in **Figure 109** could be fitted adopting the following empirical equation:

$$I = \frac{1}{AL + \frac{B}{L} + C}$$

where, for the specific case, $A = -1.168$, $B = 0.104$ and $C = -0.192$.

4.3.2 Stability of the C-ME

To study the stability of the C-MEs, an electrode was filled with Co_3O_4 and tested under oxygen evolution reaction (OER) conditions.

Co_3O_4 was chosen since it is a well-known catalyst towards water oxidation in alkaline media [30].

The C-ME tip was thus immersed in aqueous NaOH 0.1 M and biased at constant potentials ranging from 1.3 to 1.7 V (RHE) for 60 s.

Figure 110 reports the resulting Tafel plot:

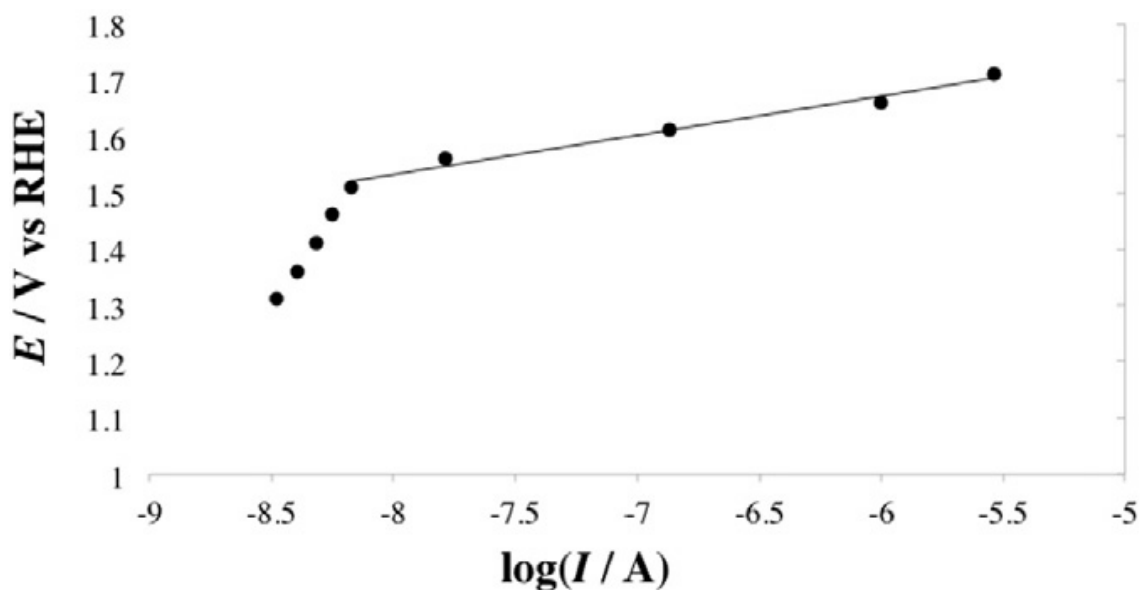


Figure 110: Tafel plot for the OER recorded on a C-ME tip filled with Co_3O_4 in NaOH 0.1 M [28].

As we can see, the presence of two charge transfer phenomena is clearly deductible: the first one is probably due to the formation of Au hydroxides/oxides or of Co(IV) sites, but proceeds at negligible rates with respect to the second one, that is in turn related to water oxidation.

This is confirmed by both the Tafel line slope (69.4 mV/dec) and the onset potential value (1.5 V), completely compatible with water oxidation on Co_3O_4 as studied on more conventional supports [29,30].

Moreover, the stability of the C-ME tip is confirmed.

4.3.3 Current efficiency evaluation

C-ME can be conveniently used also as tip for quantify the relative rates of parallel reactions. This is very interesting when dispersed electrode/photoelectrode material are under study.

Thus, a C-ME tip was filled with Co_3O_4 and linear scan voltammetries (LSV) were recorded at 2 mV s^{-1} in NaOH 0.1 M solution, saturated with N_2 . In this experiment the tip potential was varied between -0.9 and -1.3 V (RHE), while and the substrate, consisting in a 2 mm diameter Pt disk was kept at $E_{\text{sub}} = -0.4$ V (RHE).

Under these conditions, two possible parallel reactions occur at the tip: on one side the reduction of water to H_2 and on the other side the Co_3O_4 or oxygen reduction[31].

At the same time, the substrate re-oxidizes the hydrogen produced at the tip.

Before the LSV, the tip-substrate distance was set at $\approx 10 \mu\text{m}$ through approach curves, as previously explained.

Figure 111 reports the tip current as recorded, while the substrate one is firstly multiplied by -1 , then the value red at -0.9 V (RHE) was subtracted:

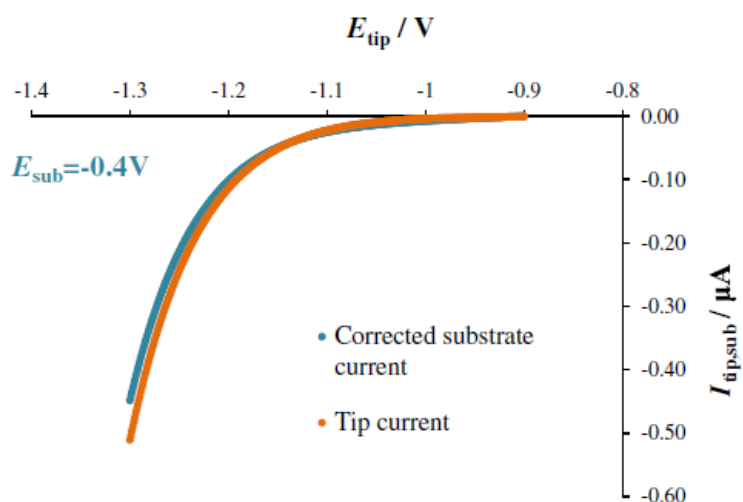


Figure 111: TG/SC experiment with a C-ME tip filled with Co_3O_4 in N_2 saturated aqueous NaOH 0.1 M. Tip-to-substrate distance is $10 \mu\text{m}$.

The comparison of tip and substrate currents shown in Figure 111 highlights that the current efficiency for hydrogen evolution is about 90%.

At the same time, it demonstrates that C-ME can be used as tip for SECM also to study the kinetics of electrode reactions (even parallel ones) on any desired conductive powder.

4.4 Conclusion

In conclusion, we here demonstrate that cavity-microelectrodes (C-MEs) can be effectively used as tip for SECM thus allowing the use of any finely dispersed material. This type of microelectrode allows the most common modes of SECM including the *feedback* and *generation/collection* ones.

Moreover, for a specific combination of C-ME tip, powder and redox species, an empiric equation is easily derived.

It is thus possible to approach the tip and determine the tip-to-substrate distance also under this non-optimal setup, often required in SECM experiments that are not carried out in the presence of high kinetics redox mediators.

This in turn allows the use of this type of tip in a wide range of application of SECM, including the rapid screening of electrocatalysts and of photoelectrode materials. In addition, the C-ME tip can be used for the study of parallel electrochemical reactions occurring at any finely dispersed electrode materials of interest.

5. Hematite/NiOOH architecture

*Based on the published paper: F. Malara, A. Minguzzi, M. Marelli, S. Morandi, R. Psaro, V. Dal Santo, A. Naldoni, *α -Fe₂O₃/NiOOH: An Effective Heterostructure for Photoelectrochemical Water Oxidation*, ACS catalysis, 5, 2015, 5292-5300

5.1. Introduction

As already explained in the *Introduction*, hematite is a very attractive semiconductor for water oxidation thanks to its high absorption of visible light, excellent stability in alkaline media, low cost, and high abundance of Fe [³², ³³].

However, its performance as a water-oxidizing photoanode shows several limits and needs a large overpotential to carry out oxygen production. Thus, several processes must be optimized.

Combining modifications in the morphology, able to enhance the photocurrents, and in the chemistry surface with the addition of a suitable overlayer, able to anticipate the onset potential, it is possible to obtain an ideal hematite photoanode.

Indeed, the deposition of an overlayer (e.g., IrO_x, Co-Pi, CoO_x) or a passivation layer (e.g., Al₂O₃, Ga₂O₃) often improves the photocurrent onset potential of hematite [³⁴, ³⁵, ³⁶, ³⁷, ³⁸].

In this part of the Thesis, a detailed study on the photoactivity of hematite photoanodes covered with an amorphous Ni-oxyhydroxide layer is presented.

As it is well-known, hydrous Ni-based electrocatalysts have shown very high activity toward OER [³⁹, ⁴⁰, ⁴¹, ⁴², ⁴³, ⁴⁴, ⁴⁵].

In order to study the effect of this amorphous NiOOH layer on the photoanode performance, the SECM was applied.

Indeed, the substrate photocurrents could be due not only to the actual activity of the semiconductor/overlayer architecture under light irradiation, but also to other parasite reaction.

On the contrary, with the SECM, it is possible to use a 25 μ m Au tip as an amperometric sensor for the local O₂ concentration, which is in turn proportional to the rate of O₂ production at the substrate, as explained in the *Experimental Section*.

For this reason, the use of SECM in the *substrate generation/tip collection (SG/TC)* mode was needed.

While the tip potential was kept fixed, a stair-step potential profile between a rest one, at which it cannot still evolve oxygen, and an oxygen evolution was applied to the substrate.

This approach allows a fine determination of the reaction onset [⁴⁶], ruling out any parasitic reaction (e.g., the oxidation of the electrode itself).

The experiments were repeated both in the dark and under solar simulation irradiation, on a bare hematite sample and one hematite/NiOOH photoelectrode.

5.2. Experimental

All chemicals were used as received. Aqueous solutions were prepared with water from a Millipore purification system. All the experiments cited were performed at room temperature.

5.2.1. Hematite/NiOOH preparation

The synthesis of hematite has been already described in the *Experimental Section*.

The amorphous NiOOH layer was synthesized through a photo-/electrodeposition procedure [⁴⁷]: hematite photoelectrodes were immersed in a Ni(NO₃)₂ 0.1 M solution with a pH 6.6 obtained by the addition of NaOH. The solution was then purged with nitrogen gas for 1 h.

The photodeposition was performed in a three-electrode cell, using a Ag/AgCl as reference electrode (RE) and Pt mesh as counter electrode (CE).

An open circuit voltage was applied to the sample and different photodeposition times were tested: 60, 300, 600, and 1200 s. The best results were obtained applying the potential for 600 s.

The photodeposition was followed by an electrodeposition at 1.2 V (Ag|AgCl 3 M) for 60 s.

The so obtained photoelectrodes were then characterized by SEM and TEM, as shown in **Figure 112**:

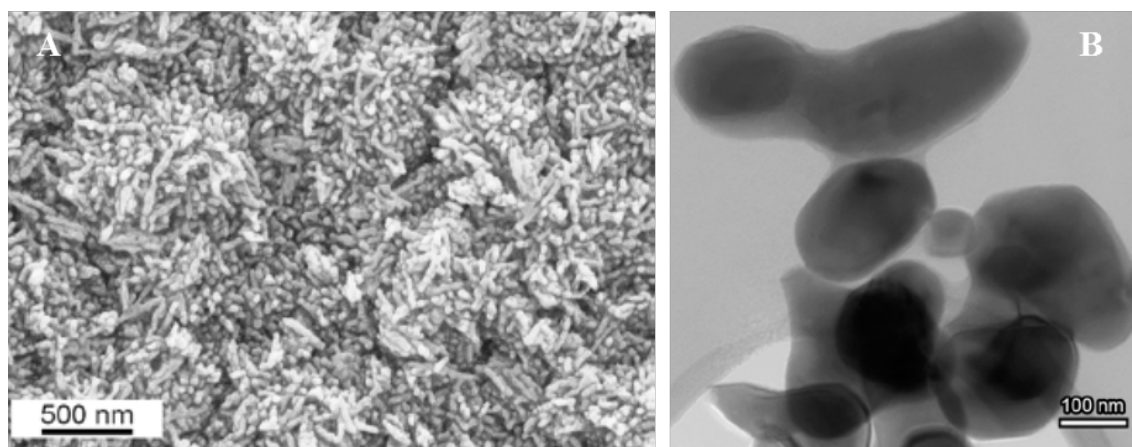


Figure 112: (A) SEM image of the hematite electrode; (B) TEM image of the coral-like hematite nanostructures, covered with an amorphous NiOOH layer.

As we can see from the SEM image, the FTO substrate is uniformly covered with small nanowires. From the TEM we can observe that the nanowires are in turn composed of nanocorals formed by interconnected crystalline globular grains.

Moreover, these nanocorals are clearly covered by a thin amorphous NiOOH layer of 1-2 nm.

5.2.2. Hematite/NiOOH characterization by SECM

SECM measurements were carried out using the CHI920C bipotentiostat (CH Instruments, Austin, Texas, USA). A 25 μm diameter Au tip was placed in its movable support, in order to be moved in the three dimensions X, Y, Z by stepper motors. A graphite tip and an Ag|AgCl (3 M KCl) electrodes were used as counter and reference electrodes respectively. To minimize the contamination with chlorine ions, the reference electrode was separated from the solution by a salt bridge consisting of a glass pipet filled with agar, containing aqueous KClO_4 0.1 M. The substrate was placed in a SECM Teflon[®] cell with an O-ring (exposed area: about 1 cm^2) and fixed onto a platform whose inclination is variable. The substrate contact was made thanks to a Cu plate.

The tip was approached at about 5 μm far from the sample. As already said, the tip-substrate distance was set performing negative feedback approach curves. These curves represent the tip current, i_t , as a function of d , tip-substrate distance, and are obtained when the tip is moved toward the substrate in the z direction.

All experiments were carried out in NaOH 1 M.

Figure 113 shows a scheme of the stair-step potential profile applied to the substrate:

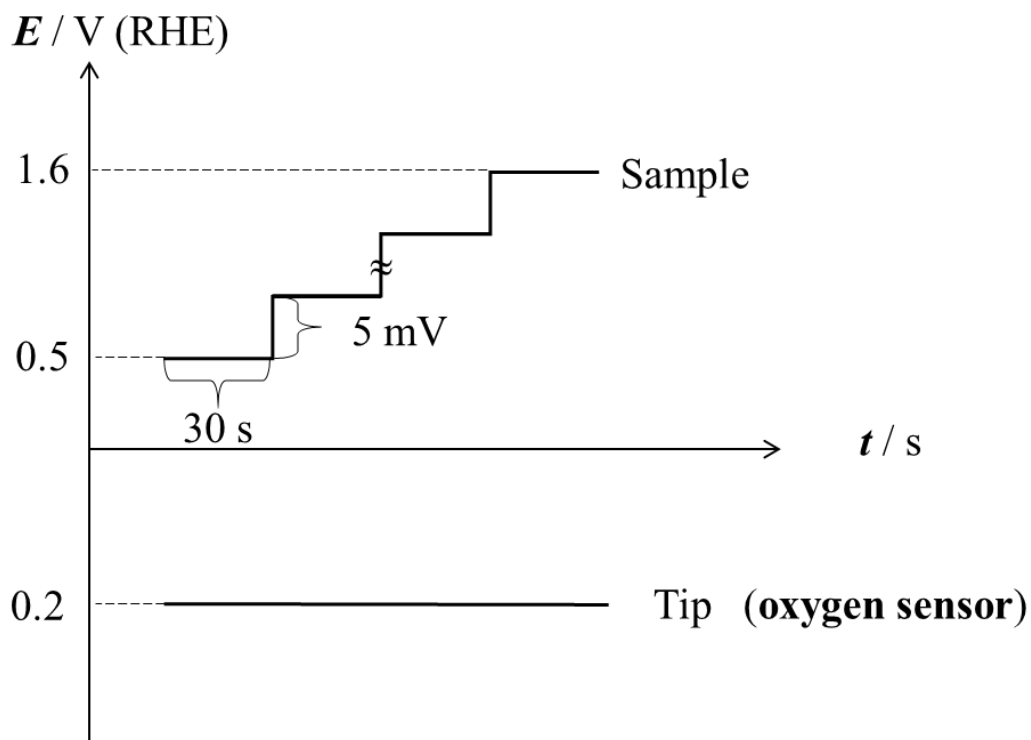


Figure 113: Pictorial scheme of a stair-step potential profile ($\Delta E = 5 \text{ mV}$; $\Delta t = 30 \text{ s}$) between 0.5 and 1.6 V (RHE) applied to the substrate. $E_{tip} = 0.2 \text{ V (RHE)}$.

As we can see in **Figure 113**, the substrate potential has been ranging from $E_{sub,in} = 0.5 \text{ V}$ and $E_{sub,fin} = 1.6 \text{ V (RHE)}$, with steps of 5 mV. Each step lasts 30 s.

At the same time, the tip acted as amperometric sensor, been biased at an oxygen reduction potential $E_{tip} = 0.2 \text{ V (RHE)}$, in order to reduce the oxygen produced by the substrate to water.

5.2.3. Tip preparation

The SECM tip was prepared following the procedure shown in the Experimental Part, using a 25 μm diameter Au wire as core material.

5.3. Result and discussion

As already said, a stair-step potential profile was applied to the substrate.

The potential ranged between $E_{sub,in} = 0.5$ V (RHE) and $E_{sub,fin} = 1.6$ V (RHE), with a potential step amplitude of $\Delta E = 5$ mV and a step duration of $\Delta t = 30$ s.

At the same time, the tip was kept at a constant ORR potential ($E_{tip} = 0.2$ V RHE), thus reducing all the oxygen produced by the substrate during these steps.

The procedure was applied both to a bare hematite and a hematite/NiOOH samples, in the dark and using a 300 W xenon arc lamp (calibrated at 100 mW/cm²) coupled to an AM 1.5 G filter as the light source.

Figure 114 shows the tip current recorded under these conditions:

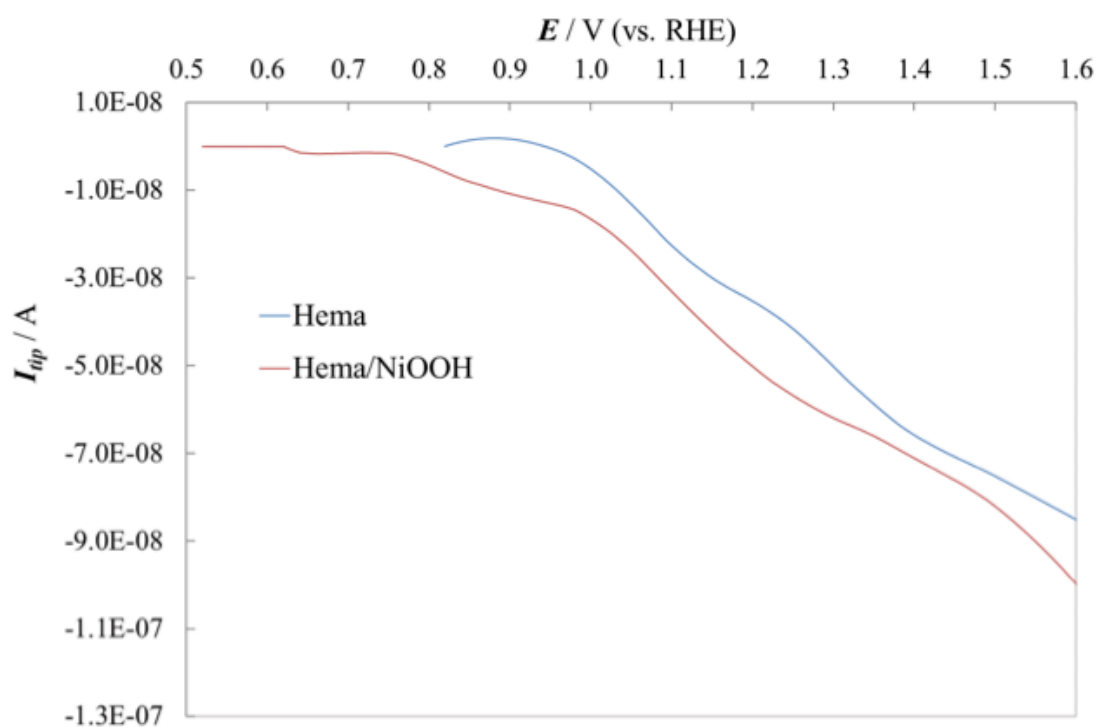


Figure 114: I_{tip} recorded when a stair-step potential profile is applied to a bare hematite and a hematite/NiOOH photoelectrodes under solar light irradiation. $E_{sub,in} = 0.5$ V (RHE); $E_{sub,fin} = 1.6$ V (RHE); $\Delta E = 5$ mV; $\Delta t = 30$ s; $E_{tip} = 0.2$ V RHE.

As we can see, comparing the tip current (I_{tip}) recorded for a pure hematite electrode and for a hematite/NiOOH electrode, it is clearly evident that the presence of the amorphous NiOOH layer led to a cathodic shift of the OER onset of about 150 mV, thus confirming the catalytic properties of this overlayer.

Moreover, its presence produces an enhancement in the hematite photocurrents, thus confirming the key role of an overlayer in the electron density of the photoanode, probably through the limitation of charge recombination phenomena.

This is another procedure useful to have reliable results about the actual activity of the material under interest. It is the most reliable method when a lab-scale electrode is tested, even if time-consuming, if compared to all the other procedures shown to decouple the actual production of oxygen to other parasite reactions.

For example, SECM images using a UME tip is useful to record inhomogeneities of the sample, or to rapidly screen spots of different materials, but it is affected by the overlapping of oxygen profiles. Moreover, SECM images are not useful when a lab-scale electrode is tested.

Another way to decouple the actual production of oxygen to other parasite reactions is the use of a C-ME as tip for SECM. It is indeed possible to fill the C-ME with the photoconverter powder, and then test it varying the tip potential and keeping the substrate one fixed, according to the TG/SC mode, in the dark and under light. The comparison of tip and substrate currents highlights the current efficiency. However, probably the light does not illuminate all the material inside the C-ME. Thus, only a small amount of semiconductor can actually work.

For this reason, the application of a stair-step potential profile applied to the substrate is the most reliable method in this context.

5.4. Conclusion

In conclusion, the optimized photo-/electrodeposition of NiOOH on hematite produced a 1–2 nm thick layer of amorphous overlayer.

The best performance was reached after 600 s of NiOOH photodeposition.

Moreover, SECM confirmed its unique features not only in the rapid screening of big libraries of materials, both deposited onto metal or semiconductor substrates, but also as suitable tool for the study of different architectures as lab-scale electrode.

Indeed, the use of a UME tip as amperometric sensor allows to properly record reliable results, ruling out parasite reaction.

Moreover, with this set-up, a fine determination of the OER onset potential is possible.

This approach was applied to one bare hematite and one hematite/NiOOH samples under solar simulation irradiation.

It was confirmed that in presence of the overlayer the OER onset potential anticipated of about 150 mV.

-
- [1] Minguzzi, A; Battistel, D.; Rodríguez-López, J.; Vertova, A.; Rondinini, S.; Bard, A.J.; Daniele, S. *J. Phys. Chem. C*, 119 (2015) 2941
- [2] Minguzzi, A.; Alpuche-Aviles, M.A.; Rodríguez-López, J.; Rondinini, S.; Bard, A. *J. Anal. Chem.*, 80 (2008) 4055
- [3] McCrory, C. C. L.; Jung, S.; Peters, J. C.; Jaramillo, T. F. *J. Am. Chem. Soc.*, 135 (2013) 16977
- [¹] Ye, H.; Park, H.S.; Bard, A.J. *J. Phys. Chem. C*, 115 (2011) 12464
- [4] Lee, J.; Ye, H.; Pan, S.; Bard, A.J. *Anal. Chem.*, 80 (2008) 7445
- [5] Yuan, D.; Xiao, L.; Jia, J.; Zhang, J.; Han, L.; Li, P.; Mao, B.; Zhan, D. *Anal. Chem.*, 86 (2014) 11972
- [6] Mandler, D, from Scanning Electrochemical Microscopy, edited by Bard, A.J. and Mirkin, M.V. (2001) 593
- [7] DOI: 10.1002/anie.201201999
- [8] Le Formal, F.; Tétreault, N.; Cornuz, M.; Moehl, T.; Grätzel M.; Sivula, K. *Chem. Sci.*, 2 (2011) 737
- [9] Zhang, C.; Fagan, R.D.; Smith, R.D.L.; Moore, S.A.; Berlinguette, C.P.; Trudel, S. *J. Mater. Chem. A*, 3 (2015) 756
- [10] Kim, J.Y.; Magesh, G.; Youn, D.H.; Jang, J.-W.; Kubota, J.; Domen, K.; Lee, J.S. *Sci. Rep.*, 3 (2013) 2681.
- [11] Sivula, K.; Zboril, R.; Le Formal, F.; Robert, R.; Weidenkaff, A.; Tucek, J.; Frydrych, J.; Grätzel, M. *J. Am. Chem. Soc.*, 132 (2010) 7436
- [12] Yamanaka, K. *Japanese Journal of Applied Physics* 28 (1989) 632
- [13] Rodriguez P. et al. *J. Am. Chem. Soc.* 133 (2011) 17626
- [14] Minguzzi, A.; Sánchez- Sánchez, C.M.; Gallo, A.; Montiel, V.; Rondinini, S. *ChemElectroChem* 1 (2014) 1415
- [15] Minguzzi, A.; Sánchez- Sánchez, C.M.; Gallo, A.; Montiel, V.; Rondinini, S. *ChemElectroChem* 1 (2014) 1415
- [16] Fernández, J.L.; Walsh, D.A.; Bard, A.J. *J. Am. Chem. Soc.* 127 (2005) 357
- [17] Leonard, K.C.; Bard, A.J. *J. Am. Chem. Soc.* 135 (2013) 15890
- [18] Minguzzi, A.; Locatelli, C.; Cappelletti, G.; Bianchi, C.L.; Vertova, A.; Ardizzone, S. et al., *J. Mater. Chem.* 22 (2012) 8896
- [19] Cachet-Vivier, C.; Keddad, M.; Vivier, V.; Yu, L.T. *J. Electroanal. Chem.* 688 (2013) 12
- [20] Locatelli, C.; Minguzzi, A.; Vertova, A.; Cava, P.; Rondinini, S. *Anal. Chem.* 83 (2011) 2819

-
- [21] Minguzzi, A.; Locatelli, C.; Cappelletti, G.; Scavini, M.; Vertova, A.; Ghigna, P. et al *J. Phys. Chem. A* 116 (2012) 6497
- [22] Minguzzi, A.; Locatelli, C.; Lugaresi, O.; Vertova, A.; Rondinini, S. *Electrochim. Acta* 114 (2013) 637
- [23] Rincón, R.A.; Battistel, A.; Ventosa, E.; Chen, X.; Nebel, M.; Schuhmann, W. *ChemSusChem* 8 (2015) 560
- [24] Botz, A.J.R.; Nebel, M.; Rincón, R.A.; Ventosa, E.; Schuhmann, W. *Electrochim. Acta*
- [25] Satpati, A.K.; Bard, A.J. *Anal. Chem.* 84 (2012) 9498
- [26] Zoski, C.G.; Aguilar, J.C.; Bard, A.J. *Anal. Chem.* 75 (2003) 2959
- [27] Sun, P.; Laforge, F.O.; Mirkin, M.V. *Phys. Chem. Chem. Phys.* 9 (2007) 802
- [28] Morandi, S.; Minguzzi, A. *Electrochem. Comm.* 59 (2015) 100
- [29] Singh, N.K.; Singh, J.P.; Singh, R.N. *Int. J. Hydrog. Energy* 27 (2002) 895
- [30] Minguzzi, A.; Fan, F.-R.F.; Vertova, A.; Rondinini, S.; Bard, A.J. *Chem. Sci.* 3 (2012) 217
- [31] Chivot, J.; Mendoza L.; Mansour C.; Pauporté T.; Cassir M.; *Corros. Sci.* 50 (2008) 62
- [32] Li, Z.; Luo, W.; Zhang, M.; Feng, J.; Zou, Z. *Energy Environ. Sci.*, 6 (2013) 347
- [33] Sivula, K.; Le Formal, F.; Grätzel, M. *ChemSusChem*, 4 (2011) 432
- [34] Barroso, M.; Mesa, C.A.; Pendlebury, S.R.; Cowan, A.J.; Hisatomi, T.; Sivula, K.; Grätzel, M.; Klug, D.R.; Durrant, J.R. *Proc. Natl. Acad. Sci. U. S. A.*, 109 (2012) 15640
- [35] Steier, L.; Herraiz-Cardona, I.; Gimenez, S.; Fabregat-Santiago, F.; Bisquert, J.; Tilley, S.D.; Grätzel, M. *Adv. Funct. Mater.*, 24 (2014) 7681
- [36] Le Formal, F.; Tétreault, N.; Cornuz, M.; Moehl, T.; Grätzel, M.; Sivula, K. *Chem. Sci.*, 2 (2011) 737
- [37] Tilley, S.D.; Cornuz, M.; Sivula, K.; Grätzel, M. *Angew. Chem.*, 49 (2010) 6405
- [38] Marelli, M.; Naldoni, A.; Minguzzi, A.; Allieta, M.; Virgili, T.; Scavia, G.; Recchia, S.; Psaro, R.; Dal Santo, V. *ACS Appl. Mater. Interfaces*, 6 (2014) 11997
- [39] Li, J.; Meng, F.; Suri, S.; Ding, W.; Huang, F.; Wu, N. *Chem. Comm.*, 48 (2012) 8213
- [40] Young, K.M.H.; Hamann, T.W. *Chem. Comm.*, 50 (2014) 8727
- [41] Gao, M.; Sheng, W.; Zhuang, Z.; Fang, Q.; Gu, S.; Jiang, J.; Yan, Y. *J. Am. Chem. Soc.*, 136 (2014) 7077
- [42] Smith, R.D.L.; Prévot, M.S.; Fagan, R.D.; Trudel, S.; Berlinguette, C.P. *J. Am. Chem. Soc.*, 135 (2013) 11580
- [43] Zhao, Z.; Wu, H.; He, H.; Xu, X.; Jin, Y. *Adv. Funct. Mater.*, 24 (2014) 4698
- [44] Louie, M.W.; Bell, A.T. *J. Am. Chem. Soc.*, 135 (2013) 12329

-
- [45] Trotochaud, L.; Ranney, J.K.; Williams, K.N.; Boettcher, S.W. *J. Am. Chem. Soc.*, 134, (2012) 17253
- [46] Maljusch, A.; Ventosa, E.; Rincón, R.A.; Bandarenka, A.S.; Schuhmann, W. *Electrochem. Comm.*, 38 (2014) 142
- [47] Kim, T.W.; Choi, K.-S. *Science*, 343 (2014) 990

Conclusions

The optimization of environmental protection and remediation and the better exploitation of renewable power sources undoubtedly represent the key issues to lead to the sustainable development of civil and industrial activities. In this context, hydrogen and electricity can be considered as the most promising and as the most adopted energy vector, respectively. The possibility of adopting the former depends on the availability of suitable devices to convert renewable energy into chemical energy. The production of H₂ from sunlight, by photoelectrochemical water splitting (PEC-WS), represents one of the most attractive processes giving the possibility of a direct use of sunlight to drive water splitting into molecular hydrogen and oxygen. Notwithstanding the strong interest for PEC-WS, its development on an industrial scale is hindered by the high costs of core materials and their inadequate efficiency and/or stability. In the last years, a lot of effort has been devoted to the study of different semiconductor/electrocatalyst combinations. In particular, recent studies highlighted the ability of electrocatalyst overlayers of inducing modifications in the semiconductor electron density or of storing the photogenerated holes, thus decreasing the probability of charge recombination. This greatly extends the possible candidates for photoelectrocatalysts and requires new efficient screening methods. In this context, scanning electrochemical microscopy (SECM) is an optimal tool for the rapid screening of big libraries of materials. Moreover, a part of the Thesis was devoted also to the study of suitable semiconductor, in order to develop a complete semiconductor/overlayer architecture.

A first part of the Thesis was devoted to the preliminary study of different materials as suitable OER electrocatalysts deposited onto Ti sheets.

They were both screened at the SECM, recording a classical SECM image, and studied by the application of the *double pulse method*.

After that, arrays of different materials composition were deposited onto a suitable photoanode. The one chosen for its low-cost and appropriate band-gap was hematite (α -Fe₂O₃).

At the end, almost 30 different compositions were screened and studied through the SECM using only four hematite samples. This confirms the usefulness of this tool when big libraries of different materials have to be tested.

The arrays were tested applying two different approaches: the first one provides the replacement of the ultramicroelectrode tip with a 200 μ m diameter white light optical fiber, that can locally

generate electron-hole pairs. The second approach provides the use of SECM in its classical set-up, using a 25 μm diameter Au tip as amperometric sensor and recording its current in the SG/TC mode. It is important to remember that the tip current is directly connected to the oxygen produced by the substrate. The experiments were repeated in the dark and under visible light, thanks to a 523 nm green LED.

The *double pulse method* has been applied to different spots and to the bare hematite, confirming a cathodic shift of the OER onset potential.

In order to confirm the SECM results, the most photoactive compositions according to it were selected and deposited onto hematite as lab-scale electrodes. They were then tested irradiating them with a solar simulator.

During my abroad period at the University of Illinois at Urbana-Champaign (UIUC), different photoanodes in the form of nanoparticles were studied. In particular, TiO_2 , BiVO_4 and hydrated WO_3 nanoparticles have been synthesized using of an innovative method based on the cathodic corrosion.

Interesting photoanodic responses upon illumination with both UV and Visible light have been obtained for most of the semiconductors, even if lower with respect to commercially available materials. However, this synthesis method is very innovative and promising, only needing an improvement.

In conclusion, we demonstrated that cavity-microelectrodes (C-MEs) can be effectively used as tip for SECM thus allowing the use of any finely dispersed material.

This allows the use of this type of tip in a wide range of application of SECM, including the rapid screening of electrocatalysts and of photoelectrode materials. In addition, the C-ME tip can be used for the study of parallel electrochemical reactions occurring at any finely dispersed electrode materials of interest.

Ringraziamenti

Un grazie enorme e di cuore va alla Professoressa Rondinini e al Professor Vertova: grazie per la fiducia accordatami in questi anni e per la grande opportunità che mi avete offerto.

Grazie al Dottor Alessandro Minguzzi per avermi supportato (e sopportato!) durante questi 3 anni; non saranno due righe ad esprimere la mia gratitudine nei tuoi confronti.

Grazie alla Dottoressa Cristina Locatelli, per la sua compagnia in studio e le colazioni al bar.

Grazie ai compagni di laboratorio. A quelli che ci sono adesso, Albertino, Tomasz, Daniele, Alba: i nostri Negroni day rimarranno nella storia.

A quelli che ci sono stati: Simone, Chiara, Tony, Elisa, Valentina e, soprattutto, la mia carissima Clio: eri la mia compagna di scrivania, ora sei una delle amiche più care che ho.

Grazie alla mia Amica con la A maiuscola, Annalisa: ci conosciamo da più di 15 anni e mi sei sempre stata accanto, senza allontanarti da me neanche quando ne avresti avuto tutte le ragioni.

Grazie a Franco, senza il quale non mi sarei neanche laureata! XD

Un grazie enorme va ai miei genitori, per il loro continuo appoggio, supporto e sostegno in qualunque momento.

Grazie a mia sorella Michela, e a tutte le volte che a detto “che noia!”. Grazie a Tommaso, mio fratello piccolo, ora più alto di me.

Grazie a Nonna Rosy, a nonno Luigi, a nonno Vincenzo, a Zia Carla, a Zia Mafalda e a Ido: mi siete sempre stati vicini, sbracciandosi dalla finestra tutte le mattine o chiamandomi l’ascensore ogni volta che uscivo.

Ora il ringraziamento più grande ed importante di tutti: a Ottavio. Se non ci fossi stato tu il dottorato non l’avrei mai fatto. Mi hai convinta e mi hai accompagnata, aiutata, sostenuta, sopportata in momenti felici, euforici, di sconsolazione, di lontananza.

Ora per noi inizia la Vita, Quella Vera.

Ho ancora un ultimo ringraziamento da fare, un po' doloroso. Grazie alla mia stella personale, la più luminosa: alla mia Nonna Luisa. So che mi avresti sempre appoggiata in questi anni. Ti sento sempre accanto a me.